EXCITED STATES
OF
MOLECULAR HELIUM AND OXYGEN

Peter Collin Hill

Feburary 1991

A thesis submitted for the degree of Doctor of Philosophy at the Australian National University

Preface

This thesis contains no material which has been accepted for the award of any other degree or diploma in any university. To the best of the author's knowledge and belief, no material previously published or written by another person has been included, except where due reference is made in the text.

Peter Collin Hill.

ACKNOWLEDGEMENTS

Many thanks to my chief supervisor Brenton Lewis for his insight and guidance. The friendly technical help from Kevin Lonsdale and Colin Dedman was indispensable. I am also indebted to Alastair Blake for his supervision of the double ion chamber and photoelectron spectrometer projects. I am particularly grateful for the organisation and the many letters written by Sabine Schregel for my research trip to investigate photoelectron spectroscopy in Europe.

The discovery of the new helium dimer ion transition would never have occurred had it not been for the strong support of Lewis Chadderton, Ian Ross, Barry Ninham, and Robert Williams. Financial support for the laser patent from Sr. Margaret Hill is gratefully acknowledged.

Finally I would like to thank Fiona Woods, Michael Hill, Peter Ringwood and Robert Leckey for their careful reading and critiques of many of the manuscripts.

ABSTRACT

The primary objective of this work is to use coupled Schrödinger wave equations (CSE) to interpret the spectra of transitions involving mixed molecular states. The secondary objective is the development of spectroscopic instruments, in particular an ultraviolet laser, tunable near 1244Å, for use as a high resolution light source.

In Part I, the spectrum of $O_2(a^1\Delta_g)$ is measured between 1190 Å and 1540 Å to obtain quantitative cross sections of higher quality than was previously available. This was necessary to take full advantage of absolute cross sections produced by the CSE based calculations. (The analysis carried out by earlier investigators relied mainly on line positions.) Three valence and three Rydberg electronic states are included in coupled Schrödinger equations that theoretically reproduce these new measurements in the region between 1270 Å and 1540 Å (primary objective). This allowed, for the first time, the correct assignment of this region. Most of the structure is due to $\Delta_u - \Delta_g$ transitions with only two bands due to $\Pi_u - \Delta_g$ transitions.

Part II introduces a study of the suitability of helium molecules for a UV laser (secondary objective). The available literature was reviewed. Although this work found no practical far UV laser, two previously unassigned continua in helium discharges are definitively assigned as transitions between the bound $He_2^+(C^2\Pi_u)$ and unbound $He_2^+(A^2\Sigma_g^+)$ electronic states. As in Part I, coupled Schrödinger equations are again used to model a variety of unexplained experimental spectra reported in the literature.

The discovery of $He_2^+(C^2\Pi_u)$ is of theoretical interest as it has at present the smallest observed bond length of any molecule. An arc-laser based on $He_2^+(C^2\Pi_u)$, predicted to be broadly tunable in the visible wavelengths, is described, and a gain feature tentatively assigned. The proposed laser belongs to a new hybrid category: " Ion-excimer lasers ".

In Part III the development of instruments for improved spectroscopic techniques is described. In furtherance of the second objective, the reasons for the selection of krypton for generation of a tunable high resolution light source by four-wave-mixing of laser radiation is explained. Also reported here is an improved technique for the use of double ion chambers and a novel design for a photoelectron distribution spectrometer.

The Appendices contain a $He_2^+(C^2\Pi_u)$ laser patent, additional oxygen spectra, and of particular importance, a summary of the theory of diatomic molecules.

Contents

Part I

O_2 ($a^1\Delta_g$) Absorption Study

Chapter 1

Introduction

1.1 Overview

In this work the absorption spectrum of O_2 ($a^1\Delta_g$) is measured using a 2.2 metre monochromator and an argon continuum light source. This spectrum provides unique information about the singlet,'u' (odd symmetry) Π, Δ and Φ states of oxygen not given by conventional ground state triplet absorption. These states cannot be accessed from the ground state in allowed dipole transitions. It may be seen from Table 1.1 that O_2 ($a^1\Delta_g$) absorption is just one of many symmetries and techniques available to investigate molecular oxygen. Features that are weak and forbidden for one symmetry may be allowed and strong for another. Each technique contributes in a different way to an overview of the excited states of oxygen. This overview, in turn, is useful in the analysis of oxygen spectra.

1.2 Aim of Study

In the years leading up to this study, the Ultraviolet Physics Group at A.N.U. had extensively studied transitions from ground state $O_2(X^3\Sigma_g^-)$. In particular, the following had been developed:

- Stabilized 2.2 m monochromator and an argon continuum lamp source[1, 2].
- Successful description of the Schumann-Runge band system of O_2 between 1750 – 2050 Å using a variety of techniques including a perturbation theory treatment of the predissociation line widths[3, 4].
- Explanation of the band structure of O_2 at wavelengths < 1300 Å by considering the interaction of valence and Rydberg potentials, using coupled Schrödinger wave equation techniques (for examples of the technique involving other molecules see Refs. [5], [6] and [7]).

- Investigation of the rotational structure of forbidden transitions, including improvement of the existing Hönl-London factors[8].

Initial States of Oxygen:

Electronic [a] State	Lifetime (s)	Energy above ground (eV)	Occurrence in Nature	Method of Production	Yield (%)[c]	Probe [b] Technique
$X^3\Sigma_g^-$	∞	0	everywhere	n.a.	100	A,B,C
$a^1\Delta_g$	3876[d]	0.977	30 to 80 Km	bubble[e]	65	n.a.[f]
			Max at 50 Km	O_3 photolysis	100	A
			12 700 Å	**microwave**	**20**	**A**,C
			sky glow	discharge	6	none
$b^1\Sigma_g^+$	12	1.626	7619 Å, 8645 Å	discharge	1	A
			day glow	microwave	0.01	C[g]

Probe Techniques:

Probe	Resolution (Å)	Signal to Noise	Maintenance requirement	Application
A Excimer Lamp	0.06	good	very low	Broad, weak features, states accessed by dipole transitions
B UV laser	0.008	poor	continual	fine structure not covered by 'A'
C Multiphoton ionization	0.008	good	continual	states accessed by two-photon transitions [h]

[a] Isotopes O^{16} and O^{18} are used for additional information

[b] The letter symbol A, B, C, are explained in the bottom table.

[c] Typical values, Yield = $\frac{[\text{Electronic State}]}{[\text{Ground State}]}$

[d] lifetime at room temperature, completely destroyed for T < -100 ^{0} C

[e] for use in COIL laser

[f] contamination problems prevent the measurement of the absorptivity

[g] The identification[9] should be treated with caution due to the low yield [10, 11] of this technique.

[h] i.e. 'g' symmetry states

Table 1.1:**Summary of oxygen studies.**

With this back ground, transitions from $O_2(a^1\Delta_g)$ could be analysed using the computer codes and techniques developed for transitions from the ground state. Knowledge of both ground state and metastable state transitions, together with limited *ab initio* potential calculations, provides a firm interlinking basis from which to analyse the excited states of oxygen.

The absorption spectra of ground state oxygen (triplet) contained features that where attributed to forbidden triplet-singlet transitions. Some forbidden triplet-singlet bands were so weak that they became evident only at liquid nitrogen temperature[12]. The need for more information to conclusively identify these features (triplet-singlet transitions) provided the impetus for the metastable state absorption study in which the analogous transitions (singlet-singlet) are allowed and strong. The symmetry of the metastable molecule, that leads to the additional and complementary information contained in its spectra, also means that it is strongly forbidden to decay to the ground state. Consequently it has a lifetime of one hour [13] making it possible to generate the state and measure its absorption cross section before it decays.

The experimental part of this study aims to produce metastable O_2 $(a^1\Delta_g)$ and measure its UV absorption, while the theoretical part seeks to model these measurements.

Metastable $O_2(a^1\Delta_g)$ absorption has been extensively studied [14, 15, 10, 16] and assigned using classical band analysis. Such analysis is, however, deficient where there is significant valence–Rydberg interaction or perturbation as found in the $O_2(a^1\Delta_g)$ spectrum. **This study applies coupled Schrödinger wave equation techniques to account for valence-Rydberg potential interactions.**

This study provides:

- correct assignment of metastable absorption features,
- semi-empirical potential curves,
- examples of coupling.

The study confines itself to the analysis of the 1270 Å – 1540 Å region. With the large amount of data collected, and the techniques available, there is scope for many further detailed investigations. For instance, the analysis of the 1260 Å metastable oxygen feature (Fig. C.5) involves the use of twenty or more coupled equations and is outside the scope of this thesis. Some of the additional scans are contained in Appendix C.

The scientific interest in O_2 $(a^1\Delta_g)$ is largely centred on the aforementioned spectroscopic information, and atmospheric observations. The reactions in the atmosphere involving this state will be discussed briefly in the following section, by way of introduction, because they yield insights into the methods of metastable production encountered in this study. In Chapter 2 the methods of production are then reviewed and the reason for the use of the microwave generation technique discussed. The apparatus is then outlined; the function of the individual components is described. Chapter 3 gives an account of how the experimental outputs are converted into cross sections. The

experimental results obtained with this apparatus are then presented and interpreted in Chapter 4, while the theoretical background behind the interpretation included in Appendix A.

1.3 Industrial and Atmospheric Importance

Recently the metastable state has aroused commercial interest as the basis for a chemical oxygen-iodine laser (COIL) which operates in the near infra-red 13 150 Å[17]. It is reported to have an efficiency of conversion of chemical to light energy of greater than 75% [17].

The metastable state is produced in the atmosphere by the photodissociation of ozone[18]. Some of the relevant chemical reactions are given in the following table:

$O_2 \xrightarrow{h\nu} O + O$
$O_2 + O + X \rightarrow O_3 + X, X = O_2, N_2$ etc.
$O_3 \xrightarrow{h\nu} (a^1\Delta_g)O_2 + (^1D)O$
$(^1D)O + O_2 \rightarrow (b^1\Sigma_g^+)O_2 + (^3P)O$
$(^1D)O \rightarrow (^3P)O + h\nu_{6300\mathring{A}}$
$(a^1\Delta_g)O_2 \rightarrow O_2 + h\nu_{12000\mathring{A}}$
$(a^1\Delta_g)O_2 + (a^1\Delta_g)O_2 \rightarrow O_2 + (b^1\Sigma_g^+)O_2$
$(a^1\Delta_g)O_2 + O_3 \rightarrow O_2 + O_2 + O$

Table 1.1: Atmospheric Reactions

The ozone layer exists at altitudes between 10 and 50 Km, with a maximum concentration at 25 Km. Ozone is bound by approximately 1 eV and can liberate about 4 eV of energy in an oxidizing reaction. Ozone absorbs weakly in the infra-red and visible wavelengths. At light energies in the ultraviolet (the Hartely continuum) there is sufficient energy to break the ozone bond and form the spinless atomic (^1D) and molecular ($a^1\Delta_g$) excited states.

In the atmosphere this state is found [1] chiefly between 30 and 80 Km [18]. Once produced, it may survive to decay naturally to the ground state and produce the observed glow at 12 000 Å. Alternatively it may be quenched by other gas molecules[19]. Wayne[20] discusses of the role of this state in the terrestrial, and planetary atmospheres.

[1] by rocket studies

Chapter 2

Experiment

2.1 Previous Approaches: Photographs and Photomultipliers

In 1967 Huffman *et al.* identified metastable $O_2(a^1\Delta_g)$ absorption in microwave excited oxygen[21]. By the early 1970s these absorption bands had been thoroughly investigated. The work took the form of photographic studies [15, 14], and quantitative (but lower resolution) measurements of the absorption with a photomultiplier[10]. The former provided the exact wavelength location of spectral features, as the photographs themselves could be accurately calibrated. The latter allowed absorption to be quantitatively measured[1] because the photocurrents gave a linear representation of the amount of light accepted. These two approaches culminated in the tentative identification of many bands. The weaker features and the broad structure of the absorption continuum were yet to be adequately explained. A more detailed study was required; that would produce spectra with the details found in the photographs, and accurate values for the relative absorption found in the quantitative studies. Modelling of the bands (here measured) would then allow definitive assignments. With this knowledge, the modelling of the experimental spectrum could guide the development of semi-empirical potential curves and couplings.

The current study, which used photomultipliers, could then rely: 1) on the use of the photographic studies, atomic emission and absorption lines for wavelength calibration and, 2) on the broad quantitative studies to select the best operating parameters under which to measure a particular band or wavelength region.

[1] to an accuracy of 20 – 50 %

2.2 Methods of Metastable Production

Four methods have been used to produce metastable oxygen: bubble-type chemical generation, photolysis of ozone, microwave method, and pulsed discharge.

2.2.1 Chemical

The bubble-type chemical generation used for COIL (see Sec. 1.3) is inappropriate for the generation of the metastable state for spectroscopic purposes because of contamination by the other reagents. The generation involves the bubbling of chlorine gas through a basic solution of hydrogen peroxide to generate at best a 60% yield [22] of metastable state oxygen,

$$H_2O_2 + 2NaOH + Cl_2 \rightarrow O_2(^1\Delta) + H_2O + 2NaCl \quad . \tag{2.1}$$

The metastable state is used to populate an atomic level of iodine, that then lases. The contamination problem leaves the photolysis of ozone and the microwave methods as the only viable techniques. The former produces near $> 95\%$ [19] metastables while the latter produces at most 20% [10]. The following discussion will relate the details of each method and then justify the selection of the microwave method for the production of metastables in this study.

2.2.2 Photolysis of Ozone

Photolysis of ozone [23] involves the production and concentration of ozone, and then its photodissociation with a light source emitting over the range of 2000 – 3000 Å (this is analogous to the production of $O_2(a^1\Delta_g)$ in the atmosphere). The production of ozone is typically done with a commercial ozonator. In such an apparatus, a high tension supply strikes a silent discharge across neon, a glass wall, and flowing oxygen. Some 4% yield of ozone is achieved. Traditionally, the concentration of ozone was achieved by liquification at its condensation temperature of -80° C [19]. This process is dangerous as liquid ozone is explosive. Investigators[23] were able to circumvent this problem by condensing the ozone in cooled silica gel normally used for removing moisture. The coolant used was a mix of dry ice and acetone. Special silica gel has to be used, as the moisture indicating dye normally found in commercial supplies renders it ineffective for the absorption of ozone. The gel is then isolated and pumping on it extracts pure ozone, which is then subjected to light from a krypton dimer lamp. The oxygen atoms produced are removed by passing the mixture over hot MnO_2. The result is 100% yield of metastable $O_2(a^1\Delta_g)$ state.

A 100 % metastable fraction would be desirable in the situation where the absorption of ground state oxygen presents difficulties. The region 1270 – 1540 Å did not require this yield to produce results. In general, the weaker absorption continuum of the metastable state is smooth and broad and can be adequately resolved in the presence of a groundstate background. Also, the rotational structure found in the bands is relatively strong and can therefore be resolved. It was decided that

the limited advantages of having near 100% metastable yield were outweighed by the advantage of simplicity that the lower yield microwave excitation technique offered.

2.2.3 Microwave Generation

The microwave excitation technique involves the production of the metastable state through electron impact. A microwave cavity [24] is coupled to a tube that supplies a flow of oxygen to the absorption cell. Energy supplied at 2450 MHz (as per a domestic microwave oven) drives the discharge. The initial source of ions is supplied by a high voltage tickler. The discharge extends from the walls of the supply tube in towards the centre. The ion concentration attenuates the microwave energy due to a skin effect. A total pressure of at least 0.5 Torr is desirable to make repetitive striking of a discharge easy. An argon or helium buffer gas was used to raise the total pressure for a given partial pressure of oxygen < 0.5 Torr [10]. In this study, this process gave a yield of metastables in the range 6.5 – 13 %. The yield depended only on the partial pressure of oxygen and was unaffected by the power level of the microwave discharge. This study found, in agreement with Ogawa and Ogawa[10], that the optimum yield was acheived using 0.2 Torr partial pressure oxygen.

That flowing conditions are only required in the microwave, but not the photolysis technique, suggests that the flow is not required simply to reduce quenching by impurities. Possibly, the build up of species produced by the microwave discharge could destroy this metastable state.

2.2.4 Pulsed Discharge

Vasileva *et al.*[25] investigated pulsed electrical discharges as an energy efficent technique of producing the metastable state for COIL lasers. Although few details of the apparatus used are reported, the requirement for vacuum feed-throughs make it more difficult to build than the microwave technique (for which one simply clips on a cavity). Although Vasileva *et al.*[25] say the technique is capable of producing 17%, yield the maximum percentage actually reported was less than 6%. By comparision the microwave technique is more efficent and simple than the pulsed discharge technique.

In summary, the microwave technique produces only $\sim$ 10% metastables and thus is more limited in terms of the wavelength range of the spectrum that it can access. Its advantages are the simple implementation of the technique and the ease with which it can be reliably automated - switching on and off the microwave generator enables the subtraction of the ground state contribution. Of the two techniques suitable for this work – photolysis of ozone and microwave excitation – the overall simplicity of the microwave technique led to its selection.

2.2.5 Production at Low Temperatures

One significant deficiency in previous work was the lack of observations of the absorption spectrum at low, liquid nitrogen temperature. A finding in the current work is that **there are no metastables present at temperatures below -100° C** and this naturally prevented measurement at liquid nitrogen temperature. A thermocouple monitored the cell temperature, while the average temperature of the gas could be checked by observation of the ground state oxygen spectra. The metastable state oxygen could be seen to disappear over a range of a few degrees. A seperate apparatus would have to be built, capable of cooling the cell to specified temperatures, in order to determine the exact cut off temperature. The spectra of the cold gas would have been less convoluted with higher rotational lines, and thus serving as a significant aid to analysis.

2.3 Experimental Apparatus

The apparatus consists of a light source, a monochromator, an absorption cell, and a light detector (Fig. 2.1).

The initial attempts to measure the absorption of the metastable state used the existing standard absorption apparatus that had been used for ground state studies. In this configuration, the lamp was connected directly to the monochromator with the desired wavelength emerging from the exit slit. A beam splitter then diverted some of this light to be monitored, the rest passing though an absorption cell to be detected. These attempts failed due to the fact that ultraviolet light was produced by the microwave excited oxygen. The excitation region was placed a considerable distance from the cell with several bends in the connecting tubing to break the direct optical path. A dog-legged pin-hole in a teflon block was placed in the tubing to eliminate the possibility of reflected light reaching the absorption cell. The unwanted light signal was undiminished, indicating that excited species were flowing around the bends into the region, and glowing. The glowing species was not determined as the glow was too weak to be analysed with a monochromator but the registration of the signal in a solar-blind photomultiplier meant the light must have been ultraviolet. Such glow could in principle be subtracted, but in practice the background light signal swamped the desired signal, rendering this configuration useless.

The final configuration was similar to that used by other metastable oxygen investigators [14, 10], with the absorption cell placed between the lamp and the monochromator (which discriminated against the unwanted absorption cell glow)

The monitor, which detected the light before it entered the cell, was not adversely affected by the glow from it. This was because the lamp light at this range is now many orders of magnitude brighter than the glow.

The inclusion of a monitor, the degree of automation, and the techniques used to limit the degradation of the windows in the system, are some of the ways in which some improvements have

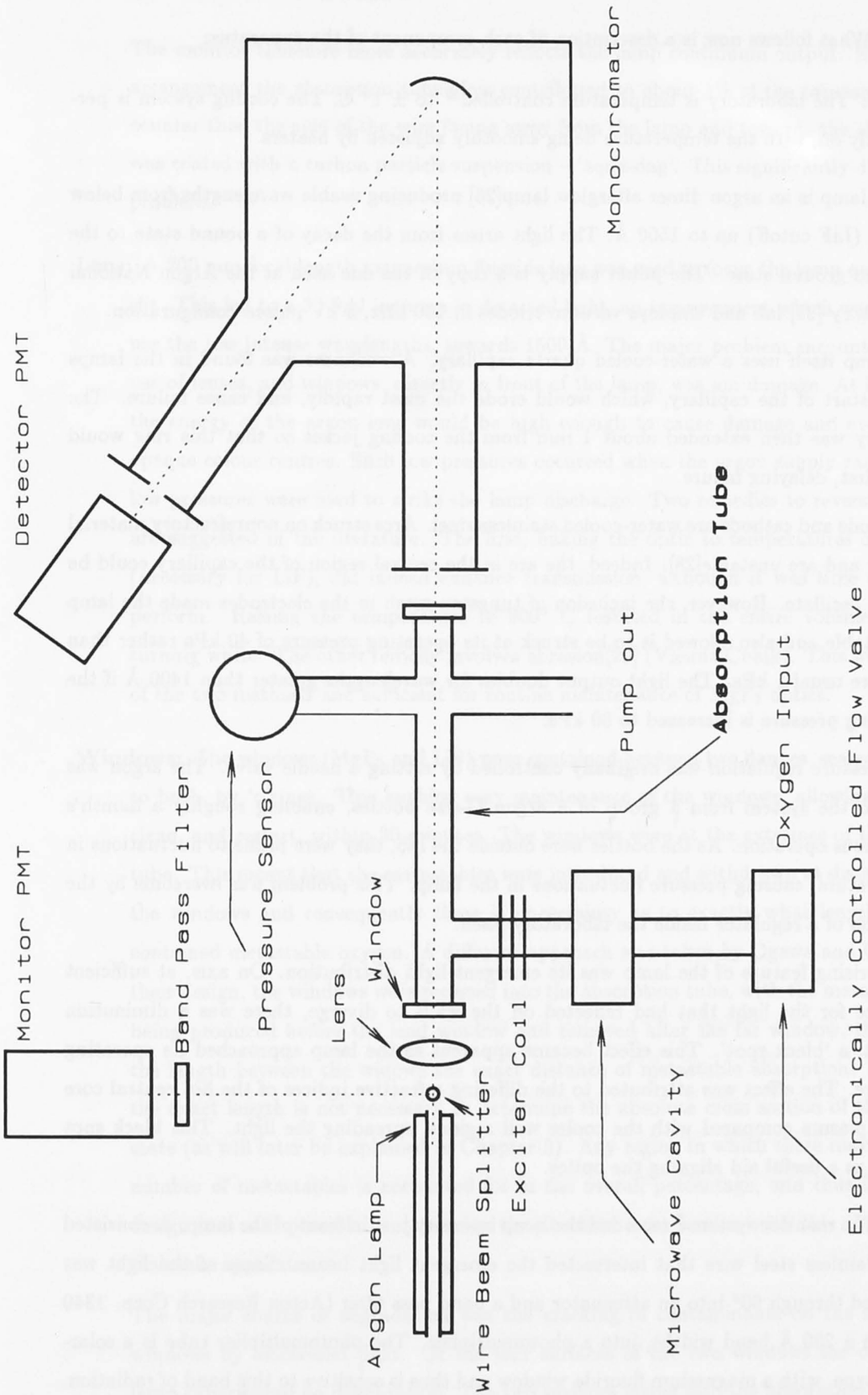

Figure 2.1: Apparatus

been made. What follows now is a description of each component of the apparatus:

Laboratory: The laboratory is temperature controlled [2] to $\pm$ 1^o C. The cooling system is permanently on, with the temperature being smoothly adjusted by heaters.

Lamp: The lamp is an argon dimer afterglow lamp[26] producing usable wavelengths from below 1090 Å (LiF cutoff) up to 1500 Å. The light arises from the decay of a bound state to the unbound ground state. The power supply is a copy of the one used at the Argon National Laboratory [27] lab and employs vacuum triodes in 100 kHz, 5 kV pulsed configuration.

The lamp itself uses a water-cooled quartz capillary. A weakness was found in the lamps at the start of the capillary, which would erode the most rapidly, and cause failure. The capillary was then extended about 1 mm from the cooling jacket so that this ring would erode first, delaying failure.

The anode and cathode are water-cooled stainless steel. Arcs struck on nonrefractory material wander and are unstable[28]. Indeed, the arc in the central region of the capillary could be seen to oscillate. However, the inclusion of tungsten mesh in the electrodes made the lamp more stable and also allowed it to be struck at its operating pressure of 40 kPa rather than the more usual 1 kPa. The light output doubles for wavelengths greater than 1400 Å if the operating pressure is increased to 80 kPa.

The pressure regulation was originally controlled by setting a needle valve. The argon was fed into the system from a group of 8 argon G-size bottles, enabling roughly a month's continuous operation. As the bottles were outside the lab, they were prone to fluctuations in temperature, causing pressure fluctuations in the lamp. This problem was overcome by the inclusion of a regulator inside the laboratory itself.

A surprising feature of the lamp was its emergent light distribution. On axis, at sufficient distance for the light that had reflected off the walls to diverge, there was a diminution of light, a 'black spot'. This effect became apparent as the lamp approached its operating pressure. The effect was attributed to the differing refractive indices of the hot central core of the plasma compared with the cooler wall regions, spreading the light. This black spot served as a useful aid aligning the optics.

Monitor: The monitor system [3] recorded the lamp intensity just in front of the lamp. It consisted of a stainless steel wire that intersected the emergent light beam. Some of the light was reflected through 90^o into an attenuator and a band pass filter (Acton Research Corp. 1340 Å with a 200 Å band width), into a photomultiplier. The photomultiplier tube is a solar-blind type, with a magnesium fluoride window and thus is sensitive to this band of radiation.

[2] control system designed and built by Colin Dedman, U.V. Physics Group, ANU.

[3] designed and built by Colin Dedman, UV Physics Unit, AMPL, Canberra.

The monitor therefore more accurately reflects the lamp continuum output. Even with this arrangement the absorption tube glow contributed to about 1% of the measured signal. To counter this, the side of the wire facing away from the lamp and towards the absorption cell was coated with a carbon particle suspension – 'aqua-dag'. This significantly diminished the problem.

Lens: A 200 mm focal length magnesium fluoride lens was used to focus the lamp output onto the slit. This led to a 30 fold increase in detected light, an improvement which was necessary to use the less intense wavelengths, towards 1500 Å. The major problem encountered with the use of lenses, and windows, directly in front of the lamp, was ion damage. At low pressures, the energy of the argon ions would be high enough to cause damage and eventually form opaque colour centres. Such low pressures occurred when the argon supply ran out or when low pressures were used to strike the lamp discharge. Two remedies to reverse the damage are suggested in the literature. The first, baking the optic to temperatures of 500° C [29] (necessary for LiF), did indeed enhance transmission, although it was time consuming to perform. Raising the temperature to 900° C resulted in the entire volume of the optic turning white. The other remedy involves abrasion[29] (Vienna Chalk). This was the quicker of the two methods and sufficient for routine maintenance of MgF_2 optics.

Windows: The windows (MgF_2 and LiF) were contained between two flanges, sealed with respect to both, by 'o'rings. This enabled easy maintenance of the windows, allowing a shutdown, clean, and restart, within 30 minutes. The windows were at the extremes of the absorption tube. This meant that the metastables were introduced and withdrawn at distances between the windows and consequently there is uncertainty as to exactly what length of the tube contained metastable oxygen. A different approach was taken by Ogawa and Ogawa[10]. In their design, the windows were recessed into the absorption tube, with the metastable oxygen being produced before the lead window and removed after the far window, thereby having the length between the widows the exact distance of metastable absorption. Knowledge of the exact length is not necessary to determine the absolute cross section of the metastable state (as will later be explained in Chapter 3). Any region in which there may be a reduced number of metastables is accounted for in the overall percentage, and thus in the current design it is still possible to determine the absolute cross section with this simpler, easy to maintain apparatus.

The major source of degradation was the cracking of contaminants on the surface of the windows by ultraviolet light. Of the four surfaces of the two windows the one facing the lamp experienced no degradation. The two surfaces facing into the absorption tube decayed rapidly when the tube was evacuated (which was done every two data points in order to monitor the lamp flux). The degradation was avoided and even reversed by running the

microwave discharge at high power with 0.5 Torr of oxygen for several minutes. The surface facing the monochromator vacuum was then apt to decay the most rapidly. In the absence of a lens, the central region of this window would quickly develop a brown film. This region corresponded to a minima in the output of the lamp. The extra intensity of light incident upon the window originated from reflection from the walls of the tube. The final solution was that of filling the monochromator with argon. This removed the need to place light baffles in the absorption tube to reduce the extra light reflected from the walls. By supplying a pressure of argon on the far side of the window, and never letting it be pumped down by the diffusion pump, the system could be operated for several weeks without maintenance. This source of difficulty may have been why Yamawaki[14] decided not to employ a far window, but to use a differential pumping system instead.

Absorption Tube: The tube is fabricated from quartz so that it may be reliably cycled down to liquid nitrogen temperatures. The tube provided for an absorption length of 30 cm. The metastables were introduced at a junction some 30 mm from the front end of the tube. The inlet tube passed through the liquid nitrogen cooling jacket and then extended for a distance beneath this in order to allow the attachment of a microwave cavity and an exciter coil. This was then connected by flexible stainless steel bellows to the gas inlet, an arrangement which essentially put little mechanical strain on the quartz. The lamp end of the main tube was sealed onto a window via an aluminium flange. This small amount of metal exposed to the gas did not measurably affect the metastable production. The monochromator side of the main tube was sealed onto a window, and then this onto the monochromator. The entire assembly was held together in a teflon block, which included a pressure measuring port and a extraction port. The block had to be baked at 300° C for 24 hours before it was clean enough not to cause serious contamination problems.

Liquid Nitrogen Operation: The cell has a jacket for liquid nitrogen which is filled from a 4 litre dewar. The ends of the main tube are heated with nichrome wire to maintain the 'o'rings at room temperature. Temperature sensors and the spectrum of ground state oxygen confirmed that the cell reached liquid nitrogen temperatures, however, the metastables had completely disappeared by $\sim$ -100° C. As the microwave generator is at room temperature, the metastables are created but then destroyed upon entering the cooler regions. At present there is insufficient information about the absence of the metastable species at low temperature to offer even a speculative explanation.

Microwave Excitation System: The system employed a standard medical 2450 MHz microwave power supply (Kiva Instrument Company) and Evenson cavity[24] (Opthos Instrument Company). The cavity clipped around the inlet tube. The total pressure of gas necessary to strike the discharge was greater than 0.5 Torr. The yield of metastables was not power dependent

after the discharge glow had extended across the entire cross section of the tube. Additional power beyond this level only created more atomic oxygen. Although in theory this would boost the effective fraction of metastable to ground state oxygen, high power conditions led to a more variable output. At low powers there is no longer the need for forced air cooling of the cavity. Traditionally a Tesla coil 'Tickler' is necessary to strike the discharge. Such a device is very electrically noisy, sending spurious signals to the photon counting systems and moving the monochromator through its automated drive. A wire coiled a few times around the inlet tube and driven at 50 Hertz and 2500 V provided a low-noise method of striking the discharge. The fact that the exciter and the microwave power could be switched on and off by computer allowed this to be done for each data point.

Pressure Control: The pressure was measured using a capacitance manometer (Datametrics Barocel pressure sensor). This was placed at the end of a tube leading to the end of the main absorption tube. As there was no net flow of gas in the tube leading to the manometer there was no pressure drop across its length and thus the pressure measured was that at the end of the main absorption tube. There is, however, a pressure gradient down the main tube and thus the measured pressure is not the average pressure. The main role of the manometer was to maintain constant flow conditions. This was done with control circuitry and a servo valve. The pressure control was only needed for the maintenance of constant conditions, as the cross section for the metastable state was deduced from the ground state cross section, which in turn was determined in static conditions.

The opportunity was taken, whenever the cell was emptied for each data point, to re-zero the manometer.

Monochromator: The process of optimizing the 2.2 metre normal incidence VUV scanning monochromator (Minuteman) took place over several years [1, 2]. Over the two years the data was taken, there was no degradation in the 0.06 Å resolution, and over months of continuous operation there were drifts of less than 0.5 Å. The monochromator was mechanically stabilized with additional supports, the entire system being encased in a foam and perspex cabinet/oven, temperature controlled to $\pm 0.2^{o}C$. The lead screw and cam were replaced and remachined, to improve accuracy, and the residual lead screw error measured, tabulated and accounted for in the results. No wavelength drift was observed if the wavelengths were changed at slower speed by the computer control rather than the faster external control. Calibration lines from impurities in the lamp are listed in Appendix C. The calibration of each scan was routinely checked with these lines, which were stored in a file and superimposed on lamp spectra.

Light Detection: Magnesium fluoride (EMI G26 E314) and, later on in the program, lithium fluoride (EMR 5429) windowed solar-blind photomultipliers were used in photon counting

mode[30]. Essentially the gains were set to saturation so that each pulse counted corresponded to a photon incident on the tube. Pulse counting has the advantage of being insensitive to drifts in the gain of the photomultipier tubes.

Computer Control: The system was fully automated and could take data for days unattended, controlled by an IBM compatible PC running a fourth generation language called 'Asyst'[31]. In particular, the following tasks were some of those performed by the computer:

1. move to a wavelength accounting for
   - backlash
   - lead screw error
   - last calibration
2. read the light counts and subtract the backgrounds
3. control the pressure
4. monitor the cell and room temperature
5. cycle the system through
   - measure light with no gas in the cell
   - fill cell to a particular pressure
   - ground state oxygen measurement
   - measurement with microwave on
   - move to the next wavelength
   - measurement with microwave on
   - ground state oxygen measurement
   - empty cell
   - measure light with no gas in the cell
   - move to the next wavelength

The cycle is organised to acquire two data points for every cycle of filling and emptying.

Processing of Data: The data was transferred from the control computer to a mainframe. Files of emission lines, and results from other investigators could then be used to check and, if need be, calibrate the wavelengths. Curves were superimposed and the effective number density of the various species deduced. The exact procedure is outlined in Chapter 3.

Chapter 3

Cross Section Calculation

3.1 Determining the Percentage Yield of Metastables

In this experiment, the light from the lamp is measured for three different absorption conditions: absorption cell **empty**; absorption cell with a pressure, P, and the microwave discharge **off**; and absorption cell with a pressure, P, and the microwave discharge **on**. I_{empty}, I_{off}, and I_{on} can be divided by the monitor counts of the respective counting periods to account for lamp fluctuations between the periods. Although this source of error is reduced, the three additional numbers increase the statistical error. Let q = $\left(\frac{1}{cell\ length \times number\ density}\right)$ cm^2 then, at a given wavelength of light, for a metastable state yield, r ;

$$\begin{aligned} \sigma_{metastable} &= \frac{1}{r}(\sigma_{total} - (1-r)\sigma_{ground}) \\ &= \frac{1}{r}\frac{1}{q}\left(ln(\frac{I_{on}}{I_{empty}}) - (1-r)ln(\frac{I_{off}}{I_{empty}})\right) . \end{aligned} \tag{3.1}$$

The metastable yield, r, is a function of the pressure, the absorption cell geometry, and the microwave discharge conditions. A single parameter, r, has to be determined to produce the correct shape of metastable oxygen spectrum albeit in relative units. For band analysis and for the coupled Schrödinger wave equation simulations, it is the *shape* of the absorption spectrum that provides a significant amount of information.

Ogawa and Ogawa[10], who were the first to make quantitative measurements of the metastable state, adjusted r such that they got $\sigma_{metastable} = 0$ at 1500 Å. (The theoretical model presented later confirms that the cross section is comparitively small at this wavelength, $\sim 10^{-19}$ cm^2.) This principle may be extended and r selected so that:

1. $\sigma_{metastable} > 0\ \forall\lambda$,

2. $\sigma_{metastable}$ made equivalent to a known magnitude,

3. $\sigma_{metastable} = 0$ where theoretically predicted,

4. $\sigma_{metastable}$ has no σ_{ground} structure,

5. there is consistency in shape of the overlap with adjoining scans taken under different conditions.

Using computer graphics to superimpose scans, it was possible to select quickly a value for r that best met the above criteria. The selection of an appropriate r is illustrated in Fig. 3.1 (The ground state bands are assigned in Ref. [32], the metastable state in Ref. [14]) To assist in this process most scans were made under standardized conditions : microwave power at 2 – 6 watts; measured pressures of 3 and 1 Torr for 100% O_2 or 1.6 and 0.8 Torr for 10% O_2 in argon. As r can be expected to be fixed for a particular set of conditions, standardized conditions limited the number of different values of r and assisted cross-checking, while the variety of conditions allowed the transmission to be selected that gave the best results. Scans of weak features were extended to include identifiable strong features to ensure fidelity. r was in the range of 6 to 12% and was able to be determined to an accuracy of ± 0.5%.

The error in $\sigma_{metastable}$ associated with an error in r is given by differentiating Eq. 3.1 to give;

$$\Delta\sigma_{metastable} = \Delta r \frac{\sigma_{metastable} - \sigma_{ground}}{r} \tag{3.2}$$

Thus if r is overestimated, $\sigma_{metastable}$ will be too low for $\sigma_{metastable} < \sigma_{ground}$ and too high for $\sigma_{metastable} > \sigma_{ground}$.

In the microwave technique, the effect of atomic oxygen is an issue that is still to be adequately resolved. Atomic oxygen is produced by the microwave discharge, particularly at higher powers[10]. For the wavelengths under investigation, it only has line absorption, so for most of the spectrum is it a completely transparent gas, not impacting on the shape of the spectrum, as r is selected so as to generate the correct shape. The magnitude of the metastable state cross sections will be underestimated in proportion to the amount of atomic oxygen present. (For example, if there is 1% atomic oxygen, 10% metastable state, 89% ground state oxygen, the metastable oxygen cross section will be underestimated by 10%). In practice, this means that the deduced dipole transition moments will be low, but the semi-empirical curves, the various coupling strengths, and the explanation for the metastable state spectrum (all of which are deduced from the shape), will still be accurate. As microwave power increased, the metastable yield remained constant but more atomic oxygen was produced[10]. Naturally, this suggested that the lowest practicable power be used and low powers were used in this study.

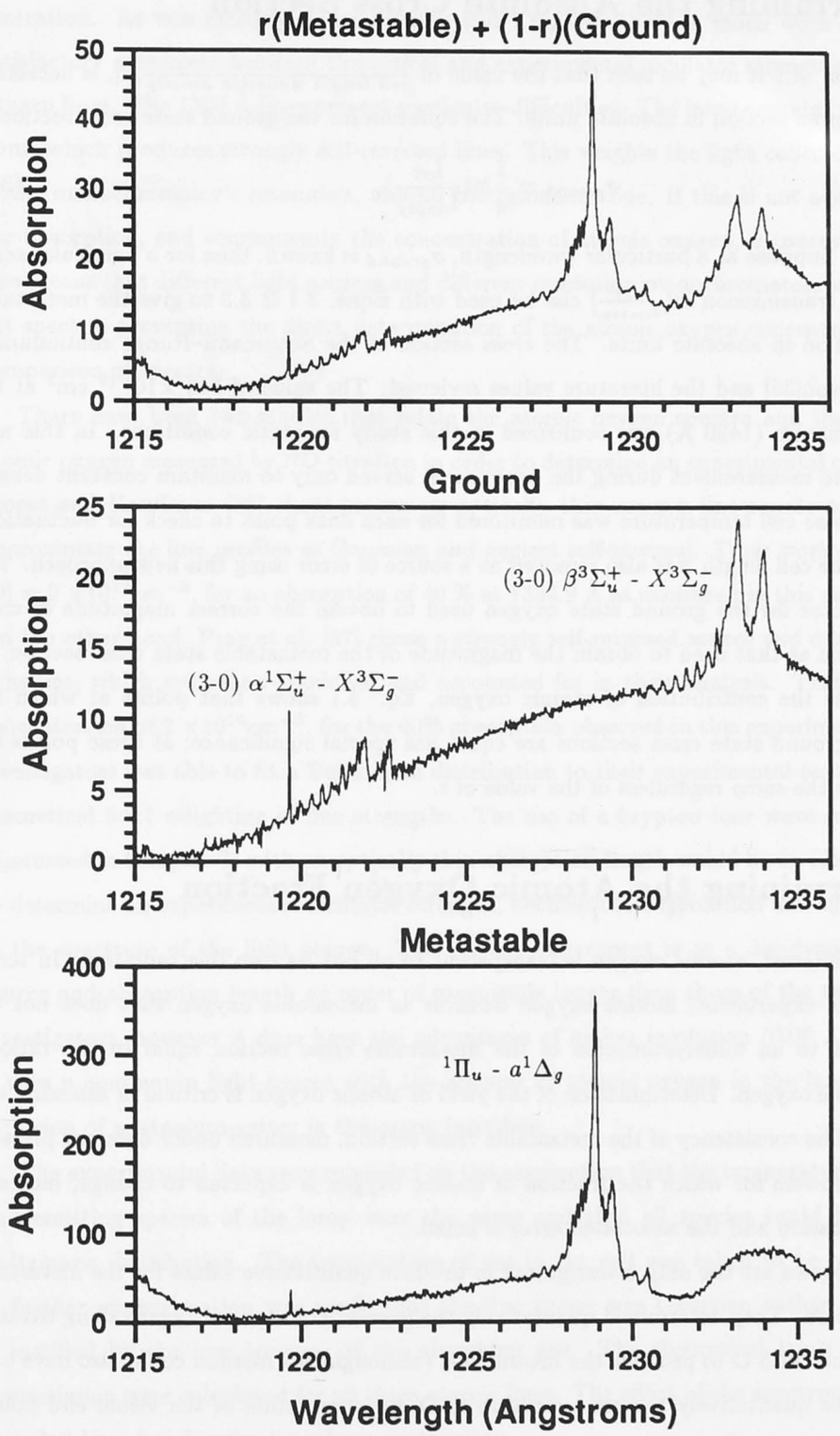

Figure 3.1: Subtraction of the ground state spectrum (middle) from the microwave excited spectrum (top) with r = 10% yields the metastable state spectrum (bottom). The ground state spectrum would then be scaled to give the correct absorption units. The feature occurring at $\sim$ 1219.5 Å is caused by noise pick-up during the empty cell measurement for that channel.

3.2 Determining the Absolute Cross Section

From the equation 3.1 it may be seen that the value of $\frac{1}{cell\ length \times number\ density}$, q, is necessary to calculate the cross section in absolute units. The equation for the ground state cross section,

$$\sigma_{\text{ground}} = \frac{1}{q}\ln(\frac{I_{\text{off}}}{I_{\text{empty}}}), \tag{3.3}$$

yields this value. Suppose at a particular wavelength, σ_{ground} is known, then for a particular scan, the ground state transmission $\ln(\frac{I_{off}}{I_{empty}})$ can be used with Eqns. 3.1 & 3.3 to give the metastable oxygen cross section in absolute units. The cross section of the Schumann–Runge continuum is measured by Gibson[33] and the literature values reviewed. The value of 143 $\times 10^{-19}$ cm^2 at the peak of the continuum (1420 Å) was confirmed in this study for static conditions. In this new approach, pressure measurement during the experiment served only to maintain constant density conditions. Likewise cell temperature was monitored for each data point to check for fluctuations during a scan. The cell length was also removed as a source of error using this new approach. The multiplication factor for the ground state oxygen used to obtain the correct magnitude of cross section is the same as that used to obtain the magnitude of the metastable state cross section.

If one neglects the contribution of atomic oxygen, Eq. 3.1 shows that points at which the metastable and ground state cross sections are equal has special significance; at these points the cross sections are the same regardless of the value of r.

3.3 Determining the Atomic Oxygen Fraction

In the region of interest, atomic oxygen is transparent to all but its own line radiation. In terms of the metastable experiment, atomic oxygen behaves as metastable oxygen that does not absorb. This leads to an underestimation of the metastable cross section equal to the ratio of atomic/metastable oxygen. Determination of the yield of atomic oxygen is critical in assessing this source of error. The consistency of the metastable cross section, measured under different pressure and microwave powers for which the fraction of atomic oxygen is expected to change, indicates that the concentration and the associated error is small.

Ogawa and Ogawa are the only investigators to produce quantitative values for the metastable oxygen cross section. They determined qualitatively the presence of atomic oxygen, using titration of NO which reacts with O to produce the brown NO_2 (although this method could also have been used to determine quantatively the concentration of O, by observation of the visual end point). Ogawa and Ogawa found that the yield of metastable species was independent of microwave power but that the O yield increased with power. Thus in Ogawa's experiment the microwave power was kept to a minimum, and this was followed in the current study.

This current investigation did, however, measure atomic absorption lines. The amount of absorption and the oscillator strength could then be used to determine the atomic oxygen con-

centration. As was recently noted by Hey and King[34], there is much work needed to obtain satisfactory agreement between theoretical and experimental oscillator strengths for many atomic oxygen lines. The 1300 Å lines present particular difficulties. The lamp contains trace oxygen (< 3 ppm) which produces strongly self-reversed lines. This weights the light collected in a bandwidth of the monochromator's resolution, around the resonance line. If this is not adequately modelled the absorption, and consequently the concentration of atomic oxygen, is overestimated[35]. This also means that different light sources and different resolution monochromators will produce different spectra, preventing the direct determination of the atomic oxygen concentration through the comparison of spectra.

There have been two studies that relate the atomic oxygen spectra and the concentration of atomic oxygen measured by NO titration in order to determine an experimental oscillator strength. Morse and Kauffman [36] chose to use an optically thin oxygen line source so that they could approximate the line profiles as Gaussian and neglect self-reversal. Their work predicts the value $[O] = 2 \times 10^{12} cm^{-3}$, for an absorption of 40 % at 1304.9 Å as measured in this current experiment. On the other hand, Prag et al. [37] chose a strongly self-reversed source and much higher number densities, which were later modelled and accounted for in their analysis. Their work suggests a concentration of $2 \times 10^{14} cm^{-3}$, for the 40% absorption observed in this experiment. Neither of the investigators was able to fit a Boltzmann distribution to their experimental results and attain the theoretical 5:3:1 weighting of line strengths. The use of a krypton four wave mixing light source (discussed in Chapter 7) with an optically thin absorption length would be an ideal tool with which to determine an experimental oscillator strength, because of its resolution and the lack of structure in the spectrum of the light source. The current experiment is at a disadvantage, with a light source and absorption length an order of magnitude longer than those of the two aforementioned investigators, however it does have the advantages of higher resolution (0.06 Å – 1 Å), and that it uses a continuum light source with the amount of atomic oxygen in the lamp reduced by the inclusion of a titanium getter in the argon inlet line.

The experimental data were modelled on the assumption that the temperature of the absorbing and emitting species of the lamp were the same and that all species could be described by a Boltzmann distribution. The temperature of gas in the cell was taken to be room temperature. A further approximation was made that the line shape was Gaussian rather than Voigt. This is justified by the low pressure of the absorbing gas. The theoretical lamp emission and cell transmission were calculated for all three atomic lines. The effect of the spectrometer function was included by a fast Fourier transform convolution.

For a Doppler broadened self-reversed emission with a continuum background,

$$I_o = (A\mu e^{-Bx^2} + C)e^{-D\mu e^{-Bx^2}}, \tag{3.4}$$

where A, C etc. are constants to be determined, while μ is the population of the level

λ(Å)	1302.2	1304.9	1306.0
ΔE (eV)	0	0.01970	0.02770
μ	5τ	3τ	1τ

Table 3.1: Wavelengths, energies amd populations of atomic oxygen

and τ is the Boltzmann factor for a level at a particular temperature. Thus I_o is fitted by the factors A,C,D and the temperature.

The emission transmitted through the absorbing cell is given by

$$I_a = (A\mu e^{-Bx^2} + C)e^{-D\mu e^{-Bx^2} - F\mu e^{-Gx^2} - H}, \tag{3.5}$$

with the additional factors of the atomic and molecular absorption F and H respectively to be determined. Atomic oxygen has a Doppler width at room temperature G equivalent to 0.237 cm^{-1}.

All six lines, three emission and three transmission, were similtaneously fitted. The conditions used produced 10% yield of metastable states in 0.1 Torr partial pressure of oxygen with 2 watts of microwave energy. The emission line at 1306 Å is the most optically thin and thus least in error. The value of the F parameter for the three lines was found to be 2.2 $\pm$0.1. With a cell length of 30.6 cm this F parameter corresponds to an absorbtivity, σ' of 0.16 $\pm$ 0.03. The concentration of atomic oxygen, [O], is then given by

$$[\mathrm{O}] = 1.13 \times 10^{12}/f \int \sigma'(\mu)\delta\nu \quad . \tag{3.6}$$

For a theoretical oscillator strength[38] f of 0.031,

$$\begin{aligned}
[\mathrm{O}] &= 1.13 \times 10^{12}/0.031 \times 0.16 \pm 0.03 \times 0.237 && (3.7)\\
&= 6.1 \pm 0.4 \times 10^{11} cm^{-3} && (3.8)\\
&= 1.7 \pm 0.1 \times 10^{-5} Torr && (3.9)\\
[O]/[O_2(a^1\Delta_u)] &= 1 \times 10^{-2}/4.3 \times 10^{-5} Torr && (3.10)\\
&= 0.17 \pm 0.1\%. && (3.11)
\end{aligned}$$

The presence of atomic oxygen thus leads to an underestimate of the singlet cross section of < 0.2%.

3.4 The Impact of Ground State Oxygen

Although the absorption due to the ground state species was subtracted to give the cross section for the metastable species, there is a certain minimum transmission at which saturation effects are seen. This is illustrated in Fig. 3.4. The stray light was determined at various wavelengths

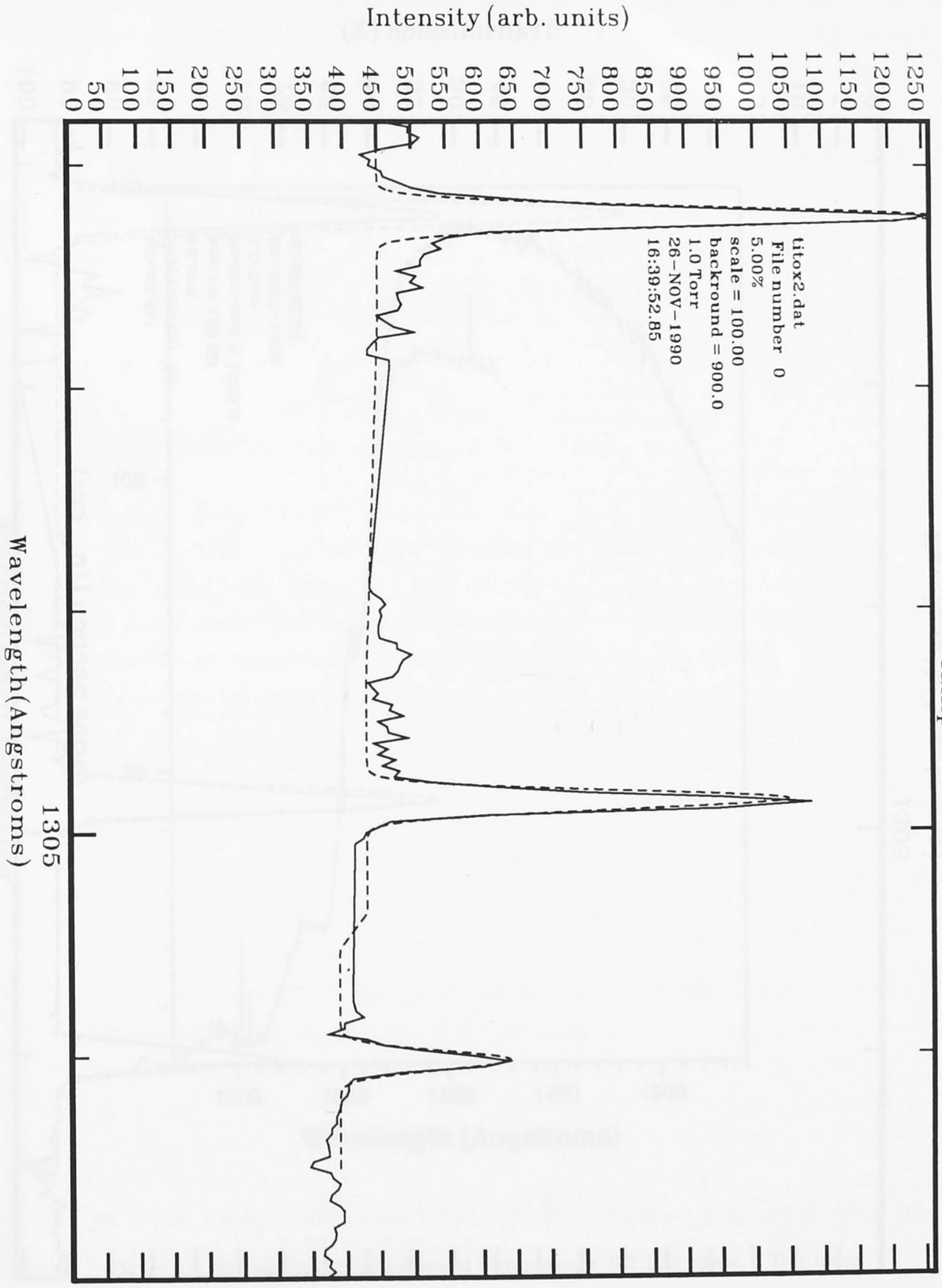

Figure 3.2: Oxygen emission lines of the argon dimer lamp: Solid – experiment, Dashed – theoretical fit.

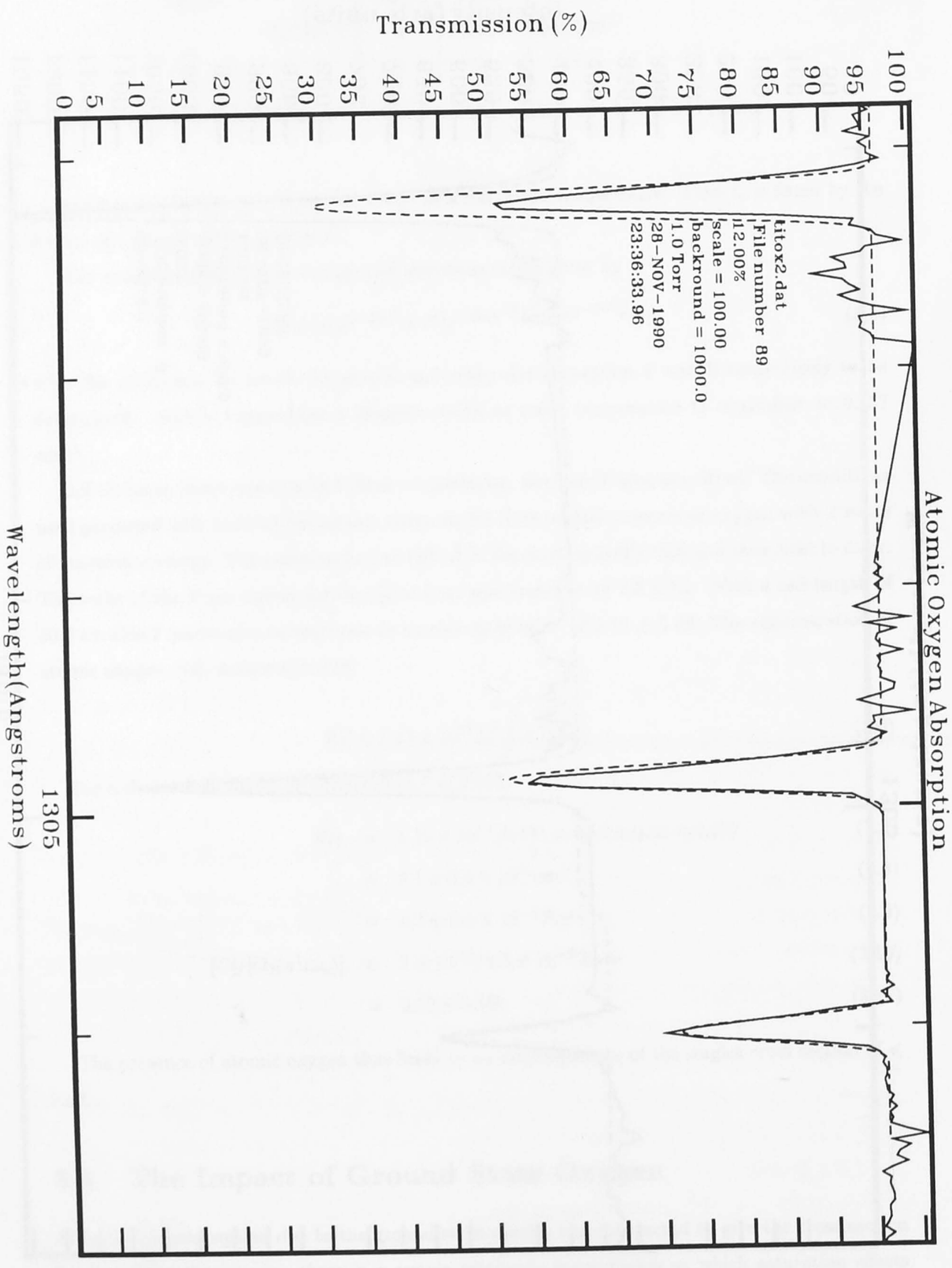

Figure 3.3: Transmission through the absorption cell with the microwave on: Solid – experiment, Dashed – theoretical fit.

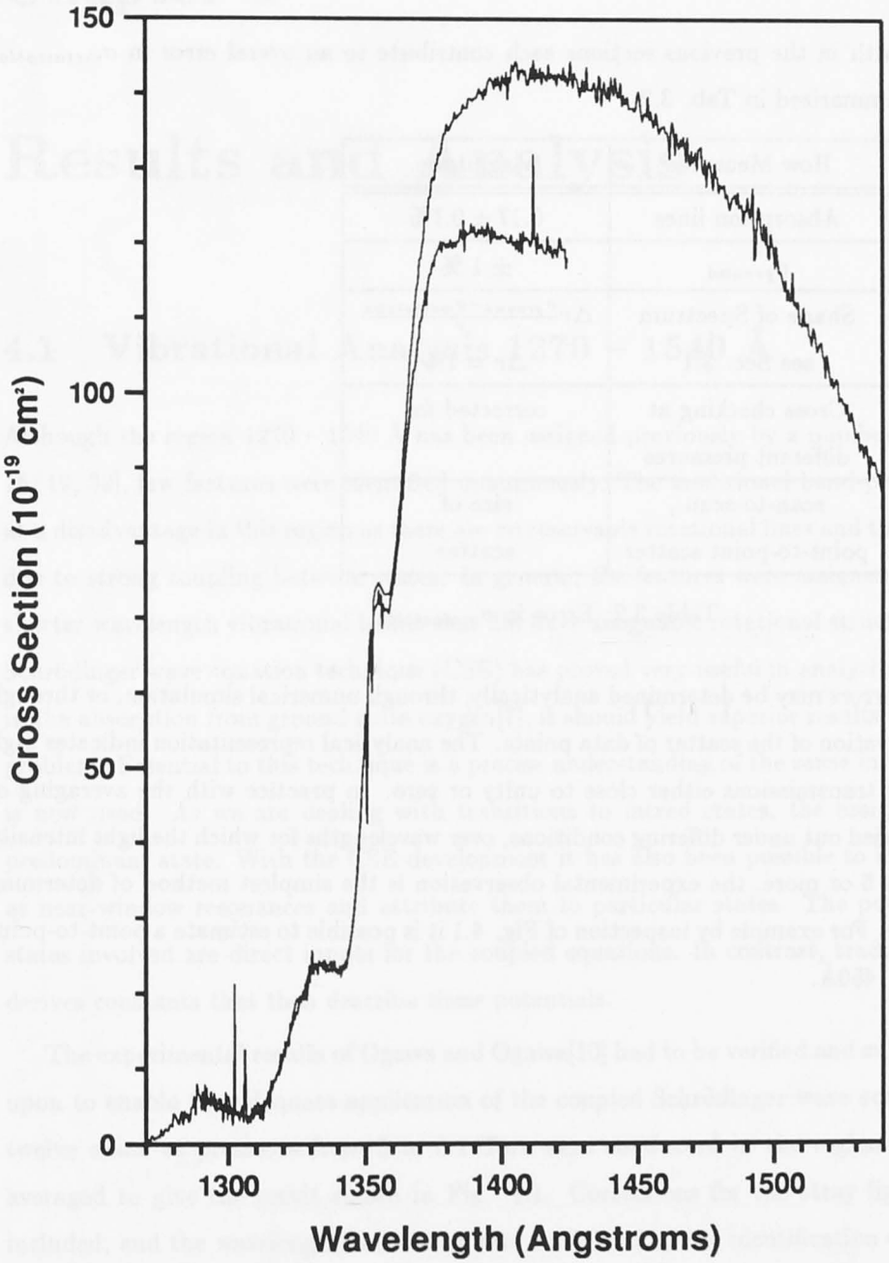

Figure 3.4: Saturation of cross section at high pressure: 0.2 Torr upper, 3 Torr lower.

by measuring the cross section as a function of pressure. For the Schumann-Runge continuum the stray light signal was 0.9 ±0.2%. All features were scanned at several pressures to check and correct for stray light effects if necessary.

3.5 Errors

The effects dealt with in the previous sections each contribute to an overal error in $\sigma_{metastable}$. These errors are summarized in Tab. 3.2.

Source of Error	How Measured	Magnitude
Atomic Oxygen	Absorption lines	$0.17 \pm 0.1\%$
Number Density	σ_{ground}	$\pm$ 1 %
r	Shape of Spectrum see Sec. 3.1	$\Delta r \frac{\sigma_{ground} - \sigma_{metastable}}{r}$ $\Delta r = 1\%$
Stray Light	Cross checking at different pressures	corrected for
Statistical noise	scan-to-scan , point-to-point scatter	size of scatter

Table 3.2: Error in $\sigma_{metastable}$

The statistical errors may be determined analytically, through numerical simulation, or through experimental observation of the scatter of data points. The analytical representation indicates high statistical error for transmissions either close to unity or zero. In practice with the averaging of dozens of scans carried out under differing conditions, over wavelengths for which the light intensity varies by factors of 5 or more, the experimental observation is the simplest method of determing the statistical error. For example by inspection of Fig. 4.1 it is possible to estimate a point-to-point error of ± 15% at 1450Å.

Chapter 4

Results and Analysis

4.1 Vibrational Analysis 1270 – 1540 Å

Although the region 1270 – 1540 Å has been assigned previously by a number of investigators[14, 16, 19, 39], few features were identified unanimously. The traditional band-progression analysis is at a disadvantage in this region as there are no resolvable rotational lines and there are irregularities due to strong coupling between states. In general, the features were assigned by extrapolation of shorter wavelength vibrational bands that did have assignable rotational structure. As the coupled Schrödinger wave equation technique (CSE) has proved very useful in analysing a similar situation in the absorption from ground state oxygen[7], it should yield superior results when applied to this problem. Essential to this technique is a precise understanding of the sense in which word "assign" is now used. As we are dealing with transitions to mixed states, the assignment refers to the predominant state. With the CSE development it has also been possible to identify features such as near-window resonances and attribute them to particular states. The potential curves of the states involved are direct inputs for the coupled equations. In contrast, traditional band analysis derives constants that then describe these potentials.

The experimental results of Ogawa and Ogawa[10] had to be verified and substantially improved upon to enable the adequate application of the coupled Schrödinger wave equation theory. Some twelve scans at pressures from 3 to 0.1 Torr were conducted in the region 1270 – 1540 Å and averaged to give the result shown in Fig. 4.1. Corrections for the stray light signal (1 %) are included, and the wavelength calibration was confirmed by the identification of impurity emission lines in the lamp spectrum.

From 1270 – 1400 Å there is reasonable agreement with Ogawa and Ogawa[10], except that this study detected a weak new band at 1310 Å. Ogawa and Ogawa reported this region to have a cross section beneath the limits of their detection, $< 3 \times 10^{-19}$ cm^2, perhaps because they had overestimated their percentage yield of metastables. In this experiment, at 1310 Å a cross section

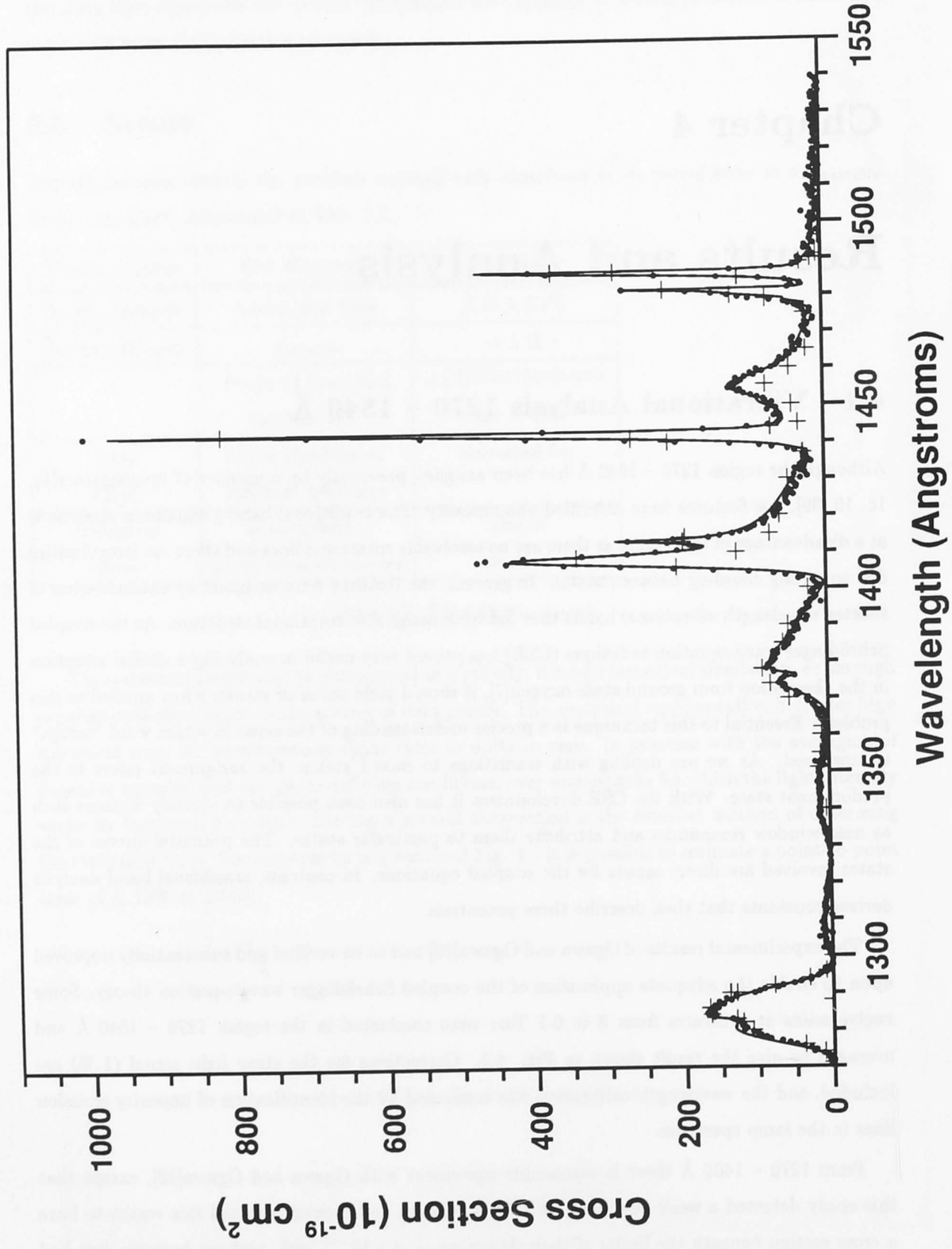

Figure 4.1: $a^1\Delta_g$ spectrum: + Ogawa and Ogawa (experimental), • this study (experimental), –this study (theoretical).

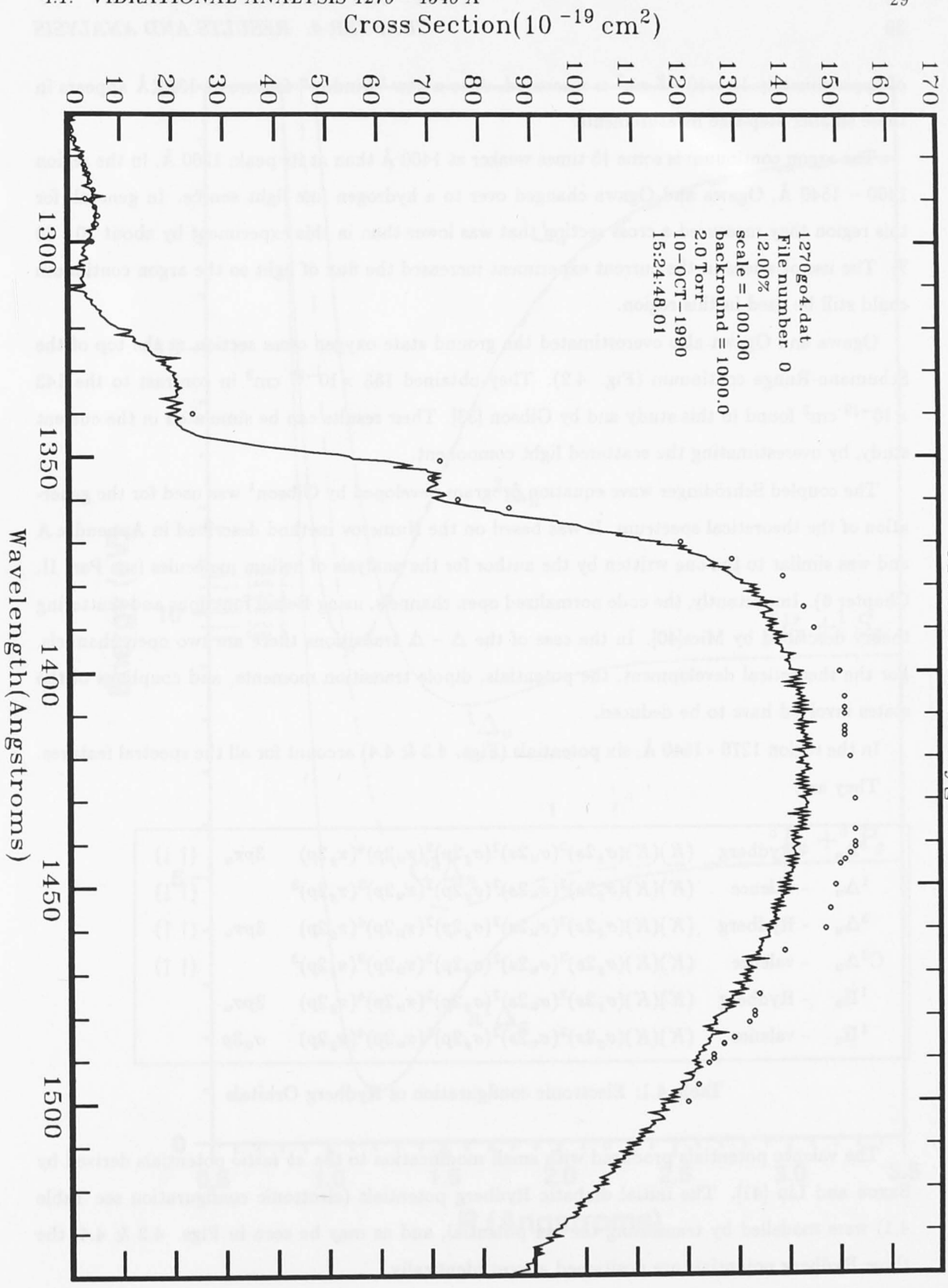

Figure 4.2: Ground state oxygen absorption: Ogawa and Ogawa (o),this work (–).

of approximately 10 $\times 10^{-19}$ cm^2 is measured. Also a new "window" feature at 1377 Å appears in these smaller step-size measurements.

The argon continuum is some 15 times weaker at 1400 Å than at its peak, 1260 Å. In the region 1400 – 1540 Å, Ogawa and Ogawa changed over to a hydrogen line light source. In general, for this region they measured a cross section that was lower than in this experiment by about 20 - 30 %. The use of a lens in the current experiment increased the flux of light so the argon continuum could still be used in this region.

Ogawa and Ogawa also overestimated the ground state oxygen cross section at the top of the Schumann-Runge continuum (Fig. 4.2). They obtained 153 $\times 10^{-19}$ cm^2 in contrast to the 143 $\times 10^{-19}$ cm^2 found in this study and by Gibson [33]. Their results can be simulated in the current study, by overestimating the scattered light component.

The coupled Schrödinger wave equation program developed by Gibson[1] was used for the generation of the theoretical spectrum. It was based on the Numerov method described in Appendix A and was similar to the one written by the author for the analysis of helium molecules (see Part II, Chapter 6). Importantly, the code normalized open channels, using Bessel functions and scattering theory described by Mies[40]. In the case of the $\Delta - \Delta$ transitions there are two open channels. For the theoretical development, the potentials, dipole transition moments, and couplings of the states involved have to be deduced.

In the region 1270 - 1540 Å, six potentials (Figs. 4.3 & 4.4) account for all the spectral features. They are:

$^1\Delta_u$	- Rydberg	$(K)(K)(\sigma_g 2s)^2(\sigma_u 2s)^2(\sigma_g 2p)^2(\pi_u 2p)^4(\pi_g 2p)$	$3p\pi_u$	$(\uparrow\downarrow)$
$^1\Delta_u$	- valence	$(K)(K)(\sigma_g 2s)^2(\sigma_u 2s)^2(\sigma_g 2p)^2(\pi_u 2p)^3(\pi_g 2p)^3$		$(\uparrow\downarrow)$
$^3\Delta_u$	- Rydberg	$(K)(K)(\sigma_g 2s)^2(\sigma_u 2s)^2(\sigma_g 2p)^2(\pi_u 2p)^4(\pi_g 2p)$	$3p\pi_u$	$(\uparrow\uparrow)$
$C^3\Delta_u$	- valence	$(K)(K)(\sigma_g 2s)^2(\sigma_u 2s)^2(\sigma_g 2p)^2(\pi_u 2p)^3(\pi_g 2p)^3$		$(\uparrow\uparrow)$
$^1\Pi_u$	- Rydberg	$(K)(K)(\sigma_g 2s)^2(\sigma_u 2s)^2(\sigma_g 2p)^2(\pi_u 2p)^4(\pi_g 2p)$	$3p\sigma_u$	
$^1\Pi_u$	- valence	$(K)(K)(\sigma_g 2s)^2(\sigma_u 2s)^2(\sigma_g 2p)^2(\pi_u 2p)^4(\pi_g 2p)$	$\sigma_u 3p$	

Table 4.1: Electronic configuration of Rydberg Orbitals

The valence potentials produced with small modification to the *ab initio* potentials derived by Saxon and Liu [41]. The initial diabatic Rydberg potentials (electronic configuration see Table 4.1) were modelled by translating the ion potential, and as may be seen in Figs. 4.3 & 4.4, the three Rydberg potentials are positioned almost identically.

The Rydberg potentials have a similar shape because the electron in the outer Rydberg orbital does not contribute significantly to the nature of the bond in the ion core. The three Rydberg states are of similar energy as they have the same principal quantum number (n=3) and orbital

[1] U.V. Physics Group, A.N.U., Canberra

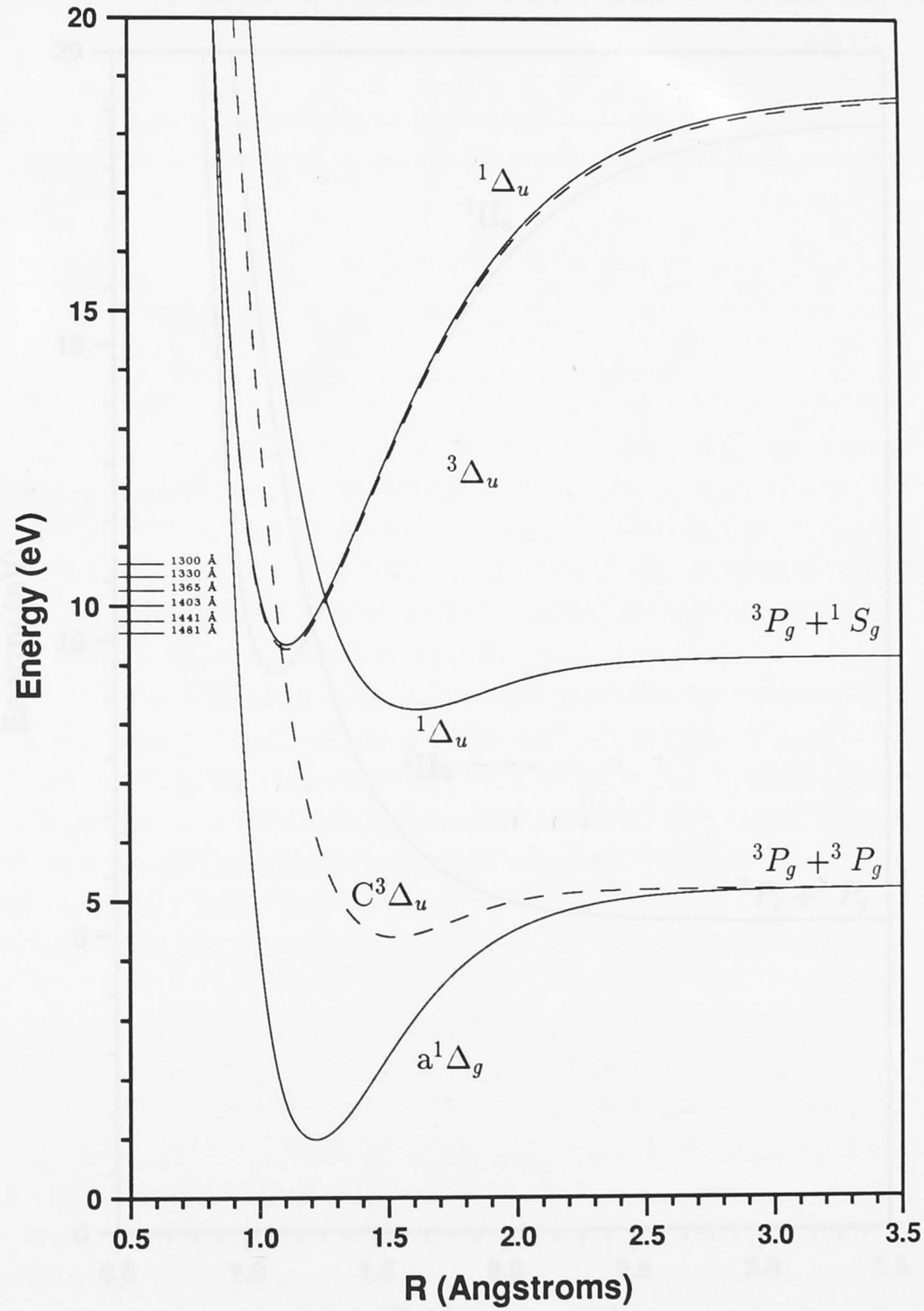

Figure 4.3: Δ symmetry, diabatic potential energy curves of O−2. Solid – singlet, dashed – triplet. 0 eV is the minimum in the ground state potential. The energy of $^1\Delta - ^1\Delta$ zero cross sections (Fig. 4.5 Frame 1) are marked and correspond closely to the diabatic energy levels.

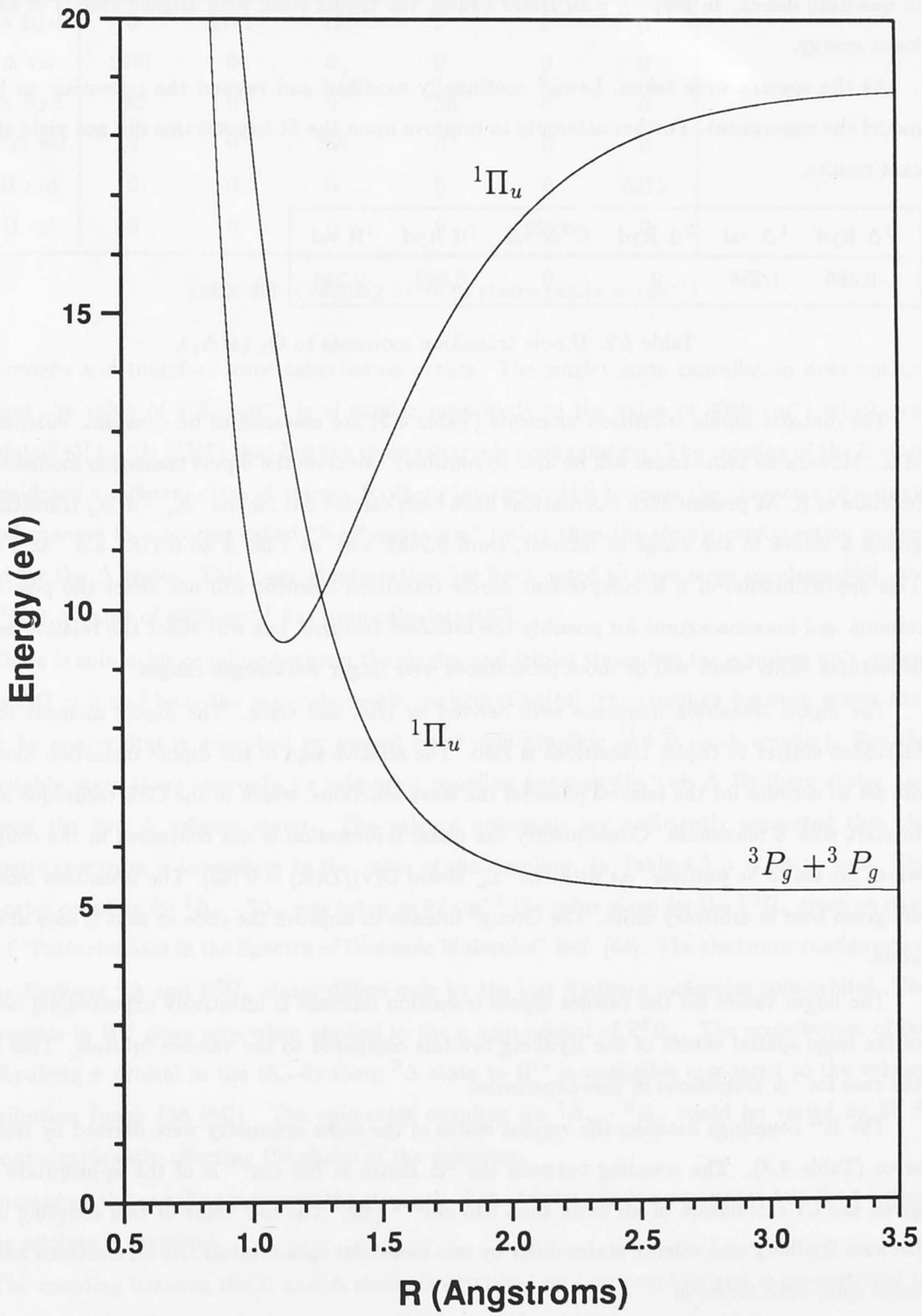

Figure 4.4: $^1\Pi$ states.

angular momentum (p) that would lead to a similar overlap with the ion core giving a similar value of quantum defect. In keeping with Hund's rules, the triplet state with aligned spin is of slightly lower energy.

As the spectra were taken, Lewis[2] continually modified and revised the potentials to better model the experiment. Further attempts to improve upon the fit beyond this did not yield significant results.

$^1\Delta$ Ryd	$^1\Delta$ val	$^3\Delta$ Ryd	$C^3\Delta$ val	$^1\Pi$ Ryd	$^1\Pi$ val
-0.386	1.258	0	0	0.693	-0.246

Table 4.2: Dipole transition moments to O_2 ($a^1\Delta_g$).

The diabatic dipole transition moments (Table 4.2) are assumed to be constant, independent of R . Modern *ab initio* codes will be able to routinely calculate the dipole transition moments as a function of R. At present such calculations have been carried out for the $^1\Delta_u - a^1\Delta_g$ transition[42] giving a values in the range of interest, from 0.9652 a.u. at 1.08 Å to 0.7182 a.u. at 1.35Å . This approximation of a R-independent dipole transition moment will not affect the position of minima and maxima except for possibly the broadest features, but will affect the relative heights of features. This effect will be more pronounced over larger wavelength ranges.

The dipole transition moments were derived by trial and error. The dipole moment for the forbidden singlet to triplet transitions is zero. The relative sign of the dipole transition moments are set to account for the relative phase of the wave functions, which in the CSE technique are set to start with a maximum. Consequently the phase information is not contained in the couplings which are set to be positive. As with the $^3\Sigma_u^-$ states D(v)/D(R) = 0 [43]. The transition moments are given here in arbitrary units. The Group[3] intends to improve the code so that it uses absolute units.

The larger values for the valence dipole transition moment is intuitively expected[44] because of the large spatial extent of the Rydberg orbitals compared to the valence orbitals. This is not the case for $^1\Delta$ transitions in this experiment.

The H^{el} couplings between the various states of the same symmetry were derived by trial and error (Table 4.3). The coupling between the $^3\Delta$ states is 750 cm^{-1} is of the appropriate order given the CI calculation of no more than 645 cm^{-2} [43]. The low value of this coupling occurs because Rydberg and valence states differ by two molecular spin-orbitals. As all electrons have the same spin, both terms in

$$H^e \propto < \phi_a\phi_b \mid 1/r_{12} \mid \phi_c\phi_d > - < \phi_a\phi_d \mid 1/r_{12} \mid \phi_c\phi_b > \tag{4.1}$$

[2]U.V. Physics Group, A.N.U., Canberra

[3]ibid.

	$^1\Delta$ Ryd	$^1\Delta$ val	$^3\Delta$ Ryd	$C^3\Delta$ val	$^1\Pi$ Ryd	$^1\Pi$ val
$^1\Delta$ Ryd	0	2751	92	0	0	0
$^1\Delta$ val	2751	0	0	0	0	0
$^3\Delta$ Ryd	92	0	0	750	0	0
$C^3\Delta$ val	0	0	750	0	0	0
$^1\Pi$ ryd	0	0	0	0	0	6272
$^1\Pi$ val	0	0	0	0	6272	0

Table 4.3: Coupling between states (units = cm^{-1})

are nonzero and therefore some cancellation occurs. The singlet state cancellation does not occur and the value of 2751 cm^{-1} is of similar magnitude to the value of 4000 cm^{-1} which was calculated[43] for O_2 ($^3\Sigma^+$) that has the same electronic configuration. The crossing of the Π state is considered a different class of valence-Rydberg interaction[44] because the character of a single orbital changes in a process called "Rydbergization" rather than the simple configuration mixing found for the Δ states. This class of interaction has been noted to have large repulsions[44]. For O_2 ($^3\Pi_u$), a value of 8500 cm^{-1} has been calculated[43].

There is spin-orbit coupling between the singlet and triplet states but the coupling only occurs when $\Delta\Omega = 0$ and have the same electronic configuration[44] (the coupling between states that differ by one orbital is described by second order spin-coupling and is much smaller). For the metastable state there can only be spin-orbit coupling between the two Δ Rydberg states and between the two Δ valence states. The valence potentials are sufficiently separated that the synthetic spectrum is insensitive to the value of the coupling. In Table 4.3 it is set to zero. The spin-orbit coupling for $^1\Delta_u$ - $3\Delta_u$ was taken as 92 cm^{-1} the value given for the $F^3\Pi_u$ given on page 217 of "Perturbations in the Spectra of Diatomic Molecules" Ref. [44]. The electronic configuration of the Rydberg $^3\Delta$ and $F^3\Pi_u$ states differs only by the last Rydberg molecular spin-orbital. The l_z operator in H^{so} gives zero when applied to the σ spin-orbital of $F^3\Pi_u$. The contribution of the the Rydberg π orbital in the the Rydberg $^3\Delta$ state to H^{so} is negligible compared to the valence contribution (page 108 [44]). The spin-orbit coupling for $^1\Delta_u$ - $^3\Delta_u$ could be varied by 50 % without significantly affecting the shape of the spectrum.

Increasing the coupling increases the strength of the triplet window resonance but the position of the minima is invariant.

The coupling between the Π and Δ states is described by L-uncoupling and is proportional to $(J(J+1)+2)^{\frac{1}{2}}$. This complexity is not explicitly considered in the coupling here.

The various levels of theoretical development are represented in Fig 4.5.

Frame 1 gives the cross section for only the T = 0 K, the coupled valence and Rydberg $^1\Delta$ - $a^1\Delta$ transition. The bound Rydberg transition at 1481.5 Å is so narrow that the simulation

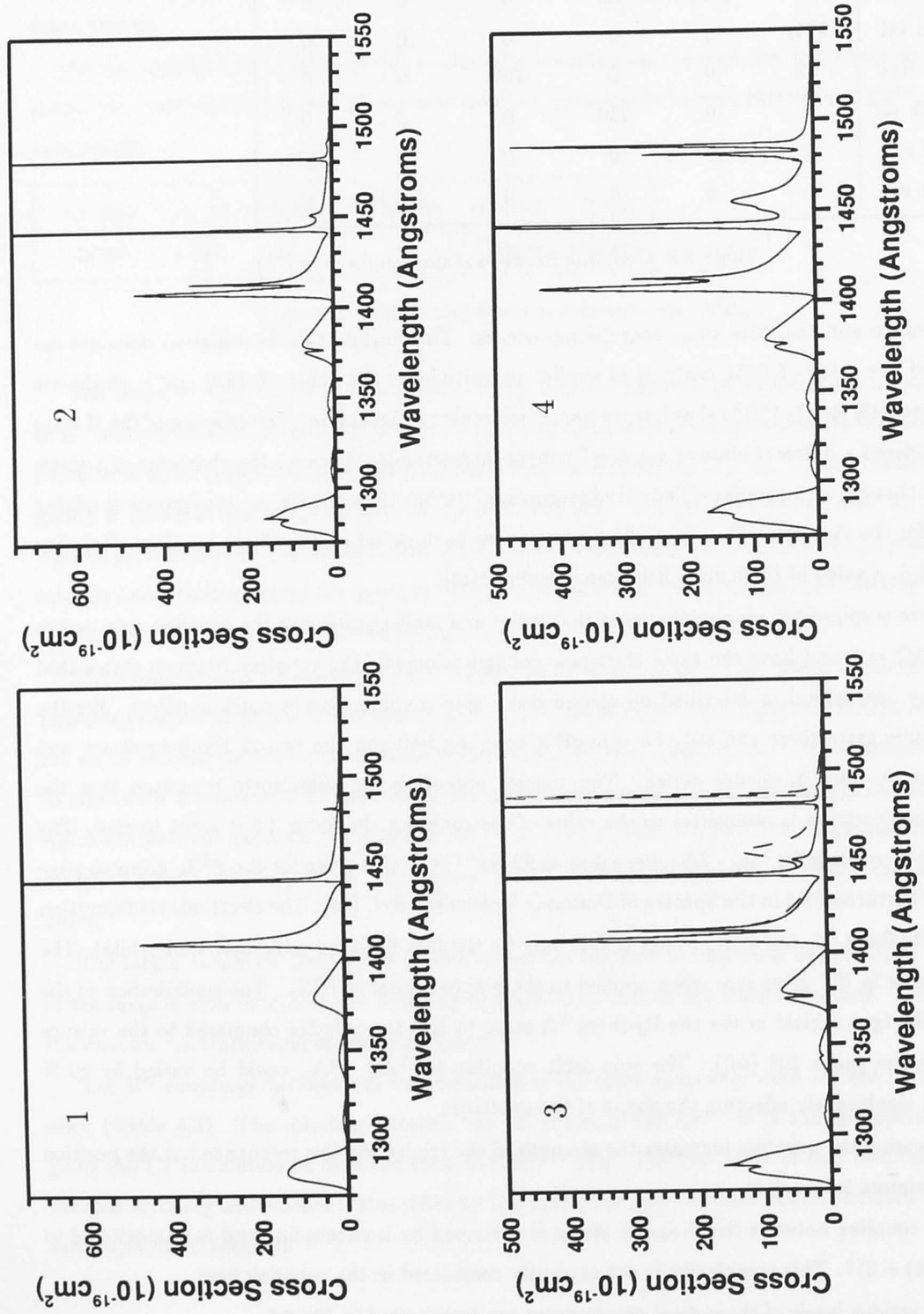

Figure 4.5: Increasingly sophisticated theoretical models (discussed in text). Dashed line corresponds to the II contribution.

stepped over the feature. The zeros rather than the maxima correspond to the diabatic Rydberg energy levels. Many general features of the experimental spectrum are explained.

Frame 2 is at T = 0 K but now includes the triplet contribution. The introduction of coupling to the triplet state fixes the general position of minima, maxima, and "window" resonances allowing the shape of the Δ potential curves to be determined. The 1481.5 Å feature, becoming broader, is now seen.

Frame 3 is T = 0 K ($^1\Delta$, $^3\Delta$) + $^1\Pi$ - $^1\Delta$. The inclusion of the valence and Rydberg Π potentials (Fig 4.4) now provides an explanation of all the bands in the region.

Frame 4 is for T = 300 K. As explained further in the Appendix A this is done by including a $J(J+1)/R^2$, centrifugal term, in the potential functions. The Boltzmann factor and the Hönl-London factors (rotational wave function overlap integrals) for the various rotational transitions are also included. The relative strength of a band does not change with temperature, though the shape broadens. The final frame took over 24 hours to compute, and thus fitting high temperature scans with the CSE technique is clearly time consuming. If liquid nitrogen scans were possible they would have allowed a simpler, more well-defined fitting.

The match between the current theory and experimental results allows the features to be identified with confidence.

The broad features of the spectrum may be interpreted in terms of the CSE theory thus:

Positions of Minima: As discussed in Appendix A, the positions of the minima are fixed close to the energy levels of the diabatic Rydberg state. To illustrate this, the zeroes as the appear in Frame 1 of Fig. 4.5 are marked on the potential energy diagram, Fig. 4.3.

This may be seen in Fig. 4.3 for the singlet and triplet states in Frames 1 and 2 respectively.

Diminished Cross Section near Curve Crossing: The overall shape of the cross section dips near the 1325 Å with stronger bands on either side of this. This corresponds, in energy, to the position of the $^1\Delta$ avoided crossing (see Fig. 4.3). The heights of the 1285 Å, 1310 Å and 1345 Å features are particularly sensitive to the value of the coupling between the singlet Δ states. This effect is more pronounced for the Π states with have a larger repulsion (Table 4.3: 6272 cm^{-1}) leading to a broader minimum. The Π bands on the short wavelength side of the minimum are seen at 1229 Å and beyond, and are outside the region under investigation.

Triplet Contribution: The triplet Rydberg potential is slightly lower in energy than the singlet Rydberg potential. This leads to the triplet zeros occurring at slightly longer wavelengths than the singlet zeros. The $^3\Delta$ features appear (1490, 1452, 1413, 1377, 1343, 1312, and 1285 Å) as resonances near the $^1\Delta$ maxima.

As the dipole transition moments for singlet to triplet transitions are zero, they are only manifest in their influence on the wave functions of the allowed transitions. This process has been termed 'borrowing' of intensity. Consequently, only the Hönl-London factors of allowed transitions are relevant for the CSE treatment. The value of the triplet coupling determined the strengths and shapes of the 'window' resonances.

Roll off at > 1500 Å and cut-off at 1535 Å: This is analogous to the Schumann-Runge continuum and band structure. In both cases, the upper potential is bound beneath a certain energy (see Fig. 4.3, the lowest $^1\Delta_u$ state), creating a continuum cut-off. The Δ valence transition will exhibit band structure at energies for which it is bound. These bands are inaccessible with the existing apparatus as the argon continuum lamp produces little light at these wavelengths. The reduction in dipole moment at greater distances [42], and reduced Franck-Condon overlap will lead to very weak bands that would have to be detected against a strong oxygen background. The Π valence transition is unbound at all internuclear separations and exhibits a steadily reducing continuum as its Franck–Condon overlap diminishes. In contrast to Ogawa and Ogawa [10] who attribute this region to a Π transition, this theoretical analysis shows clearly that it is of Δ in origin.

Δ and Π contributions: The Π state contributes only to the longest band and the broad feature at 1455.5 Å with the sharp bands broadening at shorter wavelengths as their character changes from Rydberg to valence. Δ - Π transitions have $\Delta\Omega = -1$ and therefore strong Q branches, while for the Δ - Δ transitions this branch has much reduced intensity (see Appendix A: Theory of Diatomics).

Dipole Transition Moments: The dipole transition moments are here considered to be independent of internuclear separation. *Ab initio* calculations, or the cross-referencing of different transitions would be necessary to determine the radial dependence of the transition moment. As the valence transition moment is increased with respect to the Rydberg transition moment, the shorter wavelength part of the spectrum becomes stronger.

This study is able to assign all the bands in the region 1270 – 1540 Å. Save for the 1486.5 and 1455.5 Å features that are Π in origin, the rest of the spectrum results from $^1\Delta$ states that contain $^3\Delta$ window resonances. These assignments are a significant advance on those of earlier investigators (Table 4.4). Instead of using the position of an individual band in relation to shorter wavelength, more easily identified bands, the entire region was modeled as a whole. Not only are the positions of the bands correctly reproduced by the theoretical simulation, the shape and relative cross sections are modeled. The couplings, dipole moments, and potential curves used to do this are realistic given the *ab initio* calculations, and physical picture of the oxygen molecule.

In conclusion, the combination of careful measurements and a theoretical technique which models valence-Rydberg interactions, has successfully accounted for the bands in the 1270 - 1540 Å

region. Semi-empirical potential curves, couplings and dipole transition moments have been derived with the approximation of a constant dipole transition moment, and neglecting of the effects of higher potentials.

Position (Å)	Alberti *et al.*[16] (1968)	Yamawaki [14] (1972)	Collins *et al.*[19] (1973)	Katayama *et al.*[39] (1977)	This work (1990)
1495.6	-	-	$^1\Sigma_u^-$	-	-
1486.5	?	$^1\Delta_u$	$^1\Delta_u$	$^1\Pi_u$	$^1\Pi_u$
1481.5	?	$^1\Delta_u$	$^1\Delta_u$	$^1\Delta_u$	$^1\Delta_u$
1455.5	-	$^1\Pi_u$	$^1\Pi_u$	-	$^1\Pi_u$
1442.7	?	$^1\Delta_u$ [a]	$^1\Delta_u$	$^1\Pi_u$	$^1\Delta_u$
1413.0	-	$^1\Pi_u$	$^1\Delta_u$	$^1\Delta_u$	$^3\Delta_u$
1407.0	-	$^1\Delta_u$	$^1\Delta_u$	$^1\Pi_u$	$^1\Delta_u$
1380.0	-	$^1\Pi_u$	$^1\Delta_u$	-	$(^1\Delta_u, ^3\Delta_u)$ [b]
1345.0	-	$^1\Pi_u$	-	-	$(^1\Delta_u, ^3\Delta_u)$ [b]
1310.0	-	-	-	-	$(^1\Delta_u, ^3\Delta_u)$ [b,c]
1285.0	-	-	?	-	$(^1\Delta_u, ^3\Delta_u)$ [b]

? Observed but not assigned.

[a] Identified two Δ bands superimposed.

[b] $^1\Delta_u$ accounts for the broad band, $^3\Delta_u$ accounts for the window resonance in the band.

[c] The theoretically predicted $^3\Delta_u$ window resonance was not resolved. This band was absent in Ogawa and Ogawa's measurements.

Table 4.4 The upper-state assignments of bands by various investigators for the range 1270 – 1540 Å.

4.2 Individual Bands 1270 – 1540 Å

The inclusion of the rotational effects in the CSE technique lessens the need for a separate rotational analysis, as the rotational structure is reproduced directly in the theoretical simulation (Fig. 4.5,

Frame 4). However, band modelling is a computationally rapid way of extracting B values and identifying branches. The effect of coupling between states is accounted for by the inclusion of suitably shaped Fano profiles for the rotational lines, and the final results of the analysis can be expected to be consistent with the semi-empirical curves generated for the coupled Schrödinger equation technique.

In the current study no rotational line structure was resolved experimentally in this wavelength region.

In particular there are three bands in this region worthy of further discussion:

1481.5 Å band: Yamawaki[14] reported rotational lines for the Δ - Δ band at 1481.5 Å. Some ten scans were taken of this region in order to identify rotational lines. The structure was not discernible and must be smaller than the noise in the scan.

1442.7 Å band: The 1442.7 Å feature is the strongest one in this region and for this reason Ogawa and Ogawa [10] suggest its use to determine the concentration of metastables. In this study, however, a peak cross section of $1275 \pm 60 \times 10^{-19}$ cm^2 was determined, as opposed to Ogawa and Ogawa's value of 823×10^{-19} cm^2. In Fig. 4.1 the wavelength step size misses the peak for both the theoretical and experimental curves. Fig.4.6 has a 0.02 Å step size and shows its true magnitude.

1285 Å Band: The 1285 Å (Fig. 4.7) peak would be more suitable for the determination of the fraction of metastables because it is broader. As with the 1442.7 Å peak, it has a significantly stronger cross section than ground state oxygen. It is a band that fits less well with the CSE theory. If the valence potential is lowered in the energy region of this band a better fit is obtained. The introduction of additional higher potentials that would be responsible for this localized effect is outside the scope of the current work.

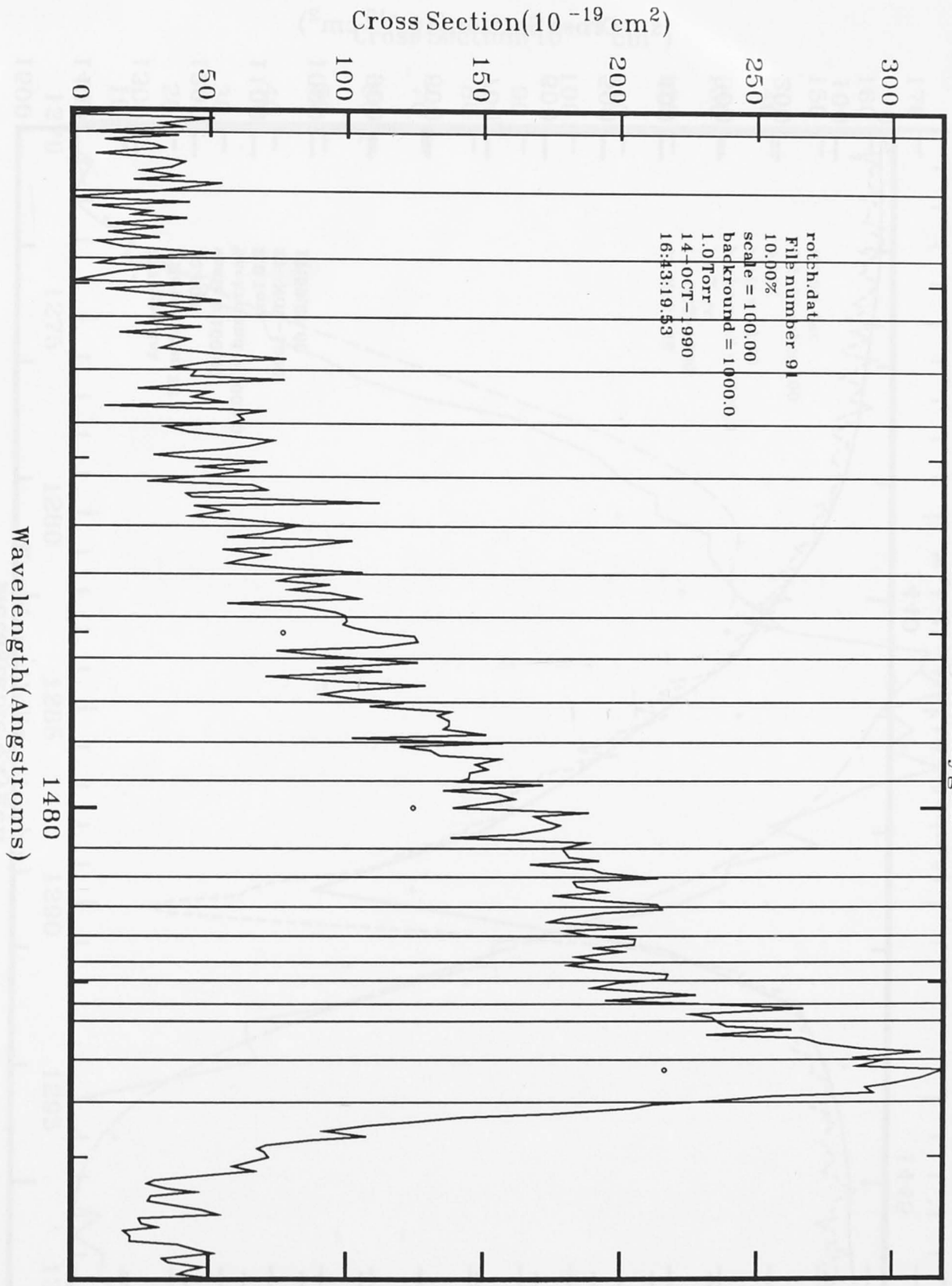

Figure 4.5: 1481.5 Å band. Solid line represents measurements taken in this work, circles represent Ogawa and Ogawa, vertical lines mark the positions of lines identified by Yamawaki.

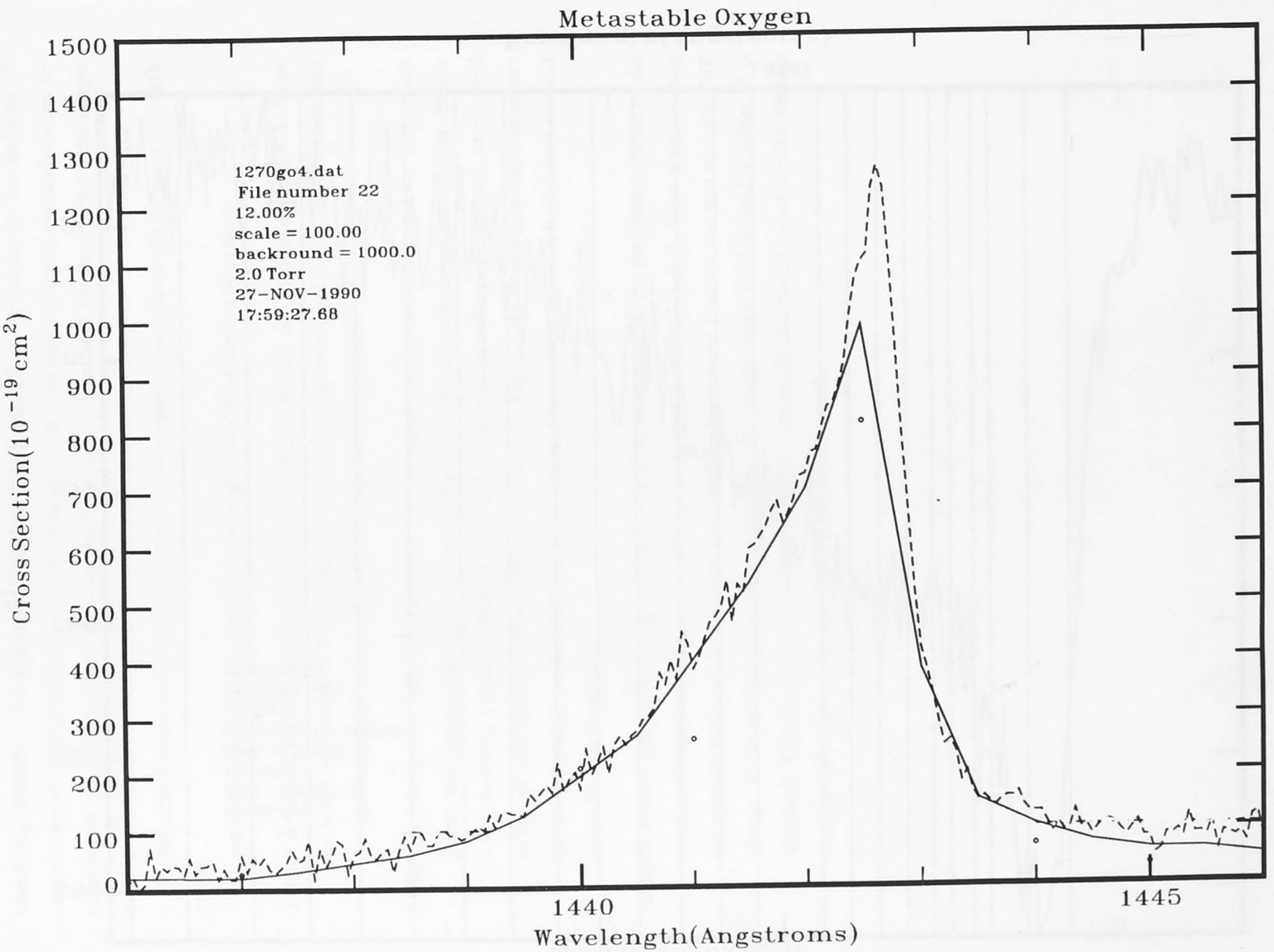

Figure 4.7: 1442.7 Å band. circles - Ogawa and Ogawa, solid line - this work at 0.5 Å steps, broken line - this work at 0.02 Å steps.

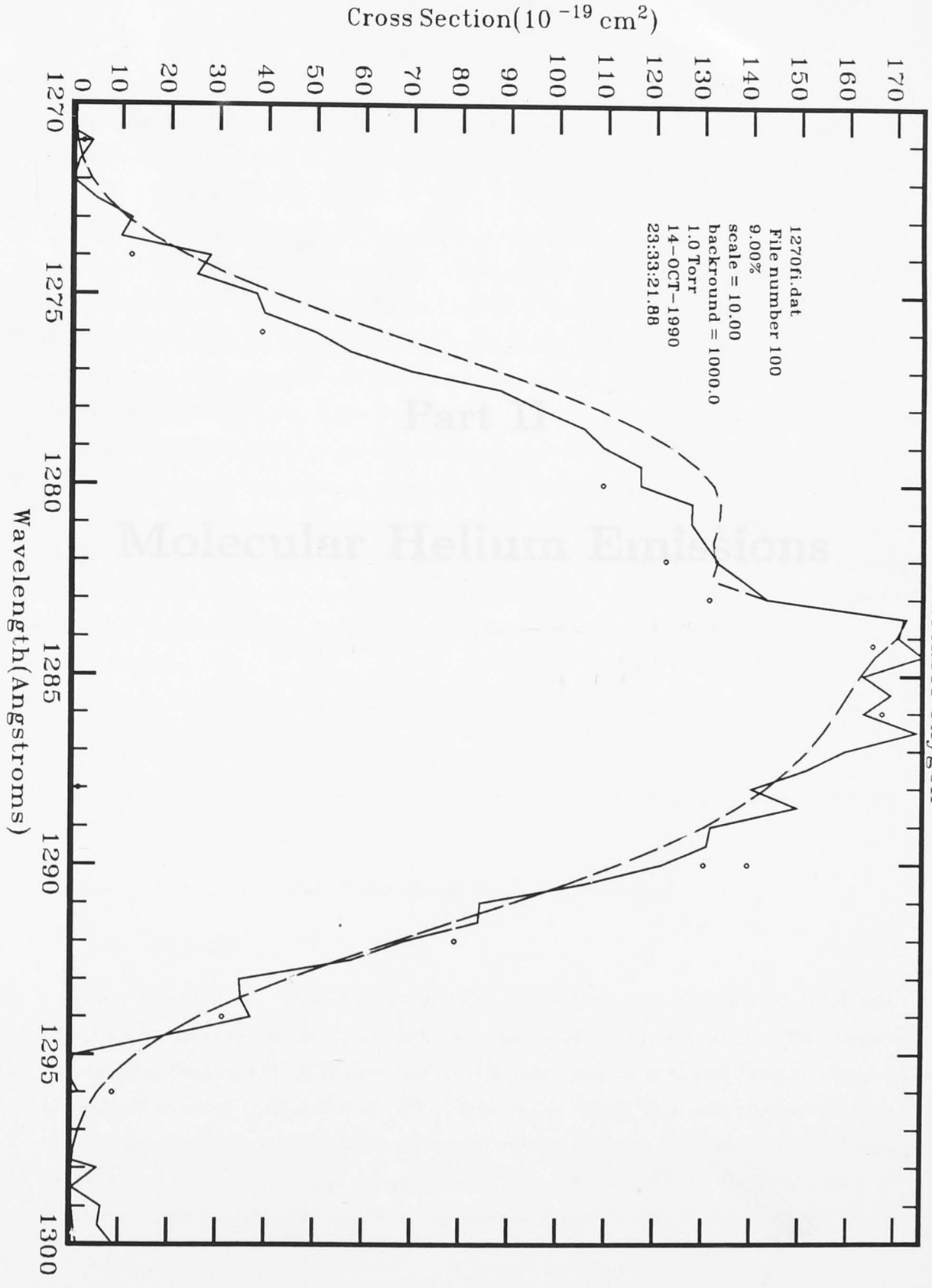

Figure 4.7: 1285 Å peak:circles - Ogawa and Ogawa, solid line - experiment, broken line - theory.

Part II

Molecular Helium Emissions

Introduction to Part II

Although the ultraviolet continua of noble gas dimer sources (employed in Parts I & III of this thesis), are used extensively in spectroscopy, there is perhaps less known about them than the majority of gases they illuminate.

Through work with helium lamps that produced the Hopfield continuum I became interested in whether they could be made into lasers. The unbound lower state meant that there was a population inversion. A lot of other factors have to be considered when exploring the feasibility of a laser: the upperstate population, the plasma reactions, and the lifetimes. For excimer lasers which operate in the afterglow and molecular beam lasers as proposed by Baldwin[45] the life time is critical. The thinking at the time was that, as the lifetime of the lighter noble gases had progressively longer lifetimes, helium should have a reasonably long lifetime. A vast amount of research has been done on helium dimers under many different conditions. Although Delaoche *et al.*[46] have developed computer codes that accurately describe the reactions in a typical helium dimer afterglow source, a review was necessary to understand the implications of the various experiments carried out since the 1930's. Chapter 5 [4] looks at the feasibility of helium dimers as ultraviolet laser sources (secondary thesis objective) and shows that the lifetime of the upperstate is only 0.55 nsec.

Having gained an understanding of the problems of lasers, the review turned up some as yet unexplained continua that

1. occurred during the excitation discharge (this meant that the lifetime of the molecule involved was no longer critical)

2. were very efficient ($>$ 50 % of the light originated from molecules)

3. were very bright.

I was able to convince Dr. David Swanton of ANU's Research School of Chemistry to collaborate by calculating potential energy curves that where then used to calculate spectra. The research is detailed in Chapter 6 [5]. Huffman's continua (in pulsed and dc arcs) and Tanaka's continua are assigned as a He_2^+ ($C^2\Pi_u$) to He_2^+ ($A^2\Sigma_g^+$) transitions. He_2^+ ($C^2\Pi_u$), with all three electrons in bonding orbitals, has a very small bond length, which means that it decays to a very steeply repulsive part of the He_2^+ ($A^2\Sigma_g^+$) potential curve. This explains the large wavelength range of Huffman's continuum and the prediction that associated laser (patent in Appendix B) will be

[4] a review as it appears in Physical Review A

[5] published as a Brief Report in Physical Review A

tunable throughout the visible. A band observed by Huffman at 6050 Å was tentatively assigned as stimulated emission from this transition.

Often the question is raised of the formation of a molecule at an energy level of 45 eV in an arc where all species have an energy of about 1 eV. Indeed, the formation via collision and other processes from lower electronic states is very low. However, the formation by association depends on the concentration of ions ($> 1\%$ in arcs), neutrals, and He (2^3P) and the nature of the potential curves. The formation of the 45 eV quartet dimer ion[47] at high yield in very low energy discharges is another example of molecular formation.

For this work the computer programs were written independently of those existing in the Group[6]. Before publication, the theoretical results were cross-checked with the existing codes. This also served to verify the reliability of the Group's programs used for the theoretical modelling conducted in Part I.

[6]U.V. Physics Group A.N.U.

Chapter 5

Ultraviolet Continua of Helium Molecules

PHYSICAL REVIEW A VOLUME 40, NUMBER 9 NOVEMBER 1, 1989

Ultraviolet continua of helium molecules

Peter C. Hill
1 Hope Street, Dickson, Canberra, Australian Capital Territory, Australia
(Received 12 December 1988)

The many bands and continua of helium are reviewed, categorizing them by wavelength. Excited helium clusters dissociate, producing ultraviolet light. The population mechanisms of these molecules are deduced by using spectra, potentials, and the time evolution of excited atoms and molecules. Quartet ion recombination is proposed as accounting for the second decay component in low-energy afterglows. The roles of He_2^+ and helium clusters are identified. Data available in the literature are used to calculate a lifetime of 0.55 nsec for the "metastable" state $A\,^1\Sigma_u^+$ at 700 Torr. This lifetime gives a theoretical upper limit for the cross section for stimulated emission of 9×10^{-18} cm^2. The feasibility of a helium dimer laser that operates at 825 Å is assessed.

I. INTRODUCTION

During the 1920s and 1930s, ultraviolet bands and continua were discovered in helium discharges. In 1924, Lyman discovered a band at 600 Å and later Hopfield found a series of weaker bands at longer wavelengths associated with this band. Then, in 1929 Hopfield discovered a continuum[1,2] (1000–600 Å) that was later to be named after him. This ultraviolet light is generated by the photodissociation of molecular helium. Variation of pressure, temperature, and discharge method results in a wide variety of spectra (Fig. 1). Such variability is indicative of the complex decay channels, which are the subject of this work.

Historically, three factors have motivated research into these continua: (1) the helium discharge lamp is a cheap and compact source of vacuum ultraviolet (VUV) radiation, (2) information yielded about He_2 can be used to test molecular theories, and (3) He_2 plays an important role in the discharge kinetics of excimer lasers in which helium is employed as a buffer gas. In the future, it may be possible to build a helium dimer laser that will generate coherent radiation[3] at wavelengths inside the Hopfield continuum. Similar dimer lasers have already been developed for the heavier noble gases[4,5] but at longer wavelengths.

Proton-excited discharges, pulsed discharges, and dc discharges all produce distinct spectra that originate from different mechanisms. This work reviews the current understanding of these reaction mechanisms and proposes new mechanisms in the light of recent data and discoveries. Sections II–V provide an analysis of the main types of helium continua and bands, categorizing them by wavelength. From the insights obtained about the origins of these spectra regions, molecular lifetimes are reduced in Sec. VI and are used to comment on the feasibility of a helium dimer laser in Sec. VII.

II. 600-Å BAND

A pulsed beam of 4-MeV protons fired into helium at 100 Torr produces an afterglow (spectrum *A* in Fig. 1).[6]

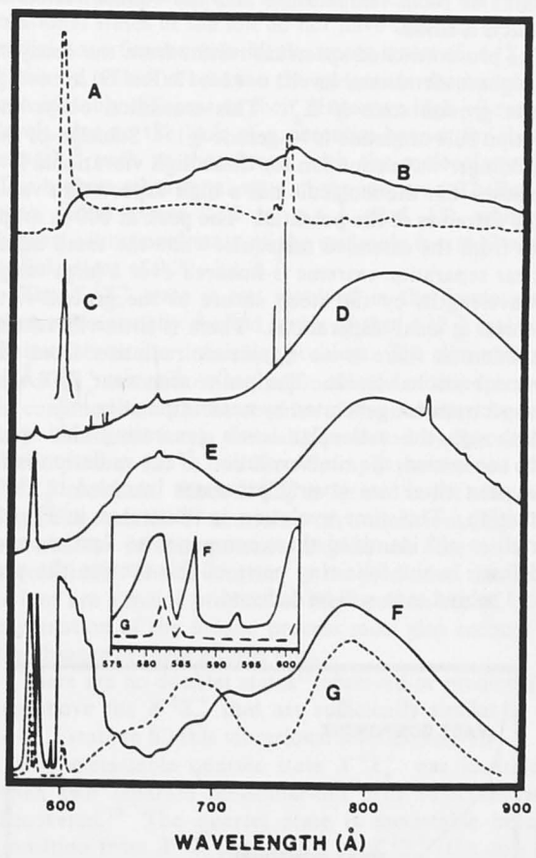

FIG. 1. Helium continua: *A*, 100 Torr, proton excited (Ref. 6); *B*, 600 Torr, proton excited (Ref. 6); *C*, 77 K, molecular beam (Ref. 3); *D*, 45 Torr, pulsed (Hopfield) (Ref. 60). *E*, 24 Torr pulsed (Hopfield) (Ref. 61); *F*, ac with no charging capacitor ("uncondensed") (Ref. 26); *G*, ac with charging capacitor ("condensed") (Ref. 26). Spectra *F* and *G* are from photographs and have a nonlinear intensity scale. This figure was created by digitizing original figures found in the references.

Molecular-beam discharges[3] (spectrum *C* in Fig. 1) and low-energy 3 mA dc discharges[7] produce similar spectra.

The reaction mechanisms responsible for spectrum *A* are detailed in this section. The excited molecules that photodissociate to generate this distribution of radiation are identified, then the reactions that form these molecules are discussed. It is proposed that two reaction mechanism be required to describe adequately the formation of the excited molecules: association (proposed by Mies and Laslett Smith[8] and recombination of quartet ions (proposed in this paper).

Proton-beam excitation is unique among methods of excitation because only a low power (a fraction of a watt) is deposited in the helium. Further, the initial composition and energy of excited helium have been calculated;[6] this has not been done for other sources. In contrast with conventional lamps discussed in later sections, the gas remains at room temperature and the concentration of products is small.

The proton-excited spectrum results from the decay of the highest vibrational levels, $v=16,17$ (Ref. 9) in $A\ ^1\Sigma_u^+$ to the ground state $X\ ^1\Sigma_g^+$. This transition obeys the selection rule ungerade (u)↔gerade (g).[10] Solution of the Schrödinger wave equation for these high vibrational levels shows that the molecule has a high expectation value at the extremes of the potential. The peak at 600 Å originates from the extended molecule, while the small internuclear separation extreme is smeared over a large range of wavelengths by the steep nature of the ground-state potential at small separations. There is little vibrational relaxation as there is no significant radiation from the lower vibrational levels. The peaks seen near 750 Å in this spectrum are generated by neon impurities.[11]

Although the molecular levels generating this spectrum are known, the time evolution of the radiation indicates that there are several processes involved in their formation. This time evolution is illustrated in Fig. 2. Bartell *et al.*[6] identified three components: first, second, and fast. In the following parts of this section the processes behind each will be deduced.

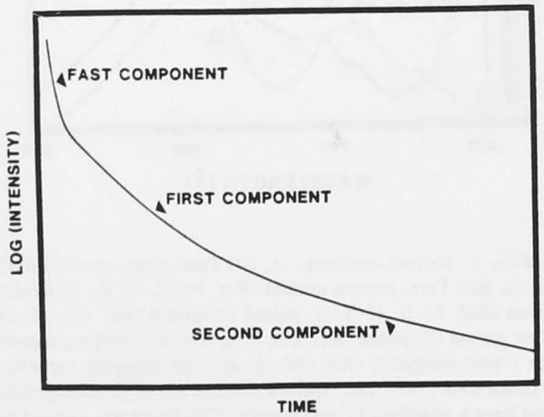

FIG. 2. Time evolution of a proton-excited afterglow, showing fast, first (association), and second (quartet-ion recombination) regions.

A. First component — association process

Bartell *et al.*[6] have identified a process that will generate this proton-excited spectrum: three-body association—

$$\mathrm{He}(2\,^1S)+2\mathrm{He}\xrightarrow{\text{slow}}\mathrm{He}+\mathrm{He}_2(A\,^1\Sigma_u^+, v=\max)\xrightarrow{\text{fast}}3\mathrm{He}+h\nu_{600\text{-Å band}}\,. \tag{1}$$

The $A\ ^1\Sigma_u^+$ molecule has a potential barrier of maximum height of 0.05 eV at an internuclear separation of 3.1 Å.[9] The Maxwellian distribution of velocities v,

$$P(v)=4\pi\left[\frac{m}{2\pi kT}\right]^{3/2}v^2\exp\left[\frac{-mv^2}{2kT}\right], \tag{2}$$

indicates that at room temperature ($kT=0.025$ eV) 34% of atomic collisions have sufficient energy to form this molecule. While the molecule is in a continuum state, with an internuclear separation less than 3.1 Å, a further collision with a neutral atom may cause the molecule to relax into a bound state.

Equation (1) indicates that there should be a relationship between the population of the $2\ ^1S$ state and the final radiation. Since the decay rate of the $A\ ^1\Sigma_u^+$ molecule (~ 0.55 nsec for $v=0$ at 700 Torr—see Sec. VI) is much faster than the formation rate [$\sim 30\,000$ nsec at 100 Torr—Eqs. (1) and (3)] the formation of the $A\ ^1\Sigma_u^+$ dimer is the rate-limiting step in the series of reactions that produce the final radiation. If the dimer is formed by the association process, characterized by Eq. (1), then the amount of light produced is proportional to the concentration of $2\ ^1S$. Therefore it is reasonable to attribute to the associative process the component of the radiation that has the same decay rate as the $2\ ^1S$ metastable atom.

The destruction rate of the metastable $2\ ^1S$ atom, k_m, measured in the same proton-beam apparatus used to create this spectrum,[12] is

$$k_m=220P+1.4P^2\,, \tag{3}$$

where P is in units of Torr. The first-order term may be attributed to collision-induced radiative decay to the $1\ ^1S$ state. Payne *et al.*[12] suggest that the second-order pressure term corresponds with the proposed three-body association mechanism in Eq. (1).

Bartell *et al.*[6] found that the 600-Å band radiation-decay curve (after an initial spike in intensity they called the "fast component") could be fitted by the expression

$$I_v=A_1\exp(-k_1t)+A_2\exp(-k_2t)\,. \tag{4}$$

The first and second terms of this equation refer to the first and second components of the radiation, respectively. For the radiation measured at 601 Å,[6] the pressure dependence of k_1 may be approximated by

$$k_1=6380+382P+1.09P^2\,. \tag{5}$$

The similarity between the destruction rate for the metastable atom [Eq. (3)] and for the $A\ ^1\Sigma_u^+$ molecule [Eq. (5)], as illustrated in Fig. 3, and the favorable kinetics of the association reaction at room temperature, are

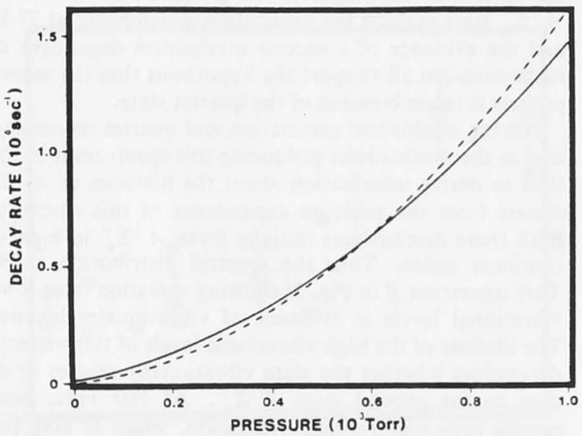

FIG. 3. Pressure dependence of the decay rate of $2\,^1S$ measured by Payne *et al.* (Ref. 12) (dashed) and of the first component of the decay rate of the $A\,^1\Sigma_u^+$ dimer as determined from data in Bartell *et al.* (Ref. 6) (solid).

compelling evidence that the reaction mechanism for the first component is association. The small discrepancy between the pressure dependence of the formation rate [Eq. (3)] and of the radiation rate [Eq. (5)] may correspond to the lifetime of the $A\,^1\Sigma_u^+(v=\max)$ molecule limiting the radiation rate at higher pressures.

B. Second component—quartet-ion recombination

The second term in Eq. (4) is consistent with a separate process that also produces vibrationally excited $A\,^1\Sigma_u^+$ molecules. At pressures below 100 Torr A_2, the coefficient of the second process, is greater than A_1. This indicates that the second process a significant source of $A\,^1\Sigma_u^+$ molecules at low pressures. The decay rate of the second process, k_2, displays no pressure dependence but shows a strong sensitivity to the initial energy of the electron-ion pairs created by the proton beam. For instance, when the initial energy per electron-ion pair drops from 43.8 to 40.0 eV, the decay rate of the second process at 200 Torr increases by 80% compared with only 10% for the first.[6] This energy sensitivity of the second process is suggestive of electronic recombination, which depends on the electron temperature among other factors.

The association process does not provide a plausible explanation of the formation of this spectrum in a dc discharge struck in the expanding jet of a molecular beam with its nozzle cooled to 77 K.[3] The average energy of the atoms in this beam is $\ll 0.007$ eV. The 0.05-eV potential barrier would make the formation of the dimer by association less likely at lower temperatures, yet Baldwin *et al.* found that there is six times more radiation at 77 K than at room temperature.

This evidence suggests a second mechanism; general principles may be invoked to aid in its identification. To generate a spectrum of this shape this second mechanism must exclusively populate the high vibrational levels of $A\,^1\Sigma_u^+$ (as was the case for the association mechanism). Expressed in terms of the Franck-Condon principle, this means that the radial wave function of the parent molecule must have significant spatial overlap with the high rather than the low vibrational levels. Knowledge of the association process (Sec. II A) adds further constraints. The association process depletes the population of the $2\,^1S$ atoms, and thus this species is not involved. Other metastable and resonantly trapped atoms are too low in energy or of too short a lifetime to form the molecule directly. These considerations will be used to eliminate molecular neutrals and doublet ions as parent molecules.

A vibrationally excited $X\,^2\Sigma_u^+$ ground state of He_2^+ is a potential parent molecule, but may be ruled out for these two reasons: (1) the ion does not remain in high vibrational states but instead undergoes rapid vibrational relaxation to the ground state $v=0$ (Ref. 13), recombining to become the lower vibrational states of the $A\,^1\Sigma_u^+$ molecule (as described in the Sec. V), and (2) the high vibrational states of the ion do not have sufficiently similar radial wave functions to fill the upper states of $A\,^1\Sigma_u^+$ exclusively. This is because the potentials themselves are considerably different at their respective high vibrational levels, due to the lack of a potential barrier for the ion state[14,15] such as that found with the molecular state.[9] The highest vibrational state of the ion is $v=22$ (Ref. 16) with radial extent 0.78 to >4 Å (Ref. 15), while the highest vibrational state of the molecule is $v=17$ with a radial extent of 0.73–3.1 Å.[9]

The $X\,^2\Sigma_u^+$ state is not involved in the formation of these vibrationally excited levels of the $A\,^1\Sigma_u^+$ molecule. This raises an ion deficiency problem. The elimination of the $X\,^2\Sigma_u^+$ state's role in the production of this spectrum, in conjunction with the absence of the radiation from the low vibrational levels normally produced by this state (a broad peak at 825 Å, see Sec. V), imply the absence of the $X\,^2\Sigma_u^+$ molecule. Since $X\,^2\Sigma_u^+$ is formed in the afterglows from the reaction of neutrals with atomic ions [Eq. (13)], the absence of this molecule implies the absence of the atomic ions. This is contrary to the prediction that atomic ions are a major product of these proton beams.[6] Any explanation of the second process must also account for the absence of these atomic ions.

There are no doublet states[17] observed or predicted lying above the $X\,^2\Sigma_u^+$ that are sufficiently similar to the $A\,^1\Sigma_u^+$ state to fill this vibrational level exclusively.

The metastable quartet state $X\,^4\Sigma_u^+$ was identified[18] when two separate molecular-ion drift velocities were discovered.[19] The quartet state is metastable because transition from $X\,^4\Sigma_u^+$ to $A\,^2\Sigma_g^+$ or $X\,^2\Sigma_u^+$ (the only ion states of lower energy) breaks the selection rule: quartet $\not\rightarrow$ doublet. This ion, consisting of He^+ and He $2\,^3S$, is faster than the $X\,^2\Sigma_u^+$ ion, which consists of He^+ and He $1\,^1S$, because the latter undergoes resonant collisions as it drifts through the He $1\,^1S$. This quartet state was observed to be the exclusive product of low-power, narrow-pulsewidth discharges.[19] The slower $X\,^2\Sigma_u^+$ could only appear if sufficient time were allowed for decay of the $X\,^4\Sigma_u^+$ state. As there is no potential barrier preventing formation of the quartet state, this dimer may be formed by simply multibody thermal collisions of ions with $2\,^3S$:

$$He + He^+ + He(2\,^3S) \rightarrow He_2^+(X^4\Sigma_u^+) + He \,. \quad (6)$$

Recombination of this quartet-ion state can produce the 100-Torr proton beam spectrum *A*. In the highest vibrational level this bound particle has internuclear separations ranging from 2.3 to 8.4 Å and will recombine to the high vibrational levels of the $A\,^1\Sigma_u^+$ state at radius of 2.3–3.1 Å (Fig. 4). This range of overlap explains the exclusive population of states having a large radial extent. Because the quartet ion is a product of these low-energy afterglows and recombines to produce this radiation, it merits consideration for the second process.

The metastable $2\,^3S$ atoms act as a sink for helium ions, solving the ion deficiency problem. Quartet-ion formation [Eq. (6)] competes successfully with neutral atoms that would otherwise form the ground ion $X\,^2\Sigma_u^+$ state. This is why this process is observed to the exclusion of other processes that would produce radiation from the lower vibrational levels—the Hopfield continua.

The confirmed existence of the quartet state in the afterglow, the lack of Hopfield radiation indicating the absence of the ground-state molecular ion, the overlap of the radial extents of this quartet potential with the $A\,^1\Sigma_u^+$ potential leading to the population of the observed levels, the height of the potential barrier of the $A\,^1\Sigma_u^+$ state making the association insignificant at 77 K, and the evidence of a second mechanism dependent on recombination all support the hypothesis that the second process is recombination of the quartet state.

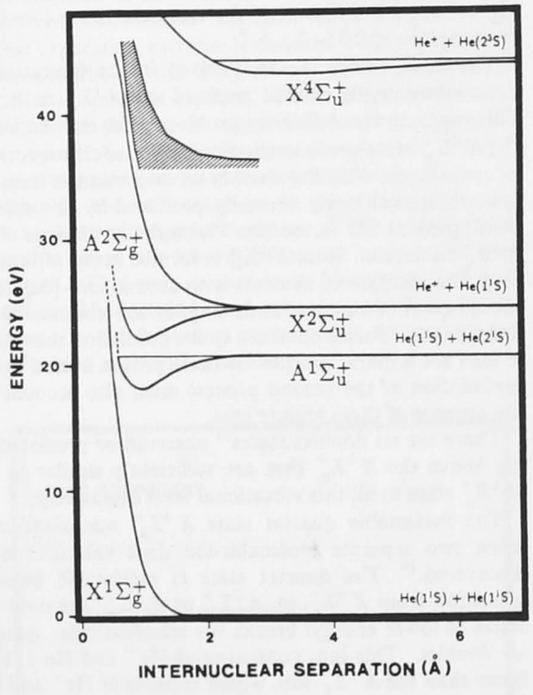

FIG. 4. Potential-energy curves of various electronic states of He_2 and He_2^+. The fine horizontal lines indicate the radial extent of the topmost vibrational levels of the various potentials. At this scale the potential barrier of the $A\,^1\Sigma_u^+$ state (0.05 eV) is not seen. The shaded region shows the possible energy and radial extent of the potential that by decaying to the $A\,^2\Sigma_g^+$ state would generate the 1050–4000-Å continuum. Source (top to bottom), Refs. 18, 14, 16, 16, and 62.

Having established association and quartet recombination as the mechanisms producing this spectrum it is possible to derive information about the lifetimes of $A\,^1\Sigma_u^+$ dimers from the pressure dependence of this spectrum. Both these mechanisms initially form $A\,^1\Sigma_u^+$ in high vibrational states. Thus the spectral distribution at 600 Torr (spectrum *B* in Fig. 1) showing radiation from lower vibrational levels is evidence of vibrational relaxation. The lifetime of the high vibrational levels of this molecule determines whether the state vibrationally relaxes or decays to the ground state $X\,^1\Sigma_g^+$. At 100 Torr, decay occurs before vibrational relaxation, while at 600 Torr there is relaxation before decay. This means that the decay rate of the molecule in the high vibrational states does not increase with pressure as much the vibrational relaxation rate.

C. Fast component

The fast component of the proton spectra is described by Bartell *et al.*[6] At 203 Torr the fast component has a decay rate of 7.2×10^6 sec^{-1} as opposed to 0.12×10^6 sec^{-1} for the first (associative) component—some 60 times faster. The fast component has a spectral range of 950–630 Å. This indicates that the fast radiation originates from the lower vibrational levels of $A\,^1\Sigma_u^+$ and not from the $D\,^1\Sigma_u^+$ state, as proposed by Bartell *et al.*[6] The $v=0$ level in $D\,^1\Sigma_u^+$ radiates as a smooth peak principally within a range of wavelengths from 740 to 600 Å (675 Å feature on the 24-Torr spectrum *E* in Fig. 1 and Ref. 20) and cannot account for the 950-Å radiation. The ratio of intensity of the fast component to the other components is constant with pressure and wavelengths from 660 to 950 Å.[6] As the explanation of Bartell *et al.* has been the only one proffered, the reaction mechanism responsible for generating the fast component of the spectra, therefore, is as yet unknown. Two hypotheses as to the origin of the fast component merit consideration: (1) the fast component results from different conditions in the early afterglow, (2) the fast component is caused by the decay of the $B\,^1\Pi_g^+$ molecule.

At the beginning of the afterglow there may be a sufficient concentration of electrons for the process of superelastic collisions to become significant. This effect was illustrated by Lawler *et al.*[21] who measured a much higher the decay rate of the $2\,^1S$ state in a pulsed electrical discharge than that found in the late afterglow of a proton-beam apparatus[12] (Fig. 5). The decay rate of the fast component coincides with the higher decay rate of the $2\,^1S$ state. It might be possible that in the fast component the $A\,^1\Sigma_u^+$ is formed by association [Eq. (1)] its decay rate reflecting the rapid decay rate of the $2\,^1S$ state, and is spectral extent speculatively explained by vibrational relaxation of the high vibrational levels (corresponding with the shorter wavelength radiation) by electrons. This hypothesis is refuted by the unperturbed level

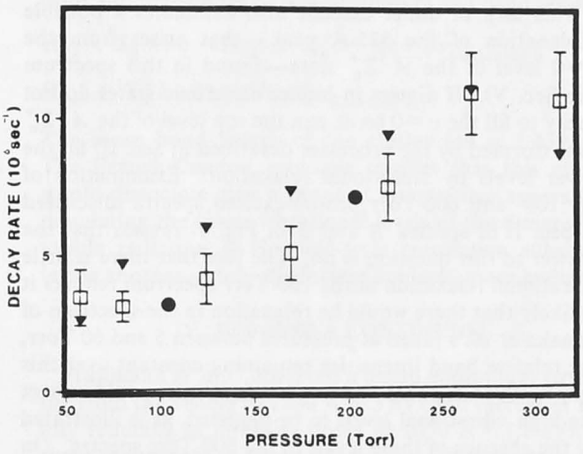

FIG. 5. Pressure dependence of decay rates: squares denote $2\,^1S$ in a pulsed discharge (Ref. 21), wedges denote $2P^3$ in a pulsed discharge (Ref. 21), and circles denote fast component of dimer decay in proton-excited helim (measured from data provided in Ref. 6). The solid curve is the decay rate of $2\,^1S$ measured in proton beam apparatus (Ref. 12) (also shown in Fig. 2).

of radiation from the higher vibrational levels during the time of the fast component. Firstly, this indicates that there is not a period of enhanced $2\,^1S$ decay, and secondly, these high vibrational levels are not destroyed by the supposed high concentration of electrons. Instead, the fast component appears to be a superaddition from a process not involving $2\,^1S$.

The $B\,^1\Pi_g^+$ state may be formed by association of neutral atoms with the $2\,^1P$ state (helium atoms). The selection rules allow this to decay the $A\,^1\Sigma_u^+$ state and thereby create the fast component. The fixed ratio of $2\,^1S$ to $2\,^1P$ created by the proton beam[6] would explain the fixed ratio of intensities of the fast and slower components.

This process also explains "prompt molecular emission" in conventional pulsed lamps described by Villarejo *et al.*[22] In the initial excitation pulse, there is emission within the same wavelength regions of the fast component. Disturbingly, as Villarejo *et al.* noted, there is insufficient time to form the $X\,^2\Sigma_u^+$ dimer ions that would normally account for this radiation (see Sec. V). Association of $2\,^1P$ atoms during the excitation pulse would provide a plausible explanation of this phenomenon.

In summary, the quartet state of the ion recombines to form the high vibrational level of the $A\,^1\Sigma_u^+$ state, which in turn decays to the ground state yielding this particular spectrum. The existence of the quartet channel in addition to the association channel accounts for a two-term decay-rate equation. The quartet channel could also explain the production of this spectrum by molecular beams in which the number of collisions and temperature would make the association unlikely on kinetic grounds. The formation of excited dimer ions by association of ions and metastable atoms may explain the absence of Hopfield continuum with this spectrum, even though atomic ions are produced by the proton beam.

III. 600–700-Å BAND SERIES AND 2100–6100-Å CONTINUUM

When the 600-Å band, discussed in the Sec. II, was investigated with high-resolution spectrometers, it was found to be the most intense and narrowest of a series of 14 or more bands stretching to longer-wavelength regions (F in Fig. 1). In this section, a nexus will be established between this band series and a broad continuum, the validity of which rests on the interpretation of the origins of this band series.

In the literature two explanations have been advanced for this band series: (1) the band series represents nodes in the wave function of the highest vibrational level,[7,8] and (2) the band series is the result of radiation from successive vibrational levels.[23] These explanations are not mutually exclusive.

The generation of this band series by a single vibrational level—the first hypothesis—places a number of constraints upon the position and relative intensity of these bands.

(1) The spectra must be calculable using the ground- and excited-state potentials.

(2) Since the wave functions are not affected by discharge conditions, the relative intensity of successive bands must likewise be constant under varying conditions. Minor variations may be argued for by reference to the effect of different populations of rotational levels.

(3) Since the wave function increases at the extremes of the bound potential, and the ground-state potential flattens at larger internuclear distances, the shortest-wavelength band should have the greatest intensity.

In fact, the first peak at 600 Å can be one-sixth of the intensity of the second at 601 Å.[7] This is accounted for in Sando's[9] simulation by a hybrid of the two explanations—using the two uppermost, quasibound, levels. The topmost $v=17$ level causes the 600-Å peak; this level can dissociate, explaining the weaker intensity of this peak. The $v=16$ level causes the 601-Å peak and subsequent bands result from nodes in its wave function. Sando explains the filling of these levels by free-free radiative emission.[24]

The proposition that the 600-Å band series is the result of radiation from a series of vibrational levels—the second hypothesis—was semiquantitatively described by Tanaka and Yoshino.[23] They map the position of the maxima onto the location of vibrational levels in the $A\,^1\Sigma_u^+$ state. In support of this proposition, the first seven absorption bands, which correspond to transitions of the ground state to the upper state, were found to coincide with the band peaks. The energy shifts between the emission and absorption spectra are semiquantitatively explained by consideration of the position of the maxima in the upper state in relation to the ground-state wave function of energy kT.

Perhaps the most compelling evidence that the bands between 600 and 700 Å originate from different vibrational levels is their apparent freedom from constraints (2) and (3), as shown in Table I. There is no agreement between experiment and the theoretical results. In particular, the band-to-band variability of the 20-K experimental

result (produced by an electron beam incident on superfluid helium[25]), shows no indication of being generated by the projection of a single vibrational state onto a smooth ground-state potential. Further, the absence of the first three bands may indicate that these levels are not formed at all, rather than being formed and then absorbed by the intervening gas, as was proposed by Stockton *et al.*[25] The work of Tanaka and Yoshino[23] shows that the absorption bands in this region are not sufficiently broad to block out this radiation.

The validity of the second hypothesis, that this spectrum is generated from a distribution of vibrational levels, is pivotal to an explanation of the visible continuum which is found to accompany this spectrum. If a cluster dissociates to form a $A\,^1\Sigma_u^+$ dimer, it will fill a distribution of levels consistent with its range of internuclear separations upon fragmentation, which is likely to be different from that of a higher dimer level. Thus the generation of this spectrum from a distribution of states—hypothesis 2—is a necessary precondition for a reaction that creates this spectrum by clusters populating the $A\,^1\Sigma_u^+$ state. Evidence for such a reaction is presented in the remaining part of this section.

In 1958 Tanaka *et al.*[26] reported the spectrum *F* seen in Fig. 1. An ac power supply for a commercial sign, with no charging capacitor (denoted as "uncondensed"), was used. This spectrum has been produced in dc discharges at room and liquid-nitrogen temperatures[7] and by bombarding superfluid helium at 20 K with electrons.[25] The band intensity in the spectrum of Tanaka *et al.* has been shown to increase with pressure up to 60 Torr.[27] The intensity of the band may still increase at higher pressures; however, this was not determined due to deterioration of discharge conditions.

The only molecular bands observed in the spectrum of Tanaka *et al.* were weak triplet bands; these are not directly involved in the singlet cascades which result in vuv radiation from the singlet $A\,^1\Sigma_u^+$ state. Further, these bands diminished with increasing pressure, contrary to the trend of the vuv radiation. This indicates that this spectrum is not generated by the decay of higher dimer neutral and ion states to the $A\,^1\Sigma_u^+$ state, as such transitions would produce molecular band radiation.

This lack of dimer cascade also eliminates a possible explanation of the 825-Å peak—that arises from the $v=0$ level of the $A\,^1\Sigma_u^+$ state—found in this spectrum (see Sec. V). If dimers in higher electronic states do not decay to fill the $v=0$ level, can the top level of the $A\,^1\Sigma_u^+$ state (formed by the processes described in Sec. II) fill the lower levels by vibrational relaxation? Examination of the 100- and 600-Torr proton-excited spectra (discussed in Sec. II B, spectra *A* and *B* in Fig. 1) reveals that the answer to this question is no. The fact that there is little vibrational relaxation in the 100-Torr spectrum renders it unlikely that there would be relaxation in the spectrum of Tanaka *et al.*'s taken at pressures between 5 and 60 Torr, the relative band intensities remaining constant over this range. Even if there were relaxation, one would expect the high vibrational levels to be depleted, as is illustrated by the absence of these levels in the 600-Torr spectra. On the contrary, in the spectrum of Tanaka *et al.*'s the highest band has the strongest intensity.

As both the cascade from higher dimer states and vibrational relaxation have been eliminated as viable explanations of the 825-Å feature, a further explanation is required. The process for the band series hypothesized in this paper also accounts for the filling of these lower vibrational levels.

The mechanism responsible for the band series is revealed by examination of an apparent by-product: a weak *continuum* stretching from the visible 6100 to $\simeq$2100 Å (Ref. 27) observed in conjunction with the 600–700-Å band series. The vuv and visible continua both increased with pressure. The 2100-Å radiation (5.9 eV) is consistent with transitions from the highest vibrational levels of molecules corresponding to atoms with large principle quantum numbers to the lowest levels in the $A\,^1\Sigma_u^+$ state.

The existence of this continuum implies that the intermediate species is multibody, most probably He_3^*. Balasubramanian *et al.*[15] have recently treated theoretically He_3^+, an ionic species known to exist in discharges. It was determined to be the major ionic species at 82 K.[28] This cluster can be used to illustrate the process that

TABLE I. Intensity ratios of successive peaks in the 600–700 Å series (e.g., spectrum *F* in Fig. 1). The ratio of successive peaks is given in order to minimize the effects of spectrometer functions.

Peak ratios	Intensity ratios Experimental (300 K)[a]	Experimental (20 K)[b]	Theoretical (300 K)[c]
601/600	1.149	>1	0.83
602/601	0.260	>1	0.30
605/602	0.500	>1	0.30
608/605	0.577	0.76	0.50
613/608	0.626	0.92	0.51
619/613	0.723	0.56	0.61
627/619		0.79	0.57

[a]Reference 27.
[b]Reference 25.
[c]Reference 24.

leads simultaneously to this continuum and band series:

$$\begin{aligned} &He_3^+(^2\Sigma_g^+)+e \rightarrow He_2(A\,^1\Sigma_u^+)+He+h\nu_{6100-2100\,\text{Å}}, \\ &He_2(A\,^1\Sigma_u^+) \rightarrow He+He+h\nu_{600-1000\,\text{Å}}. \end{aligned} \tag{7}$$

The mean bond length of the cluster ion is 1.239 Å.[15] The Franck-Condon principle implies that this cluster would dissociate over a range of internuclear separations populating the lower vibrational levels of the dimer. The visible radiation is Hopfield-style continuum subsisting inside another—only the former contains more bodies.

IV. 1050–4000-Å CONTINUUM

Huffmann *et al.*[29] observed a broad continuum stretching from the visible to 1500 Å (8.3 eV) and thereafter rapidly reducing in intensity down to 1050 Å (11.8 eV). In their experiment a lamp was connected to a dc power supply in parallel with a capacitor which charged up to the lamp breakdown voltage and then discharged through the lamp. The continuum began at pressures of 150 Torr; although the Hopfield dimer continuum (Sec. VI) occurred with it, by about 200 Torr, the broad continuum was much stronger. The optimum operating pressure was 800 Torr. Since the repetition rate diminished with pressure the optimum pulse brightness may be at still higher pressures.

The existence of a continuum implies that some of the energy of decay is lost into fragments; therefore the species involved is multibody. The energy associated with a 1050-Å photon is too great to be that from a transition between the excited levels of the dimer (<6 eV) unlike the scenario for the 2100–6100-Å continuum in the Sec. III.

Huffman *et al.*, attributed this continuum to levels in He_2^+ on the basis of the high concentration of He^+, deduced from the broadening of He II radiation. They noted that information about the levels of He_2^+, then unavailable, would help in the identification of the likely reaction mechanism. Despite considerable progress in this area since the publication of their paper in 1960, there is still no clear explanation of this spectrum.

$X\,^2\Sigma_g^+$ states of He_2^+ have been accurately mapped using information gained from scattering experiments.[17] The $X\,^2\Sigma_u^+$ bound ground state is also accurately known.[15] It can be concluded from the value of these potentials (see Fig. 4) that the bound-bound $g \rightarrow u$ transitions are too great in energy (19 eV) to account for this radiation. A transition to the unbounded ground $A\,^2\Sigma_g^+$ (see Fig. 4) state from an excited $X\,^2\Sigma_u^+$ state could generate such a continuum. To date there are no calculations or measurements of excited $X\,^2\Sigma_u^+$ states in helium molecular ions. However, there are calculations for heavier elements, briefly reviewed by Krauss and Mies,[30] indicating that these excited $X\,^2\Sigma_u^+$ states are bound. Energy considerations dictate the radial extent of any bound state (including cluster ions) dissociating into this potential, to be within the shaded region of Fig. 4.

When Bogdanova *et al.*[31] bombarded helium impregnated metal with electrons they discovered He_2^{+*} ions of lifetime at zero pressure of 170±20 nsec. Although they calculated the ion's formation energy to be 44±2 eV, this result must be questioned as the energy of the decay products—an ion (24.59 eV) and a $3\,^3D$ (23.0 eV) or a $4\,^3D$ atom—is greater than 46 eV. The decay to these triplet atomic states indicates that the ion is a quartet state lying above and perhaps crossing the quartet potentials that dissociate to these triplet atoms. Being a quartet state it can only decay to the ground quartet state (Sec. II B) and thus could not generate this spectrum. This analysis is consistent with the failure to observe this continuum in their experiment.

He_2^{2+} appears to be an alternative explanation of this spectrum. The high density of He II radiation signifies the high densities of the double ions. The ground state of He_2^{2+} is bound between approximately 0.5 and 1.0 Å and could not produce such a continua.[17] Yagisawa *et al.*[32] have calculated the first 11 excited states of He_2^{2+}, none of which is capable of generating this radiation.

Trimer and heavier cluster ions are also possible candidates. At room temperature and 800 Torr, 4% of cluster ions are trimers. This percentage, proportional to pressure, is an extrapolation from work by Gusinov *et al.*[33] Information about He_3^{+*} and ungerade He_2^{+*} would help in the identification of a likely reaction mechanism.

Note added in proof. Blint[34] has calculated $^2\Sigma_u^+$ potentials for He_2^+. The first excited $^2\Sigma_u^+$ state has its first vibrational level at an energy of approximately 48 eV with a radial extent consistent with the shaded region of Fig. 4. I am presently attempting to confirm whether or not this molecule produces this spectrum on decay to the $A\,^2\Sigma_g^+$ state by simulating the spectrum.

V. 600–1000-Å HOPFIELD CONTINUUM

A pulsed discharge is the mostly widely used method of producing the Hopfield continuum (*D*, *E*, and *G* in Fig. 1). It attains a claimed 1% efficiency in converting electric energy to vuv light in the afterglow (700 Torr, 15 keV, 20 ka, 10-nsec pulse).[35] This high efficiency makes this process a prime candidate for a vuv dimer laser. In this section the important states and mechanisms involved in the formation of the spectrum are reviewed and the contribution of metastable states discussed.

A. Photodissociating molecules

The Hopfield continuum is caused by the decay of the first four vibrational states of $A\,^1\Sigma_u^+$ and $D\,^1\Sigma_u^+$ to the ground state $X\,^1\Sigma_g^+$.[20] The contribution of the $D\,^1\Sigma_u^+$ decreases steadily with pressure until by 100 Torr it is not observed. The relative populations of the vibrational levels are to high in energy to be thermal; rather they are the result of the recombination of molecular ions.

B. Molecular ions

To analyze the lifetime of the dimers and to achieve efficient light sources it is important to understand the process leading to the formation of these radiating states. The sequence of events occurring in the afterglow is formation of $He_2^+ X\,^2\Sigma_u^+$, vibrational relaxation to the $v=0$ level, recombination, and then cascade to the $A\,^1\Sigma_u^+$ and

$D\,^1\Sigma_u^+$ states. The molecular ion may be formed by a number of processes, including the association of neutral atoms with excited atoms, and the association of neutral atoms with ions.

If an excited helium atom has a principle quantum number $n > 3$ then the reaction, known as the Hornbeck-Molnar[36] process is exothermic:

$$\mathrm{He}^* + \mathrm{He} \rightarrow \mathrm{He}_2^*(v = n) \ . \tag{8}$$

This reaction involves the crossing of the potential involving the excited atom with the $X\,^2\Sigma_u^+$ (Ref. 37) ion potential leaving the ion in the vibrational level of the crossing. Its subsequent relaxation [Eqs. (10) and (11)] accounts for the extremely large atomic cross sections for this process; the $3\,^3D$ state, for instance, has a cross section of 1.4×10^{-15} cm^2.[38]

Multibody formation by direct combination of a helium ion with ground-state atoms has been investigated by Russell:[39]

$$\mathrm{He}^+ + \mathrm{He} + \mathrm{He} \rightarrow \mathrm{He}_3^+ \rightarrow \mathrm{He}_2^+[X\,^2\Sigma_u^+, (v = \max)] + \mathrm{He} \ . \tag{9}$$

This process has been measured by observing the change in ion-drift velocity upon the formation of the molecular ion. The reaction has been established as the major method of molecular ion production.[40] This reaction is three body, proceeding twice as fast at liquid-nitrogen temperatures as at room temperature and has a measured rate of $\kappa = 1.10(t/300)^{-0.38}\times10^{-31}$ cm^6 sec^{-1}.[39] The crucial aspect of this reaction is that it does not generate any ultraviolet light in the hot plasma conditions of an ordinary dc discharge; for this it is necessary to use the afterglow of a pulsed discharge. At some step, the series of reactions that generate the excited dimer breaks down, eliminating the radiation. The dimer itself can survive to radiate in the hot plasma, as evidenced by the prompt molecular emission discussed in Sec. II C.

Once He_2^+ is formed it rapidly relaxes to the $v = 0$ level. This is facilitated by the overlap of this potential with a large number of molecular potentials[13] allowing a cycle of autoionization

$$\mathrm{He}_2^*(v = n) \rightarrow \mathrm{He}_2^+(v = n - 1) + e \tag{10}$$

and recombination

$$\mathrm{He}_2^+(v = n - 1) + e + e \rightarrow \mathrm{He}_2^*(v = n - 1) + e \tag{11}$$

to proceed. The electron remains in a high Rydberg state and can be autoionized by a vibrational quantum, resulting in rapid vibrational relaxation of He_2^+. The ion's vibrational relaxation rates have been measured to be five times faster than gas collisions, which also relax the molecule. As recombination and the cascade to the radiating states contain the rate-limiting step, this process will be dealt with in Sec. VI.

C. Role of metastable atoms and molecules

Metastable atoms are important in determining the kinetics of the afterglow; they can modify the electron-energy distribution by superelastic collisions.[41] They can form dimers through neutral collisions and can generate ions through metastable-metastable–atom collisions. Further, they can react with atomic ions to form excited dimer ions (Sec. II). Finally, metastable atoms themselves may be formed by the dissociation of dimers and dimer ions. With so many potential reactions, interpretation of the time evolution of metastable-atom populations is difficult. The significant factor in this discussion of metastable atoms is the extent to which they couple to the final radiation. Radiation trapping adds further complexity owing to the fact that it enhances the population of resonant states so that they also appear to have metastable lifetimes.

Section II B illustrated a reaction in which metastable $2\,^1S$ molecules reacted with neutral atoms. Another example involving $2\,^3S$ (Ref. 42) is

$$\mathrm{He}(2\,^3S) + n\mathrm{He} \rightarrow \mathrm{He}_2(a\,^3\Sigma_u^+) + (n - 1)\mathrm{He} \ . \tag{12}$$

This forms an ungerade dimer which is precluded from radiating to the ground state by its parity. Even though this reaction is in strong reverse equilibrium, reaction of the product with impurities or metastable-metastable–atom collisions [Eq. (14)] serves as a sink for $\mathrm{He}(2\,^3S)$ and may explain the decay rate of $\mathrm{He}(2\,^3S)$ observed by Horiguchi *et al.*[43] The height of the potential barrier for this reaction has been calculated to be 0.08 eV.[16]

The populations of $2\,^1S$ and $2\,^3S$ are coupled in conditions of high electron density by a weak spin-exchange reaction discovered by Phelps[44],

$$\mathrm{He}(2\,^1S) + e \rightarrow \mathrm{He}(2\,^2S) + e \ , \tag{13}$$

who determined its rate to be 3.5×10^{-7} cm^3 sec^{-1}.

Metastable-metastable–atom reactions,

$$\mathrm{He}^* + \mathrm{He}^* + n\mathrm{He} \rightarrow \mathrm{He}^+ + n\mathrm{He} + e \ , \tag{14}$$

have been found by Biondi[45] to have a rate of 4×10^{-9} cm^3 sec^{-1}. Such reactions are important as they couple the metastable-atom population to species that eventually create the Hopfield radiation, and also provide an explanation for the decay of $a\,^3\Sigma_u^+$.[46] In low-pressure discharges[48] the electron population almost doubles after the termination of the pulse due to this mechanism. Hirabayashi *et al.* deduce an increase by a factor of 12 in electron population.[47] Trace impurities are found to be critical to the rate of metastable-atom conversion.

The formation of metastable atoms may be achieved by one of two processes. (1) Metastable atoms from excited atoms: Collisional-radiative recombination theory describes the atomic recombination and the Saha-Boltzmann equation[47] in the radiative regime[48] describes the cascade to the metastable atom. (2) Metastable atoms from excited dimers: this process becomes significant at higher pressures.

An important result from the analysis of the first process is that in the afterglow the electron temperature rapidly falls to the ambient temperature of the gas.[48] Controlling the operating temperature of the lamp will determine the electron-energy distribution in afterglows.

The second process constitutes a significant dimer loss channel. Generation of excited helium atoms associated with the recombination of He_2^+ has been observed.[49] The atomic 10 830-Å radiation from the $2\,^3P$ to $2\,^3S$ transition has an anomalous decay curve in that it follows that of the helium molecules. The following reaction has been proposed[50] for the generation of $2\,^3P$:

$$\begin{aligned} &He+He_2^+ \rightarrow He_3^+ , \\ &He_3^+ + e \rightarrow He(2\,^3P)+2He , \\ &He(2\,^3P) \rightarrow He(2\,^3S)+h\nu_{10\,830\ \text{Å}} . \end{aligned} \tag{15}$$

This is one example of a class of possible reactions called Rydberg dissociative recombination, in which recombination can occur at different stages. This reaction is only feasible for He_2^* molecules with energy greater than the dissociation products.

In summary, the concentration of metastable and other species in the afterglow will determine which of many complex reaction paths will dominate, and whether the presence of metastable atoms will impede or enhance the final radiation.

VI. LIFETIMES

Any comment on the feasibility of a helium dimer laser relies upon an understanding of molecular lifetimes. Firstly, the lifetime of the upper state bears on issues within the lasing process itself, such as cross section, competing mechanisms, and laser design. Secondly, the lifetimes of processes that lead to the upper state determine which method of excitation most effectively fills this state.

The lifetime of the metastable $A\,^1\Sigma_u^+$ state at 700 Torr (Ref. 51) 0.55 nsec. This is calculated from

$$I=\frac{\delta N}{\delta t}=\kappa N , \tag{16}$$

where N is the population of $A\,^1\Sigma_u^+ = 6.1\times10^{11}\ \text{cm}^{-3}$, κ is the rate, and the photon density is $I=1.1\times10^{21}$ photons/cm^3 sec. The decay rate may be influenced by the electron and neutral density and thus may be slower at lower pressures. Measurements of the intensity and population, similar to those made by Stevefelt *et al.*,[51] are required at different pressures to determine the pressure dependence and the natural lifetime. 0.55 nsec is a lower limit of the natural lifetime of this molecule. Lifetimes for other noble gas dimers, at pressures > 100 Torr are for Ar_2, 2.9 μsec; Kr_2, 265 nsec; and Xe_2, 100 nsec.[52]

Gand *et al.*[35] show that, in the operation of a conventional pulsed source, the higher pressures achieve brighter peak intensities and thus greater population of the upper state. Consequently, the 700-Torr value of the lifetime is relevant to the operation of lasers.

For a lasing process it is critical to utilize the method that achieves a large population of the upper state. The level before the rate-limiting step in a cascade will have the largest population. Nonexponential recombination rates lead to complex evolution of populations in the afterglow radiation. To date that has been no completely successful quantitative description of this time evolution. What follows is a qualitative description.

In a high-energy pulse the high concentrations of electrons and metastable atoms lead to the reactions and the Hopfield radiation described in Sec. V. The reactions and periods described for a low-energy pulse in Sec. II are no longer appropriate. The decay curves of a high-energy pulse afterglow contain three regions: deadtime, molecular-decay limited, and recombination limited. The extents of these regions depend upon competition between mechanisms in varying discharge conditions.

There are two mechanisms of recombination: collisional

$$He_2^+ + e + e \rightarrow He_2^*(\text{low electronic states}) + e , \tag{17}$$

and radiative,

$$He_2^+ + e \rightarrow He_2^*(\text{high electronic states}) . \tag{18}$$

The two mechanisms are not distinct and are best described by a hybrid theory, "collisional-radiative recombination."[53] This theory is embodied in the experimental value for the recombination rate by Deloche *et al.*:[54]

$$\alpha_{CR}=[\alpha_c+k_1(\text{He})]\mathcal{T}^{-x}+k_2(e)\mathcal{T}^{-y} , \tag{19}$$

where α_{CR} is the rate of combination, $\alpha_c < 5\times10^{-10}$ cm^3 sec^{-1}, $k_1 = 5\pm1\times10^{-27}$ cm^6 sec^{-1}, $k_2 = 4.0\pm0.5^{-20}$ cm^6 sec^{-1}, and $\mathcal{T}=T_e/293$ K. $x=1\pm1$, while $y=4.0\pm0.5$.

Collisional recombination occurs more rapidly at low electron temperatures. Increasing the density of electrons will significantly increase the intensity of the initial radiation. Most importantly, collisional recombination tends to form the lower electronic states, namely, $A\,^1\Sigma_u^+$. This offers two advantages.

(1) At sufficiently high electron densities the recombination rate is faster than the intermediate states decay rate. By circumventing these slower steps a higher peak intensity and a higher population of the $A\,^1\Sigma_u^+$ state can be achieved.

(2) There are fewer losses to dissociative or other reaction channels.

When the electron density reduces, radiative recombination is the dominant reaction and the molecular ion forms higher excited states. The decay tends to take a $u \rightarrow g \rightarrow u$ path to the $A\,^1\Sigma_u^+$ state, while in these states the molecules may dissociate. In these conditions some 70% of dimers are calculated[54] to dissociate without generating the Hopfield continuum.

This path produces the molecular bands observed in the visible region. Initially, the molecular band decay rate is less than the uv radiation[51] because the molecular bands do not include radiation from the collisional path. While the recombination rate is faster than the decay rate of intermediate molecular states, the latter is the rate-limiting step. This corresponds to the intermediate decay region where the decay rate departs from the recombination rate.

Ultimately, the recombination rate will become slower than the molecular radiation rate. Once more, recombination will be the rate-limiting step.

Using data from Gand *et al.*[35] and Huffman *et al.*,[55] it may be induced that the product of the pressure and the time required to reach a maximum intensity of 800-Å light is constant over a pressure range of 44–700 Torr,

$$P\tau = 5.40 \pm 0.20 \times 10^{-5} \text{ Torr s} . \tag{20}$$

This may be interpreted as the time required for the electron-energy distribution to decrease to a point which permits molecular recombination to commence.

The significance of the recombination of the molecular ion in the production of the dimer is demonstrated by the phenomenon of dead time. Huffmann *et al.*[55] observed that at 44 Torr, regardless of intensity, there was a 20-ns dead time between the excitation pulse and the commencement of the afterglow. Observation of He $2\,^1S$ shows that at 50 Torr (Ref. 43) it monotonically decays over 20 nsec. A plausible explanation for these phenomena is as follows. At this gas pressure the He $2\,^1S$ undergoes superelastic collisions with electrons, maintaining a high electron temperature which in turn prevents the recombination of the molecular ion until the population of He $2\,^1S$ is depleted. The cross section for superelastic collision at 300 K has been measured to be 3×10^{-14} cm^2.[44]

Analysis of lifetimes is crucial to laser design. For the design involving molecular beams described by Baldwin *et al.*[3] a lifetime with the highest vibrational level of the $A\,^1\Sigma_u^+$ state of the order of milliseconds would be required for it to survive for a reasonable gain length. Considering other laser schemes, the efficiency of collisional recombination, together with the short lifetime of the dimer, heighten the importance of achieving an intense pulse with a high electron density.

VII. FEASIBILITY OF A HELIUM DIMER LASER

A population inversion between the excited states (lifetime 5×10^{-10} sec) and unbound ground state (lifetime 10^{-14} sec) makes it possible to build a helium dimer laser that will produce tunable radiation in the region of 800 Å. This region is already accessed by tripling and other four-wave sum-mixing technique using gases as a nonlinear medium. The efficiency of such conversions is at best 1×10^{-4}.[56] Free-electron lasers and optical klystrons[57] are other areas that will, in time, produce coherent light at these wavelengths.

The equation determining the gain criterion[5] is

$$\sigma_{\text{atom}} = \frac{\lambda^4}{8\pi\tau c\Delta\lambda} = 9\times10^{-18} \text{ cm}^2 , \tag{21}$$

where λ is the wavelength (825 Å), σ is the cross section for stimulated mission, τ is the natural lifetime (>0.55 nsec), and $\Delta\lambda$ is the width of the transition; in this case, 125 Å is on the basis of the spectrum of Gand *et al.*[35] The value 9×10^{-18} cm^2 is the maximum value of the cross section for stimulated emission. This compares favorably with the cross section for Ar_2 of 1×10^{-17} cm^2 in which laser action has been demonstrated (60 atm at 1260 Å, the end mirrors having 5% reflectivity[4]). Dimer lasers have already been achieved in argon and xenon, the major problems being radiation damage to the optics.

The cross section per molecule is inversely proportional to the lifetime τ. The population of the upper state is proportionate to τ making σ_{tot} independent of τ. Therefore, the upper-state lifetime is of secondary importance, pertaining to issues such as the bandwidth of the outcoming radiation and the susceptibility of the upper state to alternate reactions (if the molecule has a long lifetime it is likely to react). Paramount to lasing is the population of the excited state (N); the method that produces the greatest peak intensity is best suited to stimulated emission. Critical to achieving a large peak intensity is rapid recombination and direct formation of the $A\,^1\Sigma_u^+$ state found in high-pressure, high-electron-density pulsed discharges.

Mirrors at the end of the cavity will reduce the gain requirements. Tungsten has a reflectivity of 25% in this region,[58] while iridium coated with aluminum (400 Å) (Ref. 59) has a theoretical normal incidence reflectivity of 70% at 825 Å. If the reflectors also polarize the light, one example being a corner reflector, this would increase the effective gain by a factor of up to $\sqrt{2}$. Such a corner reflector can be made to focus the radiation by constructing it with two toroidal mirrors that are designed to image at a grazing angle of 45°. The mirrors are cut and joined at an angle of 90°.

Despite the apparent feasibility of this laser, there are engineering problems to overcome. Not the least of these is the fact that this wavelength of radiation is absorbed by air (as is 1260 Å).

In summary, the $A\,^1\Sigma_u^+$ state has a cross section for simulated emission comparable to other dimers in which lasing has been demonstrated. A large population of this state can be obtained in high-pressure pulsed discharge and there are high reflectivity mirrors available for the ends of the resonant cavity.

VIII. CONCLUSION

This work has identified key population mechanisms of He_2^*. Quartet-ion recombination was hypothesized to explain the time evolution of proton-excited afterglows. Various continua were linked with different processes, highlighting the role of clusters and molecular ions. The Hopfield continua were discussed in order that the feasibility of vuv laser be accessed.

Future enquires into this topic might address the nature of the potential responsible for the 1050–4000-Å continuum, the lifetime of the higher vibrational levels in the $A\,^1\Sigma_u^+$ molecule, and vibrational relaxation mechanisms. Insights into molecular physics gained and the potential commercial applications, especially lasers, would reward such investigations.

[1]J. Hopfield, Phys. Rev. **35**, 1133 (1930).
[2]J. Hopfield, Phys. Rev. **36**, 784 (1930).
[3]K. Baldwin, R. Swift, and R. Watts, Rev. Sci. Instrum. **58**, 812 (1987).
[4]W. Wrobel, H. Röhr, and K. Steur, Appl. Phys. Lett. **36**, 113 (1980).
[5]M. Hutchinson, Appl. Phys. **21**, 95 (1980).
[6]D. Bartell, G. Hurst, and E. Wagner, Phys. Rev. A **7**, 1068 (1973).
[7]A. Laslett Smith, J. Chem. Phys. **49**, 4817 (1968).
[8]F. Mies and A. Laslett Smith, J. Chem. Phys. **45**, 994 (1966).
[9]K. Sando, Mol. Phys. **23**, 413 (1972).
[10]G. Herzberg, *Molecular Spectra and Molecular Structure,* Vol. 2 of *Spectra of Diatomic Molecules,* (Van Nostrand, Princeton, NJ, 1950).
[11]R. Kelly and L. Palumbo, Naval Research Laboratory Report No. 7599, 1972.
[12]M. Payne, G. Hurst, M. Nayfeh, J. Judish, C. Chen, E. Wagner, and J. Young, Phys. Rev. Lett. **35**, 1154 (1975).
[13]J. Stevefelt, Phys. Rev. A **8**, 2507 (1973).
[14]A. Khan and K. Jordan, Chem. Phys. Lett. **128**, 368 (1986).
[15]K. Balasubramanian, M. Z. Liao, and S. H. Lin, Chem. Phys. Lett. **142**, 349 (1987).
[16]K. Sunil, J. Lin, H. Siddiqui, P. Siska, and K. Jordan, J. Chem. Phys. **78**, 6190 (1983).
[17]A. Metropoulos, C. Nicolaides, and R. Buenker, Chem. Phys. **114**, 1 (1987).
[18]E. Beaty, J. Browne, and A. Dalgarno, Phys. Rev. Lett. **16**, 723 (1966).
[19]J. Madson, H. Oskam, and L. Chanin, Phys. Rev. Lett. **15**, 1018 (1965).
[20]H. Michels, R. Hobbs, and J. Peterson, Chem. Phys. Lett. **134**, 571 (1987).
[21]J. Lawler, J. Parker, L. Anderson, and W. Fitzsimmons, Phys. Rev. Lett. **39**, 543 (1977).
[22]D. Villarejo, R. Herm, and M. Ingram, J. Opt. Soc. Am., **56**, 1574 (1966).
[23]Y. Tanaka and K. Yoshino, J. Chem. Phys. **50**, 3087 (1969).
[24]K. Sano, Mol. Phys. **21**, 439 (1971).
[25]M. Stockton, J. Keto, and W. Fitzsimmons, Phys. Rev. A **5**, 372 (1972).
[26]Y. Tanaka, A. Jursa, and F. LeBlanc, J. Opt. Soc. Am. **48**, 304 (1958).
[27]Y. Tanaka and K. Yoshino, J. Chem. Phys. **39**, 3081 (1963).
[28]C. de Vries and H. Oskam, Phys. Lett. **29A**, 299 (1969).
[29]R. Huffman, Y. Tanaka, and J. Larrabee, J. Opt. Soc. Am. **52**, 851 (1962).
[30]M. Krauss and F. Mies, *Excimer Lasers* (Springer-Verlag, Berlin, 1979), Vol. 40, Chap. 2.
[31]I. Bogdanova, V. Marusin, and V. Yakhontova, Opt. Spektrosk. **60**, 1138 (1986) [Opt. Spectrosc. (USSR) **60**, 705 (1986)].
[32]H. Yagisawa, H. Sato, and T. Watanabe, Phys. Rev. A **16**, 1352 (1977).
[33]M. Gusinow, R. Gerber, and J. Gerardo, Phys. Rev. Lett. **25**, 1248 (1970).
[34]R. Blint, Phys. Rev. A **14**, 2055 (1976).
[35]M. Gand, A. Bouchoule, and J. Stevefelt, Appl. Phys. Lett. **35**, 50 (1979).
[36]A. Hornbeck and J. Molnar, Phys. Rev. **84**, 621 (1951).
[37]J. Cohen, Phys. Rev. A **13**, 86 (1976).
[38]M. Teter, F. Niles, and W. Robertson, J. Chem. Phys. **44**, 3018 (1966).
[39]J. Russell, J. Chem. Phys. **84**, 4394 (1986).
[40]A. Phelps and S. Brown, Phys. Rev. **86**, 102 (1952).
[41]C. Gorse, J. Bertagne, and M. Capitelli, Phys. Lett. A **126**, 277 (1988).
[42]J. Pouvesle and J. Stevefelt, J. Chem. Phys. **83**, 2836 (1985).
[43]S. Horiguchi, M. Saito, K. Nakamura, and T. Nakaya, Opt. Commun. **60**, 383 (1986).
[44]A. Phelps, Phys. Rev. **99**, 1307 (1955).
[45]M. Biondi, Phys. Rev. **82**, 453 (1951).
[46]G. Myer and A. Cunningham, J. Chem. Phys. **67**, 1942 (1977).
[47]A. Hirabayashi, Y. Nambu, M. Hasuo, and T. Fujimoto, Phys. Rev. A **37**, 77 (1988).
[48]C. Collins and W. Hurt, Phys. Rev. **167**, 166 (1967).
[49]C. Collins and W. Hurt, Phys. Rev. **179**, 203 (1969).
[50]D. Bates, J. Phys. B **17**, 2363 (1984).
[51]J. Stevefelt, J. Pouvesle, and A. Bouchoule, J. Chem. Phys. **76**, 4006 (1982).
[52]B. Stoicheff, *Frontiers of Laser Spectroscopy of Gases,* edited by A. Alves, J. Brown, and J. Hollas (Kluwer Academic, Dordrecht, 1988), p. 63.
[53]D. Bates, A. Kingston, and R. McWhiter, Proc. R. Soc. London **267**, 297 (1962).
[54]R. Deloche, P. Monochicourt, M. Cheret, and F. Lambert, Phys. Rev. A **13**, 1140 (1976).
[55]E. Huffmann, J. Larrabee, Y. Tanaka, and D. Chambers, J. Opt. Soc. Am. **55**, 101 (1965).
[56]G. Hilber, A. Lago, and R. Wallenstein, J. Opt. Soc. Am. B **4**, 1753 (1987).
[57]J. Ortega, Y. Lapierre, B. Girard, M. Billardon, P. Elleaume, C. Bazin, M. Bergher, M. Velge, and Y. Petroff, IEEE J. Quantum Electron. **QE-21**, 909 (1985).
[58]I. Sobel'man and V. Vinagradov, *Advances in Atomic and Molecular Physics: On the Problem of Extreme UV and X-ray Lasers* (Academic, New York, 1985), Vol. 20, p. 327.
[59]G. Hass and W. Hunter, Appl. Opt. **6**, 2097 (1967).
[60]R. Huffmann, J. Larrabee, and D. Chambers, Appl. Opt. **4**, 1145 (1965).
[61]W. Lindermann, Ph.D. thesis, Adelaide University, 1982.
[62]F. Van Duijneveldt, Chem. Phys. Lett. **143**, 435 (1968).

Chapter 6

Ultraviolet Continua of He_2^+

ABSTRACT

Two previously unclassified helium optical emission continua, seen in arc and other discharges, are found to result from a transition between excited states of He_2^+. *Ab initio* potential curves are calculated for the states involved and semi-empirical spontaneous emission spectra are obtained which fit experimental data. The corresponding cross section for stimulated emission suggests the possibility of a laser with a tuning range of 2500 Å to 10 000 Å peaking at $\sim$ 6000 Å. A broad band emission at $\sim$ 6050 Å maybe evidence of laser gain.

Pacs : 33.70.w

Most ultraviolet continua of helium molecules result from electronic He_2 transitions in the relatively cool conditions of a pulsed discharge afterglow.[1] Two continua which occur *during* a discharge are explained here in terms of vibrational bands of a He_2^+ electronic transition. As this transition has a bound upper state and an unbound lower state, there is a population inversion, and the possiblity of a new kind of laser.

Huffman *et al.*[2] generated an intense continuum, 1050 – 4000 Å, using a self-triggering helium discharge (100 – 800 Torr). A capacitor (0.06 μF) connected directly across a 100 mm long capillary arc[3] lamp discharged repetitively as a power supply charged it towards 10 kV. The continuum became observable only at pressures > 100 Torr. By 200 Torr it was brighter than the Hopfield[4] continuum, becoming the dominant emission. With increasing pressure, the intensity of the He II lines also increased, indicating increased temperature. The existence of He II lines in this arc and not in the instances discussed below indicate temperatures significantly higher in the long pulsed arc of Huffman. The purity conditions required for the Hopfield continuum could be relaxed for Huffman's continuum.[2] Insensitivity to impurity is consistent with the simple association formation reaction proposed later. The 2^3S–n^3P series in the published[2] spectrum allows an estimation of the electron density. The Inglis-Teller relation[5] gives a value of 3.3 $(+6.7/-2.1) \times 10^{16}$ cm^{-3} at 600 Torr. Huffman *et al.* suggested that the most likely cause of the continuum was He_2^+ but in the absence of potential curves reached no definitive conclusion.

Under the same conditions as those for the main continuum, Huffman *et al.* [2]

observed a single broad emission band at $\sim$ 6050 Å (photon energy = 2 eV), the width of which was not reported. This emission increases in intensity with pressure as does Huffman's continuum. No explanation has been offered for the origin of this band. The neutral atomic and molecular emissions are absent, or diminishing in intensity, rendering an explanation in terms of these species difficult. Inspection of the potential curves[6] for spontaneous transitions amongst excited states of He_2^+ provides no obvious explanation of this broad visible band.

Simon and Rodgers[7] examined a short arc which had the same continuum features as Huffman *et al.*'s long arc[2]. In a published[7] photographic plate the continuum is clearly visible. The 5 mm long discharge was powered by welding supplies that generated 250 A dc. The existence of this continuum in steady state conditions indicates that the molecular state responsible is continuously produced – a prerequisite for a continuously operating laser. The arc was imaged onto the slit of a monochromator and then onto a photographic plate enabling the radial extent of the light to be determined. The continuum was confined to the central region of the discharge. Simon and Rodgers[7] found the central region to have a temperature of 4000 – 4800 K, and electron density of 1.2 (+2.1/–0.2) $\times$ 10^{16} cm^{-3} at 850 Torr and 100 A.

In a water-cooled lamp powered by the transformer for a commercial advertising light (10 – 50 mA) at pressures > 100 Torr, Tanaka observed a different continuum,[8] but only a qualitative description of the emission is available. The weak featureless continuum extends from $\sim$ 2100 – 6500 Å and beyond with a flat maximum near

4000 Å. With increased pressure the intensity of the continuum was found to be enhanced at the expense of atomic line and molecular band emissions.

The main aim of this work was to find a satisfactory model for Huffman's continuum.[2] Somewhat unexpectedly, the analysis yielded an explanation for Tanaka's continuum[8] as well. Earlier it was thought, that due to the cool, low power, conditions of Tanaka's continuum, that a different mechanism, possibly involving trimers was responsible for this very broad featureless continuum[1].

As for the Hopfield emission, Huffman's continuum results from a bound to unbound state transition. Unlike the Hopfield continuum, however, the spectrum maintains the same shape over a range of pressures. This suggests that, in contrast to the Hopfield case, there is only one upper state involved in this transition.

Huffman's spectrum has a range from 1050 – 4000 Å (11.8 – 3 eV). Inspection of the potentials[6,9,10] (Fig. 1) for He_2, He_2^+ and He_2^{++} reveals that the only lower state for which the transitions would have the required energy range is $He_2^+(A^2\Sigma_g^+)$. The selection rules for allowed transitions restricts the upper states to those with uneven inversion symmetry. The energy of the emitted light imposes further restrictions, leaving only two possible upper states: $D^2\Sigma_u^+$ formed from He (2^3S) and He^+; and $C^2\Pi_u$ formed from He(2^3P) and He^+. *Ab initio* potential curves were calculated for both these symmetries and the spectra resulting from a transition to the $A^2\Sigma_g^+$ state determined.

Blint's potential curves [6] were further improved through a full configuration in-

teraction (CI) calculation [14] using his basis set. The results for the $D^2\Sigma_u^+$ and $C^2\Pi_u$ states are shown in Fig. 1 which emphasizes appreciable lowering of his $C^2\Pi_u$ potential curve at internuclear separations R < 0.8 Å. Spontaneous emission spectra were calculated from the potential curves using a coupled Schrödinger equation technique, [15] necessary to account for an avoided crossing of the $A^2\Sigma_g^+$ and $B^2\Sigma_g^+$ states at 45 eV, with a coupling[6] of 0.78 eV. This technique uses diabatic potentials and coupling which are calculable from the adiabatic curves generated by the *ab initio* calculation. The diabatic dipole transition moments were assumed to be independent of R over a range of 0.65 – 0.85 Å.

The nature of the sodium salicylate scintillator, used at the exit slit of the monochromator[2], is important for both interpretation and calculation of the spectrum. Such a scintillator has practically constant quantum efficiency over the wavelength range of the spectrum.[16] Hence the vertical scale of the spectrum given in Ref. 2 is proportional to the number of photons incident on the detector. Accordingly, the calculation contains a wavelength factor λ^{-5}. An additional signal is expected above 3500 Å as the light scatters through the scintillator and can be detected by the photomultiplier[17].

The upper state can be identified by comparing the theoretical and experimental results. The $D^2\Sigma_u^+$ is not the upper state because the calculated spectrum predicts for Huffman's smooth continuum Fano minima caused by quantum mechanical interference between the two coupled lower $A^2\Sigma_g^+$ and $B^2\Sigma_g^+$ states. The $C^2\Pi_u$ state

undergoes transitions to below avoided potential crossing of the A and B $^2\Sigma_g^+$ generating a smooth continuum. The $He_2^+(C^2\Pi_u - A^2\Sigma_g^+)$ spectrum most closely parallels the experimental observations. Thus this transition is the likely origin of Huffman's continuum.[2]

The model used to identify the transition only included the v = 0 level of the *ab initio* $C^2\Pi_u$ potential curve. This is, admittedly, simplistic as the emission is known to be from a gas above 4000 K and hence will have contributions from higher vibrational levels. It is possible that Tanaka's continuum is caused by transitions from the v = 0 vibrational level and that Huffman's continuum is from higher vibrational levels. A semi-empirical curve (Fig. 1 inset) was developed to model the experimental results (Huffman *et al.*'s quantitative spectrum[2] and Tanaka *et al.*'s qualitative description[8]). As there are no other upper states lower in energy than $C^2\Pi_u$ the lowering of the semi-empirical curve adds no ambiguity to the assignation. The accuracy of this curve is limited by the accuracy of the He_2^+ $(A^2\Sigma_g^+)$ potential curve[11], the approximation that the dipole transition moment is constant, and uncertainties in Huffman's data like grating and scintilator efficiency.

The room temperature spectrum, so obtained, indeed successfully describes the major features of Tanaka's continuum (Fig. 2). At higher temperatures, radiation from the v=1 level dominates because of a greater Franck Condon overlap and the λ^{-5} factor in the radiation rate equation. The theoretical spectrum fits Huffman's continuum for all temperatures $\geq$ 4000 K. Tunneling through the $C^2\Pi_u$ state poten-

tial barrier and the influence of a second minimum (0.3 eV beneath the dissociation energy of 45.4 eV at R = 2.9 Å Ref. 6) may explain the lack of radiation from levels higher than v =1. The matter is open until better potential curves are available. An attempt was made to explain the inflection in Huffman's continuum[2] near 2000 Å in terms of transtions from v > 1 was unsuccessful due to the spectral broadness of each vibrational contribution.

Comparison of the integrated area of the continuum with that of the line structure[2] indicates that a substantial fraction ($\gg 50$ %) of the radiant energy of the discharge is released in this transition. In a helium discharge, energy is stored in lower atomic excited states, either as metastable states or as resonantly trapped radiation. This energy is liberated when the excited states form molecules, achieve new symmetries, and can radiate.

A three-body momentum transfer collision is required for a $C^2\Pi_u$ molecule, consisting of He^+ and $He(2^3P)$, to drop into a bound state.

$$He + He^+ + He(2^3P) \rightarrow He + He_2^+(C^2\Pi_u) \quad (1)$$

$$He_2^+(C^2\Pi_u) \rightarrow He_2^+(A^2\Sigma_u^+) + \nu \rightarrow He + He^+ + \nu \quad (2)$$

This state has a calculated[6] potential barrier of 1.6 eV, the lowest for any of the excited doublet states, making it the most likely reaction. Collisional relaxation lowers the molecule through the vibrational levels swinging the equilibrium towards the formation of the molecule. The association of $He(2^3S)$ and He^+ in low energy discharges to form $He_2^+(^4\Sigma_u^+)$ in preference to the ground state dimer ion is a similar

type of reaction[18]. In overview, the conditions of an arc may be seen as facilitating catalytic conversion by He^+ of $He(2^3P)$ to $He(1^1S)$ and a photon, explaining the dominance of the continuum radiation.

Recombination of He_2^{++} and subsequent radiative decay may also have a role in creation of the $C^2\Pi_u$ state. Ground state He_2^{++}, formed by the collision of two helium ions, requires a threshold energy[10] of 3.5 eV to overcome its potential barrier. If such dimer di-cations exist, they would form the $C^2\Pi_u$ state upon recombination because of the similar ranges over which the two molecules are bound, and the high electron densities favoring the formation of lower excited states. (For an example involving He_2^+, see Ref. 19.)

Simon and Rodgers[7] reported electron densities in the range $10^{16} - 10^{18}$ cm^{-3} for continuous arcs at pressures of 500 to 5000 Torr. The high electron densities will then facilitate rapid three-body collisional recombination. Recombination of $He_2^+(X^2\Sigma_u^+)$ leads to the Hopfield continuum.[1] As the Hopfield continuum is only seen very weakly, it may be inferred that this state is a minor ionic species. One important reaction discussed by Bates[20], involving the destruction of $He_2^+(X^2\Sigma_u^+)$ and the production of $He(2^3P)$, which is in turn necessary for the creation of the $C^2\Pi_u$ state is;

$$He_2^+(X^2\Sigma_g^+) + He + He \rightarrow He_3^+ + He, \tag{3}$$

$$He_3^+ + e \rightarrow He(2^3P) + He + He. \tag{4}$$

Further investigation is required to predict the concentration of $He_2^+(C^2\Pi_u)$.

As the lower state in the transition is unbound there is automatically a population inversion. The spontaneous emission rate per unit wavelength, $W_{ab}(\lambda)$, is related to the stimulated emission cross section, σ_{stim}, by

$$\sigma_{stim} = W_{ab}(\lambda)\frac{\lambda^4}{8\pi c}. \tag{5}$$

In the absence of a value for the lifetime for $He_2^+(C^2\Pi_u)$, only the relative magnitude of the $\sigma_{stim}(\lambda)$ can be deduced. The spontaneous emission curve for Tanaka's continuum (Fig. 2) and Eq. (3), are used to calculate the cross section for stimulated emission (Fig. 2). If the lifetime were 2 ns the cross section would be 10^{-16} cm^2 at 6050 Å. The dipole transition moment is currently being calculated in order to predict the lifetime. A possible explanation of the lone broad emission band[2] found at $\sim$ 6050 Å may be laser gain. Although this would indicate very high gain for a path length of only 100 mm this proposition gains plausibility from the observation that the 6050 Å feature is near the peak in the cross section for stimulated emission and that the feature was only seen when the accompanying spontaneous emission spectrum from the C state was strong.

A He_2^+ transition has been identified which explains both Huffman's and Tanaka's continua. A laser using such a transition would be useful because of its simplicity and possible tuning range. Further theoretical analysis of the lifetime and of the population of the $C^2\Pi_u$ state to assess the merit of such a laser is in progress.

I greatly appreciate the *ab initio* calculations performed by David J. Swanton for this work.

I. REFERENCES

[1] P. Hill, Phys. Rev. A. **40**, 5006 (1989).

[2] R. Huffman, Y. Tanaka, and J. Larrabee, J. Opt. Soc. Am. **52**, 851 (1962).

[3] J. M. Somerville 'Methuen's monographs on physical subjects: The Electric Arc' Butler and Tanner (1959).

[4] J. Hopfield, Astrophys. J.**72**, 133 (1930).

[5] D. Inglis and E. Teller, Astrophys. J. **90**, 439 (1939).

[6] R. Blint , Phys. Rev. A. **14**, 2055 (1976).

[7] D. Simon and K. Rodgers, J. Appl. Phys. **37**, 2255 (1966).

[8] Y. Tanaka, A. Jursa, and F. LeBlanc, J. Opt. Soc. Am.**48**, 304 (1958).

Y. Tanaka and K Yoshino, J. Chem. Phys. **39**, 3081 (1963).

[9] M. Ginter and R. Battino, J. Phys. Chem. **52**, 4469 (1970).

[10] H. Yagisawa, H. Sato, and T. Watabe, Phys. Rev. A **16**, 1352 (1977).

[11] A. Metropolous, C. Nicolaides, and R. Buenker, Chem. Phys. **114** ,1 (1987).

[12] K. Sunil, J. Lin, H.Siddiqui, P. Siska, and K. Jordan, J. Chem. Phys. **78** 6180 (1983).

[13] J. Van Lenthe, R. Vos, J. Van Duijneveldt- Van de Rijdt, and F. Van Duijneveldt, Chem. Phys. Lett. **143**, 435 (1988).

[14] M. W. Smidt, J. A.Boats, K. K. Baldridge, S. Koseki, M. S. Gordon, S. T. Elbert, and B. Lam, "The G.A.M.E.S.S. program", Quantum Chemistry Program Exchange Bulletin **7**, 115 (1987).

[15] L. Torop, D. McCoy, A. Blake, J. Wang, and T. Scholz, J. Quant. Spectrosc. Radiat. Transfer **38** , 9 (1987).

[16] J. Samson, 'Techniques of Ultraviolet Spectroscopy', (John Wiley & Son, New York, 1967) p. 214.

[17] RCA tube handbook hb-3 vol.3-4 (1960).

[18] E. Beaty, J. Brown, and A. Dalgarno Phys. Rev. Lett **16**, 723 (1966).

[19] J. Stevfelt, J. Pouesle, and A. Bouchle, J. Chem. Phys. **76**, 4006 (1982).

[20] D. Bates, J. Phys. B. **17** ,2363 (1984).

II. CAPTIONS

Fig. 1: *Ab initio* potential curves. The states of even inversion symmetry are indicated by dashed lines, those of odd by solid lines. The sources for the curves from top to bottom at R = 1 Å are: Refs 11, this work, 11, 6, 11, 11, 12, 13. Inset: Potential curves for the $C^2\Pi_u$ state. The upper curve is from Ref. 6. The middle curve was calculated using Blint's basis but with a full C.I. The lowest curve is the semi-empirical curve. Also shown are the wave functions of vibrational levels v = 0 and 1.

Fig. 2: Relative experimental and semi-empirical emission rates. (circles): Huffman's continuum[2]. (solid curve): calculated, temperature > 4000 K. (dashed curve): calculated, temperature = 300 K. (dotted curve): stimulated emission cross section, v = 0.

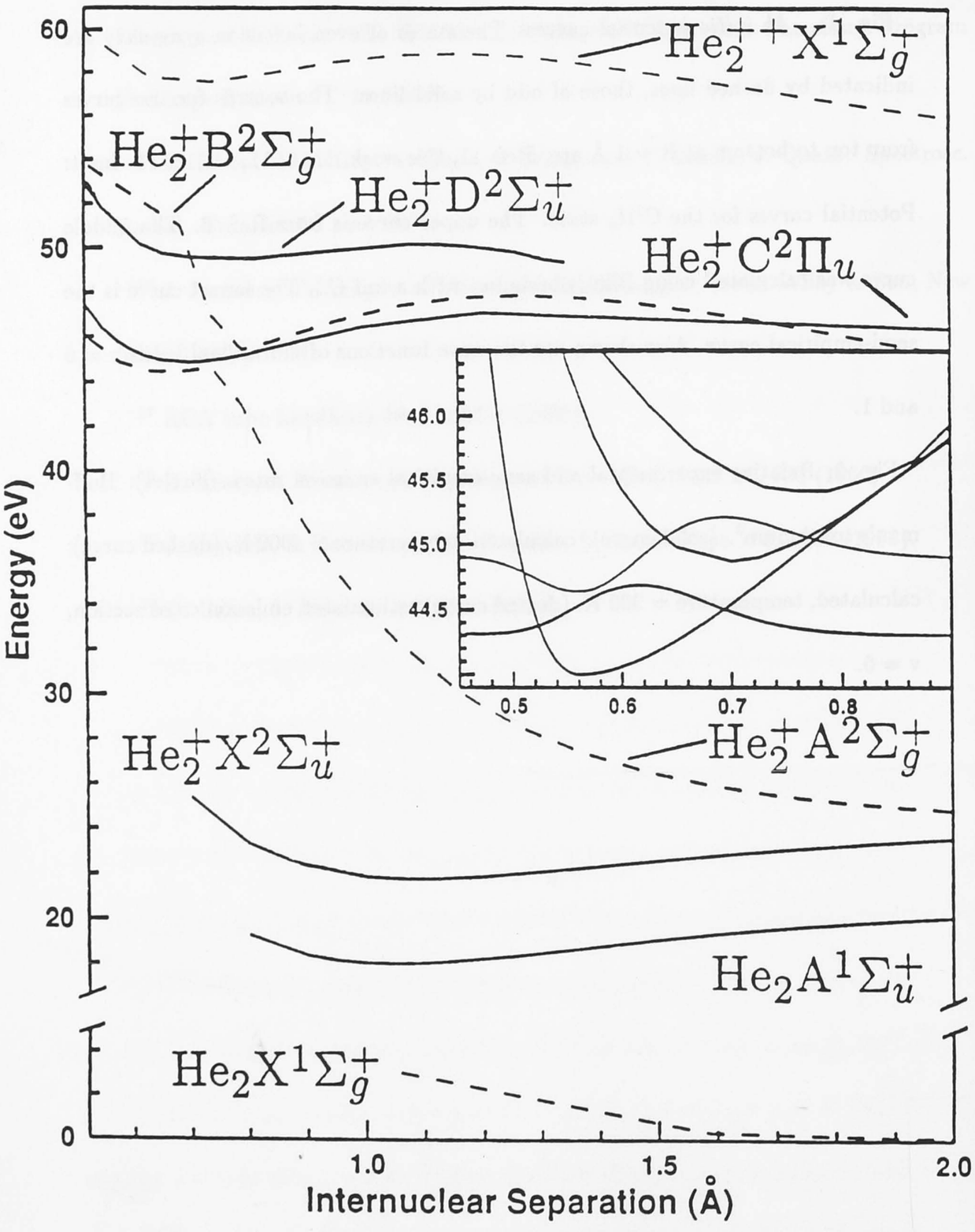
$He_2^{++}X^1\Sigma_g^+$
$He_2^+B^2\Sigma_g^+$
$He_2^+D^2\Sigma_u^+$
$He_2^+C^2\Pi_u$
$He_2^+A^2\Sigma_g^+$
$He_2^+X^2\Sigma_u^+$
$He_2A^1\Sigma_u^+$
$He_2X^1\Sigma_g^+$
Energy (eV)
Internuclear Separation (Å)
Wavelength (Å)
60
50
40
30
20
0
1.0
1.5
2.0
2000
4000
6000
8000
10000
46.0
45.5
45.0
44.5
0.5
0.6
0.7
0.8

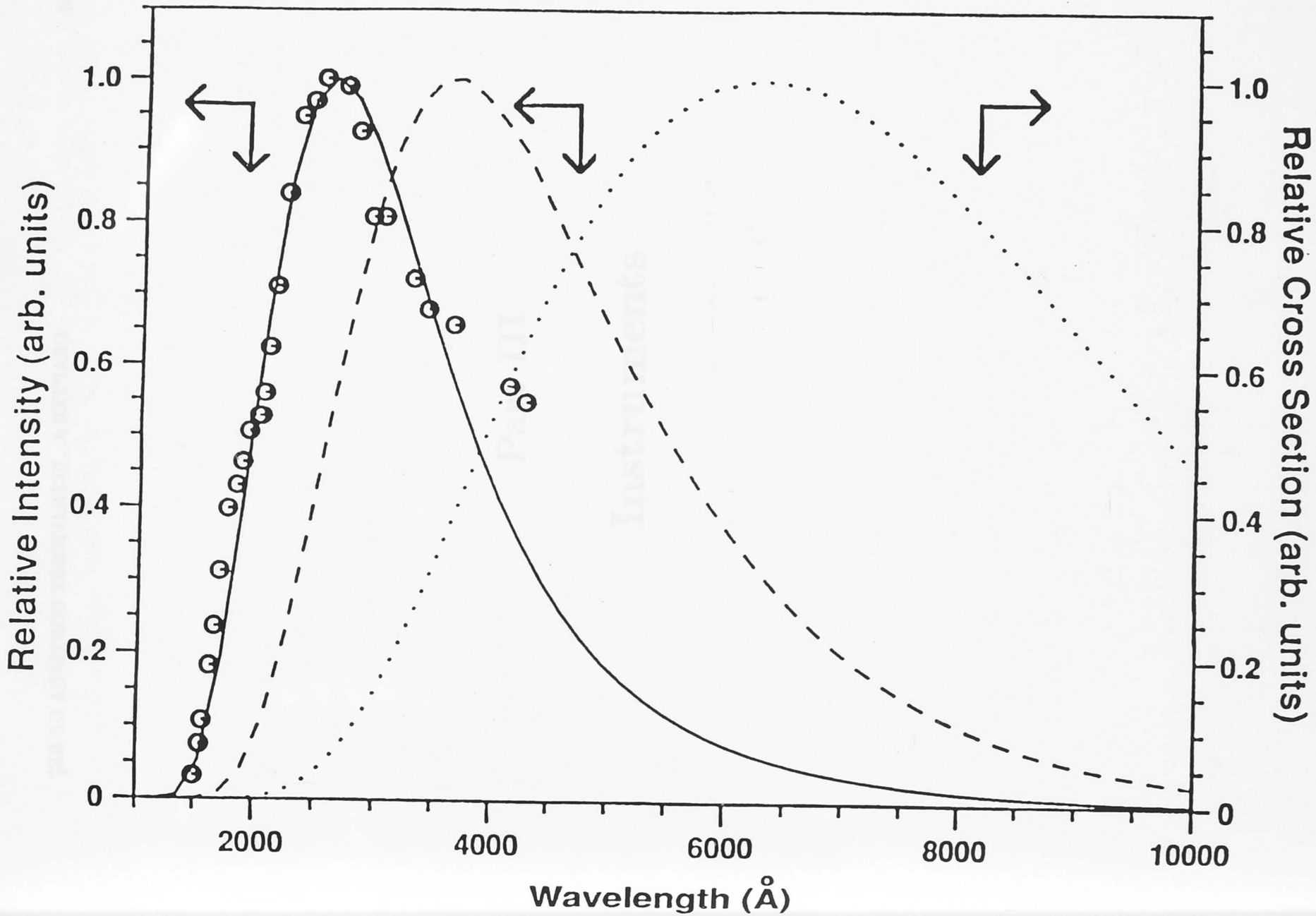
Relative Intensity (arb. units)
Relative Cross Section (arb. units)
Wavelength (Å)
0
0.2
0.4
0.6
0.8
1.0
2000
4000
6000
8000
10000

Part III

Instruments

Outline of Part III

Along with the development of improved theoretical techniques (discussed in Parts I and II) made available by advances in computing power, there is a need for increasingly sophisticated instruments. In Part III, instruments that were developed during the Ph.D. program for improved spectroscopic techniques (the secondary objective of the thesis) are described. Chapter 7 discusses the background research and construction of, a high resolution VUV laser source intended to allow more detailed studies of molecular fine structure (Tab. 1.1). This device exploits an ion chamber, which is discussed in detail in Chapter 8. Double ion chambers, in particular, have uses in calibrating light sources, and providing absolute cross sections. This chapter investigates expanding the versatility of these basic devices and outlines some of the practical problems in employing them. The double ion chamber was developed for use with photoelectron angular distribution spectrometer, the design of which is described in the final chapter. Such a device could be expected to extend the information provided by absorption cross sections – namely the phase difference between the molecular wave functions.

Chapter 7

Nonlinear Mixing in Krypton

The objective of this part of the Ph.D. program was to determine the best method of generating, and then produce, laser radiation at $\sim$ 1244 Å, so as to further a recent study by Lewis *et al.*[48]. The theory and the experimental setup are referred to here only briefly, as detailed descriptions are available from other investigators[49, 50]. This Chapter does not attempt a didactic development [51] but comments on the key concepts that led to the selection of the particular technique employed.

The advantages of gases: Gaseous nonlinear mixing media enjoy several advantages over liquids and solids: they can have good transmission right down to XUV; they are not prone to radiation damage; and their density can be easily controlled using pressure to achieve phase matching. The gas may be contained between windows in a sealed cell or alternatively techniques involving molecular beams[52] rotating disk shutters and frozen solid crystals [53] of rare gas are used. These latter designs are primarily for production of radiation above the lithium fluoride cut-off, and are not appropriate for this application, in which windows can be used.

Requirements for Four Wave Mixing: The medium is driven by the incident electric field **E**. The polarization field **P**, set up in response to the driving wave, radiates at the new wavelength due to nonlinear terms in the expansion

$$P^{(n)}_{\alpha_s}(r, w_s) = \frac{n!N}{2^{n-1}} \sum_{\alpha_1 \ldots \alpha_n} \chi^{(n)}_{\alpha_s, \alpha_1 \ldots \alpha_n}(-w_s; w_1 \ldots w_n) \times E_{\alpha_1} \ldots E_{\alpha_n} \quad , \tag{7.1}$$

where N is the number density. For four wave difference mixing, the power produced in a focused beam [54] is given by:

$$P_4 = \frac{144\pi^2 n_4}{c^2} \frac{k_0^4 k_1^2 k_2}{k_4^2 k' n_1^2 n_2} \mid \chi^{(3)} \mid^2 \; P_{10}^2 P_2 \mid F_2 \mid^2 \quad , \tag{7.2}$$

where

$$| F_2 |^2 = \frac{2k'}{\pi b} \int_0^{2\pi} 2\pi r dr \, | \int_{-\xi}^{\xi} \frac{e^{-i(b\Delta k\xi"/2) - r^2/bH(\xi,\xi")}}{(1+i\xi")(k" - ik'\xi")H(\xi,\xi")} d\xi" \, |^2 \quad , \tag{7.3}$$

where

$$H(\xi,\xi") = \frac{1+\xi"^2}{k" - ik'\xi"} \frac{i(\xi" - \xi)}{k} \quad , \tag{7.4}$$

and

$$\begin{aligned} k_o &= w - 4/c \quad , \\ k' &= 2k_1 - k_2 \quad , \\ k" &= 2k_1 + k_2 \quad , \\ \xi &= 2(z - z_0)/b \quad , \\ b &= 2\pi w_0^2 n_1/\lambda_1 \quad . \end{aligned} \tag{7.5}$$

b and z have their usual meaning in terms of the standard laser optics of a Gaussian beam[55]. A focused beam has the advantage over parallel beam interactions in that the length is defined by the optics rather than by the confinement of gas. The phase mismatch parameter is bΔk ($\Delta k = k_4 - (2k_1 - k_2)$).

The optimization of third harmonic frequency mixing can be seen from the above equations to depend on three general factors which in turn depend on the experimental conditions (*italics*):

1) **the phase matching integral** $| F |^2$, *-pressure, gas mix, proximity to single-photon resonances, geometry of the beam*

2) **the pump beams** *-power, k,*

3) **the third order nonlinear susceptibility** χ *-pressure, proximity to two-photon resonances.*

The phase matching integral depends critically on what mixing scheme is adopted i.e.;

Phase Matching Conditions for Tight Focusing:

mixing scheme	F(Δk < 0)	F(Δk > 0)	bΔk_{opt}	dispersion required	comment on feasibility
$w_1 + w_2 + w_3$	$\pi^2 (b\Delta k)^2 e^{\frac{b\Delta k}{2}}$	0	-2	negative	not possible as all gases have $\Delta k > 0$ at 1244Å
$w_1 + w_2 - w_3$	$\pi^2 e^{\frac{-b\Delta k}{2}}$	$\pi^2 e^{\frac{b\Delta k}{2}}$	0	small	reduce pressure
$w_1 - w_2 - w_3$	0	$\pi^2 (b\Delta k)^2 e^{\frac{b\Delta k}{2}}$	2	positive	no w_1 laser source

Four wave sum mixing uses the longest wavelength photons which are more easily produced with more power. The use of shorter wavelength light needed in difference mixing, is difficult

to produce and more prone to losses through competing processes. The dispersion requirements ultimately dictate what scheme is possible. On the one hand, because optimum phase matching conditions are not met experimentally, and other processes like breakdown occur, the theoretical conversion efficiencies predicted are not achieved. On the other hand, because of this, the theoretical restrictions predicted are, in practice, not as rigorous.

Theoretical[49] and experimental[56] studies have shown difference mixing in krypton to be the most practical method of VUV generation in the region required. What follows now is an examination of why alternative schemes are less appropriate.

The selection of the krypton: For four wave sum frequency mixing, $| F |^2$ is zero for positively dispersive media ($\Delta k = k_4 - (2k_1 - k_2) > 0$). There are no reported [57, 58, 56, 59, 60] negatively dispersive gases (such as mercury, etc.) with energy levels below 1244 Å, that are suitable to for use in the region of 1244 Å. Therefore it is not possible to use four wave sum mixing. Sum frequency mixing would have intrinsic advantages over difference mixing: for frequency tripling only one pump beam is required; for two-photon resonance sum frequency mixing, there is no need for frequency doubling in a crystal to reach the resonance. More complicated schemes to achieve phase matching, by having beams incident at angles, and the use of a negatively dispersive buffer gas, might provide a solution but have not so far been reported for this wavelength. For the wavelengths in this region at which xenon is negatively dispersive, phase matching has been achieved by mixing it with krypton[60].

This leaves four wave difference mixing in media with energy levels above 1244 Å as the only method to produce the required radiation. The phase matching requirement is less stringent, being optimised at Δk=0[54]. The value of Δk is dominated by the generated light – the other longer wavelengths, as they are much further from resonance, have a negligible contribution. Δk is calculated for tripling[60] using the Sellmeier [61] formula and is, for practical purposes, graphically indistinguishable from that calculated for the resonance difference mixing schemes. The phase matching requirement can be fulfilled by reducing the number density. This also reduces the effective χ leading to an optimum pressure at which to operate a cell that achieves the best product phase matching, $| F |^2$, and nonlinear susceptibility , $| \chi |^2$[57]. $| F |^2$ is also a function of the beam optics. For the cases described by Bjorklund[54] this quantity increases as the relative beam waist constricts ($b/l \rightarrow 0$), for all values of $b\Delta k$. Generally, the tighter the beam waist b, the higher the efficiency of production, until higher order nonlinear effects and self-defocusing, arise.

Although the system may be phase mismatched ($\Delta k \neq 0$), momentum is conserved. To achieve this conservation, light is produced at angles to the driving beams [54].

Link with theoretical calculation performed in Part II: The nonlinear susceptibility χ is a tensor. For the field of frequency w_4 in the z direction, produced by the incident fields

frequency w_1,w_2,w_3 respectively in the x,y,z directions, the nonlinear susceptibility is written $\chi^{(3)}_{zxyz}(w_4{:}w_1,w_2,w_3)$. Most of the 81 possible tensor components for four wave mixing are zero or related to one another, leaving only three distinct values. These tensor components can be calculated directly, *ab initio*, from the results produced from the *ab initio* calculation techniques as used for He_2^+ in Part II of this thesis, thus:

$$\begin{aligned} \mathbf{P} &= trace\mu\rho^3 = g\chi\mathbf{E} \ , \\ trace\mu\rho^1 &= dipole\ moment \ , \\ \rho^j_{mn}(t,w) &= \tfrac{i}{2\hbar}e^{iw_{mn}t}\int_{-\infty}^{t} A(t')(e^{-i(w-w_{mn})t'} + e^{-i(w+w_{mn})t}) \times [\mu,\rho^{(j-1)}]dt' \ , \end{aligned} \tag{7.6}$$

where

$$w_{mn} = (E_m - E_n)/\hbar - i/T_{mn} \ . \tag{7.7}$$

The dipole transition moment μ and density matrix ρ can be calculated for the SCF levels and then converted to the CI representation. $A(t')$ is the field incident on the medium.

Resonances in Krypton: χ is resonantly enhanced when the transition is coincident with intermediate energy levels as described by the following resonance formula[51],

$$\chi^{(n)}(-w_s;w_1...w_n) = \frac{l_T}{n!\hbar^n}\sum_{gb_1...b_n}\varrho(g)\frac{<g\mid \mathbf{e}_s\mu\mid b_1><b_1\mid \mathbf{e}_1\mu\mid b_2> .... <b_1 n\mid \mathbf{e}_n\mu\mid g>}{(\Omega_{b_1g}-w_1...-w_n)(\Omega_{b_2g}-w_2...-w_n)...(\Omega_{b_ng}-w_n)}, \tag{7.8}$$

where l_T is a permutation multiplier, $\varrho(g)$ is the Boltzmann weighting of the ground state, and $\Omega_{b_1g} = w_{b_1g} - i\Gamma_{b_1g}$ with Γ representing a classical damping term related to the lifetime of a particular state. $\mathbf{e}_s$ is the light vector with frequency w_s. For a resonance case, a term in the denominator will become very large, leading to a single term in the summation dominating the process. Of the many possible transitions in both xenon and krypton, as Hilber *et al.*[57] suggests, and Miyazaki *et al.*[52] finds, the Kr[1/2,0] two-photon transition (Fig. 7.1) produces more light than lower transitions, by about an order of magnitude. Currently there are investigations into the feasibility of using the 5p' level at 1020.9 Å [62]. In the proposed scheme 6100 Å radiation is doubled in a KDP crystal and then the fundamental radiation after passing through a half-wave plate is recombined in a cooled BBO crystal to reach wavelengths as short as 1970 Å [63]. The resonance at 1237.8 Å leads to both enhanced susceptibility and a deterioration of phase matching conditions. As the generated light approaches 1244 Å, optimal power production is achieved by reducing the pressure.

Experiment: The experimental setup is copied exactly from the one at Imperial College[50] and is shown in Fig. 7.2. This was done to achieve a working system in the shortest possible time. A XeCl excimer laser (Lambda Physik EMG 201 MSC) pumps two dye lasers (Lambda Physik FL 3002). The blue laser employs Stilbene 3 dye to generate 4250 Å radiation that is

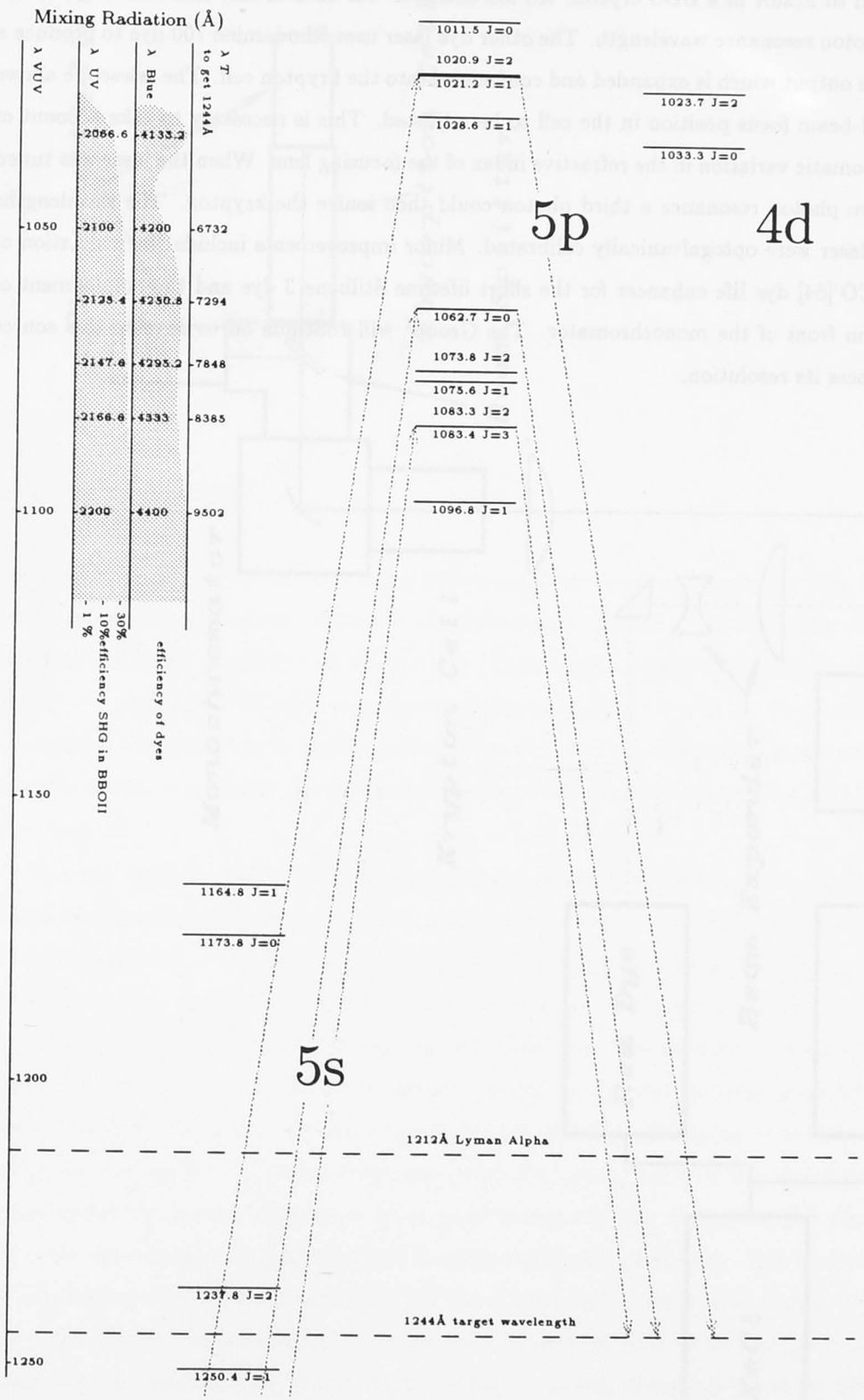

Figure 7.1: Krypton Energy Levels: The up arrow indicates a two-photon resonance transition, the down arrow indicates the difference-photon transition to the output level.

doubled to 2125Å in a BBO crystal. An ion chamber was used to fine tune this laser to the two-photon resonance wavelength. The other dye laser uses Rhodamine 700 dye to produce a tunable output which is expanded and confocused into the krypton cell. The telescope allows the red beam focus position in the cell to be adjusted. This is necessary to take account of the chromatic variation in the refractive index of the focusing lens. When the laser was tuned to a two photon resonance a third photon could then ionize the krypton. The wavelengths of the laser were optogalvanically calibrated. Minor improvements include the utilization of 'DABCO'[64] dye life enhancer for the short lifetime Stilbene 3 dye and the employment of a lens in front of the monochromator. The Group[1] will continue on to develop this source and assess its resolution.

[1]UV Physics group, AMPL, ANU, Canberra

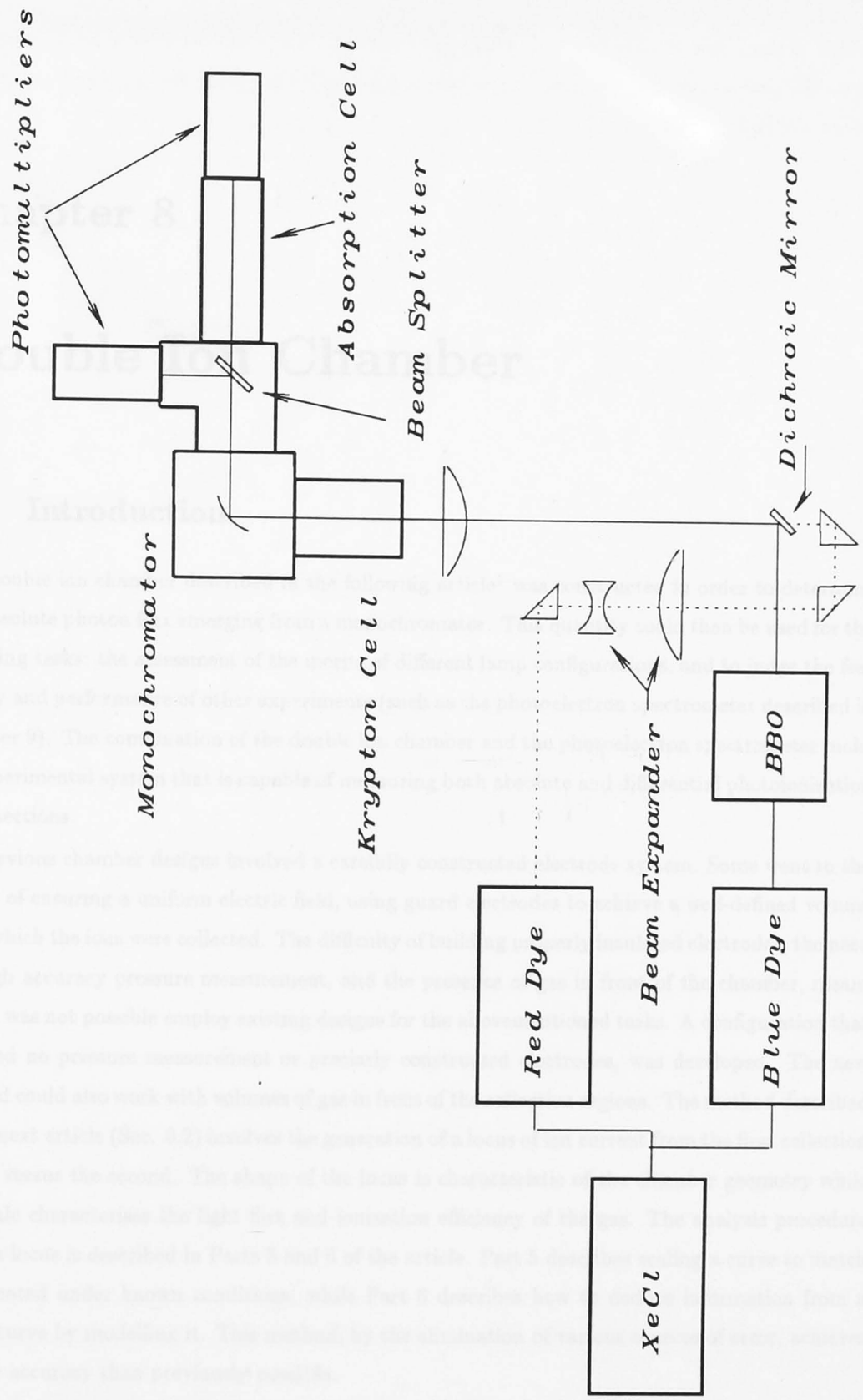

Figure 7.2: Apparatus

Chapter 8

Double Ion Chamber

8.1 Introduction

The double ion chamber described in the following article[1] was constructed in order to determine the absolute photon flux emerging from a monochromator. This quantity could then be used for the following tasks: the assessment of the merits of different lamp configurations, and to judge the feasibility and performance of other experiments (such as the photoelectron spectrometer described in Chapter 9). The combination of the double ion chamber and the photoelectron spectrometer make an experimental system that is capable of measuring both absolute and differential photoionization cross sections.

Previous chamber designs involved a carefully constructed electrode system. Some went to the extent of ensuring a uniform electric field, using guard electrodes to achieve a well-defined volume from which the ions were collected. The difficulty of building properly insulated electrodes, the need for high accuracy pressure measurement, and the presence of gas in front of the chamber, meant that it was not possible employ existing designs for the abovementioned tasks. A configuration that required no pressure measurement or precisely constructed electrodes, was developed. The new method could also work with volumes of gas in front of the collection regions. The method described in the next article (Sec. 8.2) involves the generation of a locus of ion current from the first collection region versus the second. The shape of the locus is characteristic of the chamber geometry while the scale characterises the light flux and ionization efficiency of the gas. The analysis procedure for this locus is described in Parts 5 and 6 of the article. Part 5 describes scaling a curve to match one created under known conditions, while Part 6 describes how to deduce information from a single curve by modelling it. This method, by the elimination of various sources of error, achieves greater accuracy than previously possible.

The closing sections (Sec. 8.3 and 8.4) looks at some of the experimental details and techniques

[1] presented as it appears in Rev. Sci. Instrum.

further to those described in article and suggests theoretical and practical developments necessary to use the chamber in the conditions where there may be more than one ion produced per photon absorbed – multiple ionization.

8.2 Interpretation of the Outputs of a Double Ion Chamber

Interpretation of the outputs from a double ion chamber

Peter Hill

Department of Physics, University of Adelaide, 5001 South Australia, Australia

(Received 18 January 1988; accepted for publication 26 March 1988)

A double ion chamber can be used to measure absolute intensities of UV light, and the absorptivity and photoionization yield of gases. New methods have been developed and tested which make double ion chambers simpler to build and use. These methods allow for collection regions of unequal length and for a body of absorbing gas in front of the chamber. Such methods make it possible to mount the chamber away from the source of ionizing UV light without displacing other experiments. The methods described use the relationship between the outputs of a chamber of nominal dimensions, over a range of gas pressures, to obtain information about the light and the gas in the chamber and the effective dimensions of the chamber. Some errors due to pressure fluctuations and uncertainties in the construction of the chamber are avoided by these methods.

INTRODUCTION

An ion chamber collects the ions created by an UV beam, typically 30–100 nm, photoionizing a gas in the chamber. A double ion chamber, as the name implies, is a chamber with two collection regions.[1]

The two ion currents are typically used to determine the absorptivity of a gas, the photoionization yield, and lamp intensity. A double ion chamber is often used to determine these quantities in preference to other instruments such as photomultipliers, photoelectron spectrometers, and calibrated UV photodiodes because it is inexpensive, because the currents and, therefore the results, can be calibrated, and because ion chambers are capable of measuring very low intensities. Ion chambers also have the advantage that stray light of energy beneath the ionization threshold of the gas in the chamber will not be detected.

It should be pointed out that there is advantage in using the double ion chamber in conjunction with other instruments. First, the double ion chamber can be used to calibrate the other instruments. Second, as the double ion chamber measures ions while other instruments measure photons and electrons it should be possible to isolate the following type of reaction:

$$\gamma + O_2 \rightarrow O^- + O^+.$$

The author's research group is employing a double ion chamber to obtain calibrated intensities of an UV lamp in order to assess the effect of changes to the system. The photoionization yield of various gases are being determined. As the yield is unity for autoionization resonances[2–4] it is hoped that the chamber will locate likely regions of interest for studying autoionization by other instruments.

I. OPERATION OF A DOUBLE ION CHAMBER

For the purpose of discussion the double ion chamber may be divided up into three regions (Fig. 1): "A" the preabsorbing region which may be present because of some other apparatus onto which the double ion chamber is attached or simply gas diffusing from the chamber through the slits that admit the UV light; "B" the first collector region, the source of i_1; and "C" the second collector region, the source of i_2.

The letters A,B,C will also be used to denote the lengths of these regions. The collectors in regions B and C are held at negative potential with respect to their surroundings. When an UV beam ionizes a gas in these regions the positive ions drift to the appropriate plates creating the output currents of the double ion chamber.

The currents i_1 and i_2 cannot be easily analyzed unless two processes are accounted for, and it can be said the currents represent photoionization in regions B and C. These processes are: cancellation of ions by the collection of the electrons on the collector and electron–ion recombination.

If electrons have sufficient energy to reach the ion collectors they will cancel out some of the current. One way to reduce the number of electrons hitting the collector is to reduce the solid angle subtended by the collector. This may be done by using rods or points as collectors, or by increasing the distance between the interaction region and the collectors. The ions, when created, only have thermal energies

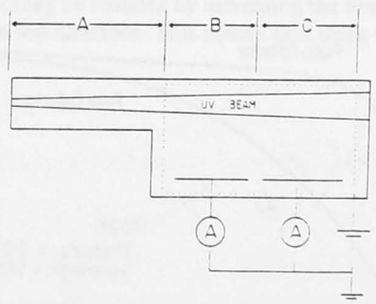

FIG. 1. A double ion chamber. A beam of UV light ionizes gas held inside the chamber. A wire mesh cage is held at a positive potential so that positive ions created in the cage drift to the plates which are at ground potential. The dimensions "A," "B," and "C" refer to regions in which the ions will not be collected, be collected by the first plate, be collected by the second plate, respectively. Electrometers then measure the currents coming from the plates.

 0034-6748/88/071237-04$01.30

(0.025 eV) and will thus drift in the electric field to the collectors. Figure 2 illustrates a collector current versus collector voltage for a point collector which is free of any artifacts due to recombination at the collector. If the photoelectrons were hitting the collection plate there would be quantized steps in the current versus voltage curve as the electrons of quantized energy are repelled. Having the collector at sufficiently low potential to repel the electrons from itself eliminates this effect.

The electron–ion recombination becomes apparent when the electron-collector cancellation has been reduced. Electron–ion recombination increases with pressure and decreases with the strength of the collecting electric field.

Once the currents faithfully reflect the photoionization occurring in their respective collection regions Lambert's law may then be used to predict the currents.

$$I_x = I_0 e^{-P273kx/760T}, \tag{1}$$

where I_0 is the intensity or photon flux from the lamp, k is the absorptivity of 1 cm of gas at STP, x is the distance (cm), and P is the pressure in Torr. Let K represent $-273k/760T$ and e is the unit of electric charge.

If γ is the photoionization yield (the fraction of photons absorbed that produce ions), then

$$i_1 = I_0 \gamma e[e^{KPA} - e^{KP(A+B)}] \tag{2}$$

and

$$i_2 = I_0 \gamma e[e^{KP(A+B)} - e^{KP(A+B+C)}]. \tag{3}$$

Even though these are nonlinear equations, because they are parameterized by P, different values of P create a sufficient number of values of i_1 and i_2 to determine the unknowns in the above equations. Hence, as the size of regions A, B, and C can be solved for, along with the physically significant quantities, it is not necessary to know them initially. Thus, the double ion chamber need not be accurately defined electrostatically to obtain high accuracy results. However, as the equations for i_1 and i_2 contain only the terms $I_0\gamma$ and KP it is thus impossible to isolate γ or K without first determining I_0 or P, respectively. I_0 can be determined by using a gas in the chamber for which $\gamma = 1$. After I_0 has been determined γ for other gases may be found. Similarly an absolute P must be measured to determine K.

Greater accuracy in measuring very small currents may be achieved by measuring charge over a fixed period of time.

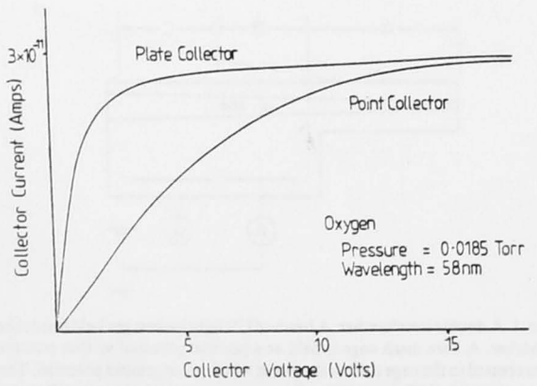

FIG. 2. Graph of collector voltage vs collector current. There is comparatively more electron–ion recombination for a point collector than for a plate collector at the same voltage.

II. ANALYSIS OF THE OUTPUTS OF THE DOUBLE ION CHAMBER

Three methods of analysis of the output currents will be explained. Each method is suited to determining different information associated with the double ion chamber. The first method expands the existing method to deal with regions of preabsorbing gas and can be used to determine k, the absorptivity, particularly well. The second method determines γ, the photoionization yield, without need to measure pressure, calibrate the outputs of the chamber, or have any knowledge of the dimensions of the chamber. The third method described, although involved, uses all data available to produce the highest accuracy results, including the dimensions of the apparatus.

The standard method of analysis will first be reviewed.

III. EXISTING METHOD; EQUAL CHAMBER SIZES

Given that $B = C$ and that we can measure absolute pressure, manipulation of Eqs. (2) and (3) yields

$$I_0\gamma e = i_1^2 e^{KPA}/(i_1 - i_2). \tag{4}$$

In earlier descriptions of the analysis[1,5] it was further stipulated that $A = 0$. The currents were then simply read from the ion chamber to yield $I_0\gamma$.

$$I_0\gamma e = \frac{i_1^2}{i_1 - i_2}.$$

Similarly K could be determined by

$$K = \frac{-1}{PB} \ln \frac{i_1}{i_2}.$$

IV. FIRST METHOD; CHAMBER WITH A PREABSORBING REGION

However, it is possible to take account of the preabsorbing region A by the following manipulation of Eq. (4):

$$\ln(I_0\gamma e) = KPA + \ln[i_1^2/(i_1 - i_2)]. \tag{5}$$

A graph of $\ln[i_1^2/(i_1 - i_2)]$ as a function of pressure will be a straight line (see Fig. 3). The zero pressure intercept will give $\ln(I_0\gamma e)$ providing the intensity of the UV beam. The slope will be KA providing the absorptivity of the gas in the chamber. An accurate knowledge of A may be obtained from the third method. An absolute value of the pressure P will yield an absolute value of absorptivity k. The ability to analyze the data with a preabsorbing region A means that the chamber may be mounted on an existing experiment with the minimum of interference. This allows for more accurate calibration of instruments like photoelectron spectrometers by a double ion chamber because the instrument and the double ion chamber can take simultaneous readings.

As there is always some preabsorbing gas, this method

eliminates the systematic error in the existing method caused by assuming $A = 0$.

A pressure reading along with the ensuring error is required in this method, but not in the second method detailed below.

V. SECOND METHOD; LOCUS OF CHAMBER CURRENTS

This method simply uses the data points (i_1, i_2) parameterized by pressure to generate a locus of points generated by Eqs. (2) and (3). (An example of which is illustrated in Fig. 4.) By varying the pressure different points along the locus are generated. The current from each collector initially increases, with increasing pressure as there is more gas to ionize, but then the currents begin to decrease as the increased amount of gas before the collectors absorbs the UV light. This method of recording the currents does not have an error due to pressure fluctuations as the readings of the currents do not require the pressure to be constant. The pressure need not be recorded.

The shape of the locus depends on the ratio of the dimensions A/B and A/C while the scale is proportional to $I_0\gamma$. In other words, a particular double ion chamber setup will produce a characteristic shape of i_1 vs i_2 locus. Increasing $I_0\gamma$ will dilate the locus as it is simply a multiplicative factor of the generating Eqs. (2) and (3). Therefore, to determine the γ_{sample} at a particular wavelength and lamp intensity I_0, all one has to do is reduce the size of the locus of a gas for which $\gamma = 1$ such that it overlaps that of the sample gas. The reduction factor then equals γ_{sample}. A plot of argon ($\gamma = 1$) and an oxygen locus for a wavelength of 68.5 nm is shown in Fig. 5. From these data γ_{oxygen} is 0.910 with a random error of ± 0.005. Inspection of the data near the turnover point indicates that the lamp intensity variation is well under 1%. As the result does not include errors from measuring pressure or the dimensions of the chamber this method has potential for great accuracy.

If the absolute pressure were to be measured the relative absorptivity of a gas could then be determined. The pressure at which the currents passed through a particular part of the locus would be inversely proportional to the absorptivity. This is so because the loci are parameterized by equations containing KP and a particular value of KP will refer to a particular part of the locus. A way of realizing this is by making C about $1.7B$ and recording the relative pressures for which $i_1 = i_2$ for various wavelengths. The ratio of collector lengths for greatest accuracy should be such that the locus intercepts the $i_1 = i_2$ line at right angles.

It is possible to further increase the accuracy of this method by offsetting the currents i_1 and i_2 with calibrated picoampere sources and running the electrometers at higher gain. This allows the experimenter to enlarge a particular part of the curve. The hook-over section is the most sensitive to changes in $I_0\gamma$ and is, thus, the best section of the curve to enlarge.

If the shape of the curve varies from gas to gas for the same operating conditions, this is a sign of some sort of error. The shape of the curve relates to the dimensions of the chamber which clearly should not change during the operation of the chamber. Typically the curves will fit in the low-pressure regions but not in the high-pressure regions because electron–ion recombination sets in at the higher pressures. This effect may be reduced by increasing the dimensions of the double ion chamber. This means that there will be the

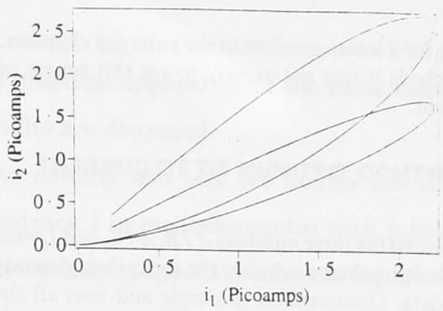

FIG. 4. i_1 vs i_2 loci. The lower curve is generated by a double ion chamber of dimensions $A = 300$, $B = 100$, and $C = 100$ mm. The curve is generated by $i_1 = 21.1\times10^{-12}\,(e^{-3P} - e^{-4P})$, $i_2 = 21.1\times10^{-12}\,(e^{-4P} - e^{-5P})$. This curve overlaps the experimental data exactly, hiding the data. The upper curve is generated by $i_1 = 21.1\times10^{-12}\,(e^{-3P} - e^{-4P})$, $i_2 = 21.1\times10^{-12}\,(e^{-4P} - e^{-5.7})$.

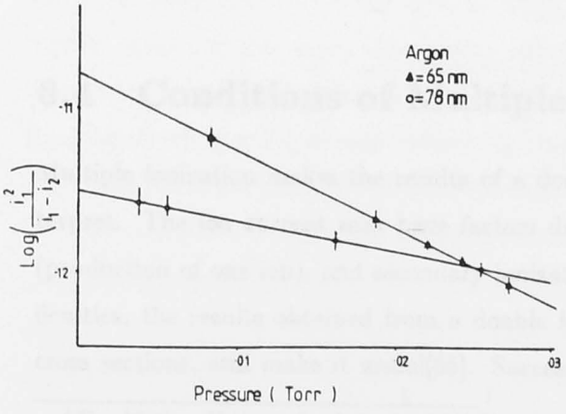

FIG. 3. Graph of pressure vs $\ln[i_1^2/(i_1 - i_2)]$. When $P = 0$ there is no gas to absorb the light before it enters the ion chamber. Thus, the intensity may be calculated by extrapolation to $P = 0$.

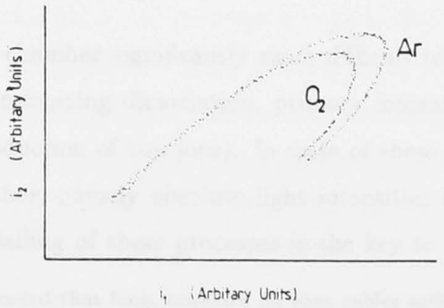

FIG. 5. i_1 vs i_2 loci for O_2 and Ar at 68.5 nm with a bandwidth of 1 nm. The intensity used was 7×10^7 photons/s.

same currents for a lower pressure in the enlarged chamber. In earlier methods it was not as easy to see this source of systematic error.

VI. THIRD METHOD; OPTIMUM FIT TO CURRENT LOCUS

In this method the three numbers A/B, A/C, and $I_0\gamma$ are found by optimizing them such that the locus they generate best fits the data. Optimization is simple and uses all the available data. If the data are given as absolute current this method will yield absolute intensities. Two techniques of optimization are suggested: computer searches and by eye.

The data may not only be used to obtain lamp intensity but also the dimensions of the apparatus, all without the need for pressure measurements. Here, now it is not necessary to know the dimensions of the apparatus to obtain meaningful data.

The following are key features of the locus equations derived from Eqs. (2) and (3):

$$(di_1/di_2)_{[p=0]} = B/C. \tag{6}$$

$$i_{1\max} = I_0\gamma e[A/(A+B)]^{A/B}[B/(A+B)]. \tag{7}$$

$$i_{2\max} = I_0\gamma e(A+B/A+B+C)^{A+B/C}(C/A+B+C). \tag{8}$$

These equations may be used to limit the search area of optimization routine. Grid and gradient searches are the most commonly used methods of multidimensional optimization. The quality of fit of a particular set of parameters to the data is generated by optimizing the pressure parameter to find the minimum error of each data point to the model. The sum of squares of these errors of the model to the data is then weighted by i_1. The weighting factor was selected because although the errors in the model due to an error in th parameters are complicated functions they are approximate ly proportional to the currents. Comparison of computec pressure to measured pressure will yield the absorptivity o the gas at each pressure. The author decided to employ th method of simulated annealing[6,7] which is computationall simple and found a global minimum in parameter space.

Locus variables were selected for a locus containing 20(data points having a standard deviation of 5% $i_{1\max}$ by usin computer graphics to superimpose the guessed locus ove the data. This visual method returned the value of locus vari ables to an accuracy of greater than 0.5%. The optimizatior programs improved the accuracy to better than 0.1%.

With these methods the double ion chamber is an inexpensive, highly accurate, versatile instrument to measure lamp intensities and properties of gases in the VUV.

ACKNOWLEDGMENTS

The programs used for this article relied on software written by Keith Briggs. Advice on using simulated annealing was also provided by Keith Briggs. Tim McKay provided the data for Fig. 5.

[1] J. A. R. Samson, *Techniques of Vacuum Ultraviolet Spectroscopy* (Wiley, New York, 1967).
[2] J. A. R. Samson, J. Opt. Soc. Am. **54**, 6 (1964).
[3] A. P. Lukirskii, Opt. Spectrosc. **9**, 262 (1960) (English translation).
[4] D. L. Eder, Appl. Opt. **3**, 1073 (1964).
[5] J. A. R. Samson, J. Phys. B **10**, 1749 (1977).
[6] K. M. Briggs, (to be published).
[7] S. Kirkpatrick, Science **220**, 671 (1983).

8.3 Description of Experiment

A description of the apparatus is given to illustrate the practical application of the locus method. Other techniques critical to achieving high accuracy results are discussed.

Two separate monochromator systems were used to develop and test the double ion chamber. The first system involved a McPherson normal incidence 1 m monochromator with a helium Hopfield light source (600 -1000 Å). A retarding grid photoelectron spectrometer was mounted on the exit slit of the monochromator. The light monitoring port was 30 cm from the exit slits, at which distance the beam had diverged to an area of 25 mm × 25 mm. This meant that it was impossible to contain the gas exclusively in the double ion chamber and still monitor the beam of light emerging from the monochromator.

The second system involved a hollow cathode lamp which could run various gases to generate their particular line spectrum. The light then passed through a McPherson 0.5 m monochromator with the double ion chamber mounted on the slits. The use of line spectra meant that the resolution was not limited by the monochromator but by the width of the emission line.

The electrodes of the double ion chamber were maintained at ground potential. They were connected with teflon-coated hookup wire to the vacuum feed-throughs. The feed-throughs required frequent and thorough cleaning to prevent accumulated contamination contributing to stray currents.

The high potential cage was constructed out of rolled wire mesh with very fine mesh capping the end of the cylinder. The entire assembly was mounted on one flange and was simply inserted into a vacuum chamber. The cage, by effectively shielding the electrodes, prevented electrical noise pickup from the lamp power supply. Twisted pair cables effectively shielded the computer (Commodore 64) data acquisition system. What noise there was, was found to mirror the frequencies of the vacuum roughing pumps. The pumps were vibrating the cables [2] connecting the ion chamber to the Keithly electrometers inducing piezo-electric pick-up.

8.4 Conditions of Multiple Ionization

Multiple ionization makes the results of a double ion chamber significantly more difficult to interpret. The ion current may have factors due to non-ionizing dissociation, primary ionization (production of one ion), and secondary ionization (production of two ions). In spite of these difficulties, the results obtained from a double ion chamber, namely absolute light intensities and cross sections, still make it useful[65]. Successful modelling of these processes is the key to the

[2] Tim McKay, Honours Student, Adelaide University (1987) noted that long, standard 50 ohm cables suffered the least noise. Some 6 m lengths showed no significant noise over and above simply terminating the Keithly at the output. Strangely, even the susceptibility to piezo electric noise seemed reduced. I can offer no explanation for the effect.

interpretation of the output of a double ion chamber, in regimes where multiple ionization from one photon occurs.

There are two ways in which a single photon can generate more than one ion. In the first process, the photon may strip the molecule of two electrons in a single interaction – double ionization. In this case, the threshold energy is the sum of the first and second ionization potentials. The doubly ionized species will collide with a neutral, ionize it, and thereby create two ions. The collection of the additional current is not affected by pressure.

The second way is impact ionization by the ejected photoelectron. The threshold for this process is twice the first ionization potential. The current measured will depend on where the electron impact occurs. If the ionization happens outside the collection region the current will not be registered. As the distance an electron travels from its production point depends on pressure, the fraction of extra current collected from this process is pressure dependent.

The analysis of the extra source of current is based on thresholds and pressure dependence. The intensity, extrapolated to zero pressure, reflects purely single and double ionization. The electrons will escape and not add to the ion current through impact ionization. At light energies beneath the double ionization threshold of helium (79.0 eV) the rate of multiple ionization for atomic gases may be determined through comparison with helium. For molecular gas the possibility of absorption without ionization introduces an ambiguity in the results. An example might be a gas for which there is 10% absorption without ionization and 10% double ionization, registering an unchanged zero pressure intensity.

To determine the rate of double ionization in a test gas, the intensity of ionizing radiation must be known (i.e. by using a singley ionized noble gas). For wavelengths above the helium double ionization threshold, a gas with a known rate of double ionization would have to be used to enable the intensity to be deduced. The double ionization efficiency plateaus soon after threshold for the noble gases. Auto-double-ionization would lead to structure in this plateau. This effect would only occur for energies above the first excitation levels of both the second and third electrons. Helium does not have this third electron, and for the other noble gases this is a large energy. Thus structure is not expected until large energies. Helium has a double ionization efficiency[65] of $3\frac{1}{2}\%$, and the rates for the other noble gases at a particular wavelength may be determined through comparison with it. Importantly, to determine the fraction of double ionization occurring the effect of photoelectron impact ionization has to be accounted for.

The measurement of photoelectron impact ionization is pressure dependent. At low pressures all the electrons will escape the collection region before producing additional ions, while at high pressures all the additional ions will be collected. At low pressures, absorption is small, the currents are small, and the accuracy of the chamber's results is reduced. To determine the zero pressure intercept, and thence the rate of double photoionization, it has been found to be desirable to fit the higher pressure data with a model and use it to extrapolate back to the zero pressure value of

the intensity.

Samson and Haddard in Eq. 3 of Ref.[65] propose;

$$i_P = i_0(1 + \gamma(\lambda)(1 - e^{-PL(l)})) \quad , \tag{8.1}$$

to represent the pressure dependant current collected, i_P, that is in excess of the current that would be collected if there were no photoelectron impact ionization, i_0. γ is the efficiency of production of ions by the photoelectron, P is the pressure and L is some fitting parameter characteristic of the typical length(l) an electron has to travel. This model provides a reasonable fit to the data but there appears to be a step structure which is characteristic of the geometry of the particular ion chamber used.

A more sophisticated model includes the fact that the electrons undergo multiple scattering and random walk out of the collection region. If it is assumed that there is no energy loss, or $\sigma_{ionization}$ is independent of energy, then,

$$\mu_e(r) = \mu_e(0)e^{-rn\sigma_{ionization}} \quad , \tag{8.2}$$

represents the number of electrons (μ_e) that survive to travel a total distance r.

The actual distance from the origin travelled will be described by a Gaussian distribution with characteristic width z;

$$z \; \alpha \; \sqrt[3]{N}\frac{1}{n\sigma_{collision}} \quad , \tag{8.3}$$

where N is the number of collisions, n is the density of scattering particles, and $\frac{1}{n\sigma_{collision}}$ is the average distance travelled between collisions. Then

$$\begin{aligned} & N = rn\sigma_{collision} \\ \Rightarrow \quad & r \; \alpha \; z^3 n^2 \sigma^2_{collision} \\ \Rightarrow \quad & \mu_e(z) = \mu_e(0)(1 - e^{-z^3 n^3 \sigma^2_{collision}\sigma_{ionization}}) \quad . \end{aligned} \tag{8.4}$$

This curve is not a simple exponential and fitting one to it at high pressure will lead to an overestimate of the intercept at zero pressure.

The step-like structure seen in Ref. [65] may be caused by different surfaces of the ion chamber (rectangular in cross section) becoming significant at particular pressures. A cylindrical chamber with a relatively confined ionization region would eliminate most of the structure, making the curve more amenable to modelling. Ion chambers in which the ends of the collection region are terminated by walls are apt to require very high pressure before all the electrons ionize within the confines of the region. Such termination is to be found in many designs[65]. Having the exit slit of the light source abutting the chamber allows differential pumping and the minimisation of the

pre-absorbing region. (The modelling of the effect of such a region is one of the topics covered in the previous article, Sec. 8.2). The volume of gas infinitesimally close to the slit will always register a reduced production of photoelectron impact ions, as some of those electrons ejected back towards the slit will be absorbed. The overall fraction of signal lost in this way will depend not only on the typical length travelled by the electrons but also the proximity of the ionization to the slit. If the optical absorption is high the electrons will be produced more closely to the slit. The effect of this particular surface would then be particularly difficult to model. The provision of a guard collection region would ensure a equilibrium flux of photoelectrons across the end boundary. The guard region would not have to be rigorously defined because it could be retrospectively modelled using the methods outlined in the preceding article.

In summary, a chamber of cylindrical geometry, with guard collection regions, would present the least difficulties when modelling conditions of multiple ionization. Section 8.2 established a method of results analysis that allowed simplifications in double ion chamber construction. Complexities had to be introduced in order to effectively account for multiple ionization. Such advances are significant, given the abilty of double ion chambers provide to fundamental absolute light intensities and cross sections in the vacuum ultraviolet.

Chapter 9

β Sensitive Photoelectron Spectrometer: Conceptual Design

9.1 Introduction

The analyser: 'Photo-Electron Angular Distribution Apparatus' (PEADA), consists of fixed position concentric spherical grids that act as a high-pass/low-pass energy filters. The photoelectrons are produced at the center by the crossing of light and molecular beams. Those electrons of the desired energy are retarded to near zero velocity at the retarding grid and are then collected over a large area using a weak electric field to guide them into a dispersive analyser to a detector, with the more energetic electrons escaping from the apparatus. The ratio of counts going into different angular segments of the analyser is used to calculate β, in a single measurement.

The theory as to why it is possible to use the flux of electrons emitted into large angular sectors rests on the shape of photoelectron distributions and is introduced in Sec. 9.2. The fundamental insight are based on the linear dependence of these distributions on β : this means that the sum over a range of angles is also linear in β. The ratio of the counts from different sectors can then be used to determine the asymmetry. PEADA achieves the collection and energy selection of photoelectrons by the use of a series of established techniques: retarding grid, penetrating field and dispersive energy analysers. These techniques are reviewed in Sec. 9.3, along with an overview of the current approaches to determing β. The detailed description of the construction of PEADA is found in Sec. 9.5. Sec. 9.6 looks at the various sources of error and discusses the optimum shape and positioning of the analysers. This section also provides a mathematical justification for the collection of electrons over large angular ranges. Sec. 9.7 deals with calibration methods. In contrast with existing designs, there is no requirement to know the polarization of the light. Finally, the advantages of superior accuracy, lack of moving parts, large acceptance angles and the insensitivity to polarization, are stated in conclusion.

9.2 Photoelectron Distributions

When gas is ionized by a single photon (angular momentum $l = 1$), both $l \pm 1$ states of the molecule are excited. The two outgoing waves interfere – constructively or destructively – depending upon their intensity and their relative phase. Photoelectron distributions arising from this process have simple forms which have many symmetries (Fig. 9.1). The entire range of three dimensional interference patterns is parametrized by a single scalar, the asymmetry parameter, β. It has a range of -1 to 2.

Within the approximations of the single electron central field model and the dipole approximation, Cooper and Manson[66] described β in terms of single electron matrix elements with appropriate weights and phase shift:

$$\beta_{mi} = \frac{l(l-1) \mid D_{mi}^{l-1} \mid^2 + (l+1)(l+2) \mid D_{mi}^{l+1} \mid^2 - 6l(l+1) D_{mi}^{l+1^*} D_{mi}^{l-1} cos\delta}{(2l+1)[\, l \mid D_{mi}^{l-1} \mid^2 + (l+1) \mid D_{mi}^{l+1} \mid^2 \,]}, \tag{9.1}$$

where $D_{mi}^{l+1} =< m(l+1) \mid e\mathbf{r} \mid i(l) >$ and is the transition dipole matrix element, and δ is the asymptotic difference between the two $l \pm 1$ wave functions. Total cross sections provide the square of the matrix element; whereas β provides additional information, namely, the phase difference between matrix elements. Measurement of the β parameter ultimately assists in the unambiguous identification of orbitals and in the testing of theoretical models.

There are further, practical ramifications of β. Spectrometers that measure simply the total photoelectron cross section independently of β[67] are limited to detection at the 'magic' angle[68] (45^o from the major axis of polarization and 56.44^o from the axis of propagation of the light). A gas with a known β may be used to calibrate spectrometers that image surfaces, but unfortunately it has rarely been possible to experimentally determine β to better than a few percent[69]. However there are gases, like helium ($\beta = 2$), which have a theoretically determined asymmetry. The need to measure β for gases has led to the design of many and varied β sensitive spectrometers. Embodied in all angular distribition spectrometer designs is an understanding of the possible shapes and orientations of the distributions themselves.

The geometrical description of a photoelectron distribution, Ψ, from a gas excited by a single photon[68] is:

$$\frac{\partial \sigma_j}{\partial \Omega} = \frac{\sigma_j}{4\pi}(1 - \frac{1}{2}\beta + \frac{3\beta}{2(g+1)}(g\ cos^2\theta_y + cos^2\theta_x)). \tag{9.2}$$

where σ_j is the partial cross section (for a specific energy of photon and ejected electron). θ_y and θ_x are angles as shown in Fig. 9.2. $g = \frac{I_x}{I_y}$. The more common description of polarization,V, is related to g by

$$V = 1 - g = \frac{I_{pol}}{I_{pol} + I_{unpol}} \ . \tag{9.3}$$

Eq. 9.2 is linear in β. The linear combination of any two distributions results in a third. (eg: 0.5 $\Psi_{(\beta=0)}$ + 0.5 $\Psi_{(\beta=2)}$ = $\Psi_{(\beta=1)}$). The sum over several σ_j or over a range of angles is also linear in β.

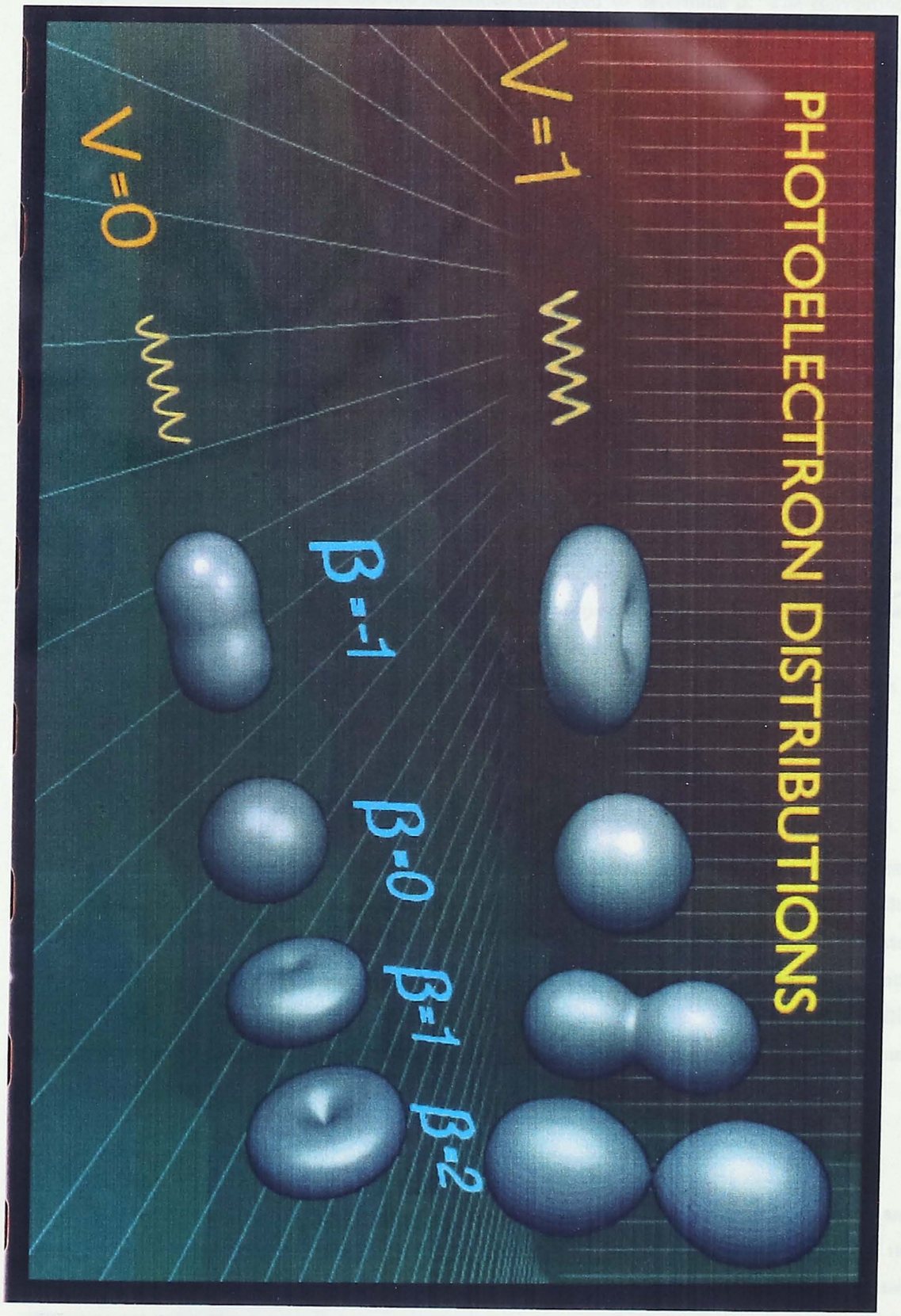

Figure 9.1: Figure 9.1: Photoelectron distributions created by polarized (V = 1) and unpolarized (V = 0) light. The linear dependence on β may seen from the smooth transition of shapes.

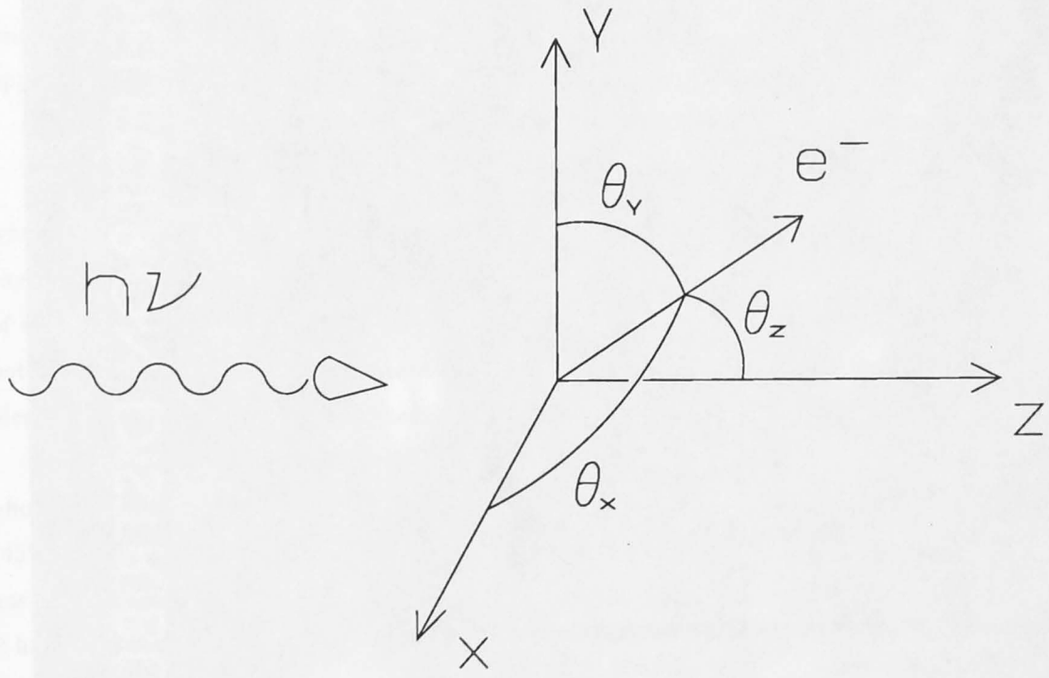

Figure 9.2: Coordinate system. The z axis is referred to as "the axis of propagation of the light". The plane formed by the x and y axes is referred to as "the plane of polarization."

Inspection of Eq. 9.2 reveals the two strategies employed to determine β. The conventional approach is to use small acceptance angles (a standard but necessary feature of dispersive electron energy spectrometers) to measure and compare fluxes at different positions most sensitive to the value of β. Typically for g = 0 (fully polarized light) , θ_z=90° (detector in the plane of polarization), and $\theta_y = 0°$ at 90°;

$$\frac{\partial\sigma_j}{\partial\Omega}_{\theta_y=90°} \propto 1 - \frac{1}{2}\beta \ , \tag{9.4}$$

$$\frac{\partial\sigma_j}{\partial\Omega}_{\theta_y=0°} \propto 1 + \frac{1}{2}\beta \ . \tag{9.5}$$

Although this approach is the most sensitive to β, it is also sensitive to g and the orientation of the polarization axis, which themselves can be functions of wavelength and time. In many designs, to counter these sources of error, the detectors move with respect to the axis of polarization. This enables the polarization of the light to be determined and accounted for. Unfortunately, these optimum sensitivity conditions (Eq 9.4, 9.5) are rarely met as the light is not fully polarized, $g \neq 0$. In the configuration with detectors in the plane of polarization of the light, the unpolarized component, found in elliptically polarized light, has no β dependence and behaves as a background signal adding only statistical noise. In fact, if the light is less than 50% polarized, the second strategy, that of sampling over angles *from* the axis of propagation of the light, yields the best results. Such is the case for a Hopfield lamp source and diffraction grating configuration[70].

PEADA employs the second strategy, but also collects over a range of angles about the axis of propagation and the resultant greater signal collected offsets a lower sensitivity to β.

9.3 Current Analysers

Refs. [69] & [71] contain papers and reviews of current analysers upon which this section comments further. In order to determine β, photoelectron spectrometers must monitor both the flux and energy of electrons ejected at different angles. Many are capable of measuring complicated electron distributions arising from multiphoton processes and from solids, and are consequently more sophisticated than is required to measure the simple distributions arising from gases. Discussed below are four categories of analyser: Time of flight (TOF), Dispersive, Retarding grid, and Penetrating field.

9.3.1 Time of Flight

TOF analysers require a pulsed light source to generate a pulse of photoelectrons. Many lasers and synchrotron radiation sources are already pulsed, and have no loss of signal due to dark time if the flight time is within the duty cycle of such a source. The whole energy spectrum can be collected. This is not necessarily an advantage, as usually only a narrow range of energies is of interest. Two different views are required to determine β. The use of two fixed analysers, typically oriented

90^o apart in the plane of polarization, suffers from detector calibration problems. A magnetic bottle[72] TOF has an acceptance angle of up to 2π sr. The theory developed in the current study can be adapted so that magnetic bottle designs can measure β (see Sec. 9.8).

9.3.2 Dispersive Analysers

The most common analysers used are spherical and cylindrical, and are now available commercially. Those of cylindrical geometry are appropriate for linear photoelectron sources, as may be encountered when a tightly collimated light beam interacts with a more diffuse molecular beam. The ratio of source size to the dimensions of the apparatus is a limit on the theoretical resolution. Large analysers, besides suffering from magnetic shielding and background gas problems, are not able to move easily inside a vacuum system. A single movable detector obviates the detector calibration problem and allows the polarization of the incident light to be determined. However, care must be taken that the apparent source size is the same from various angles.

There are three noteworthy techniques that may enhance the performance of dispersive analysers. They are polarizers, area detectors and toroidal analysers.

Polarizers[73], by rotating the axis of polarization, also rotate the photoelectron distribution. This means different views of the distribution may be had with a fixed analyser. This in turn means that the spectrometer may be large and have high resolution, as it is no longer required to move inside the vacuum system. In practice, polarizers require an unpolarized light source, and even when freshly coated, severely attenuate the source.

A band of energies can be detected with area detectors. The use of charge coupled devices (CCDs) is now common[74]. The dispersive analyser must scan each energy across the various channels to overcome the calibration problems. None the less β may be determined for a band of energies in the time it would normally take to determine just one.

Toroidal analysers sample an annular sector of photoelectrons[75]. Besides their large acceptance angle, and enhanced counts, they image different azimuthal angles. This means a position sensitive detector can be used to determine β, but because of the simple form of β, much of the position information is unnecessary.

The problem of detecting threshhold electrons by dispersive analysers, in which stray field and scattering leads to a poor signal to noise ratio, has been addressed[76] by employing time of flight gating of the signal. Such techniques could be adapted to improve the signal in the PEADA analyser as well.

9.3.3 Retarding Grid Analysers

Although retarding grid analysers can accept almost 4π sr [77], they can monitor only one energy at a time. For a line spectrum, or for detailed studies of small regions of the energy spectra, this is not a major disadvantage. Most spectrometers of this type take integral spectra by accepting

all electrons above a certain energy[77, 78]. The signal from the lowest energy electrons is lost in the statistical noise of higher energy electrons included in the integral signal[67]. Several different, differential retarding grid spectrometers have been built. One such spectrometer relies on the chromatic aberration of the lens that focuses the electrons on to the channeltron detector[79]. One of the earliest of the retarding grid analysers built by Samson[78] was adapted to measure β and is similar in appearance to PEADA. It employs spherical retarding grids that cover 4π sr. Two electron detectors are placed on a plane 45° to the major axis of polarization. One is placed at the 'magic' angle and thus monitors the total electron flux independent of the asymmetry parameter. The other is placed in the plane of polarization and thus a comparison of the two signals from the two detectors can be used to determine β. PEADA is designed not so much to collect electrons emerging at specific angles but to collect over solid angles. The values of β that are now available[69] for the calibration of analysers are sufficient to obviate the need to measure the flux at the 'magic' angle, allowing for the more sensitive set up, here proposed.

The perceived difficulty with retarding grid analysers is the complex nature of the electric field, at distances of mesh dimensions and less, away from the grid. These fields deflect near zero velocity 'threshold' electrons through large angles. The field penetrating between the mesh acts as an electrostatic lens that focuses low energy electrons through the mesh. This leads to transmission efficiencies that exceed that of the optical transmission efficiency and approach 100% for low energy electrons[67], and the effect is turned to positive advantage in PEADA.

9.3.4 Penetrating Field

In this last category of analyser, the electrons that have very low kinetic energy are trapped in an electrostatic 'funnel' formed by an earthed enclosure with a small opening through which field lines flow. The electrons drift through this high potential opening. PEADA uses this technique to collect the electrons retarded by the grids. Theoretically, 100% of the zero energy electrons are collected and the resolution is determined by the relative potential of the retaining walls of the trap and the size of the exit orifice[80]. The shape of the boundaries of the trap are not critical to its performance. Originally this technique employed grids of circular section [80], but later designs used ones of square section[81]. In practice the photoelectrons are further energy filtered by a dispersive energy analyser[81].

9.4 Design of New Analyser

A spatially well-defined source of photoelectrons, called the 'interaction region', is created by the crossing of molecular and photon beams(Fig.9.3).

A system of concentric grids – earth, retarding, outer, and shield grids, covers approximately 2π sr around the interaction region. The net effect of the grids is to filter a band of electron

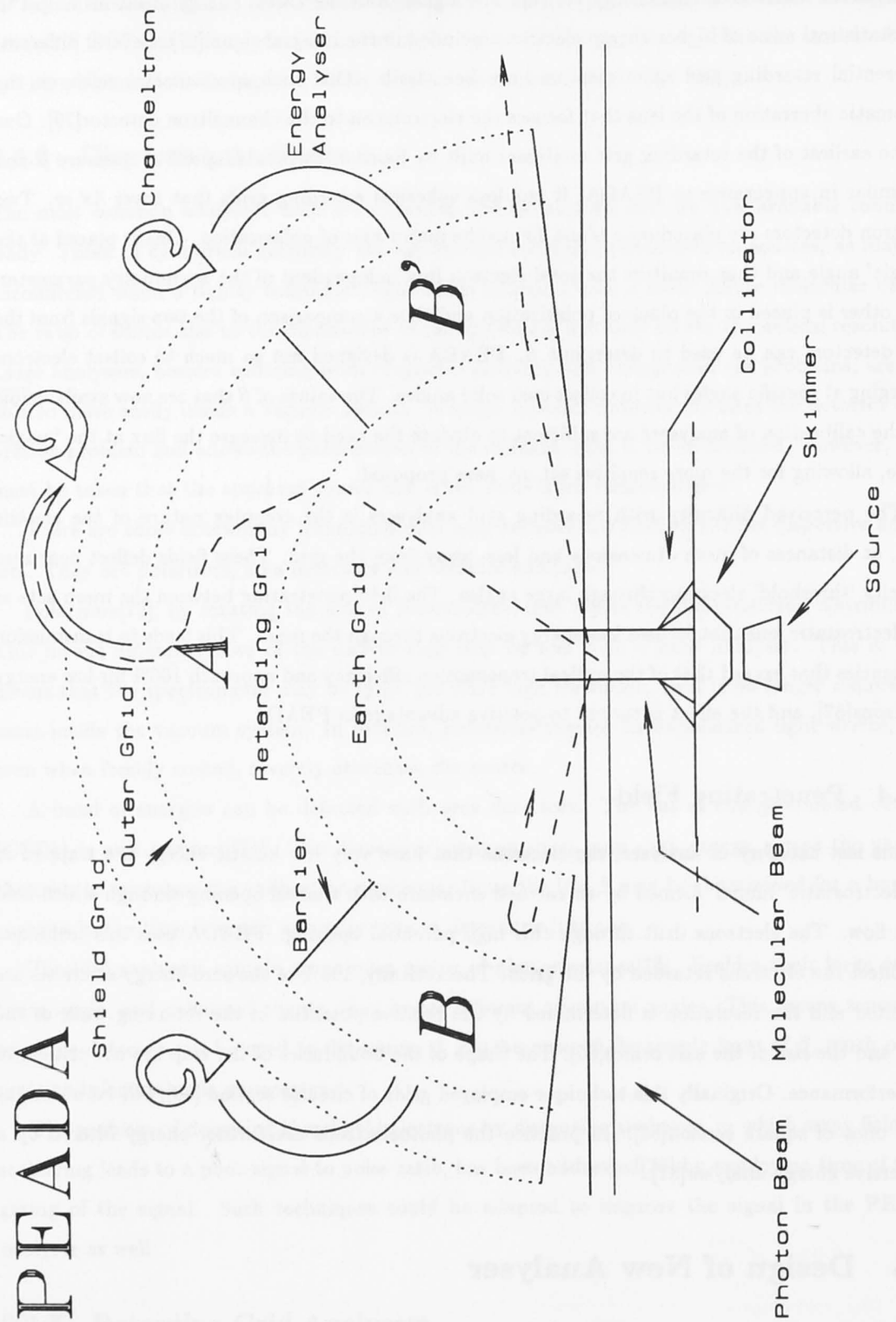

Figure 9.3: Schematic of proposed apparatus. Dashed lines represent the trajectories of repelled, accepted, and escaping electrons

energies. The earth grid (0 Volts) shields the interaction region from which the photoelectrons emanate. After passing through the earth grid, the electrons of too low energy (E < R eV) are repelled by the retarding grid (R Volts). High energy electrons continue, passing through the outer grid, which is held at the same potential as the retarding grid. These electrons pass through the shield grid (0 Volts) and escape from the apparatus. Only electrons of energy near to that of the retarding grid are collected. A potential well is created between the retarding and outer grids by a small gap in the latter grid, creating a region of higher potential. The field lines pass through this gap, terminating on the outer surface of the retarding grid and inner surface of the outer grid. The trapped electrons will eventually travel through the gap, be energy filtered, and accelerated to an energy appropriate for detection[82]. The energy filter could be a commercially available cylindrical dispersive analyser. The final filter not only rejects stray or scattered electrons, but also those originating from background gas outside the interaction region which enter the collection region at an angle, with high energy. The shield grid prevents the fields from the outer grid reaching the interaction region and distorting the distributions.

The analyser is divided into three angular sectors (named B,A,B'). The sectors are partitioned by metal barriers in the collection region between the retarding and outer grids. These barriers are held at the same potential as the retarding and outer grids and thereby form part of the trap for electrons of energies near to that of the retarding grid. The sectors are symmetric about the plane of polarization. There are two symmetric sectors, B, B', each extending from an angle of 60^o down to the axis of propagation of the light. The electrons collected in these two regions are summed and when compared with the flux through the residual central region, A, indicate the weighting of the photoelectron distribution toward, or away from, the axis of propagation of the light. The ratio of sector counts uniquely defines β. The selection of analyser attributes can be designed to optimally determine β by minimising statistical, and polarization errors.

9.5 Construction Technique

It is suggested that the analyser be fixed in position, essentially locked to the floor, with the vacuum system mounted on wheels and connected to the experiment. This allows precise alignment of the analyser in air, and a corresponding relaxation in the expense and precision required of the vacuum system. The crossed light and molecular beams may be achieved using a toroidal mirror to image the slit of the monochromator. An appropriately ground optothalmic lens could constitute an inexpensive mirror. A slit molecular beam provides the greatest density of molecules in the interaction region[83].

If the angular coverage about the axis of propagation is chosen to be $\sim 150^o$, the terminator of the spheric domes can be constructed out of stamped metal annuli. Billiard balls are cheap but high quality spherical mandrels upon which to form the grids.

The formula for a square grid mesh transmission as a function of the standard polar angles θ and ϕ, and flat grid optical transmission T, is;

$$T_{\theta,\phi} = (1 - (\sqrt{T} - 1)cosec^2(arcos(sin\theta cos\theta sin^2\phi))) \quad , \tag{9.6}$$

where θ and ϕ have their standard meaning for polar coordinates of a sphere centered on the interaction region and the z axis lying in the plane of polarization at 45^o to the axes of polarization.

The resolution of a retarding grid analyser[67] with an earth grid located at R_1 and a retarding grid located at R_2 is

$$\frac{\Delta E}{E} = (\sqrt{\frac{e}{8mE}}\mathbf{B}.\hat{\mathbf{v}}R_2 + \frac{R_1}{R_2}sin\theta) \quad , \tag{9.7}$$

where R_1 and R_2 are the radii of the earth and retarding grids, $\hat{\mathbf{v}}$ is the initial velocity of the electron and θ is the angle with respect to the normal at which the electron passes through the the earth grid. This last quantity arises from the extended nature of the interaction region. **B** is the magnetic field. R_1 cancels $sin\theta$ leaving only the dimensions of the source and the radial extent of the retarding grid to determine the energy resolution of this spectrometer.

9.6 Sources of Error and their Impact on the Analyser Design

As a source of error, polarization is dealt with first in order to establish the possibility of summing the photoelectron flux in a conic sector over a range of angles about the axis of propagation of the light to obtain a signal indepent of the polarization (Subsec. 9.6.1). The next subsection examines summing these differential conic sectors over a range of angles from the axis of propagation of the light (Subsec. 9.6.2). Together, these two subsections provide the mathematical basis for collection over large regions. Subsec 9.6.2 also investigates the optimum boundaries of the collection regions. The final subsection (Subsec. 9.6.3) deals with the problem of analyser misalignment (characterized by an angle α) with respect to the polarization axis (z axis in Fig 9.2 and its implications for the best value of angular coverage in the plane of polarization, ϕ, to select .

9.6.1 Polarization

Samson and Starace[84] show that the distribution of photoelectrons from any polarization of light (circular, elliptical, unpolarized etc.) is the same as a linear combination of distributions from light of equivalent intensity completely polarized in both axes. A detector that puts equal weighting on both minor and major axes of polarization, (i.e. is symmetric about $\theta_y = 45^o$), is thus independent of polarization. The minor and major axis of polarization can usually be determined without measurement by considering the orientation of reflectors such as diffraction gratings.

What follows is a derivation of the polarization independence of an analyser oriented symmetrically about $\theta_y = 45^o$.

A sample in the plane at 45^o to the major axis of polarization (i.e. $\theta_y = \theta_x$) will be symmetric in both axes and thus independent of g. By substitution into Eq. 9.2,

$$\frac{\partial\sigma_j}{\partial\Omega} = \frac{\sigma_j}{4\pi}(1 - \frac{1}{2}\beta + \frac{3\beta}{2}(cos^2\theta_y)) \quad . \tag{9.8}$$

Similarly, by sampling differential portions symmetrically above and below the 45^o plane, the resultant signal is independent of the polarization. For an angle $\theta_y, \theta_x, \theta_z$ summed with its image in the 45 ^{o} plane at $(\theta'_y, \theta'_x, \theta_z)$, where $\theta'_y = \theta_x, \theta'_x = \theta_y$;

$$1 = cos^2(\theta_y) + cos^2(\theta_x) + cos^2(\theta_z) \tag{9.9}$$

$$\begin{aligned}
\frac{\partial\sigma}{\partial\Omega_{\theta_y}} + \frac{\partial\sigma}{\partial\Omega_{\theta'_y}} &= \frac{\sigma_j}{4\pi}(1 - \frac{1}{2}\beta + \frac{3\beta}{2(g+1)}(gcos^2(\theta_y) + cos^2(\theta_x)) + \\
&\quad 1 - \frac{1}{2}\beta + \frac{3\beta}{2(g+1)}(gcos^2(\theta'_y) + cos^2(\theta'_x))) \\
&= \frac{\sigma_j}{4\pi}(2 - \beta + \frac{3\beta}{2}(cos^2(\theta_y) + cos^2(\theta_x)) \\
&= \frac{\sigma_j}{4\pi}(2 - \beta - \frac{3\beta}{2}(sin^2\theta_z)) \quad .
\end{aligned} \tag{9.10}$$

If the analyser is situated so that it sums equally the photoelectron flux above and below a plane 45^o with respect to the major and minor axes of polarization, it is then independent of the polarization of the light. Area collection is achieved by collecting over a range of angles θ_y such that the signal is polarization independent, and a range of angles θ_z such that the the most accurate value of β is obtained. The selection of the range of θ_z over which to sample is discussed in the following subsection.

9.6.2 Angular range covered from the axis of propagation of the light

The equation for the flux through any given differential solid angle is linear in β. The contribution from a sum of differential segments will also be linear in β. The variance in efficiency across different angles will be contained in the coefficients of the equation for the β dependence of a sector. For a sector $\mathcal{A}$ which is symmetric about the 45^o plane, and thus independent of the degree of polarization,

$$I_{\mathcal{A}} = \sigma_j(M_{\mathcal{A}}\beta + C_{\mathcal{A}}) \quad . \tag{9.11}$$

By sampling another sector, $\mathcal{B}$, it is possible to solve for β;

$$\beta = \frac{C_{\mathcal{A}} - C_{\mathcal{B}}R}{M_{\mathcal{B}}R - M_{\mathcal{A}}}, \tag{9.12}$$

where $R = \frac{I_A}{I_B}$.

The selection criterion for which areas are sampled is that of the minimising the error in β caused by the statistical error in I_A and I_B.

$$\Delta\beta = \Delta R \frac{C_B M_A - C_A M_B}{(M_B R - M_A)^2} \tag{9.13}$$

where

$$\Delta R = \sqrt{\frac{I_A}{I_B^2} + \frac{I_A^2}{I_B^3}} \ . \tag{9.14}$$

The performance of the analyser depends on the statistics (the first factor in $\Delta\beta$) and on the coefficients of the sectors (the second factor in $\Delta\beta$). The error also depends on the value of β because it affects the relative intensities R.

The coefficients for a sector spanning from $\theta_z = u$ to $\theta_z = v$ are

$$M_{u-v} = \frac{1}{4}((cos(v) - cos(u) - cos^3(v) + cos^3(u)) \tag{9.15}$$

$$C_{u-v} = cos(u) - cos(v) \ . \tag{9.16}$$

The error was found to be minimised by covering as large an area as possible. The optimum partition angle, Θ, was found to depend on the value of β. Fortunately the error surface (Fig. 9.4) is flat around the minimum, not penalizing any particular selection of Θ, for which 60^o is reasonable. A comparison of this analyser with a 'typical' moving dispersive analyser is given in Table 9.1.

9.6.3 Errors due to misalignment

Some synchrotron sources produce light which has a wandering axis of polarization because the polarization depends on which part of the beam is sampled, and in practice this is difficult control. If the axis varies this immediately destroys the symmetry conditions on which PEADA is based, and it becomes polarization sensitive. The analyser itself may also simply be misaligned with respect to the major axis of polarization.

From Fig. 9.5 it may be seen that the error is proportional to the polarization. If the light is unpolarized it has no preferred polarization axis and therefore there is no error associated with misalignment. See also in Fig. 9.5 the cancellation of errors that occurs at $\phi = 180^o$. 180^o grids are marginally harder to manufacture. In such a grid the collapse of mesh spacing that occurs in each quadrant near the rim reduces the effective transmission and ultimately the effective ϕ. Judicious orientation of the grid and the use of a sufficiently fine mesh will counter the effect of mesh collapse.

The misalignment error with respect to the major axis of polarization (described by angle α) is sensitive to β. $\beta = 0$ is a sphere and naturally, the error vanishes for this configuration because a sphere appears the same from any angle.

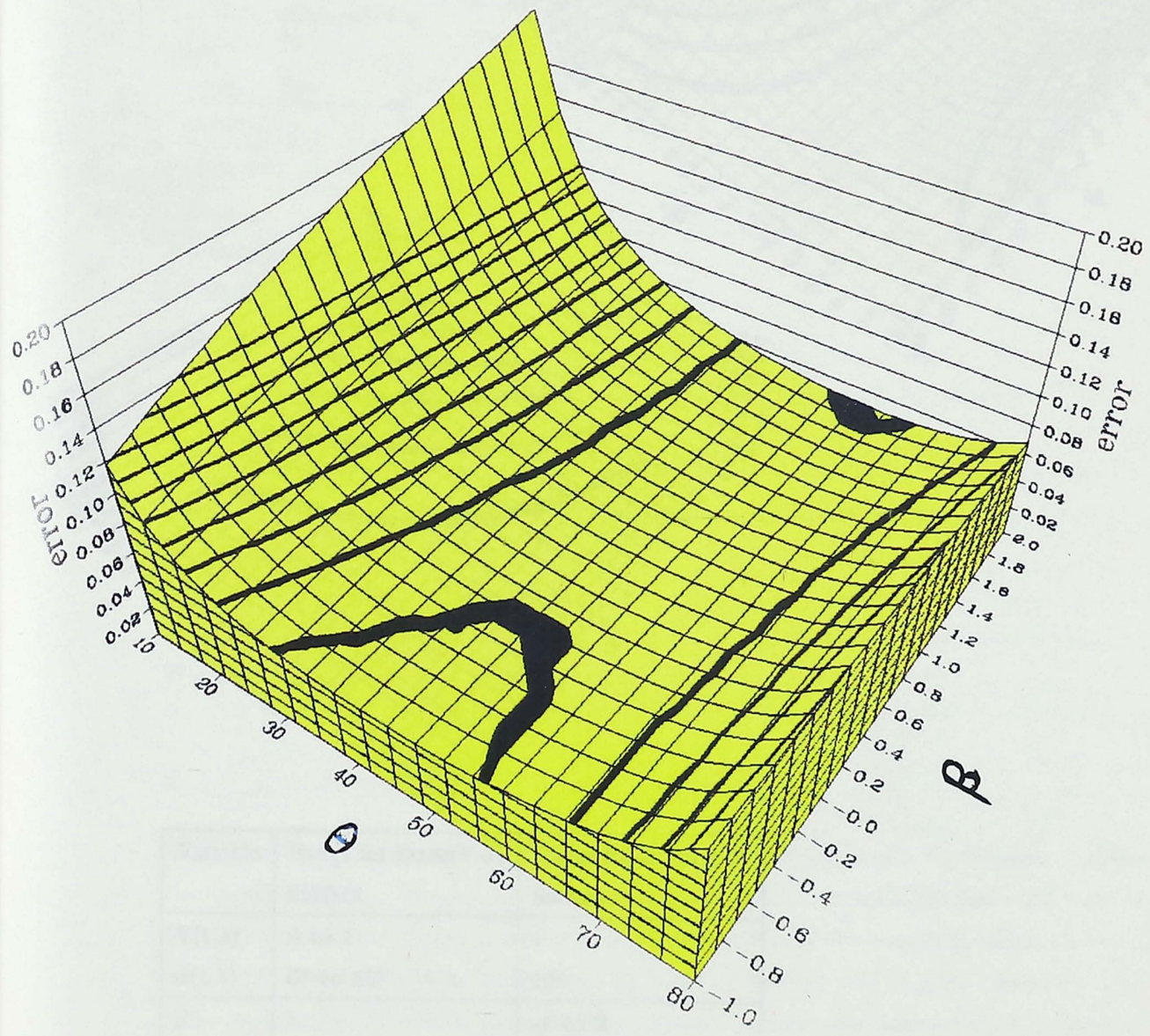

Fig. 9.4: Statistical error surface for different asymmetries β and sector division angles Θ. The optimum division is about 60^o from the axis of propagation of the light. The error scale is for 10,000 counts collected by the analyser. In practice, collection areas are limited by the need to admit light into the interaction region.

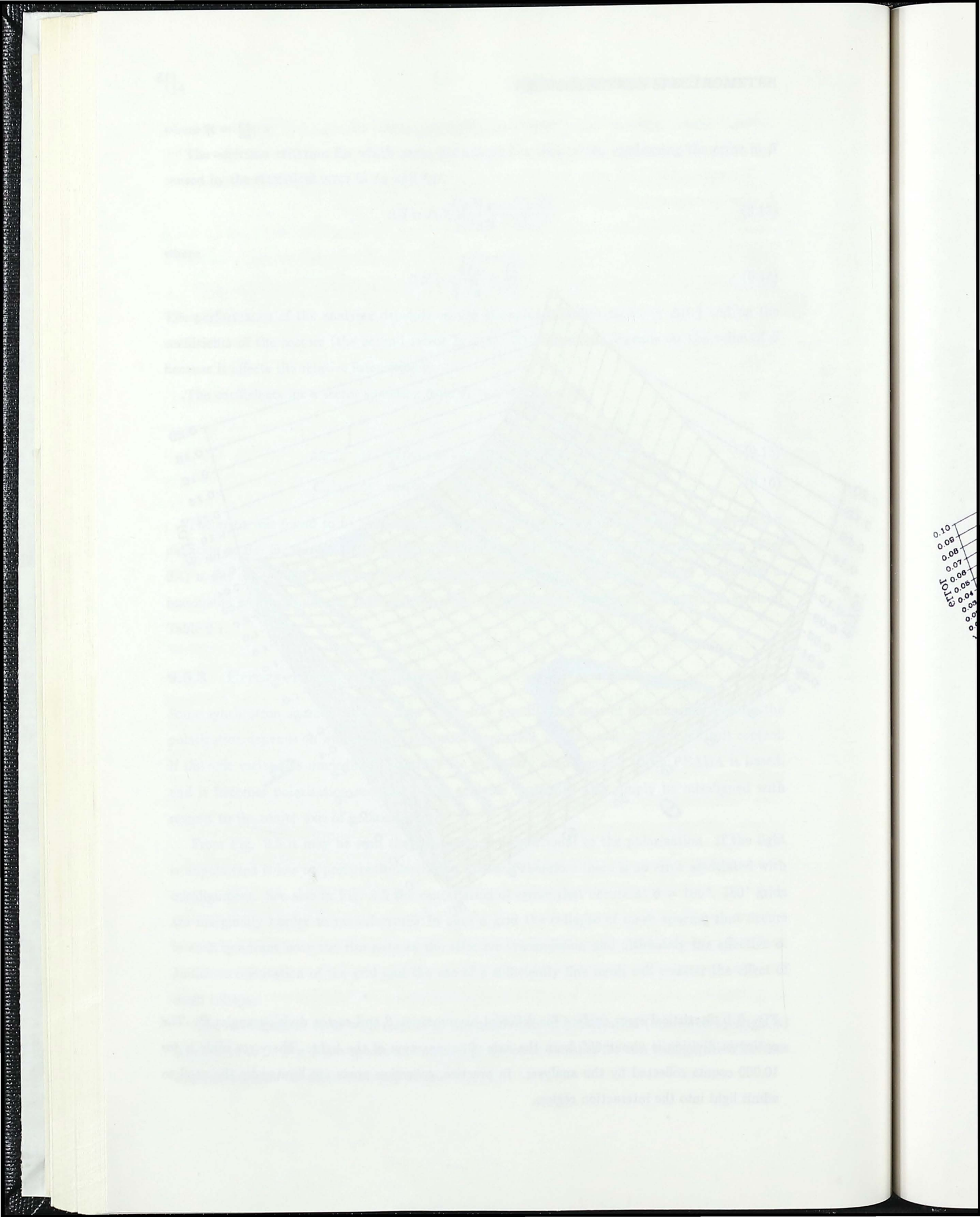
0.10
0.09
0.08
0.07
error 0.06
0.05
0.04
0.03

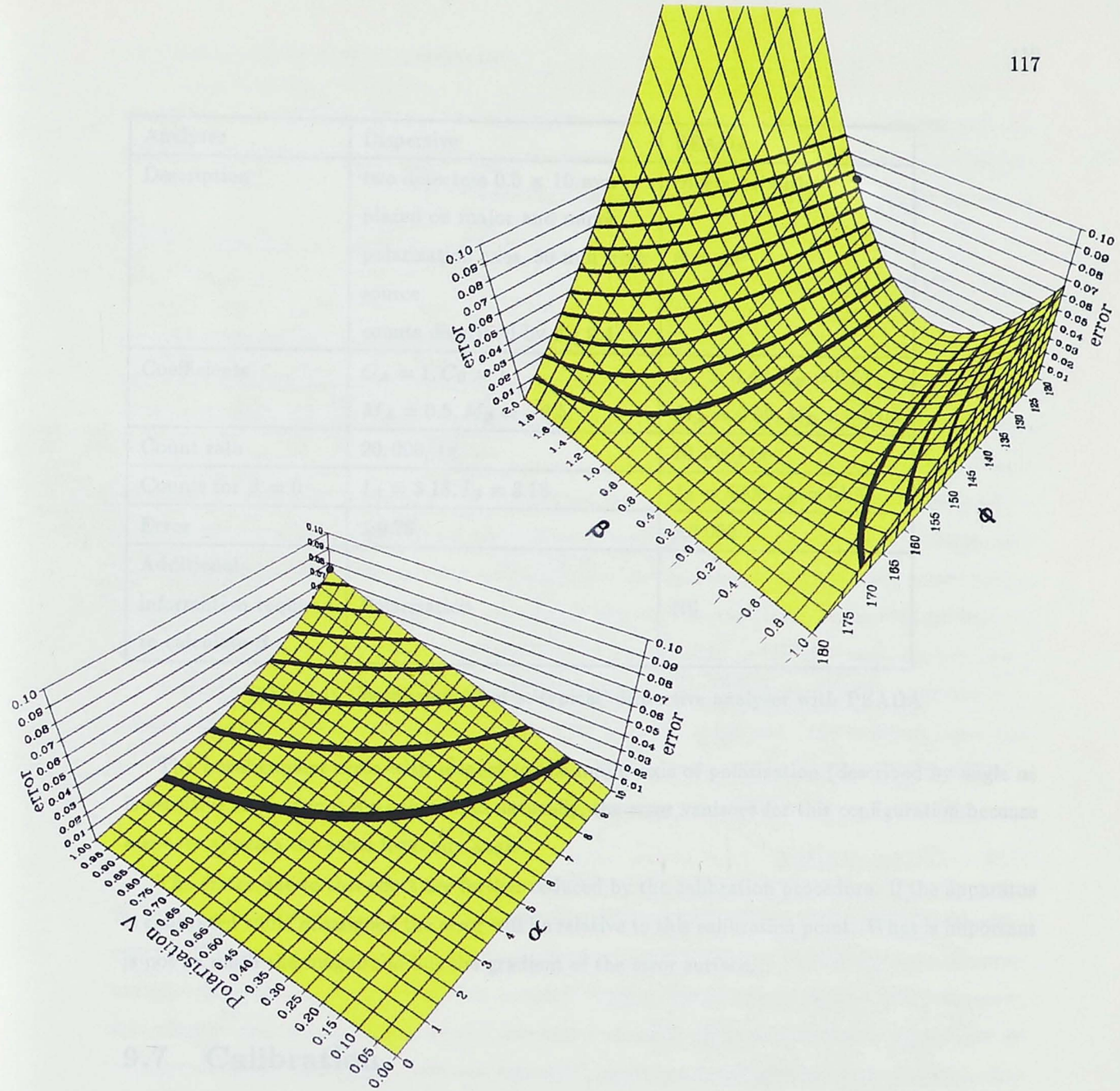

Variable	Range for Error(V,α) Surface	Range for Error(β, ϕ) Surface
V(t,λ)	**0 to 1**	1
α(t,λ)	**0° to 10°**	10°
β	1	**-1 to 2**
ϕ	120°	**180° to 120°**
Θ	60°	60°

Fig 9.5: Systematic error surfaces: Top – Error as a function of β and ϕ; Bottom – Error as a function of V and α. The apparatus parameters are described in the table.

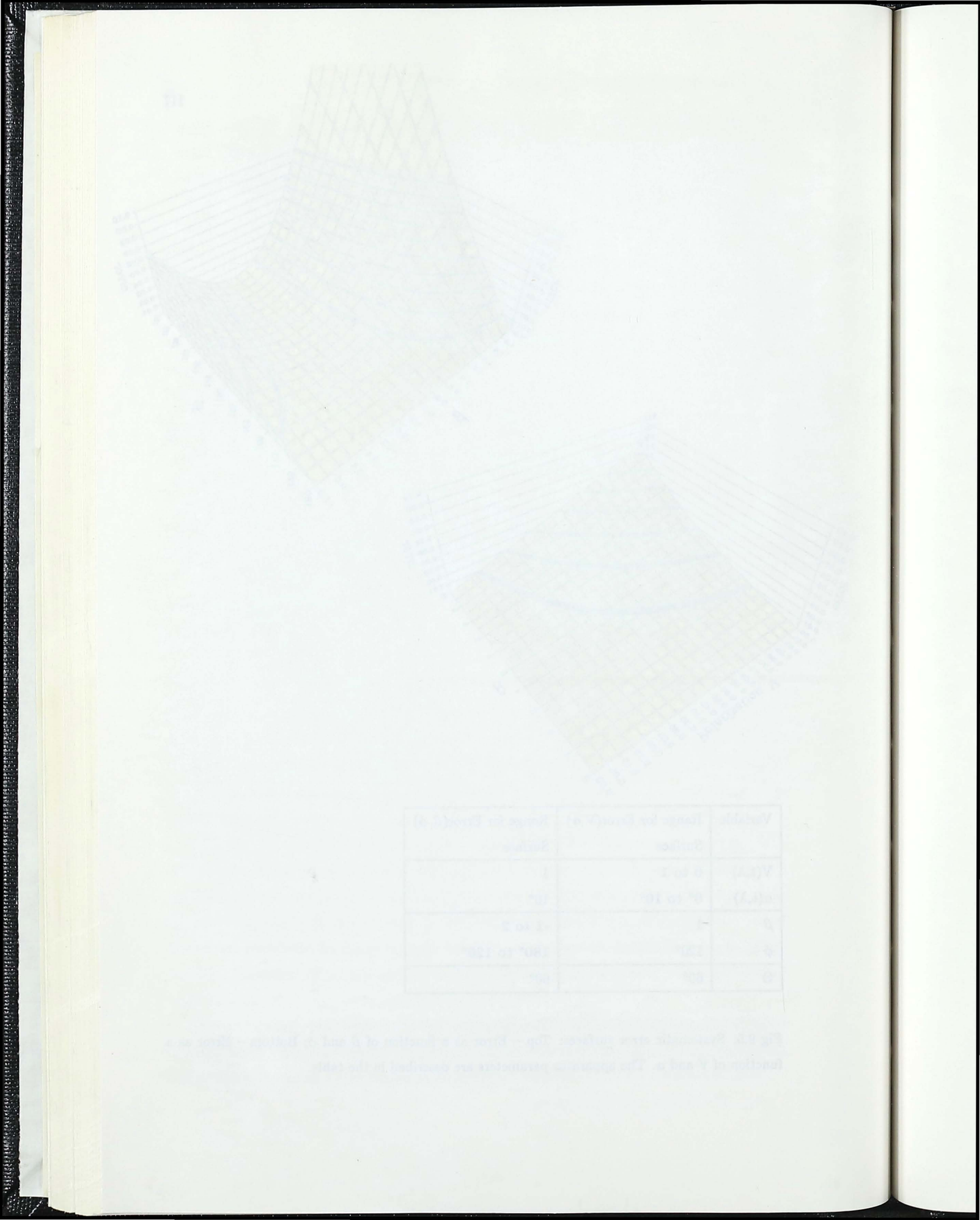

Analyser	Dispersive	PEADA
Description	two detectors 0.5 × 10 mm placed on major and minor polarization axes, 50 mm from source, counts described by Eq 9.4	covers 2π with $\Theta = 60^o$
Coefficients	$C_A = 1, C_B = 1$ $M_A = 0.5, M_B = -0.5$	$C_A = 0.49, C_B = 0.51$ $M_A = 0.09, M_B = -0.09$
Count rate	$20,000/4\pi$	$20,000/4\pi$
Counts for $\beta = 0$	$I_A = 3.18, I_B = 3.18$	$I_A = 4900, I_B = 5100$
Error	± 0.79	± 0.053
Additional information required to calculate β	Polarization	Nil

Table 9.1: Comparison of of a 'typical' dispersive analyser with PEADA

The misalignment error with respect to the major axis of polarization (described by angle α) is sensitive to β. $\beta = 0$ is a sphere and naturally, the error vanishes for this configuration because a sphere appears the same from any angle.

The errors due to this effect are further reduced by the calibration procedure. If the apparatus is calibrated while misaligned the error will be relative to this calibration point. What is important is not so much the magnitude but the gradient of the error surface.

9.7 Calibration

Although it should be possible to calculate from the experimental geometry the value of β, calibration is still necessary. Transmission and collection efficiencies vary across the grid. Inspection of Eq. 9.12 shows that three values have to be known to convert the R measured by the spectrometer into β. This means R has to be measured for known values of β. Some gases have had β evaluated over a range of wavelengths for such a purpose. Unfortunately, save for a few cases where β is known exactly (for helium $\beta = 2$), even these calibration curves only give a limited accuracy of about 5% (This was achieved[69] using large acceptance angles in a dispersive analyser. The energy resolution was not critical in this case as the noble gases that were being ionized produced electrons of well separated, discrete energy.)

The use of a device that measures absolute cross section, such as a double ion chamber[85], in conjunction with this analyser, is a particularly good combination. PEADA can be calibrated

with the double ion chamber to yield absolute cross sections without the need to know the flux of the molecular beam. Further, if the absolute cross section is measured, only two known values of β need be measured to determine the apparatus coefficients.

9.8 TOF design

If the light source and consequently the photoelectron source is pulsed, TOF techniques can be used. The major advantage is that only one analyser need be used. This configuration would not suffer from the problems brought about by post-calibration drifts in the relative efficiencies of the three electron detectors employed in PEADA.

In essence, the different sectors would not be partitioned by physical barriers, but rather by time analysis of the signal. The TOF version would have a single detector that samples from a penetrating field aperture located in the plane of polarization at 45^o to the major axis. The penetrating field collection is devised such that the electrons ejected toward the optical axis experience a weak collecting field at first and are delayed relative to those ejected closer to the plane of polarization. The time resolved signal detected will be some linear combination of the $\beta = -1$ and $\beta = 2$ distributions. The signal collected may also be a function of polarization, but careful selection of the symmetry of the apparatus will negate this effect.

9.9 Conclusion

Although the β-sensitivity of the measurement is less than that of an analyser which looks at small views, this analyser should measure β with the smallest error for a given counting time. The ability to measure β in a single measurement, without the need to know, or being detrimentally affected by, the degree of polarization of the light, is a desirable attribute of this apparatus. Finally, the lack of moving parts and the compact design (thus less sensitive to magnetic fields) increase its utility. This instrument design will allow improved measurement of photoelectron distributions giving the information beyond that provided by absorption studies alone.

Part IV

Conclusions of Thesis

Conclusions of Thesis

The two principal thesis objectives where achieved;

Use of coupled Schrödinger wave equations to explain spectra of mixed states: The absorption spectrum of the singlet delta state of oxygen was measured with improved resolution and accuracy. The region 1270 – 1540 Å was then modelled and re-assigned, using six appropriately coupled states. This showed the value of the coupled Schrödinger wave equation technique, which was used again for molecular helium. The emission continuum of helium arcs are now explained as a transition between C and A states of He_2^+. The structure that would have arisen if the transition was from a D to a mixed A and B state was not observed, eliminating this as an alternative explanation.

Development of Spectroscopic Instruments: As a tunable UV light source, four wave mixing in krypton was found to be the most appropriate technique for the analysis of the longest band of oxygen, around 1244 Å. The source was successfully built with minor technical improvements. The possibility of using helium dimers was reviewed and new laser based on He_2^+ proposed. Additional advances made during the Ph.D. program, in the area of double ion chambers and photoelectron spectrometers, are also reported.

Future work will involve a more complete analysis of the large quantity of data collected in the metastable experiment (Appendix C), particularly for wavelengths below 1270 Å. The resolution of the krypton ultraviolet laser will be measured and then used to investigate oxygen absorption. For helium molecules, high accuracy potential curves for the $C^2\Pi_u$ and other critical states are being calculated[1].

[1] David Moncrieff, SCRI Florida State University, DoE grant:DE-FC05-85ER250000

Appendix A

Theory of Diatomic Molecules

The mathematical description of the spectra of diatomic molecules is a vast subject, covered by many pedagogical works[86, 44]. This Appendix is confined to points of interest relevant to this thesis and will assume some familiarity with the topics raised.

A.1 Observables

Of interest to the spectroscopist are transitions: absorption, stimulated emission, and spontaneous emission. Broadly speaking, the spectra resulting from these processes may be thought of as containing two classes of information: *line positions* and *cross sections* (or *rates* of spontaneous emission). A theoretical understanding of a spectrum rests upon the explanation of these observables. Line positions obtained through vibrational and rotational analysis, and cross sections calculated using coupled Schrödinger wave equation (CSE) simulation, enable the identification of electronic states and yield their potential curves. Line positions correspond to bound stationary states Ψ_E, with discrete eigen energies, E, of a Hamiltonian, H,

$$E = < \Psi_E | H | \Psi_E > \quad , \tag{A.1}$$

while the cross section is related to the dipole transition moments of molecular wavefunctions,$< \Psi_{final} | \mathbf{er} | \Psi_{initial} >$ by the Einstein Coefficients.

The basis sets spanning Ψ are set by convention[1] and represent most molecules well [2]. Where this is not the case, the spectra result from mixed Ψ and are said to be 'perturbed'. The extent of mixing is crucial in deciding whether vibrational and rotational analysis, or CSE analysis (Table A.1) is the most appropriate means of analysing a spectrum. Rotational band analysis employs formulae, which although simple for unperturbed states, quickly become intractable for mixed states. Under these circumstances CSE techniques are required.

[1] to avoid confusion between the results of different authors Hund's coupling case (a) is normally assumed.

[2] The quantum numbers that describe an electronic state Ψ are constants of the motion for the molecule concerned.

Characteristic	Method of Analysis		
	Vibrational RKR –Method	Rotational	Coupled Schrödinger Wave Equation
Inputs	$E_{vibrational}$ line positions	Constants that describe the potential curves – B_v,D,ν_0 etc.and Temp.	Potential curves & Temp.
Outputs	Potential curve	$E_{rotational}$ (line posit.) → then convolute with line profiles and strengths to give cross section (Band Analysis)	Cross Section
Computation Speed	Fast	Very fast - suitable for least square analysis	Slow
Perturbation (Mixed Ψ)	n.a.	– Use Fano line profiles – Increase complexity of equations – Fails for large perturbations[a]	Introduce off-diagonal matrix elements in H

[a] Too many new parameters have to be introduced for this method to be meaningful, and such analysis has led to mis-identification of features (see Table. 4.4).

Table A.1: Methods of analysing diatomic molecular spectra

The following sections discuss in turn CSE, vibrational, and rotational analysis, and comment in the subsections on the physical principles involved.

A.2 Coupled Schrödinger Wave Equation Analysis

In this technique one calculates the cross section directly from the quantum mechanical wave functions of final and initial states. Fig. A.1 gives an overview from which the complexity and inter-relations of the CSE technique may be seen. Broadly speaking, the upper half of the diagram illustrates the calculation of the molecular wave functions, while the lower half shows their role in computing the observable, the cross section, σ. One subtlety is the reasoning behind the selection of the diabatic, Born-Oppenheimer (BO), molecular wave function basis set. The wave functions are found as solutions to the diabatic Hamiltonian. Although diabatic and adiabatic representations are equally valid[7], the former, for which the potentials cross, is far easier to mathematically represent, and with no nuclear kinetic energy, has a simpler Hamiltonian for use in the CSE technique. As the solution wave functions are the sum of BO wave functions, the cross section may be calculated far more simply using the separation of factors valid under the Born-Oppenheimer approximation (BOA).

The components of the calculation will now be described in more detail. The cross section calculation has a electrodynamics term, a population of the lower state term, and a dipole transition strength term. From Fig. A.1 it may be seen that the Einstein coefficients (the electrodynamics term) and the Boltzmann Factors (the population of the lower state term) may be dealt with separately and they are addressed in subsections A.2.1 and A.2.2 respectively. Because this study calculates absorption (O_2), and spontaneous and stimulated emission (He_2, He_2^+), the Einstein coefficients for these processes are discussed specifically. The rationale for the break up of the cross section calculation, and the nature of the perturbations, provided by the Born-Oppenheimer Approximation is discussed in Subsec. A.2.3. It is natural here to comment on the naming conventions, the Hund's angular momentum couplings, and their relation to the BOA. Next, in Subsec. A.2.4, the rotational and radial dipole transition moments are discussed. The introduction of perturbations or coupling to the Hamiltonian that result from the BOA are then treated in Subsec. A.2.5. The solution of this Hamiltonian using coupled wave equations to generate the wave functions and finally generate the cross section is shown in Subsec. A.2.6. Finally, the origin of the initial data (potential curves and dipole transition moments) needed as inputs to the CSE analysis is discussed in Subsec. A.2.7.

A.2.1 Einstein Coefficients

Einstein coefficients, A and B (that describe the transition probability between two levels), Oscillator strengths, f, (the number of classical oscillators that are equivalent to a single real atom)

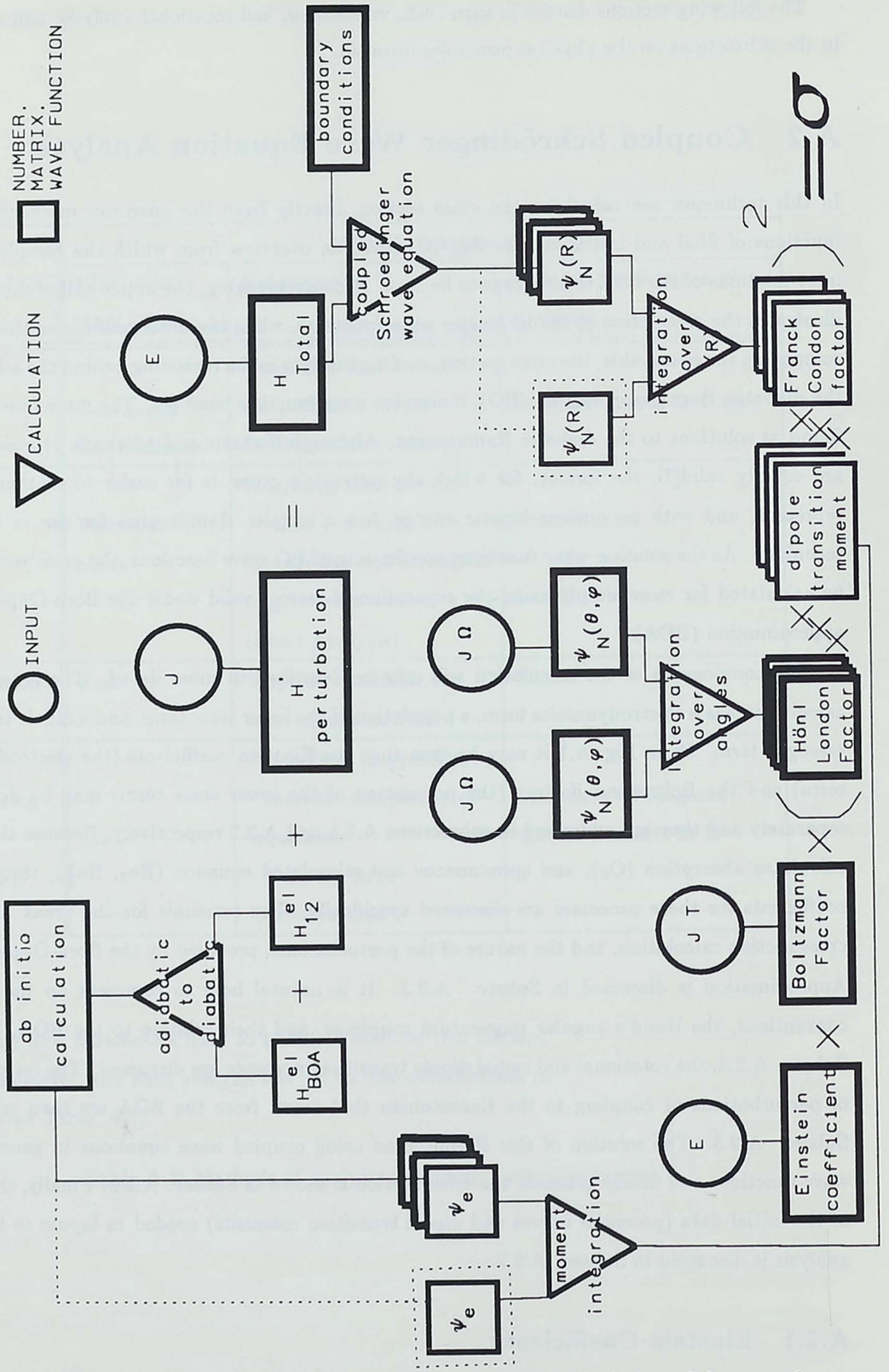

Figure A.1: CSE technique: The dotted lines indicate the initial calculation of the ground state, which is then used to overlap with (stacked) multiple final states. The symbols are defined and discussed in the text. In practice the dipole moments are approximated as constant and the Hönl-London factors are tabulated. Both the Hönl-London and Franck-Condon factors are the *squares* of the overlap integrals. The Einstein coefficient shown here does not include the transition moment which is treated separately.

and line strength, S, are all used in different circumstances to describe the same thing: the electrodynamics of molecular radiation. A valuable synopsis relating all these measures in S.I. units is found in Chapter 11 of "Spectrophysics" by Thorne[87]. Practically, in this work, these quantities are important in calculating molecular concentrations from cross sections, and as wavelength dependent factors in the calculation of theoretical spectra. The following discussion will be confined to points of interest relevant to the thesis.

Absorption and its inverse – stimulated emission – are measured as cross sections (areas), but they may also be thought of as rates per molecule per unit of electric field strength. This latter visualization is embodied in the following frequently derived (S.I.)[88] formula for dipole transitions;

$$W_{ab} = \frac{4\pi^2}{ch^2}\frac{1}{4\pi\varepsilon_0} I(w_{ab}) \mid -e\hat{\varepsilon}.\mathbf{r} \mid^2 \quad . \tag{A.2}$$

The symbols have their usual meaning. $I(w_{ab})$, $\hat{\varepsilon}$, and $\mathbf{r}$ are significant in the interpretation of the above equation. W_{ab} is the transition rate per atom and correspondingly is the rate of change of the number of photons, $\dot{n}$, while the light intensity $I(w_{ab}) = \frac{nh}{c\lambda}$. $\dot{n} \propto$ n, leads to the familiar exponential form of both the laser gain equation and Beer's law of absorption. There is a factor $\frac{1}{\lambda}$ in the cross section calculation. Care must be taken to avoid the common error of integrating cross section as a function of wavelength to obtain the total strength of transition. A cross section is ultimately determined from a ratio of photon counts, which naturally is independent of how one defines (in terms of wavelength or frequency) the light incident on the gas. Instead, the strength should be determined by integration on an energy scale. The final factor $\mid -e\hat{\varepsilon}.\mathbf{r} \mid^2$ is related to the strength S_{if} ;

$$S_{if} = \mid \int \Psi_f M \Psi_i d\tau \mid^2 \quad . \tag{A.3}$$

$\hat{\varepsilon}$ represents the direction of motion of the emergent or absorbed photon. $\hat{\varepsilon}$ is usually transformed from Cartesian coordinates,into those that represent left and right circularly polarized light about the magnetic field (z axis) and light linearly polarized along the z axis. $\mathbf{r}$, when expressed in polar coordinates, may be broken up into radial and angular parts. The additional trigonometric functions from the angular part of $\mathbf{r}$ included in the angular dipole transition integrals, are critical in the calculation of the dipole selection rules.

The oscillator strength f is a commonly used dimensionless quantity and is related[88] to the strength S by

$$f = \frac{8\pi^2 m_e c}{3he^2\lambda} S \quad , \tag{A.4}$$

with the factor 3 in the denominator being based upon the assumption of isotropic radiation.

The formula for spontaneous emission is

$$W^s_{ab} = \frac{1}{2\pi\hbar c^3}\frac{e^2}{4\pi\varepsilon_0} w^3_{ab} \mid -\hat{\varepsilon}.\mathbf{r} \mid^2 \quad . \tag{A.5}$$

When this rate is plotted against wavelength rather than frequency, the total integrated rate (= 1/lifetime) has to be conserved, so a change of variable factor has to be introduced, leading to an overall $1/\lambda^5$ for the rate of production of photons, or a $1/\lambda^6$ factor for the emitted intensity of the light.

A.2.2 Boltzmann Factor

At different temperatures, the population of the various levels of the ground state will yield different spectra. At temperatures allowing population of v" $\geq$ 1 levels hot bands will be seen in the spectrum. This is illustrated in Part II of this work where the Tanaka and Huffman continua are identified as cold and hot transitions in He_2^+. For rotational bands, cooling to liquid nitrogen temperatures is necessary to reduce the effect of the population of the higher levels. The exponentially decaying Boltzmann factor and the linearly increasing rotational degeneracy factor compete to produce a characteristic band profile.

A.2.3 Born-Oppenheimer Approximation

Molecules are mathematically described in the Schrödinger eigenvalue problem,

$$H\Psi = E\Psi \quad , \tag{A.6}$$

where H is the Hamiltonian operator, E is the scalar energy and Ψ is the wave function that describes the diatomic molecule such that $< \Psi[x] \mid \Psi[x] >$ is the probability of finding the system with the measured coordinates $[x]$. The solution of $H\Psi = E\Psi$ and the visualization of a diatomic rotor involves the uncoupling of various contributions to the Hamiltonian. Eventually the coupling is reintroduced in the form of perturbations to give a more accurate description. Ψ is approximated by the product of electronic, vibrational and rotational wave functions $\psi_e\psi_v(\frac{1}{r})\psi_r$. Each factor is then separately soluble. ψ_e[coordinates of the electrons] is the electronic wave function and $< \psi_e \mid \psi_e >$ is the electron density. The separation of Ψ into the electronic part ψ_e, and the remaining nuclear part, is known as the Born-Oppenheimer approximation, and is based on the insight that the electronic motion is comparatively fast, and thus the molecule can be represented by the familiar electronic potential energy versus internuclear separation curves. $\psi_v(\frac{1}{r})\psi_r$ describes the position of the nuclei, with ψ_v representing the internuclear separation and ψ_r describing the the orientation of the internuclear axis. As for the atomic case, this constitutes a separation into radial and angular parts, with the angular momentum and associated transition selection rules resulting from the latter.

Classification of States:

The symbol for a molecular state indicates its symmetries and quantum numbers thus:

$$(historical\ label)^{2S+1}\Lambda^{\pm}_{(g\ or\ u)} \quad . \tag{A.7}$$

A complete discussion of the individual component symbols and their meanings is given in Herzberg[86]. Suffice it to say that the symbol contains enough information to show if a transition is allowed in the Hund's case (a) coupling scheme. What is not specified is the coupling between the angular momentum components given in the symbols, these being furnished by reference to Hund's coupling cases. The allowed symmetries from the initial intercombination of atomic states are derived by Wigner and Witmer[89].

Hunds coupling cases:

The major cases of angular momentum coupling for light molecules are Hund's cases (a) and (b).

Hund's Case (a): The electronic motion is coupled very strongly to the internuclear axis. The projection on the internuclear axis of the orbital angular momentum **L** is Λ, and for the spin **S** is Σ. The total projection on the internuclear axis is $\Lambda + \Sigma = \Omega$. **J**, the total angular momentum, is simply the vector sum of Ω and the nuclear angular momentum vector **R**. The rotational levels are similar to that of a symmetric top with the restriction $\mid \mathbf{J} \mid > \Omega$ and the energy levels are suppressed by $B_v\Omega^2$. This coupling scheme is the most commonly adopted basis set.

Hund's Case (b): **S** is only very weakly coupled to the internuclear axis and is added vectorially to **N** (the sum of **R** and Λ), to give the total angular momentum **J**. For particular values of **N** and **S** respectively, J=(N+S) to (N-S), and J is a good quantum number for the transition selection rules.

For the singlet transitions of metastable oxygen studied in Part I the spin is zero and there is no distinction between Hund's coupling cases (a) and (b). As the rotation speed of the molecule increases L becomes uncoupled to the internuclear axis giving the next coupling case –

Hund's Case (d): In this case L couples to the axis of rotation of the molecule. Here the angular momentum of the two spinning nuclei is quantised with L added vectorially to it. Λ is no longer a good quantum number and a mix of Hund's (a) basis set states of different Λ has to be used to represent this case. For oxygen, an example in Part I is given where the Π and Δ are mixed by the L-uncoupling perturbation. Another consequence of L-uncoupling is Λ-doubling. As L is no longer projected onto the internuclear axis, the sign of L, or the orientation of the orbital angular momentum with respect to the nuclear rotation affects the total angular moment. The symmetric and asymmetric rotational levels lose their degeneracy giving rise to a splitting of levels. As Σ_u states of oxygen contain only symmetric levels, a Δ_u-Σ_u coupling can affect only symmetric levels.

A.2.4 Dipole Transition Moment

The dipole transition moment is

$$\begin{aligned} |R|^2 &= \left|\int \Psi_f^*(M_{elec}+M_{nuc})\Psi_i d\tau\right|^2 \\ &= \left|\int \psi'_e(\psi'_v/r)\psi'_r M_{elec} + M_{nuc}\psi_{e''}(\psi_{v''}/r)\psi_{r''}\tau\right|^2 , \end{aligned} \tag{A.8}$$

where M is the dipole moment operator. For the homonuclear molecules encountered in this study, M_{nuc} is zero. Thus, as may be seen in the following separation into angular and radial parts,

$$|R|^2 = \left|\int \psi_{v'}\left(\int \psi^*_{e'} - \sum_{all\ electrons} e\mathbf{r}\psi_{e''}d\tau\right)\psi_{v''}dr\right|^2 \times \left|\int \psi_{r'}D(\theta,\chi,\phi)\psi_{r''}sin\theta d\theta d\phi\right|^2 . \tag{A.9}$$

Homonuclear molecules can only radiate by way of electronic transitions. Transitions between rotational and vibrational levels in the same electronic states are forbidden because $\psi_{e'} = \psi_{e''}$ makes the first term in Eq. A.9 zero. $D(\theta,\chi,\phi)$ projects the molecular dipole moment in molecular coordinates, onto the laboratory frame.

The transition moment of (2J+1) energetically degenerate rotational wave functions are summed to give the total line strength S,

$$S = S_{v'v''} \times S_{r'r''} . \tag{A.10}$$

$S_{v'v''}$ corresponds to the first factor in Eq. A.9 while $S_{r'r''}$ corresponds to the second factor. $S_{r'r''}$ is known as the Hönl-London factor or rotational line strength and has been tabulated for the various quantum numbers of a symmetric top. The Clebsch-Gordon coefficients are the corresponding numbers for atomic transitions. The sum of the Hönl-London factors over all the rotational levels is normalized to unity so that if the rotational structure is not observed, it is sufficient to deal only with first vibrational term in Eq. A.9. This was done in the treatment of He_2^+ in Chapter 6 of this study.

The Hönl-London factors provide a useful insight into the relative strengths of the rotational branches[90], thus;

for $\Delta\Lambda = 0$,

$$\begin{aligned} S_J^R &= \frac{(J'+\Lambda')(J'-\Lambda')}{J'} && \simeq J' \\ S_J^Q &= \frac{(2J'+\Lambda')\Lambda'^2}{2(J'+1)} && = 0\ for\ \Sigma\ states, \simeq \tfrac{2}{J'}\ for\ \Lambda > 0 \\ S_J^P &= \frac{(J'+1+\Lambda')(J'-1+\Lambda')}{J'+1} && \simeq J' \end{aligned} \tag{A.11}$$

Summary: Q branch is weak or missing,

for $\Delta\Lambda = +1$,

$$\begin{aligned} S_J^R &= \frac{(J'+\Lambda')(J'-1+\Lambda')}{4J'} && \simeq \frac{J'}{4} \\ S_J^Q &= \frac{(J'+\Lambda')(J'+1-\Lambda')(2J'+1)}{4J'(J'+1)} && \simeq \frac{J'}{2} \\ S_J^P &= \frac{(J'+1-\Lambda')(J'+2-\Lambda')}{4(J'+1)} && \simeq \frac{J'}{4} \end{aligned} \tag{A.12}$$

Summary: Q branch is twice as strong as the other branches,

for $\Delta\Lambda = -1$,

$$\begin{aligned} S_J^R &= \frac{(J'-\Lambda')(J'-1-\Lambda')}{4J'} &&\simeq \frac{J'}{4} \\ S_J^Q &= \frac{(J'-\Lambda')(J'+1+\Lambda')(2J'+1)}{4J'(J'+1)} &&\simeq \frac{J'}{2} \\ S_J^P &= \frac{(J'+1+\Lambda')(J'+2+\Lambda')}{4(J'+1)} &&\simeq \frac{J'}{4} \end{aligned} \tag{A.13}$$

Summary: Q branch is twice as strong as the other branches.

There are no lines for which J< Λ (J < Ω, when spin is included). For the oxygen study in Part I, the $\Pi - \Delta$ transitions are distinguished from the $\Delta - \Delta$ by having an additional Q-branch.

If the electronic dipole moment,

$$\int \psi_{e'}^* - \sum e\mathbf{r}\psi_{e''} d\tau \quad , \tag{A.14}$$

is approximated as being constant over the range of integration in **r**, it can be brought outside the first factor of Eq. A.9. The remaining square of the vibrational wave function overlap integral is known as the Franck–Condon factor. This approximation is represented in the diagram, Fig. A.1 by simple multiplication of the Franck–Condon factor with the radially integrated wavefunctions. If the effect of a varying dipole transition moment were to be taken into account, then the moment should be included at the radial wave function integration stage.

For forbidden transitions between BO states the dipole moment is strictly zero. This means, in the CSE treatment, that only the Hönl-London factors for the allowed transitions are needed. The forbidden transitions gain their strength only by mixing with the allowed transitions.

A.2.5 Perturbations

The price of having a tractable basis set with which to calculate cross sections is the inclusion of perturbations (couplings) in the Hamiltonian.

Thus a theoretical development centres around finding H such that its eigenfunctions, Ψ, generate the observable lines and cross sections. H is broken up into nuclear and electronic coordinate sections by the Born-Oppenheimer Approximation. Ψ_{BO} form a basis set of exact solutions of H_{BOA}. The inclusion of off-diagonal perturbations H' with H_{BOA} yields the exact H_{total}. The exact choice of basis determines the partitioning into H_{BOA} and H'. The commonly used basis sets - Hund's cases (a) to (d) each describe best a particular coupling of angular momentum, for which each have a set of good quantum numbers. Eigen states of the perturbed H_{total} are intermediate between Hund's cases and are represented by a sum or mix of pure basis functions.

Although the separation of the angular and radial parts is necessary to develop the dipole transition moments associated with each part, the vibrational wave function can be solved for

Category	Name of Contribution	Hamiltonian Contribution	Selection Rule				Case	Value[a]
			ΔS	$\Delta\Sigma$	$\Delta\Lambda$	$\Delta\Omega$		
$\mathbf{H}_{BOA}$ (Diagonal)	Electronic	H^{EL}	0	0	0	0	all	V(R)
	Nuc. Vib.	T^N	0	0	0	0	all	0 [b]
	Nuc. Rot.	H^{ROT}	0	0	0	0	all	B J(J+1)
H' (Off-Diagonal)	Electrostatic Perturbation[b]	H_{12}^{EL}	0	0	0	0	$^1\Delta_2$ - $^1\Delta_2$	2751
							$^3\Delta_2$ - $^3\Delta_2$	750
	Relativistic Perturbation	Spin - Orbit (H^{SO})	w [c]	$\pm x$ [d]	$\mp$ x	0	$^1\Delta_2$ - $^3\Delta_2$	92
		Spin - Spin (H^{SS})	y [e]	$\pm$z [f]	$\mp$z	0		weak
		Spin - Rot. (H^{SR})	0	± 1	0	± 1		v. weak
	Rotational Perturbation	Spin - Elec. (H^{SE})	0	± 1	∓ 1	0		v. weak
		S Uncoupling	0	± 1	0	∓ 1		v. weak
		L Uncoupling	0	0	± 1	± 1	$^1\Delta_2$ - $^1\Pi_1$	F(J)[g]

[a] for O_2 $a^1\Delta_g$ 1270 – 1540 Å

[b] diabatic approximation

[c] w = 0,1,$\Sigma^{\pm} - \Sigma^{\mp}$

[d] x = 0,1

[e] y = 0,1,2,$\Sigma^{\pm} - \Sigma^{\mp}$

[d] z = 0,1,2

[d] $F(J) = \beta_{12}(J(J+1)-2)^{\frac{1}{2}}$[44]

Table A.2: Matrix elements of the molecular Hamiltonian. $\mathbf{H}_{BOA}$ +H' = $\mathbf{H}_{total}$.

each rotational level by inclusion (i.e. by addition) of the rotational energy with the electronic Hamiltonian, thus;

$$H_J = H^{el} + \frac{h}{8\pi^2 c\mu r^2} J(J+1) \quad . \tag{A.15}$$

A.2.6 Solution of the Coupled Wave Equations

The method of solution used for the coupled Schrödinger wave equations,

$$\begin{aligned} H_1\Psi_1 - E\Psi_1 &= V_{12}\Psi_2 + V_{13}\Psi_3 + \ldots \\ H_2\Psi_2 - E\Psi_2 &= V_{12}\Psi_1 + V_{23}\Psi_3 + \ldots \quad , \\ &\vdots \end{aligned} \tag{A.16}$$

is the renormalized Numerov method[91].[3] Here $H_1\Psi_1 = \nabla^2\Psi_1 + V_1(\Psi_1)$, Ψ_1 being a function of the internuclear separation, and V_1 being the diabatic potential for state 1. The diabatic potential is deduced from the adiabatic potentials resulting from *ab initio* calculations. The theory could be used directly on the adiabatic potentials, but this formulation is less amenable to calculation. The adiabatic and diabatic forms of the potentials, wavefunctions, and dipole moments have been shown to be connected via rotational transformations and the observables are independent of the representation[7].

The basic tool required for the renormalized Numerov method is the matrix,

$$T_n = \left(\frac{\mu h^2}{6\hbar^2}\right) \begin{vmatrix} V_{11} - E & V_{12} & V_{13} & \ldots \\ V_{21} & V_{22} - E & V_{23} & \ldots \\ \vdots & & & \end{vmatrix} \quad , \tag{A.17}$$

where μ is the reduced mass and n is the n^{th} step h units long, out from the start point. The unit system selected for this work was S.I. The diagonal elements include the diabatic potentials and may include rotational energy functions (Eq. A.15). The off-diagonal elements contain the perturbations. T_n is then used to calculate U_n for each point using,

$$\begin{aligned} W_n &= I - T_n \quad , \\ U_n &= 12W_n^{-1} - 10 \quad . \end{aligned} \tag{A.18}$$

We then get a ratio matrix R_n from the iteration outwards,

$$R_n = U_n - R_{n-1}^{-1} \quad , \tag{A.19}$$

and inwards,

$$\hat{R}_n = U_n - \hat{R}_{n+1}^{-1} \quad . \tag{A.20}$$

[3] This technique has lower error per step than alternatives such as the Euler method.

In both cases, care must be taken to select a suitable initial value of R that is consistent with the boundary conditions. The wave function may then be iterated by the following formula;

$$\Psi_n R_n = \Psi_{n-1} \quad . \tag{A.21}$$

R_n gives a lot of information without the need to evaluate Ψ. For instance, R becomes negative at node points, equals unity at maxima, and is less than unity as the Ψ approaches zero in a barrier.

For a single bound potential, as found in the starting states of He_2^+ and O_2 studied, a search is necessary to determine the eigen energy value by propagating the wavefunctions inwards and outwards, and then using the mismatch of gradients to guide a search for the correct energy. The bound wave function is then integrated and normalized.

For multiple bound potentials and a single open channel, the open channel is normalized at r $\rightarrow \infty$ to

$$(\frac{\mu}{8\pi^2\hbar^2 E})^{\frac{1}{4}} \quad . \tag{A.22}$$

The bound channels (0 at ∞) will automatically develop so as to be of the appropriate amplitude.

For multiple bound and open channels, the open channels have to be normalized, but also a complex phase factor has to be introduced, to match the wave functions to the inner boundary condition [40].

One characteristic of spectra involving mixed states is the proximity of the zeros in the cross section to the bound diabatic energy levels that is often observed. Taking the simple case of two interacting potentials (one of them bound) at a zero in the spectrum and in the dipole transition moment R, we have the following system of equations;

$$\begin{aligned} |R|^2 = 0 \Rightarrow D\Psi_1 + \Psi_2 &= 0 \quad , \\ H_1\Psi_1 - E\Psi_1 &= V_{12}\Psi_2 \quad , \\ H_2\Psi_2 - E\Psi_2 &= V_{12}\Psi_1 \quad , \end{aligned} \tag{A.23}$$

where D is the ratio of dipole transition moments to the ground state. Substitution yields,

$$H_1\Psi_1 - (E - DV_{12})\Psi_1 = 0 \quad . \tag{A.24}$$

E is DV_{12} above the uncoupled diabatic eigen state energy level. This establishes the connection between zeros in the spectrum and bound diabatic energy levels. This result is independent of the all-positive couplings or all-positive dipole transition moment convention adopted.

A.2.7 Initial data needed by the CSE technique

As indicated in the diagram Fig. A.1, potential curves have to be input to generate the theoretical cross sections. Matching the theoretical with the experimental spectra may be done in a iterative fashion to obtain semi-empirical potential curves. These curves may be derived from spectra using the more classical analysis described in the following sections. It can be seen from this that the CSE technique is an extension of the other analysis techniques.

The potential curves may also be computed *ab initio*, as was done for He_2^+ in Chapter 6 of this work. In future, proprietary quantum chemistry codes will be able to routinely calculate dipole transition moments. This procedure is indicated in the diagram, Fig 'A.1, however, in the current study the dipole moments are obtained by trial and error and assumed to be independent of R. The off-diagonal couplings are found by fitting theoretical trials to the experimental data.

A.3 Rydberg-Klein-Rees Analysis

In the discussion thus far, the shape of a potential is modified from its *ab initio* value such that it fits the experimental results. The Rydberg-Klein-Rees potential calculation technique constitutes a different method of analysis (albeit for bound states only) by calculating the potential directly from the position of vibrational lines, and the measurement of the rotational constants. Briefly, for a particular vibrational level, v_{max}, the minimum and maximum positions of a potential, r_{min} and R_{max} are given by;

$$(r_{max} - r_{min})/2 = f(v) = \frac{1}{2\pi}(\frac{h}{2\mu c})^{\frac{1}{2}} \int_{v_{min}}^{v_{max}} \frac{dv'}{[G_v - Gv']^{\frac{1}{2}}} \quad , \tag{A.25}$$

$$(\frac{1}{r_{min}} - \frac{1}{r_{max}})/2 = g(v) = 2\pi(\frac{2\mu c}{h})^{\frac{1}{2}} \int_{v_{min}}^{v_{max}} \frac{B_{v'}dv'}{[G_v - Gv']^{\frac{1}{2}}} \quad ,$$

where B is previously defined and $G_v = hw$. A more complete discussion is given by Tellinghiusen[92].

A.4 Rotational Band Analysis

Line positions in a band can be expressed as a series, with the coefficients dependent on the shape of the initial and final potential. An example of such a series is given for the energy levels of the P,Q, and R branches, the detailed definition of all the terms is given in Herzberg[86]:

$$
\begin{aligned}
\nu &= \nu_v + (B_{v'} + B_{v''})m + (B_{v'} - B_{v''} - D_{v'} + D_{v''})m^2 - 2(D_{v'} + D_{v''})m^3 - (D_{v'} - D_{v''})m^4 \\
m &= -J \; for \; \mathbf{P \; branch} \\
m &= J + 1 \; for \; \mathbf{R \; branch} \\
\nu &= \nu_v + (B_{v'} - B_{v''})J(J+1) - (D_{v'} - D_{v''})J^2(J+1)^2 \; for \; \mathbf{Q \; branch}
\end{aligned}
$$

where,

$$
\begin{aligned}
B_v &= B_e - \alpha_e(v + \tfrac{1}{2}) + \ldots \\
B_e &= \tfrac{h}{8\pi c I_b}, \text{ where } I_b \text{ is the average angular momentum} \\
\alpha_e &= -\tfrac{6B_e^2}{w_e} \\
D_v &= D_e + \beta_e(v + \tfrac{1}{2}) + \ldots \\
D_e &= \tfrac{4B_e^3}{w_e^2} \\
\beta_e &= D_e(\tfrac{8w_e x_e}{w_e} - \tfrac{5\alpha_e}{B_e} - \tfrac{\alpha_e^2 w_e}{24B_e^3}) \\
\nu_v &= w_e(v + \tfrac{1}{2}) + w_e x_e(v + \tfrac{1}{2})^2 + \ldots \quad .
\end{aligned}
\tag{A.26}
$$

Further modifications have been included[86] to account for spin splitting and Λ doubling. The lines are shifted overall by an additional term, $-B_v\Omega^2$. Although this term is usually included in the ν_o which is spectroscopically measured, it is not included in the *ab initio* calculations. It may be seen from the higher order terms in the various branches that there may be several band-heads, where bands turn back upon themselves. This series formulation may be characterised, without the attendant physical insight, by

$$
\sum_{lm} Y_{lm}(v + \frac{1}{2})^l (J(J + \frac{1}{2}))^m \quad . \tag{A.27}
$$

The series approximation has the advantage that a potential may be characterised by a few terms $(w_e, w_e x_e, B_e, \alpha_e)$, which themselves characterise physical concepts. All these terms are average values and not functions of internuclear separation.

A.4.1 The effect of a Fano profile and band modelling

The series expansion for the position of lines enables the construction of a band using lines that have intensities described by the Boltzmann energy distribution and the Hönl-London factors, and that are of a Fano line profile shape. Although the individual lines may not be resolvable, the band profile will display an accumulated enhancement or suppression, due to the Fano profile. Naturally, these Fano line profiles, which are determined by the coupling between states, are included in the band modelling for an adequate fit to be obtained. These profiles are automatically produced by the use of the coupled Schrödinger wave equation technique and its relationship with Fano's original theory is described in a paper by Torop[93].

Normally, band models may require the following constants:

B/	- ground state values are usually known
B//	
D/	
D//	
ν_0	
Temperature	- several values
Q	- Fano profile parameter
Oscillator strength	
a	
b	- coefficient of the underlying continuum
c	

With current computers (DEC 3000), both band analysis and rotationless coupled Schrödinger wave equation techniques take a matter of minutes, while the generation of one complete theoretical spectrum – with the rotation included – by the coupled Schrödinger technique, takes approximately twelve hours (see Fig. 4.1). This time will reduce with better codes and faster computers.

A.5 Conclusion

An overview of spectrum calculation technique used in Part I and Part II of this thesis has been given. Particular attention has been given to identifying the role of the Born-Oppenheimer Approximation and the selection of a basis set in simplifying the calculations. With the revolution of increased computing power, there is a corresponding extension in type of spectra that may be analysed.

Appendix B

Laser Patent

A LASER

This invention relates to a laser. It relates particularly to a laser in which the gain medium consists principally of a noble gas.

A laser comprises a means for the controlled excitation and de-excitation of particles in a gain medium in such a way that the de-excitation is accompanied by the emission of highly coherent electro-magnetic radiation (light). The operation of a laser generally depends upon the ability of the individual particles of the gain medium to adopt at least three separate energy states. The first energy state is an excited state which is sufficiently stable to allow a substantial number of particles to achieve that energy level simultaneously. The second energy state is a lower energy state than the first and is generally unstable to enable a low concentration of that species. In the process of stimulated emission, photons of an energy equal to the energy difference between the first and second energy level, can induce a transition from the first state to the second state that produces a second photon of identical wavelength. As this stimulated emission process is proportional to the number of photons, the medium amplifies the light. The rate of stimulated emission is therefore dependent on the amount of particles in the first energy level and the number of photons of the appropriate energy into the medium.

However, because the photons are capable of being absorbed by particles in the second energy state, reinstating the particles to the first energy state and

deminishing and preventing amplification of the light, it is desirable that the second energy state be unstable so that the particles quickly decay to a third energy state which is transparent to the photons.

In order to achieve lasing, it is important to provide conditions which favour stimulated emission of radiation as previously described, rather than spontaneous emission. This is commonly achieved by setting up standing waves in the gain medium at the wavelength of the photons emitted by the relevant energy state transitions to increase the number of photons of the relevant wavelength. Such standing waves are normally created by positioning reflective elements at opposite ends of the gain medium. The elements may be planar and parallel, they may be confocal and spherical, or they may be any other suitable configuration. The elements are generally constructed or coated to be selectively reflective of photons of the relevant wavelength. This permits the elements to confine radiation of the appropriate wavelength while allowing transmission of radiation of other wavelengths.

Transmission of laser radiation from such a system is usually effected either by allowing transmission of about 2% of radiation of the relevant wavelength through one of the reflective elements or by inserting a beam-splitting element between the two existing elements to split out approximately 2% of the radiation.

The energy level transitions which are useful particularly for gaseous atomic lasers in producing laser radiation usually result in the production of photons

having a wavelength range of a few Ångstroms. It is possible to tune the wavelength of the standing wave within this wavelength range to ensure that the laser radiation produced has a specific wavelength. Numerous different techniques are available for tuning of the wavelength. These include the use of prisms such as those described in Australian patent 284799, or the use of filters and diffraction gratings, such as lithrow mount diffraction gratings. Another suitable means for tuning comprises the use of another laser, which is already providing laser radiation of the desired wavelength, as incident radiation. Providing that the incident radiation is within the available wavelength range, the standing wave will then tend to adopt an identical wavelength.

However, the ability to tune a laser is limited by the range of wavelengths which the relevant energy level transition is capable of producing, and this range is generally very small, particularly those involving atomic energy levels.

Lasers whose gain medium is a combination of gases have been known for some time. Australian patent number 254702 describes in some detail examples of such lasers, including in particular lasers the gain medium of which is a combination of helium and neon.

The helium-neon laser takes advantage of the fact that helium has a metastable excited energy level (2^3S_1) corresponding with an excited energy level of neon ($2s_5$). Neon also has a lower energy level ($2p_9$), and the transition between the two energy levels of neon is the relevant one for the purposes of lasing.

When the mixture of unexcited helium and neon is placed in a radiation field so that partial ionisation of helium occurs, free electrons of relatively high energy are produced. These free electrons, by collision processes, excite to higher states un-ionised atoms predominantly of helium but incidentally also of neon. In particular, atoms of helium tend to be excited predominantly to the 2^3S_1 level either directly or by relaxation to that state from a higher state to which they were excited. When the excited helium atoms collide with ground state neon atoms, some neon atoms are excited to the $2s_5$ state because transfer excitation occurs between colliding atoms whose energy levels are closely matched, so that there is established a population inversion or negative temperature between the $2s_5$ state and the $2p_9$ state of the neon gas, and this permits the stimulation of emission of radiation.

However, the helium-neon lasing process is inefficient for a number of reasons. The major inefficiencies are attributable to the energetic electrons created by the ionisation of helium, inhibiting the efficient formation of the desired population inversion by promoting reactions which increase the number of neon atoms at levels other than the $2s_5$ state or by accelerating reactions which tend to restore the system to equilibrium.

Australian patent number 254702 sought to overcome these inefficiencies by pulsing the radiation used to cause the ionisation of helium so that the creation of high energy free electrons is periodic and the lifetime of

helium atoms in the 2^3S_1 level is longer than the lifetime of the free electrons. By appropriate choice of pulsing parameters it is possible to induce stimulated emission which approximates continuous lasing, but true continuous lasing is never achieved and the helium-neon laser remains inefficient.

Another type of commonly used gas laser is the excimer laser. This type of laser uses as its gain medium a noble gas in conjunction with a halide gas, and produces photons which are in the ultraviolet range. Examples of excimer lasers are lasers which comprise neon and chlorine or xenon and fluorine. Such lasers produce only a narrow range of wavelengths, typically having a range of about 1Å. Excimer lasers suffer the disadvantage that the halide gases have a corrosive effect on the vessel in which they are contained, so that frequent restoration or replacement of the vessel is necessitated. In practice, this occurs after about ten days of continuous operation. The gases are also dangerous, requiring special ventilation for the apparatus.

The operative particles creating the laser effect in excimer lasers are short-lived molecules comprising a combination of noble gas atoms and halide gas atoms. These molecules are formed in the afterglow of an electrical discharge or other suitable means of excitation, so that the laser operates as a series of pulses, each pulse comprising electrical discharge followed by a formation of molecules, followed by de-excitation and emission of laser radiation. These molecules have an unbound lower state which quickly

decays, enabling population inversion.

Another type of gas laser is the neutral dimer laser. Neutral dimer lasers involve the combination of a noble gas atom in the ground state and a further atom of the same noble gas in an excited state to form a molecule.

They have been demonstrated for most noble gases in pulsed afterglow and molecular beam techniques. They have large tuning ranges but only operate in comparatively low energy conditions, limiting their efficiencies.

No Neutral Helium Dimer laser has yet been demonstrated. It is thought that the lifetime of the molecule He_2 is too short to enable lasing in afterglows or molecular beams.

It is an object of the present invention to provide a laser, the wavelength of which can be tuned over a broad range. A further object is to provide a laser which is capable of continuous operation. A further object is to provide a laser which is powerful and efficient.

According to the present invention, there is provided a laser which uses dimer ions of a noble gas as its gain medium.

The preferred laser excitation means is an electrical discharge, and indeed any suitable means of excitation including microwave radiation and particle beam excitation may be used.

The noble gas used in the present invention may be any noble gas including helium, argon, xenon or krypton.

It is preferred that the laser of the present invention be capable of operation at high temperatures, because it has been found that noble gas dimer ions form

more readily at high temperatures (activation energy $\approx$ 1 eV) which allow for a high degree of efficiency. To this end, it is preferred that the active medium be contained within a ceramic, graphite or other refractory material vessel which is capable of withstanding high temperatures, rather than a conventional water-cooled glass vessel.

The invention will now be described in more detail with particular reference to an embodiment which uses the helium dimer ion, although it is to be understood that the invention relates to the use of any noble gas dimer ion.

Figure 1 of the drawings is an energy level diagram showing a plot of energy against inter-nuclear separation for a helium atom and a He^+ ion.

Figure 2 is a schematic representation of laser apparatus embodying the present invention.

It has been discovered that the afterglow of an electric discharge in a noble gas may give rise to the existence of noble gas dimers, consisting of two atoms of a noble gas, in an excited state which provides a suitable first state for a laser pulse emission as described above. The feasibility of a helium neutral dimer laser has been described in an article by Hill entitled "Ultraviolet Continua of Helium Molecules", published after the priority date of this specification in Physics Review A 1989, Volume 40, page 5004. Neutral dimer lasers have been demonstrated in xenon, argon and neon.

However, such dimer lasers have not yet been commonly used because of practical difficulties such as providing a sufficient population of the dimer in the afterglow of the electrical discharge, requiring the use

of expensive and exotic relativistic electron accelerators (Wrobel, Appl Phys. Let. Vol. 136, page 113, 1980).

The present invention results from the discovery of a new energy state in a noble gas dimer ion which is actually formed during the electric discharge, rather than in the afterglow. The presence of this new energy state was determined by the present inventor's analysis of experimental results, such as those given in "New Vacuum - Ultraviolet Emission Continua of Helium produced in High-Pressure Discharges", by R E Huffman, Y Tanaka and J C Larrabee, published in the Journal of the Optical Society of America, Volume 52 No. 8 (August 1962) (high energy pulse form); D Simon and K Rodgers, J. Appl. Phys. 37,2225 (1966) (continuous operation); and Y Tanaka, A Jursa and F LeBlanc, J. Opt. Soc. Am. 8,304 (1958) (low energy continuous operations).

In the energy level diagram of Figure 1, the higher energy state, having $^2\Pi_u$ symmetry and referred to in this description and for the purposes of the claims as the $C^2\Pi_u$ state, is the newly discovered energy state. The lower energy state is labelled $A^2\Sigma_g^+$. The $C^2\Pi_u$ state is bound when the inter-nuclear separation is between 0.4 and 1.2 Å so that in this region a comparatively stable molecule is formed. The $C^2\Pi_u$ state represents the interaction of an He^+ ion with a helium atom excited to the 2^3P level. Upon absorbing a photon with wavelength between 2500 and 10000 Å, the dimer ion decays to the $A^2\Sigma_g^+$ state, emitting 2 photons having wavelengths identical to that of the incident photon. As the $A^2\Sigma_g^+$ state is an unbound state,

the He^+ molecule rapidly decays into individual He^+ and He atoms, thus becoming transparent to the photons. The symbolic representation of the process is as follows:

1. $He^+ + He(2^3P) + He \longrightarrow He_2^+(C^2\Pi_u) + He.$

2. $He_2^+(C^2\Pi_u) + n\nu(2500\text{-}10000\text{Å}) \longrightarrow He_2^+(A^2\Sigma_g^+) + (n+1)\nu(2500\text{-}10000\text{Å})$

3. $He_2^+(A^2\Sigma_g^+) \longrightarrow He^+ + He + K.E.$

As can be seen from equation 1, the formation of the excited dimer ion occurs in the presence of another helium atom (any ion, electron or neutral or multiple particle which can remove momentum) which absorbs momentum, allowing the dimer ion to settle in the bound state. Equation 2 shows the stimulated emission of the excited helium dimer ion from the $C^2\Pi_u$ state to the $A^2\Sigma_g^+$ state in the presence of photon radiation having wavelength between 2500 and 10000Å with the accompanying emission of a further identical photon. Equation 3 shows the rapid decay of the $A^2\Sigma_g^+$ state into He^+ and He atoms.

This reaction is particularly favoured in high pressure high current discharges (arcs). In arcs the temperatures of all particles approach the same value, and the temperature of the gas increases to many thousands of degrees. This provides the particles with the activation energy necessary to produce the $C^2\Pi_u$ molecule. The reaction may be seen in overview as:

4. $He^+ + He(2^3P) + He \longrightarrow He^+ + He + He + \nu$.

In other words, the Helium ions in the high temperature conditions of an arc act as a catalyst to liberate the energy trapped in the excited states of Helium. This process is highly efficient and operates at high power densities.

The transitions described above provide the explanation for the continuous emission spectrum observed in the range 2500 to 10000Å for helium, as described in the article by Huffman, Tanaka and Larrabee referred to above. It will be appreciated by those familiar with lasers that this is a considerably broader emission spectrum within which the laser is tuneable than any previous laser emission spectrum, so that access may now be had to regions of the spectrum that could previously only be accessed by non-linear light-mixing techniques which were very inefficient (less than 0.1% efficient). Dyed liquids and solids can have broad ranges but can only be pumped with limited power, mostly using light as the excitation source. The present invention, on the other hand, provides a laser which may achieve greater than 50% efficiency. This may be seen by the fact that over 50% of the light given off in Huffman's experiment is continuum, the remainder being line. As the present invention uses the molecule which produces the continuum, it can use more than 50% of the available light.

Further, by a process of radiationless symmetry transition wavelengths around 300-600 Å may be achieved using the $X^2\Sigma_u^+$ ground state of He_2^+.

As the He_2^+ molecule in the $C^2\Pi_u$ state is produced in very high power output conditions, the laser of the present invention is capable of converting very large quantities of energy into laser radiation. Excimers, on the other hand, deteriorate very quickly when the energy input is increased significantly.

It is preferred that the pressure of the noble gas which forms the gain medium for the laser be approximately 2 atmosphere. The pressure may be any other suitable amount, but should in any event be greater than 200 Torr in order for the invention to work in an appropriate manner. It is further preferred that there be provided appropriate valves gauges and vacuum pump to ensure the desired pressure and purity of noble gas.

The preferred means for exciting the gain medium comprises a cathode and an anode one of which is connected to a capacitor which sends an electrical discharge through the active medium once the capacitor has reached the breakdown voltage of the active medium. Other suitable means for exciting include microwave excitation means, particle beam excitation means, flashlamp excitation means, and Tesla coils.

Because the reactions which cause the present invention to work occur during the excitation of the noble gas, rather than in the afterglow, the laser of the present invention may be subjected to continuous excitation and may provide a continuous laser pulse, provided that a sufficiently large quantity of power is available for excitation. Alternatively, the laser of the present invention may be operated in pulses by means of a

capacitor of approximately 1 microfarad, charged to approximately 30 kV, although these figures are arbitary. Ideally, the capacitor discharges along transmission lines, designed to have no impedance mismatches, when the voltage reaches such a value that an electrical discharge occurs between anode and cathode.

As an optional feature, there may be provided means for tuning the laser of the present invention, taking advantage of the broad spectrum of the noble gas dimer ion so that the laser may be tuned to operate at any wavelength within that spectrum. One suitable means for tuning is the use as incident radiation of a laser of a set wavelength within the noble gas dimer ion spectrum. The laser of the present invention will then adopt the wavelength of the input laser and amplify the incident light.

Another suitable means for tuning involves the use of filters and diffraction gratings, such as lithrow mount diffraction gratings. These may be placed according to known techniques between a mirror and the gain medium in order to feed the desired wavelength back into the active medium, ensuring that the desired wavelength becomes the one which is amplified.

If no means for tuning the laser other than the use of mirrors is used, or the active length is sufficiently long that no mirrors are required, the laser will operate at its natural wavelength of approximately 6050 Å, as evidenced by calculation and the observation of gain narrowed emission seen in Huffman's experiment.

According to the embodiment represented in Figure 3,

a noble gas such as helium is contained at a pressure of approximately 2 atmosphere within refractory discharge guide c. Refractory discharge guide c is bounded at one end by polished aluminium block mirror a and at the other end by partially transmitting mirror e.

Arranged at separate ends of refractory annular discharge guide c are cathode b and anode d. Anode d is electrically grounded, while cathode b is electrically connected to pulsed capacitor f. Pulsed capacitor f is in turn connected both to ground and via limiting resistor g to 30 kilovolt DC power supply h.

As will be seen from the foregoing, the present invention provides a laser which may be tuned within a broader range of wavelengths than any previous laser. It further provides a more efficient laser and a laser capable of continuous operation.

It is to be understood that various alterations, modifications and/or additions may be introduced into the constructions and arrangements of parts previously described without departing from the spirit and ambit of the invention.

CLAIMS:

1. A laser which uses dimer ions of a noble gas as its gain medium.

2. A laser according to claim 1 wherein the gain medium is Helium dimer ions.

3. A laser according to claim 2 wherein the radiation emitted by the laser results predominantly from the transition of He_2^+ molecules from the $C^2\Pi_u$ energy state (as hereinbefore defined) to a lower energy state.

4. A laser according to claim 1 wherein the gain medium is Neon Argon or Xenon dimer ions.

5. A laser according to any one of claims 1 to 4 further including means for tuning the wavelength of the laser radiation.

6. A laser according to any one of claims 1 to 5 wherein the gain medium is housed within a chamber constructed from a refractory material.

7. A laser according to claim 6 wherein the refractory material is a ceramic or graphite.

8. A laser according to any one of claims 1 to 7 wherein excitation of the gain medium occurs by means of periodic electrical discharge between two electrodes, with energy being accumulated in one or more capacitors between each discharge.

9. A laser according to any one of claims 1 to 7 wherein excitation of the gain medium occurs by means of continuous electrical discharge.

10. A laser substantially as herein described with reference to Figure 1 and/or Figure 2.

ABSTRACT

It has been discovered that short-lived dimer ions are created in a noble gas under high energy conditions, such as during an electrical discharge. These noble gas dimer ions have excited energy states which make them suitable for use as the gain medium in a laser. A laser created using noble gas dimer ions as the gain medium exhibits a high degree of efficiency, is tunable over a broad range of wavelengths, and may be capable of being operated continuously.

1766v

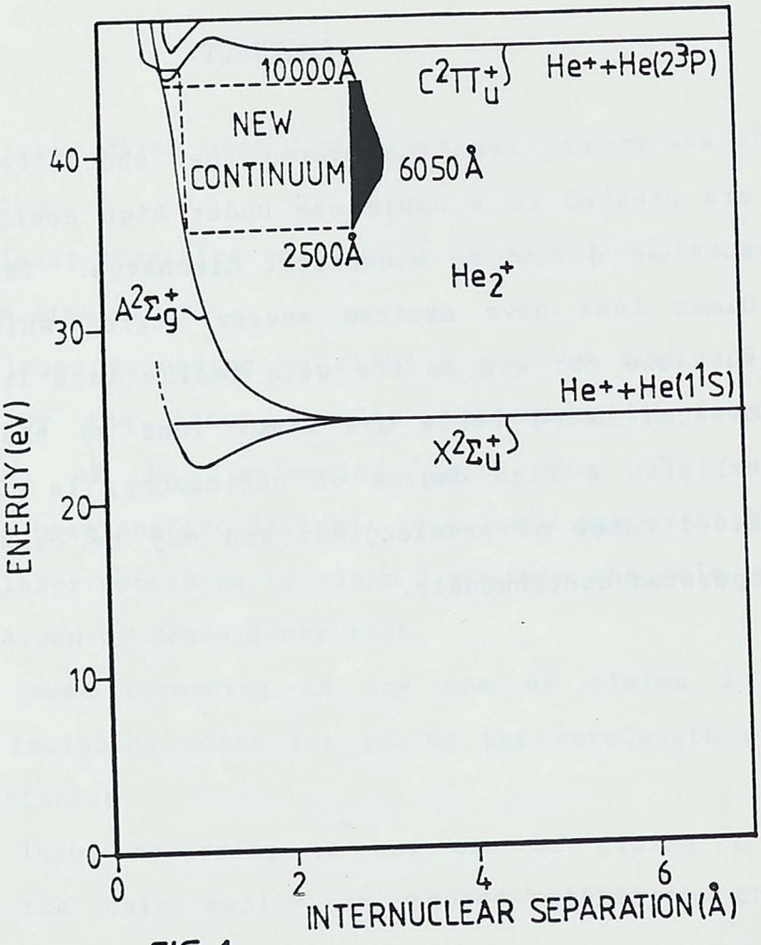
10000Å
$C^2\Pi_u^+$
$He^+ + He(2^3P)$
NEW
CONTINUUM
6050 Å
2500Å
He_2^+
$A^2\Sigma_g^+$
$He^+ + He(1^1S)$
$X^2\Sigma_u^+$
ENERGY (eV)
40
30
20
10
0
0
2
4
6
INTERNUCLEAR SEPARATION (Å)

FIG 1

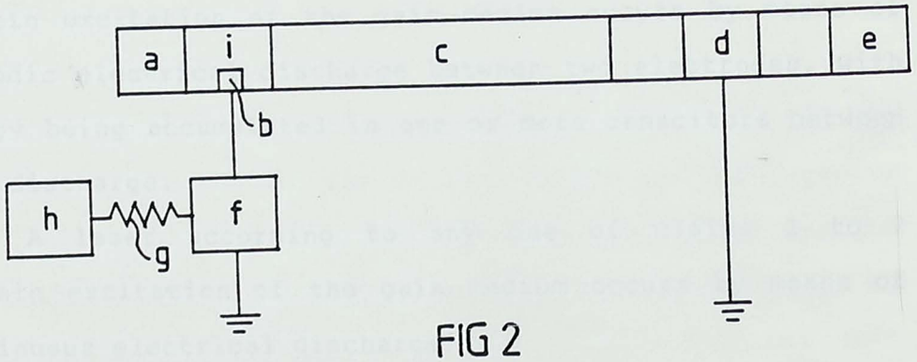
a
i
c
d
e
b
h
f
g

FIG 2

Appendix C

Additional Oxygen Results

Some 75 000 data points where collected, covering far more features that could be properly dealt with in the scope of this study. Some of the additional scans, taken in the region from 1270 Å to the lithium fluoride cutoff, are presented here. Where possible, scans were taken at a number of pressures as a means of checking for saturation effects. For ease of reference the diagram symbols are explained below, a description of each spectrum is given in sequence, and then the spectra themselves are presented.

Key to Figures

circle – Ogawa and Ogawa[10]
line – This work
vertical line – Photograph line positions reported by Yamawaki [14]

Broad Survey Scans

Scans where taken in sequence from short to longer wavelengths. Conditions for all scans were the same: 3 Torr pressure, LiF windows and 6 watts of microwave power. Regions for which the ground state cross section is above 15 $\times 10^{-19}$ cm ^{2} were of too low transmission, and hence inaccurate.

Fig C.1: Metastable Cross Section 1190 – 1270 Å.

Fig C.2: Ground Cross Section 1190 – 1270 Å.

Fig C.3: Metastable Cross Section 1090 – 1190 Å.

Fig C.4: Ground Cross Section 1090 – 1190 Å.

Individual Bands

Features that exhibit structure in the broad survey scans were investigated in more detail. Regions for which there was high ground state absorption where remeasured at lower pressures.

Fig. C.5:Metastable Cross Section 1254.5–1270 Å. There is a window resonance near 1255Å. In the region between 1258 Å and 1267 Å there may be three or more separate bands. The perturbation of every second rotational line in the region 1258 – 1262 Å may be due to a Σ state for which every second line is missing. Another band system may be seen near 1268 Å.

Fig. C.6: Cross Section with microwave on/off for the 1244Å band. The lower line represents the absorption cross section of ground state oxygen. The two lobes are the P and R branches of the 1244 Å band. Because of the high cross section a 10% mix of oxygen in argon is used giving a partial pressure of 0.1 Torr. The upper line corresponds to the total cross section with the microwave excitation and shows that there is a metastable state band almost identical to the ground state band. The use of standard operating conditions allowed the percentage of metastables and the scaling factor to be deduced from scans other wave length regions.

Fig. C.7: Metastable Cross Section for the 1244 Å band. Ogawa and Ogawa's [10] quantitative measurements confirmed the presence of this band which was rotationally resolved by Yamawaki[14]. This current study goes further by measuring band profiles, that are consistent with the line positions reported by Yamawaki.

Fig. C.8: Metastable Cross Section for the 1239 Å feature. This weak feature has not previously been specifically reported.

Fig. C.9: Metastable Cross Section for the 1229 Å feature.

Fig. C.10: Metastable Cross Section for the 1205 Å feature. The solid line corresponds to the spectrum taken at 3 Torr while the broken line corresponds to 0.3 Torr. Although there is larger statistical errors for the low pressure scan, there is evidence for a band at 1205 Åthat is not seen at higher pressures due to the reduction in transmission caused by a ground state band in this region.

Fig. C.11: Rotational Structure at 1195Å. This rotational structure has not been previously reported for this region.

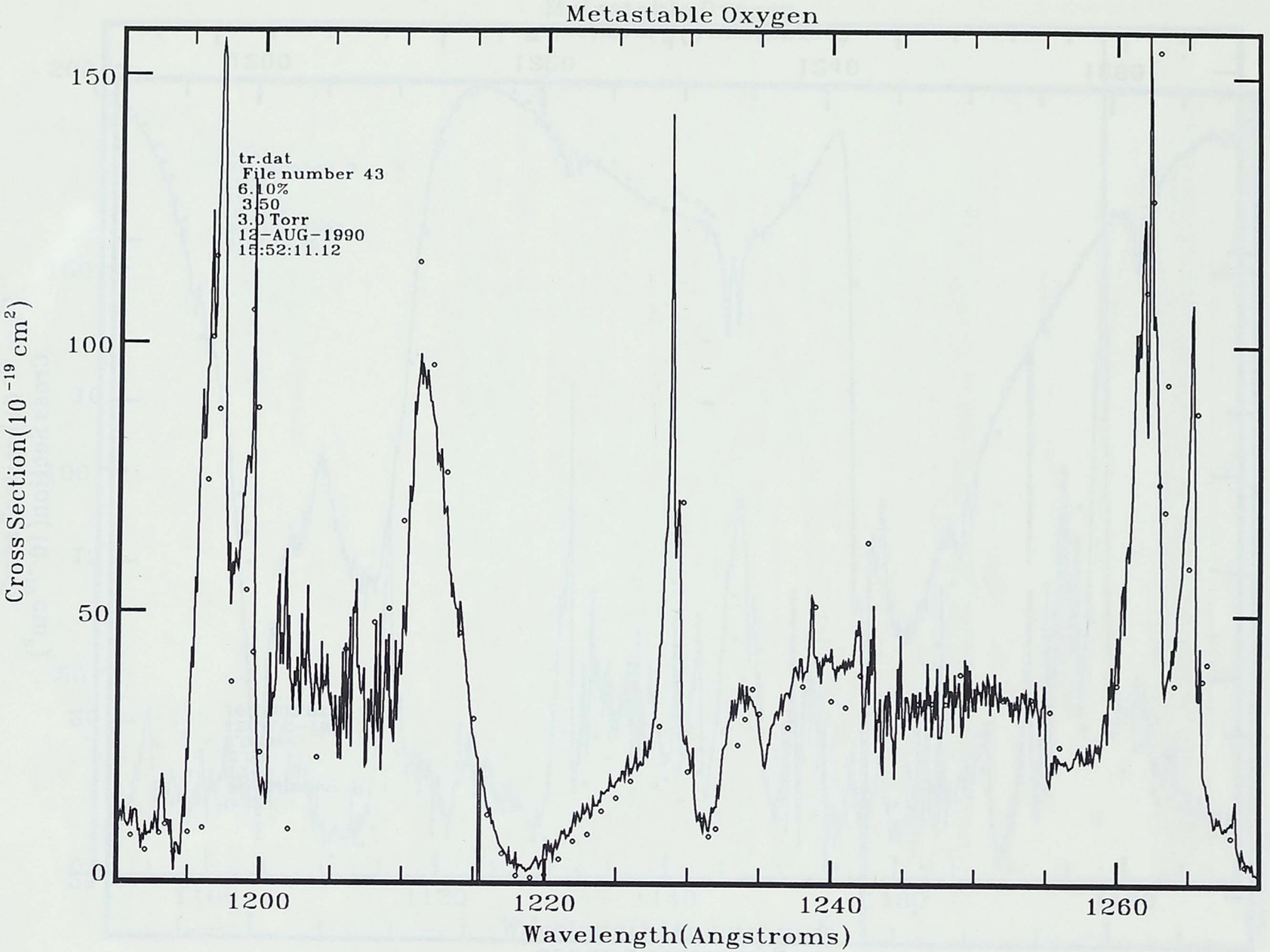
Metastable Oxygen
tr.dat
File number 43
6.10%
3.50
3.0 Torr
12-AUG-1990
15:52:11.12
Cross Section(10 -19 cm2)
150
100
50
0
1200
1220
1240
1260
Wavelength(Angstroms)

Figure C.1:

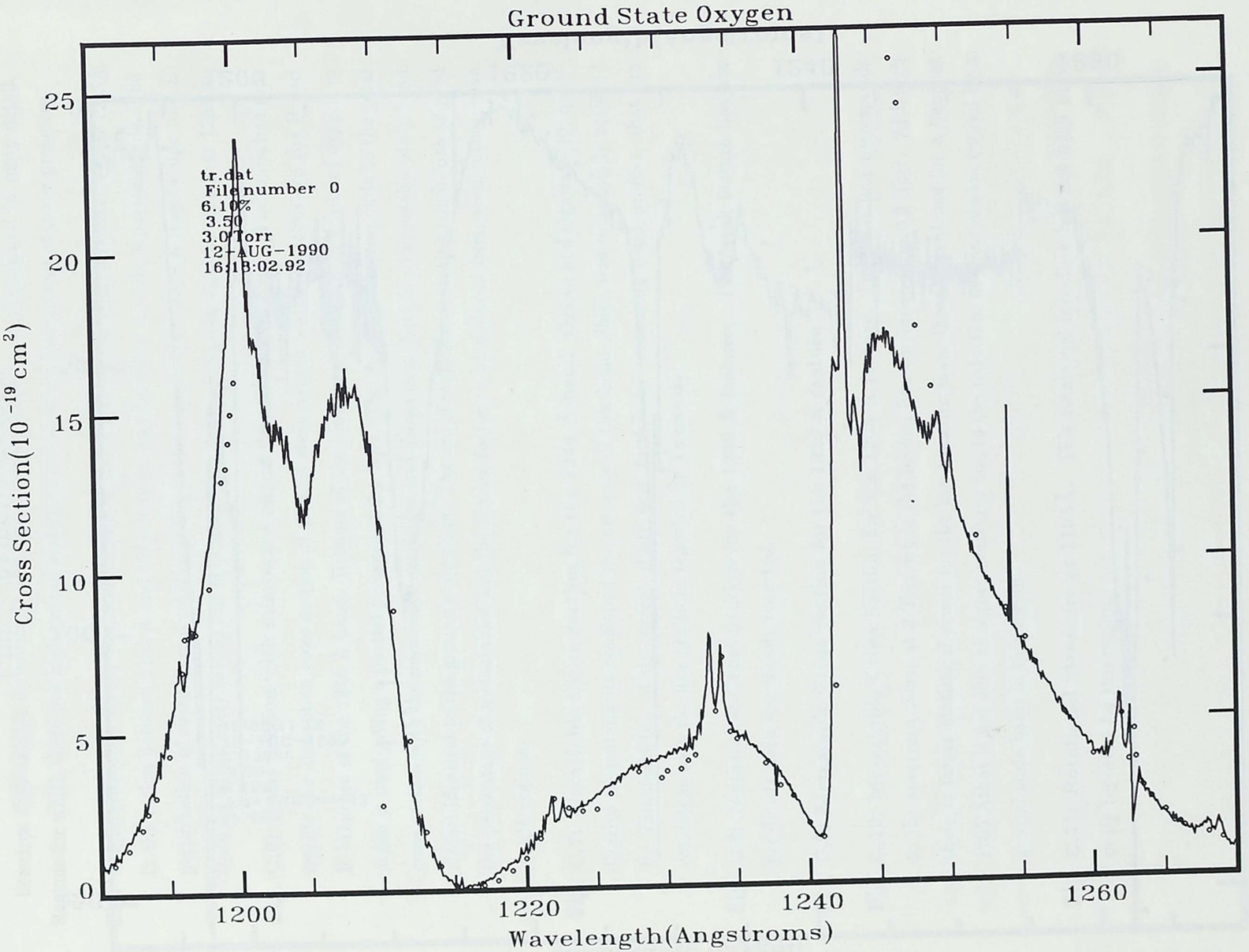
Ground State Oxygen
tr.dat
File number 0
6.10%
3.50
3.0 Torr
12-AUG-1990
16:13:02.92
Cross Section(10^{-19} cm^2)
0
5
10
15
20
25
1200
1220
1240
1260
Wavelength(Angstroms)

Figure C.2:

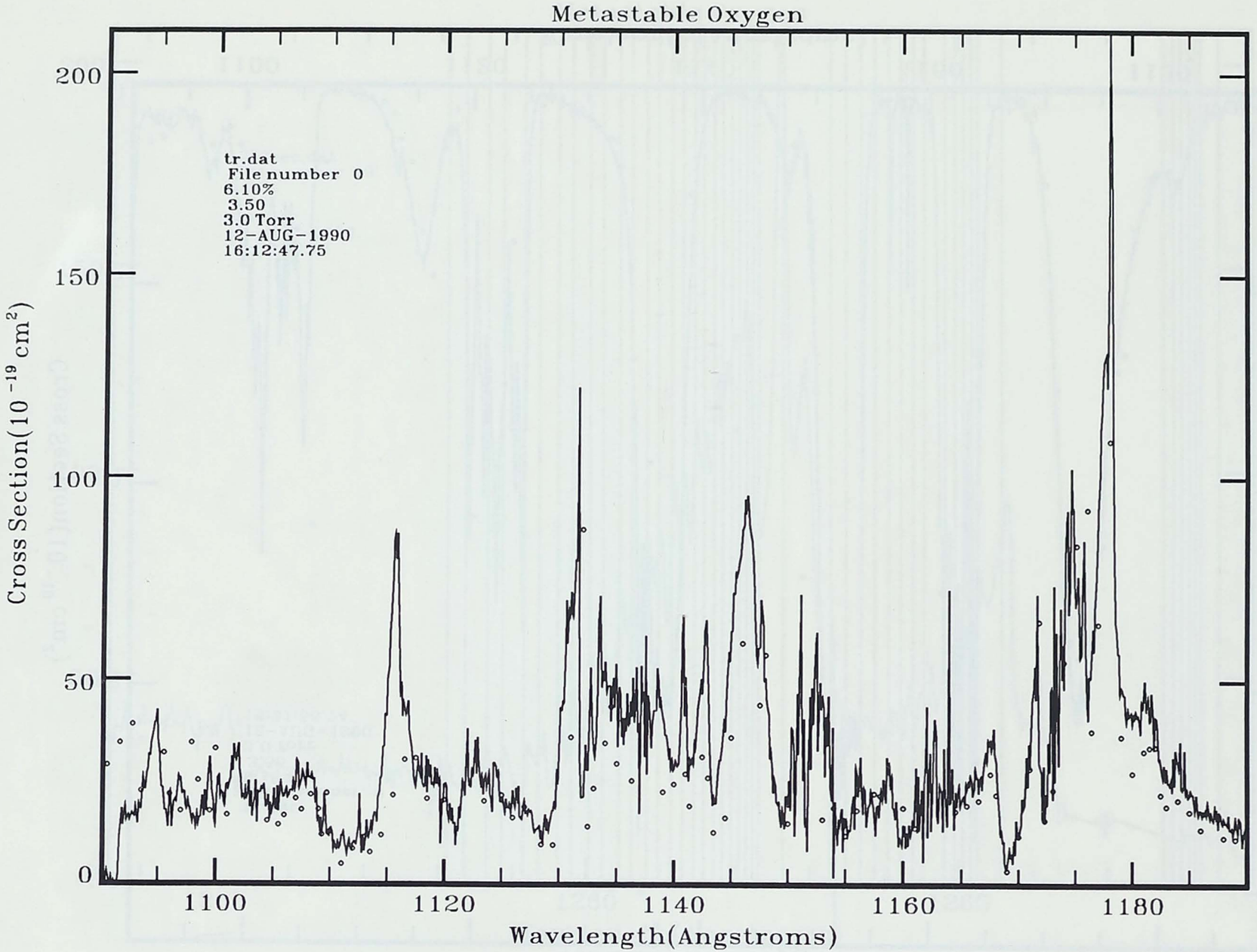

Figure C.3:

Ground State Oxygen

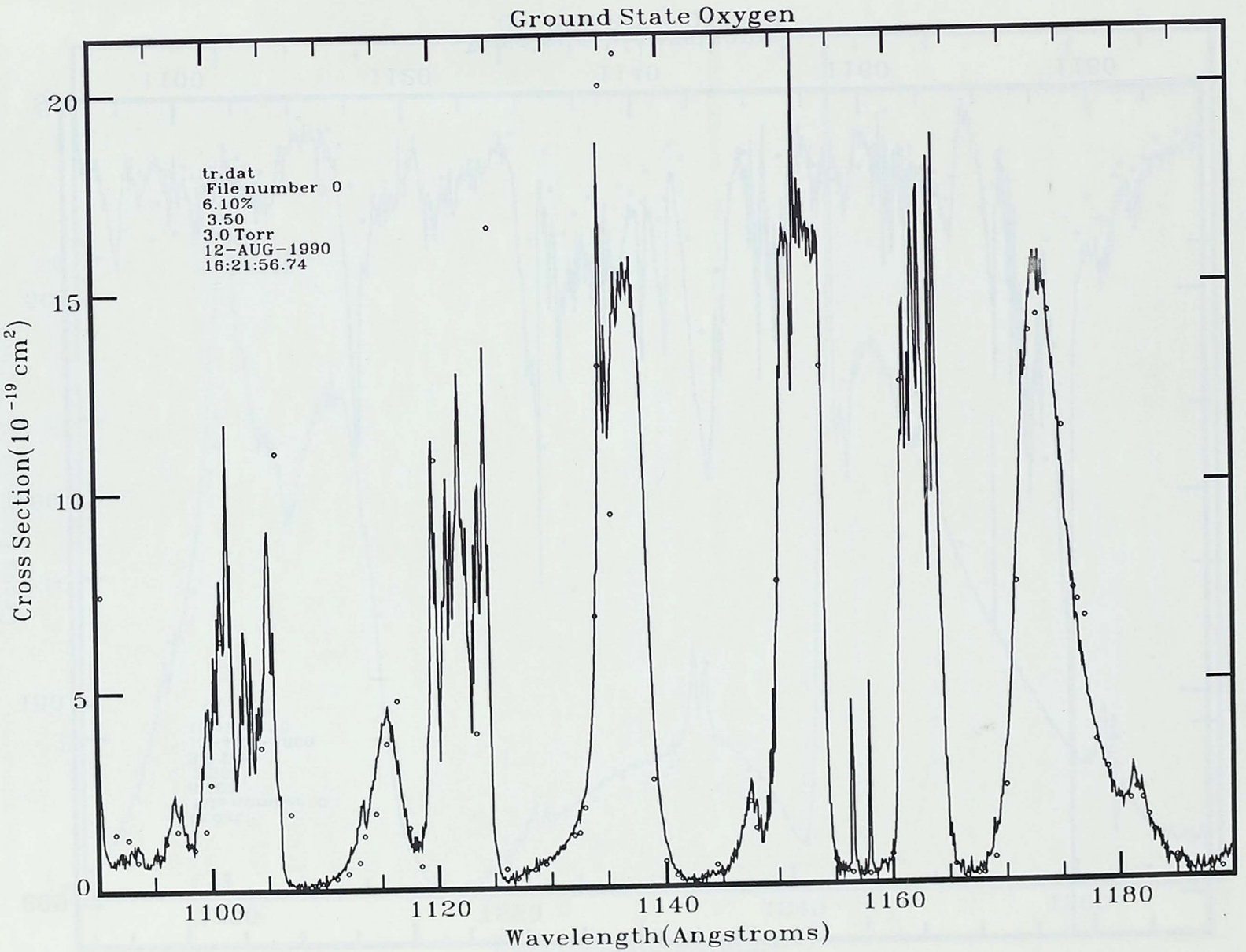
Ground State Oxygen
tr.dat
File number 0
6.10%
3.50
3.0 Torr
12-AUG-1990
16:21:56.74
Cross Section(10^{-19} cm^2)
0
5
10
15
20
1100
1120
1140
1160
1180
Wavelength(Angstroms)

Figure C.4:

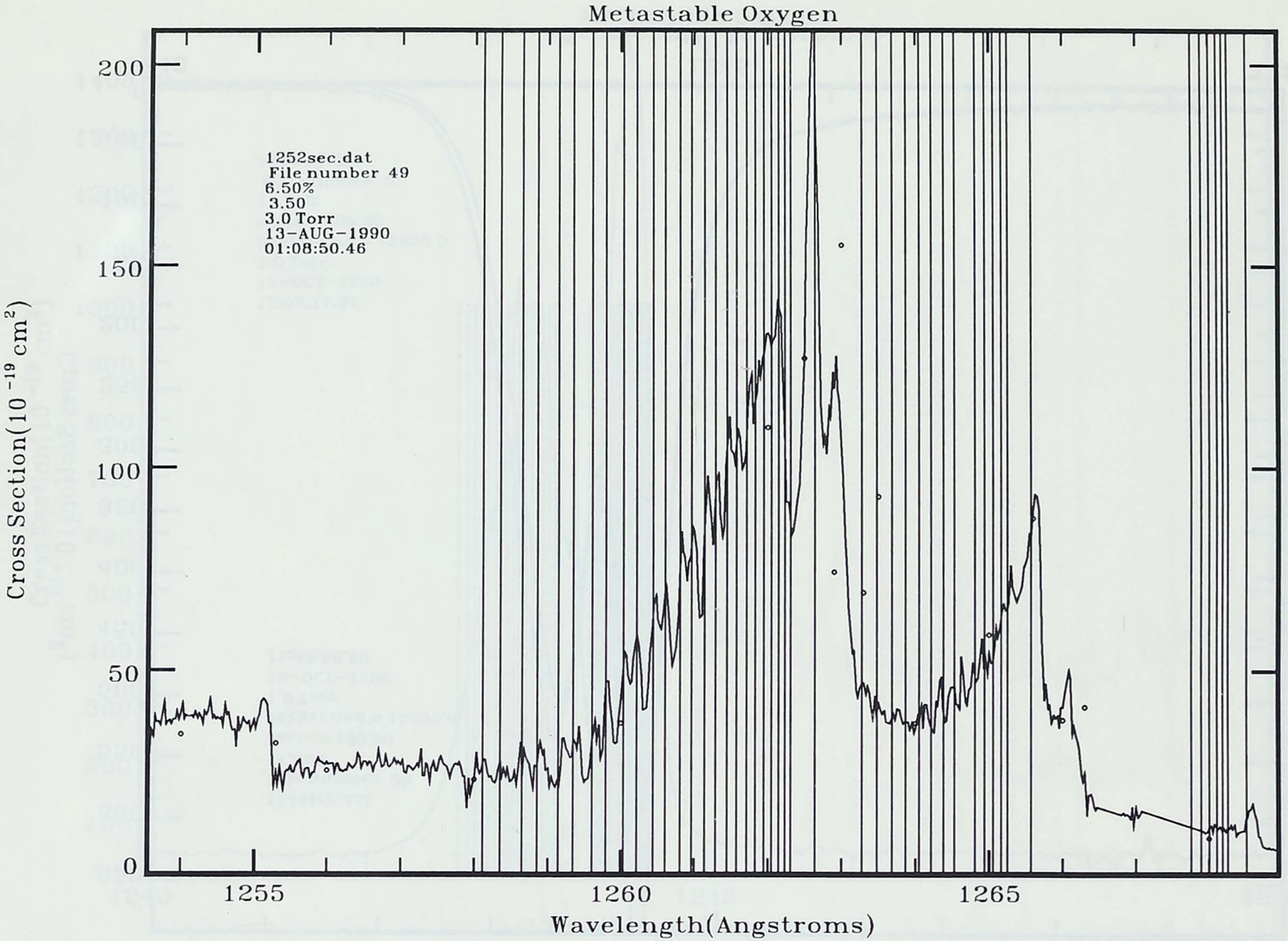

Figure C.5:

Ground State Oxygen

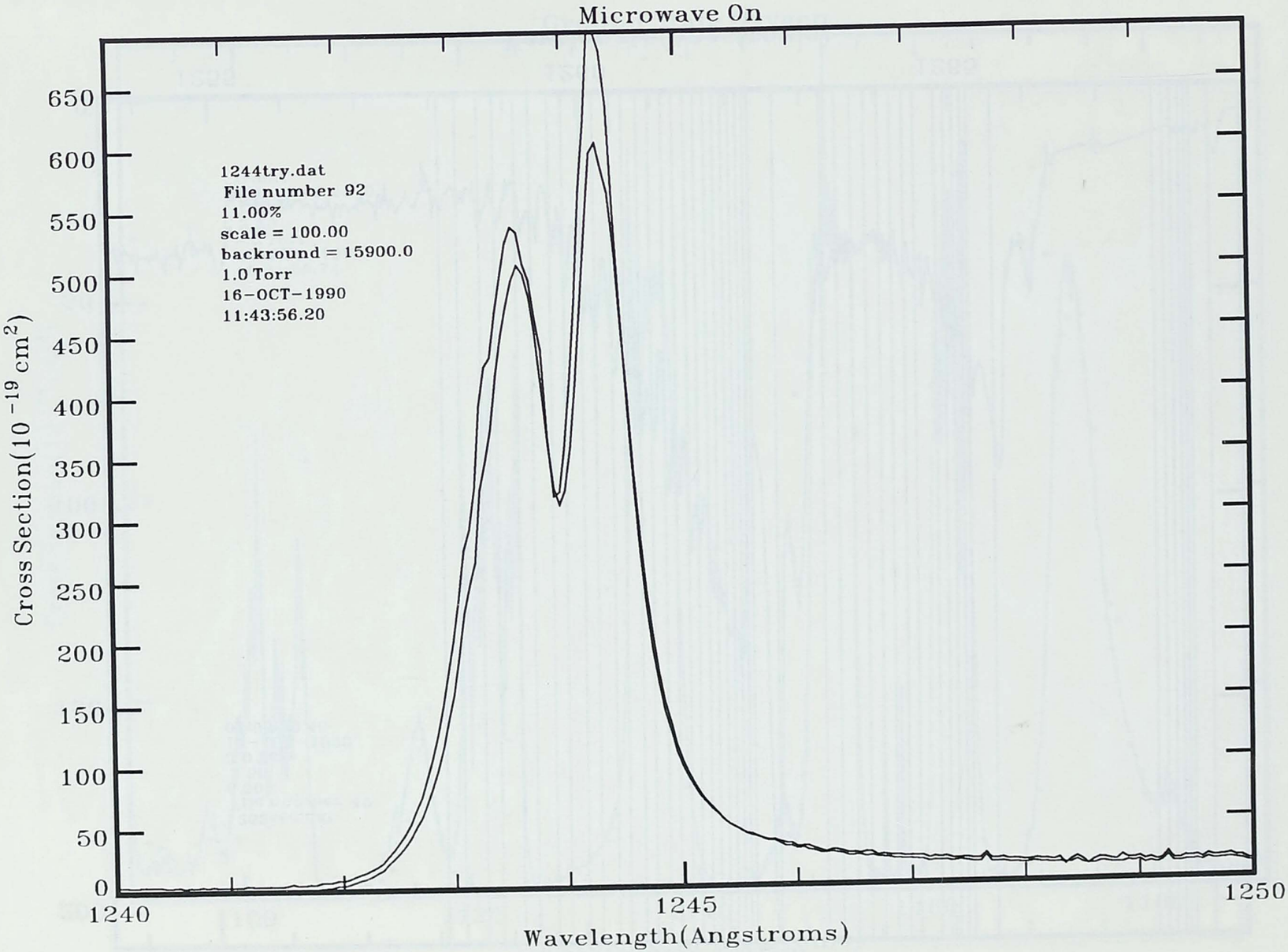
Microwave On
1244try.dat
File number 92
11.00%
scale = 100.00
backround = 15900.0
1.0 Torr
16-OCT-1990
11:43:56.20
Cross Section(10^{-19} cm^2)
650
600
550
500
450
400
350
300
250
200
150
100
50
0
1240
1245
1250
Wavelength(Angstroms)

Figure C.6:

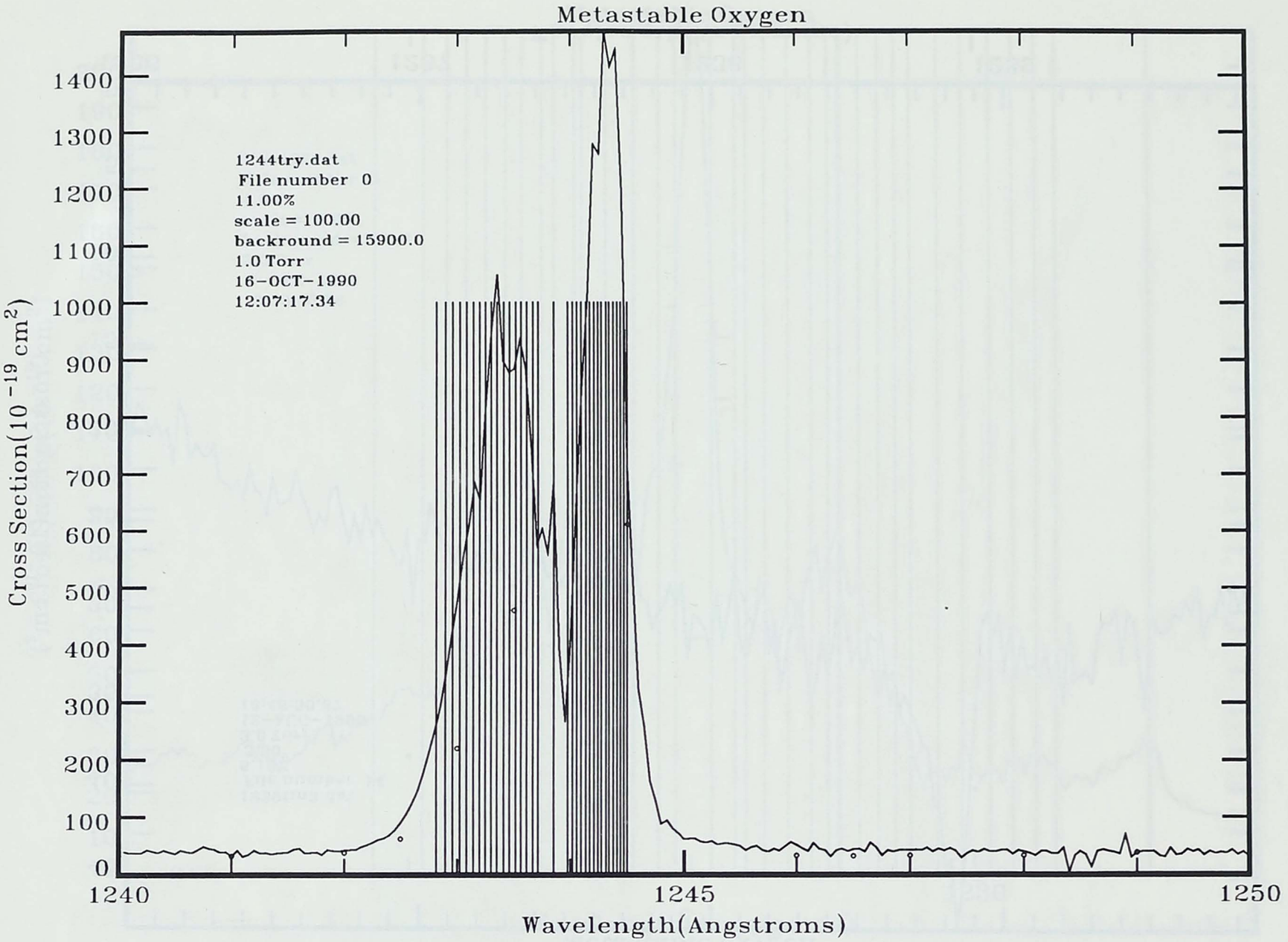

Figure C.7:

Microwave On

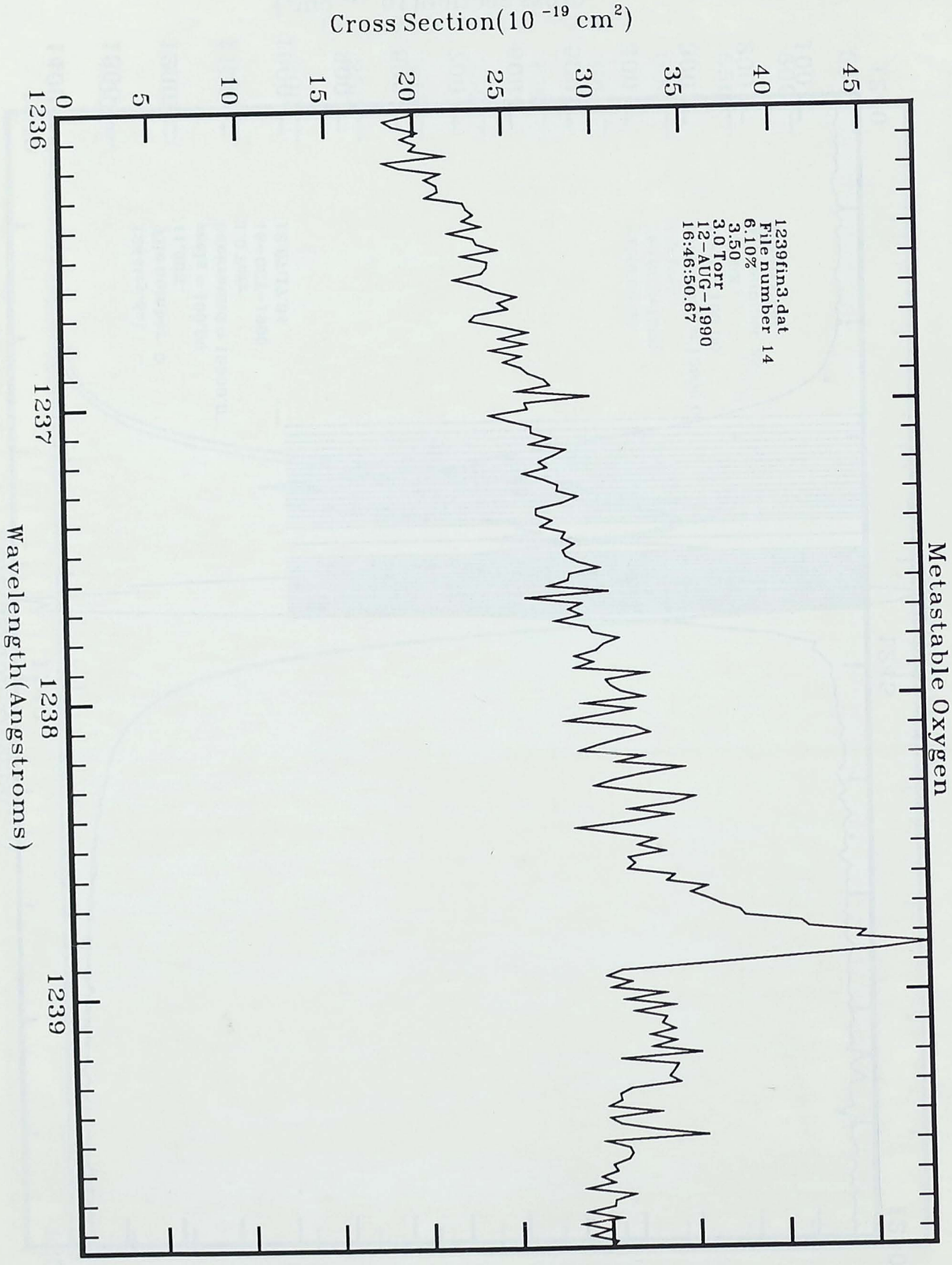
Cross Section(10^{-19} cm^2)
Metastable Oxygen
1239fin3.dat
File number 14
6.10%
3.50
3.0 Torr
12-AUG-1990
16:46:50.67
Wavelength(Angstroms)
1236
1237
1238
1239
0
5
10
15
20
25
30
35
40
45

Figure C.8:

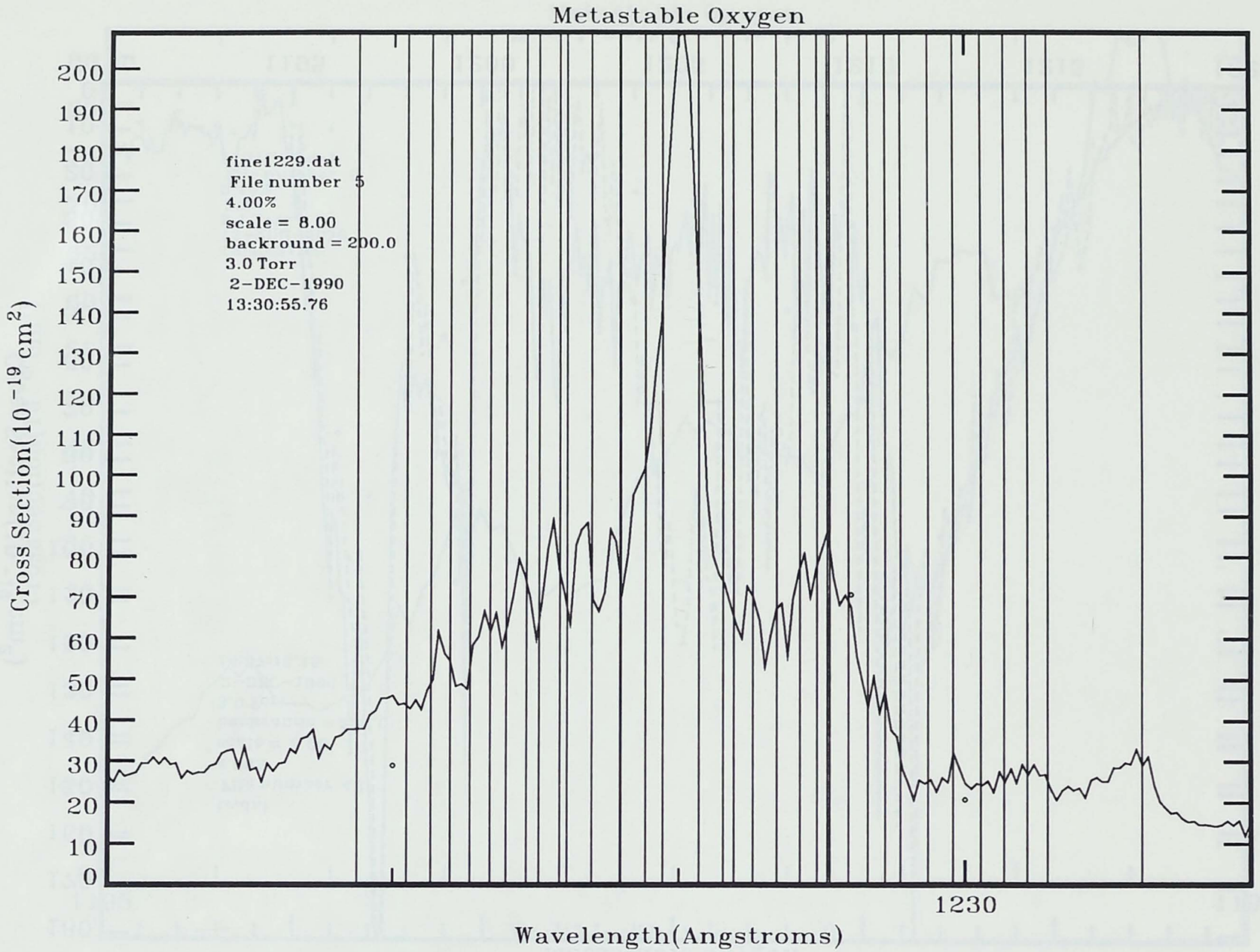

Figure C.9:

Metastable Oxygen

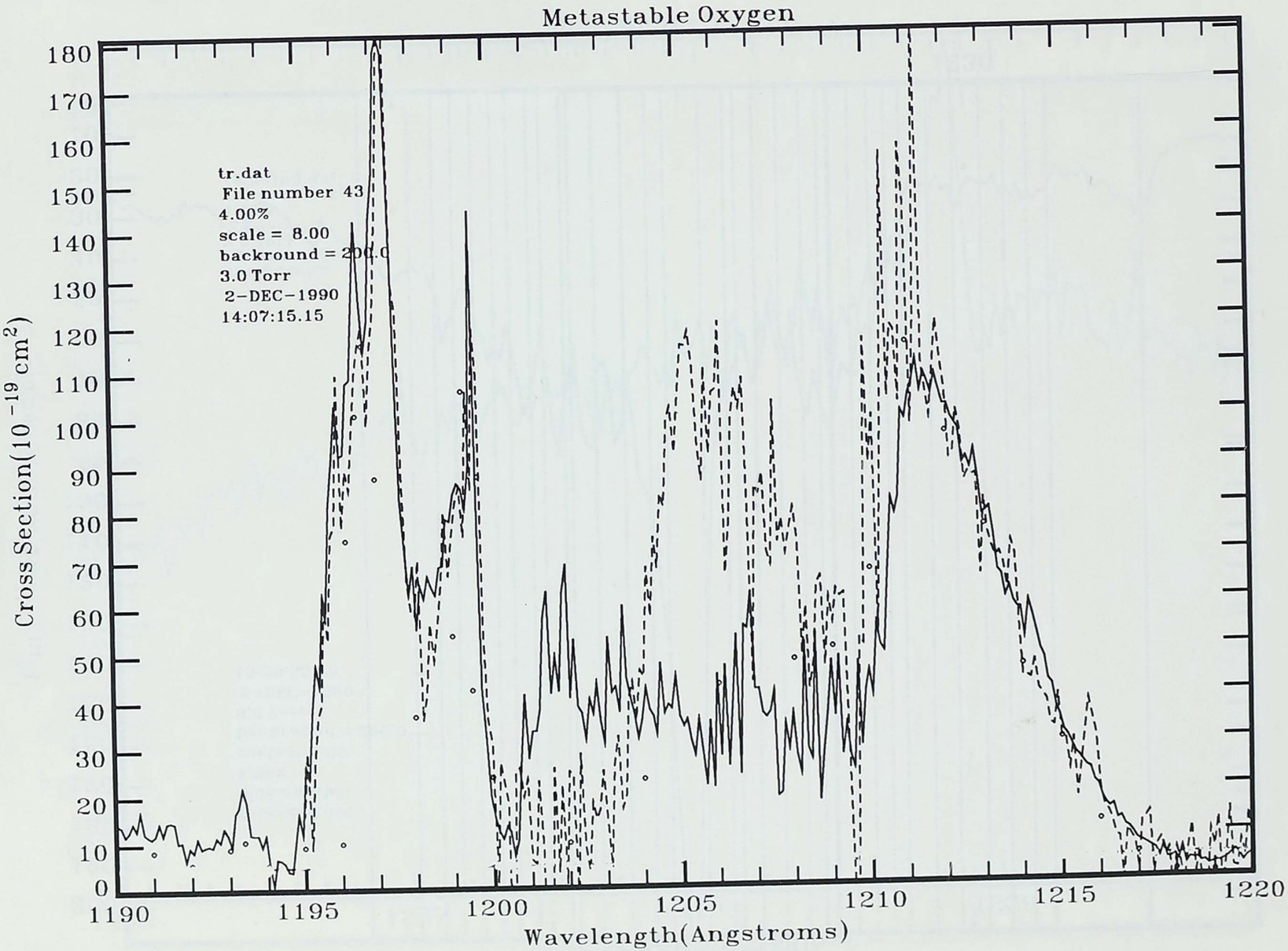
Metastable Oxygen
tr.dat
File number 43
4.00%
scale = 8.00
backround = 200.0
3.0 Torr
2-DEC-1990
14:07:15.15
Cross Section(10^{-19} cm^2)
Wavelength(Angstroms)
0
10
20
30
40
50
60
70
80
90
100
110
120
130
140
150
160
170
180
1190
1195
1200
1205
1210
1215
1220

Figure C.10:

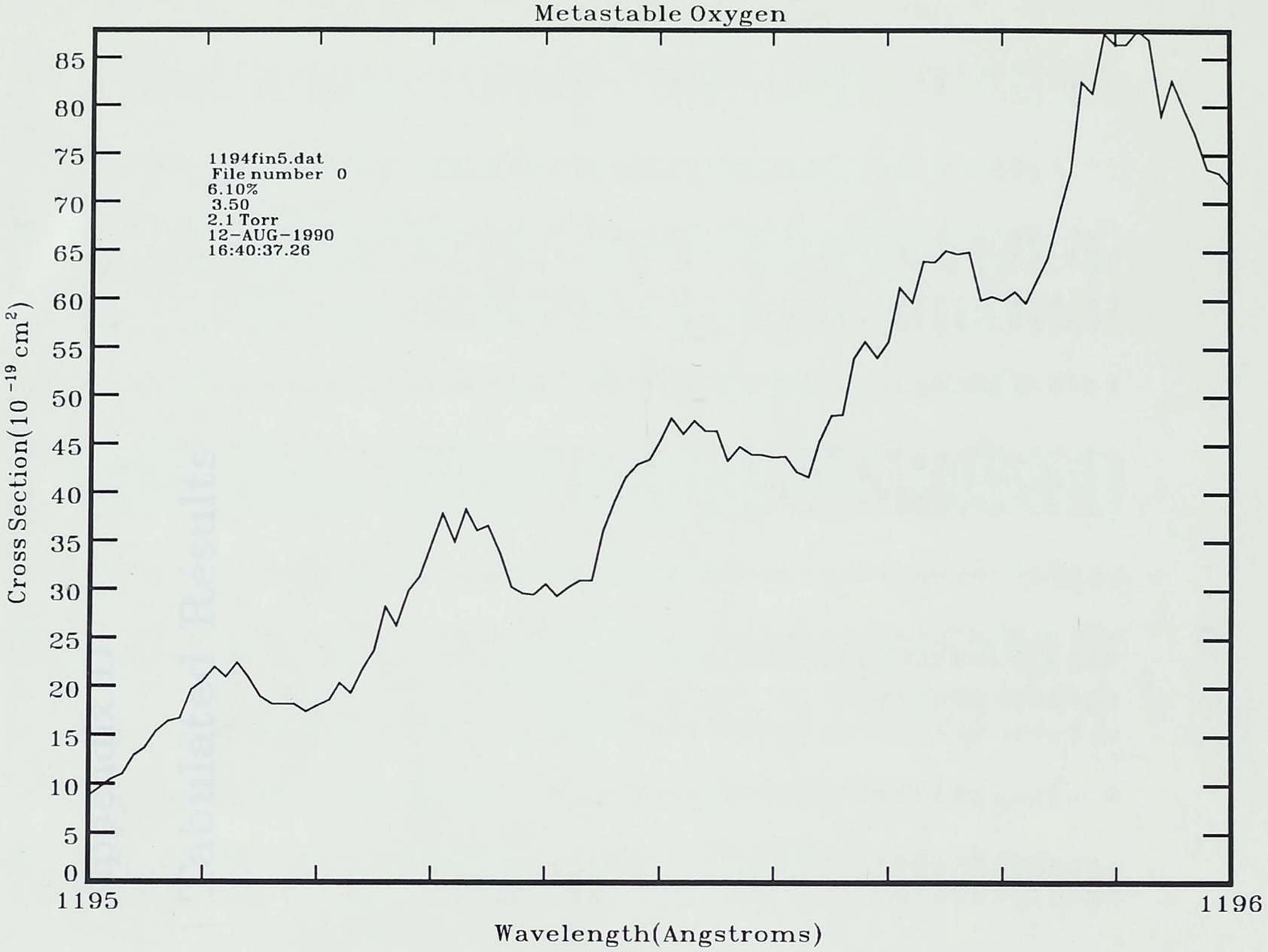

Figure C.11:

Metastable Oxygen

Appendix D

Tabulated Results

(A) Theory – $\sigma_{metastable}$, (B) Exp. – $\sigma_{metastable}$, (C) Exp – σ_{ground}, Units = 10^{-18} cm^2.

Wavelength (Å)	A	B	C	Wavelength	A	B	C
1270.0	1	1	0	1297.5	1	0	5
1270.5	1	1	0	1298.0	0	1	4
1271.0	1	4	0	1300.0	1	2	3
1271.5	2	0	0	1300.5	2	3	3
1272.0	4	6	1	1301.0	3	3	3
1272.5	7	5	1	1301.5	4	5	3
1273.0	11	7	0	1302.0	4	12	3
1273.5	16	14	0	1302.5	5	5	3
1274.0	23	27	0	1303.0	6	6	3
1274.5	32	24	0	1303.5	6	9	3
1275.0	42	31	0	1304.0	7	9	3
1275.5	53	41	1	1304.5	7	8	3
1276.0	64	51	1	1305.0	8	17	3
1276.5	76	60	1	1305.5	9	10	2
1277.0	88	70	1	1306.5	9	8	3
1277.5	98	86	1	1307.0	10	13	3
1278.0	108	92	2	1307.5	10	10	2
1278.5	116	99	2	1308.0	10	10	2
1279.0	123	103	2	1308.5	11	10	2
1279.5	128	109	2	1309.0	11	14	2
1280.0	132	121	2	1309.5	11	10	3
1280.5	133	118	3	1310.0	11	11	3
1281.0	133	124	2	1310.5	11	10	3
1281.5	132	123	2	1311.5	10	9	3
1282.0	132	126	2	1312.0	9	9	3
1282.5	138	130	3	1312.5	9	7	4
1283.0	143	137	3	1313.0	13	8	4
1283.5	172	162	3	1313.5	9	8	4
1284.0	170	160	3	1314.0	9	10	4
1284.5	165	171	3	1314.5	9	8	5
1285.0	162	162	5	1315.0	9	8	5
1285.5	160	167	4	1315.5	9	7	5
1286.0	157	156	3	1316.0	8	6	6
1286.5	155	162	4	1316.5	8	6	6
1287.0	151	149	5	1317.0	8	7	6
1287.5	147	155	4	1317.5	7	5	7
1288.0	143	139	4	1318.0	7	8	7
1288.5	137	145	4	1318.5	7	4	8
1289.0	130	132	4	1319.0	6	6	8
1289.5	122	132	4	1319.5	6	4	9
1290.0	112	107	4	1320.0	5	5	9
1290.5	102	100	4	1320.5	5	4	11
1291.0	90	93	5	1321.0	5	3	11
1291.5	79	75	4	1321.5	4	2	12
1292.0	67	68	5	1322.0	4	3	12
1292.5	55	53	5	1322.5	3	2	13
1293.0	44	44	5	1324.5	2	0	15
1293.5	35	30	5	1325.5	1	0	16
1294.0	26	30	5	1327.0	0	1	15
1294.5	19	21	5	1327.5	0	1	18
1295.0	14	17	5	1329.0	0	1	20
1295.5	9	9	4	1329.5	0	0	20
1296.0	6	6	5	1330.0	1	2	20
1296.5	3	11	4	1330.5	1	2	20
1297.0	2	3	4	1331.0	1	5	20

(A) Theory – $\sigma_{metastable}$, (B) Exp. – $\sigma_{metastable}$,(C) Exp – σ_{ground}, Units = 10^{-18} cm^2.

Wavelength (Å)	A	B	C	Wavelength	A	B	C
1332.0	2	4	21	1360.0	3	3	72
1332.5	3	4	21	1360.5	3	4	74
1333.0	3	7	21	1361.0	2	1	76
1333.5	4	4	21	1361.5	2	3	77
1334.0	5	8	21	1362.5	1	5	82
1334.5	6	7	21	1363.0	1	6	83
1335.0	7	8	21	1363.5	1	8	86
1335.5	7	9	21	1364.0	1	10	89
1336.0	8	11	21	1364.5	1	3	91
1336.5	9	9	21	1365.0	1	14	93
1337.0	10	12	21	1365.5	2	6	96
1337.5	11	13	20	1366.0	3	15	98
1338.0	12	15	20	1366.5	4	11	101
1338.5	13	15	20	1367.0	6	16	102
1339.0	14	12	20	1367.5	8	19	105
1339.5	14	13	20	1368.0	10	21	107
1340.0	15	15	20	1368.5	13	18	108
1340.5	15	14	20	1369.0	17	27	111
1341.0	16	13	20	1369.5	21	28	112
1341.5	15	13	21	1370.0	25	27	115
1342.0	15	13	21	1370.5	30	43	116
1342.5	14	12	21	1371.0	36	39	117
1343.0	13	13	22	1371.5	42	43	118
1343.5	14	14	22	1372.0	48	55	121
1344.0	15	15	23	1372.5	53	57	121
1344.5	16	13	24	1373.0	58	61	122
1345.0	16	15	25	1373.5	62	58	123
1345.5	17	11	27	1374.0	65	66	124
1346.0	17	12	30	1374.5	65	64	126
1346.5	17	12	32	1375.0	62	63	126
1347.0	17	17	35	1375.5	56	59	126
1347.5	16	14	37	1376.0	45	44	128
1348.0	16	13	40	1376.5	47	56	129
1348.5	16	12	44	1377.0	64	72	129
1349.0	16	12	47	1377.5	73	73	130
1349.5	15	15	50	1378.0	77	82	130
1350.0	15	14	54	1378.5	78	80	132
1350.5	15	15	54	1379.0	79	80	131
1351.0	14	12	60	1379.5	79	76	132
1351.5	14	7	64	1380.0	78	73	134
1352.0	13	13	66	1380.5	77	71	134
1352.5	13	19	61	1381.0	76	74	134
1353.0	12	8	70	1381.5	74	73	133
1353.5	11	2	71	1382.0	72	67	135
1354.0	11	7	72	1382.5	71	73	134
1354.5	10	9	71	1383.0	69	67	135
1355.0	10	5	72	1383.5	67	58	136
1355.5	9	5	71	1384.0	65	56	136
1356.0	8	7	72	1384.5	63	52	135
1356.5	8	8	71	1385.0	60	57	136
1357.0	7	6	71	1385.5	58	55	138
1357.5	6	3	70	1386.0	56	47	137
1358.0	6	4	70	1386.5	54	52	136
1358.5	5	7	72	1387.0	52	51	136
1359.0	4	8	72	1387.5	50	50	136

(A) Theory – $\sigma_{metastable}$, (B) Exp. – $\sigma_{metastable}$,(C) Exp – σ_{ground}, Units = 10^{-18} cm^2.

Wavelength (Å)	A	B	C	Wavelength	A	B	C
1388.5	47	38	138	1416.0	114	106	144
1389.0	45	44	138	1416.5	108	100	143
1389.5	43	40	137	1417.0	102	95	144
1390.0	41	46	138	1417.5	97	83	144
1390.5	39	40	138	1418.0	93	82	144
1391.0	37	28	139	1418.5	89	86	143
1391.5	36	37	138	1419.0	86	79	143
1392.0	34	26	139	1419.5	82	68	144
1392.5	32	35	139	1420.0	80	68	144
1393.0	30	35	139	1420.5	77	69	143
1393.5	28	32	139	1421.0	74	66	144
1394.0	26	27	139	1421.5	72	61	144
1394.5	25	24	139	1422.0	70	62	144
1395.0	23	26	140	1422.5	68	61	144
1395.5	21	27	140	1423.0	66	50	145
1396.0	19	7	141	1423.5	64	52	143
1396.5	17	22	140	1424.0	62	52	144
1397.0	16	16	141	1424.5	60	53	143
1397.5	14	14	141	1425.0	59	51	144
1398.0	12	16	141	1425.5	57	42	143
1398.5	10	20	140	1426.0	55	49	144
1399.0	8	19	141	1426.5	54	45	144
1399.5	7	16	141	1427.0	52	49	144
1400.0	5	10	143	1427.5	51	38	143
1400.5	4	8	142	1428.0	49	38	143
1401.0	4	13	142	1428.5	48	40	143
1401.5	4	16	142	1429.0	46	45	144
1402.0	5	18	143	1429.5	45	43	142
1402.5	9	37	142	1430.0	43	32	144
1403.0	15	31	143	1430.5	42	23	144
1403.5	27	54	142	1431.0	40	41	143
1404.0	46	70	143	1431.5	39	26	143
1404.5	74	104	142	1432.0	38	32	144
1405.0	113	152	143	1432.5	36	39	143
1405.5	167	206	143	1433.0	35	27	144
1406.0	233	278	144	1433.5	33	32	143
1406.5	309	355	143	1434.0	32	25	146
1407.0	383	433	143	1434.5	30	17	144
1407.5	429	473	143	1435.0	29	21	143
1408.0	426	462	143	1435.5	27	28	143
1408.5	377	410	144	1436.0	26	24	143
1409.0	314	330	144	1436.5	24	28	143
1409.5	258	268	144	1437.0	23	26	143
1410.0	215	230	144	1437.5	22	39	142
1410.5	185	201	143	1438.0	36	49	142
1411.0	168	178	144	1438.5	48	70	143
1411.5	164	177	143	1439.0	62	87	143
1412.0	178	184	145	1439.5	90	127	143
1412.5	214	214	143	1440.0	132	201	142
1413.0	285	268	144	1440.5	197	270	142
1413.5	203	206	144	1441.0	294	405	142
1414.0	167	158	144	1441.5	431	548	143
1414.5	146	143	144	1442.0	572	701	140
1415.0	132	125	144	1442.5	970	1004	143
1415.5	122	115	143	1443.0	275	381	141

(A) Theory – $\sigma_{metastable}$, (B) Exp. – $\sigma_{metastable}$, (C) Exp – σ_{ground}, Units = 10^{-18} cm^2.

Wavelength (Å)	A	B	C	Wavelength	A	B	C
1444.0	84	103	142	1471.5	24	20	132
1444.5	70	74	141	1472.0	23	19	131
1445.0	62	62	143	1472.5	22	23	131
1445.5	58	59	141	1473.0	22	12	132
1446.0	56	57	142	1473.5	21	12	132
1446.5	55	58	140	1474.0	20	23	131
1447.0	55	66	141	1474.5	20	21	130
1447.5	57	63	140	1475.0	19	17	130
1448.0	59	62	141	1475.5	19	25	129
1448.5	63	75	140	1476.0	18	16	131
1449.0	68	64	140	1476.5	20	31	130
1449.5	74	70	140	1477.0	33	36	129
1450.0	81	74	141	1477.5	23	45	128
1450.5	86	69	141	1478.0	39	51	129
1451.0	89	78	141	1478.5	52	70	129
1451.5	90	80	139	1479.0	52	100	129
1452.0	94	89	140	1479.5	76	113	127
1452.5	101	97	140	1480.0	114	128	126
1453.0	109	107	139	1480.5	136	149	126
1453.5	117	115	139	1481.0	169	184	127
1454.0	123	112	140	1481.5	267	271	127
1454.5	127	128	138	1482.0	36	46	127
1455.0	129	120	139	1482.5	25	40	125
1455.5	128	123	138	1483.0	26	29	126
1456.0	124	115	139	1483.5	33	42	125
1456.5	118	111	138	1484.0	53	49	126
1457.0	111	117	138	1484.5	84	85	126
1457.5	103	106	138	1485.0	137	142	124
1458.0	96	93	138	1485.5	225	227	125
1458.5	89	98	138	1486.0	370	374	125
1459.0	82	82	138	1486.5	472	399	124
1459.5	76	89	137	1487.0	116	124	124
1460.0	71	69	138	1487.5	51	67	123
1460.5	66	63	137	1488.0	37	39	124
1461.0	62	61	137	1488.5	31	33	123
1461.5	58	60	136	1489.0	27	28	123
1462.0	54	53	136	1489.5	25	28	122
1462.5	51	57	135	1490.0	24	31	122
1463.0	48	48	136	1490.5	22	17	123
1463.5	46	44	136	1491.0	20	11	122
1464.0	44	48	135	1491.5	18	15	123
1464.5	41	37	136	1492.0	16	15	124
1465.0	39	40	135	1492.5	15	23	122
1465.5	38	40	134	1493.0	15	20	121
1466.0	36	30	134	1493.5	14	22	120
1466.5	35	40	134	1494.0	13	10	122
1467.0	33	29	134	1495.0	13	15	121
1467.5	32	41	133	1495.5	12	13	120
1468.0	31	39	132	1496.0	12	13	120
1468.5	30	18	134	1496.5	12	11	121
1469.0	29	18	134	1497.0	11	11	119
1469.5	28	22	132	1497.5	11	4	119
1470.0	27	23	133	1498.0	11	15	118
1470.5	26	26	132	1498.5	10	14	117
1471.0	25	27	132	1499.5	10	13	117

(A) Theory – $\sigma_{metastable}$, (B) Exp. – $\sigma_{metastable}$, (C) Exp – σ_{ground}, Units = 10^{-18} cm^2.

Wavelength (Å)	A	B	C	Wavelength	A	B	C
1500.5	10	6	116	1532.5	3	4	93
1501.0	9	15	117	1533.0	3	3	91
1501.5	9	9	116	1533.5	3	10	91
1502.0	9	13	116	1534.0	3	4	91
1502.5	9	25	114	1534.5	3	10	91
1503.0	9	6	115	1535.0	3	9	90
1503.5	8	3	114	1535.5	3	0	90
1504.0	8	6	114	1536.5	2	4	90
1504.5	8	9	115	1537.0	2	1	90
1505.0	8	1	114	1537.5	2	0	89
1506.0	8	2	113	1538.0	2	2	89
1506.5	7	11	112	1539.0	1	7	87
1507.0	7	13	113	1539.5	1	9	87
1507.5	7	8	112				
1508.0	7	7	112				
1508.5	7	14	111				
1509.0	7	10	112				
1509.5	7	17	109				
1510.0	6	4	110				
1510.5	6	8	109				
1511.0	6	3	110				
1511.5	6	3	109				
1512.0	6	12	108				
1512.5	6	17	108				
1513.0	6	3	108				
1513.5	6	7	108				
1514.0	6	4	108				
1514.5	5	13	107				
1515.0	5	1	107				
1515.5	5	7	105				
1516.5	5	3	106				
1517.0	5	11	106				
1517.5	5	7	105				
1518.0	5	11	105				
1518.5	5	9	104				
1519.0	5	7	104				
1519.5	5	8	104				
1521.0	4	1	102				
1521.5	4	9	102				
1522.0	4	3	101				
1522.5	4	5	101				
1523.5	4	7	100				
1524.5	4	7	99				
1525.0	4	2	100				
1525.5	4	9	99				
1526.5	4	6	98				
1527.5	3	11	97				
1528.0	3	8	97				
1528.5	3	12	95				
1529.5	3	6	95				
1530.0	3	13	95				
1530.5	3	5	94				
1531.0	3	1	94				
1531.5	3	7	94				
1532.0	3	1	94				

Bibliography

[1] B. Lewis, *Appl. Opt.*, **22**, 1546 (1983).

[2] B. Lewis, *Appl. Opt.*, **21**, 2523 (1982).

[3] B. Lewis, L. Berzins and J. Carver, *J. Quant. Spectrosc. Radiat. Transfer*, **37**, 255 (1987).

[4] B. Lewis, L. Berzins, and J. Carver, *J. Quant. Spectrosc. Radiat. Transfer*, **36**, 209 (1986).

[5] H. Lefebre and R. Colin, *J. Mol. Spectrosc.*, **65**, 1 (1977).

[6] E. van Dishoeck, M. Hemert, A. Allision and A. Dalgarno, *J. Chem. Phys.*, **81**, 5709 (1984).

[7] J. Wang, D. McCoy, A. Blake and L. Torop, *J. Quant. Spectrosc. Radiat. Transfer*, **38**, 19 (1987).

[8] B. Lewis and S. Gibson, *Canad. J. Phys.*, **68**, 231 (1990).

[9] R. Ogorzalek Loo, W. Marinelli, P. Huston, S. Arepalli, J. Wiesenfeld and R. Field, *J. Chem. Phys.*, **91**, 5185 (1989).

[10] S. Ogawa and M. Ogawa, *Can. J. Phys.*, **53**, 1845 (1975).

[11] J. Samson and V. Petrosky, *Phys. Rev. A*, **9**, 2449 (1974).

[12] B. Lewis, S. Gibson, and J. Carver, "To be published."

[13] R. Badger, A. Wright, and R. Whitlock, *J. Chem. Phys.*, **43**, 4345 (1965).

[14] K. Yamawaki, *Absorption Spectrum of O_2 in the $a^1\Delta_g$ metastable state in the region 1090 to 1700Å*. PhD thesis, University of Southern California, 1972.

[15] L. Chang, *Rotational analysis of high resolution O_2 absorption bands in the region from 1085 to 1165Å*. PhD thesis, University of Southern California, 1972.

[16] F. Alberti, R. Ashby and A. Douglas, *J. Chem. Phys.*, **46**, 337 (1968).

[17] K. Wananabe, S. Kashiwabara and R. Fujimoto, *J. Appl. Phys.*, **59**, 42 (1986).

[18] H. Okabe, *Photochemistry of small molecules*. New York: Wiley, 1978.

[19] R. Collins, D. Husain and R. Donovan, *J. Chem. Soc. Faraday*, **69**, 145 (1973).

[20] R. Wayne, *J. Photochem.*, **25**, 345 (1984).

[21] R. Huffman, J. Larrabee and Y. Tanaka, *J. Chem. Phys.*, **46**, 2213 (1967).

[22] O. Spalek, J. Kodymova and A. Hirsl, *J. Appl. Phys.*, **62**, 2208 (1987).

[23] P. Cough and B. Thrush, *Chemistry and Industry*, **19**, 1971 (1966).

[24] F. Fehenfield, K. Evenson and H. Broida, *Rev. Sci Instrum.*, **36**, 294 (1965).

[25] A. Vasileva, I. Grishina, K. Klopoviskii, A. Kovalev, A. Osipov A. Rakhimov and T. Rakhimova, *Sov. J Plasma Phys.*, **11**, 130 (1985).

[26] Y. Tanaka, *J. Opt. Soc. Am.*, **45**, 710 (1955).

[27] J. Berkowitz, *Photoabsorption, Photoionization and Photoelectron Spectroscopy.* New York: Academic Press, 1979.

[28] J. Somerville, *Physics of Arcs.* New York: D. Van Nostrand, 1954.

[29] J. Samson, *Techniques of Vacuum Ultraviolet Spectrpscophy.* New York: Wiley, 1967.

[30] B. Candi, *Rev. Sci. Instrum.*, **21**, 2523 (1982).

[31] Macmillan Software Company, New York, *Asyst - Version 1.53*, 1985.

[32] M. Ogawa and K. Yamawaki, *Can. J. Phys.*, **47**, 1805 (1969).

[33] S. Gibson, *High resolution vacuum Ultra-violet photoabsorption in the Schumann-Runge system of molecular oxygen.* PhD thesis, Adelaide University, 1983.

[34] J.Hey and J.King, *J. Quant. Spectrosc. Radiat. Transfer*, **40**, 629 (1988).

[35] S. Penner, *Quantitative Molecular Spectroscopy and Gas Emissivities.* Reading: Addison-Wesley, 1959.

[36] F. Morse and F. Kaufman, *J. Chem. Phys.*, **42**, 1785 (1964).

[37] A. Prag, C. Fairchild and K. Clark, *Phys. Rev.*, **137**, 1358 (1965).

[38] M. Weiss, G. Lawrence, and R. Young, *J. Chem. Phys.*, **52**, 2867 (1970).

[39] D. Katayama, S. Ogawa, M. Ogawa and Y. Tanaka, *J. Chem. Phys.*, **67**, 2132 (1977).

[40] F. Mies, *Phys. Rev.*, **175**, 164 (1986).

[41] R. Saxon and B. Liu, *J. Chem. Phys.*, **67**, 5432 (1977).

[42] B. Moss and W. Goddard III, *J. Chem Phys.*, **63**, 3523 (1975).

[43] R. Buenker and S. Peyerimhoff, *Chem. Phys. Lett.*, **34**, 225 (1975).

[44] H. Lefebvre-Brion and R. Field, *Perturbations in the Spectra of Diatomic Molecules.* Orlando, Florida: Academic Press, 1986.

[45] K. Baldwin, R. Swift, and R. Watts, *Rev. Sci. Instrum.*, **58**, 812 (1987).

[46] R. Deloche, P. Monchicourt, M. Cheret and F. Lambert, *Phys. Rev. A.*, **13**, 1140 (1976).

[47] E. Beaty, J. Browne and A. Dalgarno, *Phys. Rev. Lett.*, **723**, 16 (1966).

[48] B. Lewis, S. Gibson, M. Emami and J. Carver, *J. Quant. Spectrosc. Radiat. Transfer*, **40**, 1 (1988).

[49] G. Hilber, A. Lago and R. Wallenstein, *Opt. Soc. Am. B*, **4**, 1753 (1987).

[50] J. Marangos, N. Shen, H. Ma, M. Hutchinson and J. Connerade, *J. Opt. Soc. Am. B.*, **7**, 1254 (1990).

[51] Rientjes, *Nonlinear Parametric Processes in liquids and gases.* New York: Acedemic Press, 1984.

[52] K. Miyazaki, H. Sakai and T. Sato, *Appl. Opt.*, **28**, 699 (1989).

[53] G. Schilling, W. Ernst, and N. Schwentner, *Opt. Comm.*, **70**, 428 (1989).

[54] C. Bjorklund, *IEEE J. Quantum Electronics*, **QE-11**, 287 (1975).

[55] M. Klein and T. Furtag, *Optics*. New York: Wiley, 1986.

[56] K. Miyazaki, H. Sakai and T. Sato, *IEEE J. Quantum Electronics*, **QE-22**, 2266 (1986).

[57] R. Hilbig and R. Wallenstien, *IEEE J. Quantum Electronics*, **QE-19**, 1759 (1983).

[58] A. Smith and W. Alford, *J. Opt. Soc. Am. B*, **4**, 1765 (1987).

[59] W. Jamroz, P. LaRocque and B. Stoicheff, *Opt. Lett.*, **7**, 617 (1982).

[60] R. Mahon, T. McIlrath, V. Myerscough and D. Koopman, *IEEE J. Quantum Electronics*, **QE-15**, 444 (1979).

[61] M. Born and E. Wolf, *Principles of Optics*. London: Pegamon Press, 1959.

[62] E. Eyler, "Private communications," 1990. Dept. of Phys. and Astronomy, Univ. of Delaware.

[63] W. Glad and J. Hessler, *App. Opt.*, **26**, 3181 (1987).

[64] R. Von Trebra and T. Koch, *Chem. Phys. Lett.*, **93**, 315 (1982).

[65] J. Samson and G. Haddad, *J. Opt. Soc. Am.*, **64**, 47 (1974).

[66] J. Cooper and S. Manson, *Phys. Rev.*, **177**, 157 (1969).

[67] W. Linderman. PhD thesis, Adelaide University, 1982.

[68] J. Samson and J. Gardiner, *J. Opt. Soc. Am.*, **62**, 856 (1972).

[69] D. Holland, A. Parr, D. Ederer, J. Dehmer and J. West, *Nuc. Instrum. and Methods*, **331**, 331 (1982).

[70] J. Samson and R. Cains, *Phys. Rev. A*, **173**, 80 (1968).

[71] D. Willaims, ed., *Methods of Experimental Physics*, vol. 3B. New York: Acedemic, 1974.

[72] T. Tsuboi, E. Xu, Y. Bae and K. Gillen, *Rev. Sci. Instrum.*, **59**, 1357 (1988).

[73] L. Mattson, B. Wannberg, H. Vaahuizen, I. Reineck and K. Seighan, "A focussing vuv polarizer system for valence electron spectroscophy: Performance," Tech. Rep. UUIP-1009, Institute of Physics, Uppsala University., 1979.

[74] T. Reddish, B. Wallbank, and J. Comer, *J. Phys. E*, **17**, 100 (1984).

[75] D. Brewer, W. Newell, and A. Smith, *J. Phys. E*, **13**, 114 (1980).

[76] M. Y. Adam, "Private communications," 1987. L.U.R.E. Uni. Paris Sud, France.

[77] D. Frost, C. McDowell and D. Vroom, *Proc. Roy. Soc. (London)*, **296**, 566 (1967).

[78] J. Samson, *Phil. Trans. Roy. Soc. Lond. A.*, **268**, 141 (1970).

[79] E. Staib, *J. Phys. E*, **5**, 484 (1972).

[80] S. Cvejanovic and F. Read, *J. Phys. B*, **7**, 1180 (1974).

[81] P. Hammond, F. Read, S. Cvejanovic and G. King, *J. Phys. B*, **18**, L141 (1985).

[82] L. Frank, N. Henderson and R. Swisher, *Rev. Sci. Instrum.*, **40**, 865 (1969).

[83] C. Lovejou and D. Nesbit, *Rev. Sci. Instr.*, **58**, 807 (1987).

[84] J. Samson, *J. Opt. Soc. Am.*, **59**, 356 (1969).

[85] P. Hill, *Rev. Sci. Instrum.*, **59**, 1237 (1988).

[86] G. Herzberg, *Spectra of Diatomic Molecules.* New York: D. Van Nostrand, 1966.

[87] A. Thorne, *Spectrophysics.* London: Chapman and Hall, 1988.

[88] B. Bransden and C. Joachain, *Physics of Atoms and Molecules.* London: Longman, 1983.

[89] E. Wigner and E. Witmer, *Z. Physik*, **54**, 856 (1929).

[90] F. Reiche and H. Rademacher, *Z. Physik*, **39**, 444 (1926).

[91] B. Johnson, *J. Chem. Phys.*, **69**, 4678 (1978).

[92] J. Tellinghiusen , *J. Mol. Spec.*, **44**, 183 (1972).

[93] L. Torop, J. Wang, D. McCoy and A. Blake, 1990.